

5-1-2014

## Modern to Late Pleistocene Stable Isotope Climatology of Alaska

Alison Sloat

*University of Nevada, Las Vegas*

Follow this and additional works at: <https://digitalscholarship.unlv.edu/thesesdissertations>



Part of the [Climate Commons](#), [Geochemistry Commons](#), and the [Geology Commons](#)

---

### Repository Citation

Sloat, Alison, "Modern to Late Pleistocene Stable Isotope Climatology of Alaska" (2014). *UNLV Theses, Dissertations, Professional Papers, and Capstones*. 2143.  
<http://dx.doi.org/10.34917/5836162>

This Dissertation is protected by copyright and/or related rights. It has been brought to you by Digital Scholarship@UNLV with permission from the rights-holder(s). You are free to use this Dissertation in any way that is permitted by the copyright and related rights legislation that applies to your use. For other uses you need to obtain permission from the rights-holder(s) directly, unless additional rights are indicated by a Creative Commons license in the record and/or on the work itself.

This Dissertation has been accepted for inclusion in UNLV Theses, Dissertations, Professional Papers, and Capstones by an authorized administrator of Digital Scholarship@UNLV. For more information, please contact [digitalscholarship@unlv.edu](mailto:digitalscholarship@unlv.edu).

MODERN TO LATE PLEISTOCENE STABLE ISOTOPE  
CLIMATOLOGY OF ALASKA

By

Alison Renee Sloat

Bachelor of Science in Geological Sciences  
California State University, San Bernardino  
2005

Master of Science in Environmental Sciences  
California State University, San Bernardino  
2008

A dissertation submitted in partial fulfillment  
of the requirements for the

Doctor of Philosophy - Geosciences

Department of Geoscience  
College of Sciences  
The Graduate College

University of Nevada, Las Vegas  
May 2014

Copyright by Alison R. Sloat, 2014  
All Rights Reserved



## THE GRADUATE COLLEGE

We recommend the dissertation prepared under our supervision by

**Alison Sloat**

entitled

**Modern to Late Pleistocene Stable Isotope Climatology of Alaska**

is approved in partial fulfillment of the requirements for the degree of

**Doctor of Philosophy - Geosciences**

Department of Geosciences

Matthew Lachinet, Ph.D., Committee Chair

Daniel Lawson, Ph.D., Committee Member

Steve Rowland, Ph.D., Committee Member

Ganqing Jiang, Ph.D., Committee Member

Liam Frink, Ph.D., Graduate College Representative

Kathryn Hausbeck Korgan, Ph.D., Interim Dean of the Graduate College

**May 2014**

## ABSTRACT

### **Modern to late Pleistocene stable isotope climatology of Alaska**

By

Alison R. Sloat

Dr. Matthew Lachniet, Examination Committee Chair  
Associate Professor of Geoscience  
University of Nevada, Las Vegas

Understanding modern controls on climate is necessary to interpret past climatic conditions. This project investigated the modern controls on  $\delta^{18}\text{O}$  and  $\delta\text{D}$  values in Alaskan surface waters to interpret the controls on Late Pleistocene climate variability. ArcGIS was used to develop an isoscape of modern  $\delta^{18}\text{O}$  and  $\delta\text{D}$  values of over 400 surface water samples collected across Alaska and the Yukon. It was found that winter temperature and precipitation have the greatest controls on  $\delta^{18}\text{O}$  and  $\delta\text{D}$  values in Alaska, resulting in high  $\delta^{18}\text{O}$  values along the coast of the Gulf of Alaska and low values inland toward Central Alaska. This isoscape can be applied to paleoenvironmental, modern, and future records to determine isotope-precipitation-temperature values. This is a useful tool in determining paleotemperatures of Alaska which is necessary for the interpretation of the magnitude, timing, and patterns of past response to climatic change.

Previous work suggested ancient preserved ice wedges in the CRREL Permafrost Tunnel formed syngenetically during Marine Isotope Stage 3 (MIS 3). However, a new method of determining the timing of ice wedge and pool ice formation using radiocarbon-dated DOC and  $\text{CO}_2$  reveals that the features are much younger than previously thought and are epigenetic in origin. At least five freeze events and one melt event are apparent in

the tunnel, with likely ages between 26 and 12.9 cal ka BP, during MIS 2. The prevalence of inversions in the radiocarbon ages indicates that carbon may persist for as long as 17,000 years within permafrost environments, potentially providing anomalous age dates when dating carbon in permafrost.

To better constrain the timing and climatic conditions during ice wedge formation, eight ice wedges and seven ice pools were sampled at high temporal resolution for stable isotopes and were combined with  $^{14}\text{C}$  ages of DOC from within the ice to estimate the timing of formation and climatic conditions under which they formed. Four intervals of cooling and one interval of warming were recorded in the ice wedge and pool ice, with  $\delta^{18}\text{O}$  values ranging from -28.9‰ to -20.4‰. These values range between -6.6 below and +1.9‰ above the modern snow  $\delta^{18}\text{O}$  value of -22.3‰, suggesting that some of the ice wedges formed during colder-than-modern conditions. Paleo-winter temperatures ranged from -41.6 to -11.2°C, while paleo-mean annual temperatures (MAT) ranged from -14.1 to 1.4°C, consistent with paleotemperature fluctuations observed in the Bering Sea SST and Greenland ice core records. Based on a visual correlation to the Bering Sea SST record within the ice age limits described in Chapter 3, it is suggested here that Freeze event 1 likely occurred during cooling of -12.3 to -1.2°C between 26.5 - 25.3 cal ka BP, coinciding with Heinrich event 2, while Freeze event 2 occurred during cooling of -8.8 to -2.8°C between 21.0 - 20.5 cal ka BP. One warming interval, M1, when clear pool ice formed in a melt horizon above the F1 and F2 wedges, may have occurred as paleo-MAT ranged between -9.9 and -1.2°C between 19.1 - 18.8 cal ka BP. Freeze event 3 represents the lowest (coldest)  $\delta^{18}\text{O}$  values. These values suggest that paleo-MAT ranged between -14.1 and -9.2°C, which is correlated to the coldest regional climate interval when the

Laurentide Ice Sheet reached its local maximum extent in the Yukon between 17.3 - 17.0 cal ka BP, coinciding with Heinrich event 1. Freeze event 4 has high  $\delta^{18}\text{O}$  values that are similar to those of a late Holocene ice wedge in the nearby Vault Creek permafrost tunnel; that wedge was radiocarbon-dated to ca. 3.9 cal ka, and represents the warmest ice-wedge-forming thermal event when paleo-MAT likely ranged between -1.4 and 1.4°C. The combination of low-resolution and low-fidelity radiocarbon dating, high resolution  $\delta^{18}\text{O}$  data, and paleotemperature estimates allow for more robust age constraints when compared with the well-dated Bering Sea temperature record, suggesting that ice wedges in Central Alaska formed in response to North Atlantic DO- and H-type millennial forcing of climate.

## ACKNOWLEDGMENTS

I would like to thank and express my gratitude for the support, encouragement, and knowledge provided by my advisor and committee chair, Dr. Matthew Lachniet. I would also like to thank my advisory committee, Dr. Daniel Lawson, Dr. Steve Rowland, and Dr. Ganqing Jiang for their support of my development as a researcher. I also thank Dr. Liam Frink for investing his time to act as my Graduate College representative and supporting my endeavors.

I wish to thank the National Science Foundation, the Geoscience Department at the UNLV, the Ross family (Fay and Jack Ross Scholarship), the International Arctic Research Center, and the Geological Society of America for their generous financial support of my research. This project would not have been possible without support from the researchers and staff at the USACE CRREL Permafrost Tunnel who generously extended the use of the tunnel, cold room facilities, and equipment to me. I am further grateful to my fellow Wedgette, Corinne Griffing, for spending hundreds of hours in a freezer with me cutting up ice samples. I also thank the late Dr. Devendra Lal for his hospitality and encouragement, and Dr. Timothy Jull and Alex Leonard at the University of Arizona Radiocarbon Facility for assistance with radiocarbon analyses.

I am also am thankful for my colleagues at UNLV, and to Dr. Javier Rodriguez for his support and encouragement. Thank you to all the teachers who have shared their knowledge, inspired, and believed in me. Thank you to my family and to Jeremy for their unending love and support through this process. My deepest gratitude extends to my mom, who has devoted her life to educating others, and who continually inspires me to be



a better teacher and lifelong learner, without whom none of this would have been possible or meaningful.

## TABLE OF CONTENTS

ABSTRACT .....	iii
ACKNOWLEDGMENTS .....	vi
TABLE OF CONTENTS.....	viii
LIST OF TABLES .....	xi
LIST OF FIGURES .....	xii
CHAPTER 1 DISSERTATION OVERVIEW .....	1
Purpose.....	1
Chapter 2 synopsis .....	1
Chapter 3 synopsis .....	2
Chapter 4 synopsis .....	2
CHAPTER 2 MODERN SURFACE WATER STABLE ISOTOPE CLIMATOLOGY OF ALASKA .....	5
Abstract .....	5
Introduction.....	6
Physiography and climate of Alaska.....	8
Methods.....	8
Results and Interpretation .....	11
Isoscape of Alaskan surface waters .....	11
Isoscape derivation.....	11
Isoscape residuals.....	14
Spatial variability in surface water stable isotopes .....	14
Temperature effect .....	15
Cumulative precipitation amount effect.....	16
Altitude and latitude effect.....	17

Distance from the Pacific effect.....	18
Implications for paleoclimatic reconstructions .....	21
Conclusion .....	22

### CHAPTER 3 THERMAL STRATIGRAPHY OF THE

FOX PERMAFROST TUNNEL.....	45
Abstract.....	45
Introduction.....	46
Tunnel geology .....	49
Tunnel stratigraphy .....	49
Tunnel <sup>14</sup> C ages.....	50
Methods.....	52
Results.....	55
Ice wedge and pool ice stratigraphy.....	55
Ice wedge and pool ice <sup>14</sup> C dating .....	58
Timing of freeze and melt events.....	60
Discussion.....	65
Approximate timing of freeze and melt events.....	65
Freeze event 1 – 25.9 to 21.5 cal ka BP .....	66
Freeze event 2 - <25.9 to 21.5 cal ka BP .....	67
Melt event 1 – 21.5 to 17.9 cal ka BP.....	67
Freeze event 3 – 17.9 to 12.9 cal ka BP .....	69
Freeze event 4 - <17.9 to 12.9 cal ka BP .....	70
Freeze event 5 - <17.9 to 12.9 cal ka BP .....	71
Implications for dating carbon in the permafrost environments .....	71
Summary of thermal events in the Permafrost Tunnel .....	72
Conclusion .....	72

### CHAPTER 4 VARIABLE LATE PLEISTOCENE PALEOCLIMATE

IN ALASKA FROM HIGH-RESOLUTION $\delta^{18}\text{O}$ OF	
PERMAFROST ICE WEDGES SUGGESTS NORTH	
ATLANTIC FORCING .....	82
Abstract.....	82

Introduction.....	83
Oxygen and hydrogen isotopes in paleoclimate .....	83
Methods.....	86
Results and interpretation .....	88
Ice wedge and pool ice stable isotopes .....	88
Origin of wedge and pool ice.....	89
High resolution $\delta^{18}\text{O}$ record of paleoclimate .....	91
Wedge $\delta^{18}\text{O}$ as a proxy for paleoclimate change.....	93
Paleotemperature reconstruction of freeze and melt events .....	96
Discussion .....	98
Approximate timing of freeze and melt events .....	98
Freeze event 1 .....	101
Freeze event 2 .....	103
Melt event 1 .....	103
Freeze event 3 .....	104
Freeze event 4 .....	106
Freeze event 5 .....	107
Summary of Central Alaskan paleoclimate .....	107
Conclusion .....	108
 Appendix A: Surface water sampling data .....	 120
Appendix B: Surface water temperature and precipitation data .....	129
Appendix C: isoscape residuals .....	138
Appendix D: Ice wedge stable isotope values .....	148
 References.....	 172
 VITA.....	 180

## LIST OF TABLES

### CHAPTER 2

Table 2.1. Average temperature and precipitation for sampled catchments.....	42
Table 2.2. Linear regression correlation matrix.....	43
Table 2.3. Multiple linear regression results.....	44

### CHAPTER 3

Table 3.1. Radiocarbon ages of DOC and CO <sub>2</sub> within wedges and pool ice.....	81
--	----

### CHAPTER 4

Table 4.1. Pool ice stable isotope values. ....	117
Table 4.2. $\delta^{18}\text{O}$ values and approximate paleotemperatures.....	118
Table 4.3. $\delta^{18}\text{O}$ values and approximate correlated ages of sampled ice wedges.....	119

## LIST OF FIGURES

### CHAPTER 2

Figure 2.1. Map of Alaska sampling locations. ....	24
Figure 2.2. Mean annual precipitation (MAP). ....	25
Figure 2.3. DJF precipitation ..... ..	26
Figure 2.4. JJA precipitation. .... ..	27
Figure 2.5. Cumulative MAP. .... ..	28
Figure 2.6. Mean Annual Temperature (MAT). ....	29
Figure 2.7. DJF temperatures. .... ..	30
Figure 2.8. JJA temperatures. .... ..	31
Figure 2.9. $\delta^{18}\text{O}$ values of surface water samples. ....	0
Figure 2.10. Isoscape of Alaska and the Yukon. ....	33
Figure 2.11. Map of isoscape residuals. .... ..	34
Figure 2.12. $\delta^{18}\text{O}$ and $\delta\text{D}$ surface water values. ....	35
Figure 2.13. MAT and $\delta^{18}\text{O}$ values. .... ..	36
Figure 2.14. $\delta^{18}\text{O}$ with cumulative MAP. .... ..	37
Figure 2.15. $\delta^{18}\text{O}$ change with catchment altitude. ....	38
Figure 2.16. $\delta^{18}\text{O}$ change with catchment latitude. ....	39
Figure 2.17. South to north transect of surface water $\delta^{18}\text{O}$ values in Alaska. ....	40
Figure 2.18. South to north transect of MAT, MAP, and $\delta^{18}\text{O}$ . ....	41

### CHAPTER 3

Figure 3.1. Map of USACE CRREL Permafrost Tunnel location. ....	74
Figure 3.2. Cross-section of the CRREL Permafrost Tunnel. ....	75
Figure 3.3. General stratigraphic section of the Permafrost Tunnel ..... ..	76
Figure 3.4. Stratigraphic placement of freeze and melt events. .... ..	77
Figure 3.5. Photographs of five freeze and melt events. .... ..	78
Figure 3.6. Freeze event 1 ages and $\delta^{13}\text{C}$ values ..... ..	79
Figure 3.7. Approximate timing of freeze and melt events. .... ..	80

### CHAPTER 4

Figure 4.1. Bering Sea U1340 $\delta^{18}\text{O}$ records. .... ..	109
Figure 4.2. CRREL Permafrost Tunnel location map. .... ..	110
Figure 4.3. $\delta^{18}\text{O}$ and $\delta\text{D}$ values from ice wedges and pool ice. .... ..	111
Figure 4.4. $\delta^{18}\text{O}$ values of four freeze events and one melt event. .... ..	112
Figure 4.5. Freeze event 1 ice wedge 35S $\delta^{18}\text{O}$ values. .... ..	113
Figure 4.6. Wedge 35S high resolution $\delta^{18}\text{O}$ record. .... ..	114
Figure 4.7. Freeze and melt events with $\delta^{18}\text{O}$ values. .... ..	115
Figure 4.8. Tentative correlation of $\delta^{18}\text{O}$ with Bering Sea SST record. .... ..	116

## CHAPTER 1

### DISSERTATION OVERVIEW

#### **Purpose**

Understanding modern controls on climate is necessary to interpret past climatic conditions. This project investigated the modern controls on  $\delta^{18}\text{O}$  and  $\delta\text{D}$  values in surface waters in Alaska in order to interpret the controls on Late Pleistocene climate variability. This dissertation is divided into three sections: Chapter 2: Modern isotope climatology of Alaska; Chapter 3: Thermal stratigraphy of the Fox Permafrost Tunnel; and Chapter 4: High resolution  $\delta^{18}\text{O}$  record of late Pleistocene climate in Central Alaska.

#### **Chapter 2 synopsis**

Chapter 2 investigates the spatial trends of stable isotopes from over 400 surface water samples collected across Alaska and the Yukon. ArcGIS was used to develop an isoscape of modern  $\delta^{18}\text{O}$  and  $\delta\text{D}$  values of Alaska. It was found that winter temperature and precipitation amount exhibit the strongest correlation to  $\delta^{18}\text{O}$  and  $\delta\text{D}$  values in Alaska, resulting in high  $\delta^{18}\text{O}$  values along the coast of the Gulf of Alaska and low values inland toward Central Alaska. This isoscape can be applied to paleoenvironmental, modern, and future records to determine isotope-precipitation-temperature values. This is a useful tool for determining paleotemperatures of Alaska, which is necessary not only for the interpretation of the magnitude, timing, and patterns of past response to climatic change, but also for the correlation of global climate models to obtain predictions of future impacts of climate change to the Arctic.

### **Chapter 3 synopsis**

Chapter 3 investigates the age of ancient preserved ice wedges preserved in the CRREL Permafrost Tunnel. Previous work suggested that ancient preserved ice wedges formed syngenetically (growing simultaneously during sediment aggradation) during Marine Isotope Stage 3 (MIS 3). However, a new method of determining the timing of ice wedge and pool ice formation using radiocarbon-dated DOC and CO<sub>2</sub> reveals that the features are much younger than previously thought and are epigenetic (growing after sediment aggradation) in origin. At least five freeze events and one melt event are apparent in tunnel ice deposits, with likely ages between ca. 26 and 13 cal ka BP, around the time of full glacial and subsequent deglaciation of the Northern Hemisphere. The prevalence of age-distance inversions in the radiocarbon data indicates that carbon may persist for as long as 17,000 years within permafrost environments. This observation highlights the need for the combined stable isotope analyses and <sup>14</sup>C dating of DOC within ice in permafrost environments to constrain climatic perturbations in Central Alaska.

### **Chapter 4 synopsis**

Chapter 4 investigates the high resolution stable isotopes of ice wedges from the CRREL Permafrost Tunnel to better constrain the timing and climatic conditions during ice wedge formation. Eight ice wedges and seven ice pools were sampled at high spatial- and temporal resolution for stable isotopes and were combined with <sup>14</sup>C ages of DOC from within the ice to estimate the timing of formation and climatic conditions under which they formed. Four intervals of cooling and one interval of warming were recorded in the ice wedge and pool ice  $\delta^{18}\text{O}$  record, with  $\delta^{18}\text{O}$  values ranging from -28.9‰ to -



20.4‰. These values range between -6.6 below and +1.9‰ above the modern snow  $\delta^{18}\text{O}$  value of -22.3‰, which suggests that some of the ice wedges formed during colder-than-modern conditions. Paleo-winter temperatures ranged from -41.6 to -11.2°C, while paleo-mean annual temperatures (MAT) ranged from -14.1 to 1.4°C, consistent with paleotemperature fluctuations observed in the Bering Sea SST and Greenland ice core records. Based on a visual correlation to the Bering Sea SST record within the ice age limits described in Chapter 3, it is suggested here that Freeze event 1 likely occurred during cooling of -12.3 to -1.2°C between 26.5 - 25.3 cal ka BP, coinciding with Heinrich event 2, while Freeze event 2 occurred during cooling of -8.8 to -2.8°C between 21.0 - 20.5 cal ka BP. One warming interval, M1, when clear pool ice formed in a melt horizon above the F1 and F2 wedges, may have occurred as paleo-MAT ranged between -9.9 and -1.2°C between 19.1 - 18.8 cal ka BP. Freeze event 3 represents the lowest (coldest)  $\delta^{18}\text{O}$  values. These values suggest that paleo-MAT ranged between -14.1 and -9.2°C, which is correlated to the coldest regional climate interval when the Laurentide Ice Sheet reached its local maximum extent in the Yukon between 17.3 - 17.0 cal ka BP, coinciding with Heinrich event 1. Freeze event 4 has high  $\delta^{18}\text{O}$  values that are similar to those of a late Holocene ice wedge in the nearby Vault Creek permafrost tunnel. That ice wedge was radiocarbon-dated to ca. 3.9 cal ka and represents the warmest ice-wedge-forming thermal event as paleo-MAT likely ranged between -1.4 and 1.4°C. The combination of low-resolution and low-fidelity radiocarbon dating, high resolution  $\delta^{18}\text{O}$  data, and paleotemperature estimates allow for more robust age constraints when compared with the well-dated Bering Sea temperature record. These data suggest that ice wedges in

Central Alaska formed in response to North Atlantic DO- and H-type millennial forcing of climate.

## CHAPTER 2

### MODERN SURFACE WATER ISOTOPE CLIMATOLOGY OF ALASKA

#### **Abstract**

An understanding of modern isotopes in meteoric waters across Alaska is necessary to interpret past changes in climate. The isotopic composition of precipitation is not well understood because of the scarcity of isotopic information in precipitation across Alaska. Over 400 surface water samples were collected across Alaska and the Yukon. I analyzed these samples for stable isotopes of oxygen ( $\delta^{18}\text{O}$ ) and hydrogen ( $\delta\text{D}$ ). Surface water  $\delta^{18}\text{O}$  values range from -8.1 to -25.9‰ and average -19.4‰, with the highest values occurring along the coast of the Gulf of Alaska, and the lowest values occurring in the rainshadow of the Saint Elias Mountains in the Yukon.  $\delta^{18}\text{O}$  values become more negative moving inland toward Central Alaska, a process controlled by rainout occurring during Rayleigh distillation. The main controls on  $\delta^{18}\text{O}$  in modern Alaskan surface waters include winter (DJF) precipitation and temperature. An isoscape of stable isotope values was derived with ArcGIS using the surface water  $\delta^{18}\text{O}$  and  $\delta\text{D}$  values, winter precipitation amounts, and winter temperatures. This isoscape can be applied to paleoenvironmental, modern, and future records to determine isotope-precipitation-temperature values. To determine past  $\delta^{18}\text{O}$ -Temperature ( $\delta^{18}\text{O}$ -T) relationships, the modern  $\delta^{18}\text{O}$ -T relationship of 0.55‰ increase in  $\delta^{18}\text{O}$  with 1°C increase in MAT was determined. This is a useful tool in determining paleotemperatures of Alaska which is necessary not only for the interpretation of the magnitude, timing, and patterns of past response to climatic change, but also for the correlation of global climate models to obtain predictions of future impacts of climate change to the Arctic.

## Introduction

An understanding of modern isotopes in meteoric water across Alaska and the Yukon is necessary for interpretation of past changes in climate preserved in the geologic record. Few rain gauge stations exist across Alaska, and the isotopic composition of precipitation across this mountainous yet sometimes arid, permafrost-dominated, high latitude environment is not well understood. In the absence of precipitation sampling networks, stream waters may provide a record of the isotopic composition of precipitation (Fritz et al., 1981; Lachniet and Patterson, 2009) because of the integration of the precipitation both spatially and temporally over the drainage basin (Gat, 1996; Kendall and Coplen, 2001).

Those spatial and temporal characteristics of precipitation can be explained through the process of Rayleigh distillation, whereby air masses undergo isotopic partitioning during adiabatic cooling. As air masses cool and move over continents, higher latitudes, or higher altitudes, water vapor is lost to precipitation. During this "rainout" process, distillation separates the heavier isotopes from the water vapor. The isotopically heavier precipitation falls as the air mass becomes progressively enriched in lighter isotopes. Equilibrium fractionation ( $\alpha$ ) between the air mass water vapor and condensate produced is controlled by temperature and the fraction of moisture removed from the air mass ( $f$ ) and can be modeled using the equation

$$R = R_0 f^{(\alpha-1)}$$

where  $R$  is the isotopic ratio after rainout and  $R_0$  is the initial isotopic ratio (Clark and Fritz, 1997). However, temperature and vapor fraction alone cannot explain rainout processes over landmasses. As temperature decreases and rainout occurs over

landmasses, other factors such as re-evaporation, atmospheric mixing, and moisture source can influence  $\delta^{18}\text{O}$  values in precipitation. The effects of latitude, distance from the coast, altitude, and seasonality must also be considered when evaluating isotopic spatial and temporal patterns.

It is expected that climatic change in response to future global warming will be more pronounced in the northern high latitude regions, as already observed in the Arctic (Ahmed et al., 2013; Alley and Clark, 1999; Hinzman et al., 2005; Miller et al., 2010; Osterkamp et al., 2009; Schuur et al., 2008; Serreze et al., 2000; Wiles et al., 2004). Global climate models are limited in accurately representing the water isotope cycle in their relatively coarse resolution for regional studies. Regional models consistently improve the spatial details of simulated climate compared to standard global models; however, few high resolution regional circulation models exist in the high latitude region (Lynch et al., 1995) because of a lack of high resolution climatic data. These high resolution data are needed to not only better constrain climatic controls and feedbacks in the high latitudes, but also to predict future climate change in those regions. Until now, interpolation between the sparsely-spaced Global Network of Isotopes in Precipitation (GNIP) stations in Alaska has been the standard for determining the spatial variation in  $\delta^{18}\text{O}$  in precipitation (Bowen and Wilkinson, 2002).

To improve the spatial resolution of high latitude isotopes in meteoric waters, I used surface water  $\delta^{18}\text{O}$  and  $\delta\text{D}$  data from over 400 stream waters collected in Alaska and the Yukon to create a high resolution isoscape of surface waters. These data were used to test the hypothesis that Rayleigh distillation controls  $\delta^{18}\text{O}$  values from the Gulf of Alaska to the Arctic Ocean. This study also identified spatial trends, moisture sources, and

physiographic controls of modern climate in the region. This information provides a basis for modeling future changes in climate and identifying past changes in climate.

### ***Physiography and climate of Alaska***

The Aleutian Low (AL) pressure system controls moisture and precipitation patterns in southern Alaska, and has shifted both in strength and position over decadal and millennial time scales (Clegg and Hu, 2010; Overland et al., 1999). A strong AL carries warmer and moister storms along a meridional trajectory from the south to the north, while a weak AL shuttles colder and drier storms along a zonal trajectory from the west and northwest eastward (Rodionov et al., 2005). Precipitation is strongly continental, controlled by the Alaska Range to the south, the Kuskokwim Mountains to the west, and the Brooks Range to the north, creating a rain shadow effect over much of Central Alaska (Mock et al., 1998). Central Alaska is characterized by a continental climate with long, cold winters and short, warm summers influenced by air masses originating in the Arctic, Gulf of Alaska, and Bering Sea (Kokorowski et al., 2008; Mock et al., 1998; Streten, 1974). Mean annual precipitation in Fairbanks is 276 mm, typically falling in the form of rain during the months of June, July, and August (Muhs et al., 2001).

### **Methods**

Water samples were collected during the summers of 2009-2011 from approximately 400 springs and streams spanning 58°-70° N latitude and 135°-151° W longitude in Alaska and the Yukon Territory (Figure 2.1 and Appendix A). Water samples were collected at easily accessible pullouts or from roadway bridges using a plastic bucket attached to a rope. Samples were immediately transferred to 30-mL

Nalgene bottles with no head space and sealed with electrical tape. Each sampling location was photographed and recorded using Geographic Positioning System (GPS) coordinates. Vegetation and water color characteristics were recorded. Samples were shipped to the Las Vegas Isotope Science (LVIS) laboratory for isotopic analyses.

Oxygen and hydrogen isotope ratios of water samples were measured with a ThermoElectron high temperature conversion elemental analyzer (TC/EA) by reaction with glassy carbon at 1,450°C in a helium carrier gas stream to produce H<sub>2</sub> and CO gases. Isotopic ratios of oxygen ( $\delta^{18}\text{O}$ ) and deuterium ( $\delta\text{D}$ ) were determined on a ThermoElectron Delta V Plus isotope ratio mass spectrometer relative to two internal standards calibrated to SLAP (Standard Light Antarctic Precipitation) ( $\delta^{18}\text{O} = -55.5\text{‰}$ ,  $\delta\text{D} = -428.0\text{‰}$ ) and VSMOW (Vienna Standard Mean Ocean Water) ( $\delta^{18}\text{O} = 0.0\text{‰}$ ,  $\delta\text{D} = 0.0\text{‰}$ ) and reported in per mil (‰) concentrations. Precisions were better than 0.3‰ for  $\delta^{18}\text{O}$  and 3‰ for  $\delta\text{D}$ . Deuterium excess ( $d$ ) values were calculated using

$$d = \delta\text{D} - 8 \times \delta^{18}\text{O}.$$

Isotopic values and climatic variables were plotted and analyzed using ArcGIS version 10.0 to determine spatial patterns of  $\delta^{18}\text{O}$  values. A 300-m resolution digital elevation model (DEM) (USGS, 1997) in ArcGIS was used to determine physiographic variables, including catchment latitude, catchment longitude, catchment altitude, catchment area, and distance to the Pacific Ocean. Using the Watershed tool in ArcGIS, the catchment of each sampled location was delineated. The area, latitude, longitude, altitude, and distance to the Pacific Ocean of the midpoint of each catchment was determined using the Identify tool in ArcGIS. Climatic variables, including mean annual temperature (MAT), winter (December, January, and February) average temperature

(DJF T), summer (June, July, and August) average temperature (JJA T), mean annual precipitation (MAP), cumulative mean annual precipitation (CumMAP), winter precipitation (DJF P), and summer precipitation (JJA P), were determined for each sampling location in ArcGIS (Appendix B) using the WorldClim dataset layers (Hijmans et al., 2005). This dataset contains weather station temperature and precipitation data spanning the years 1961 - 1990 that was interpolated and modeled at a higher resolution of 30-arc-seconds or 1 km<sup>2</sup> to produce GIS data layers of monthly total precipitation and monthly mean temperature. Mean annual temperature (MAT) is the average of the monthly temperature values, while the mean annual precipitation (MAP) is the sum of the monthly average precipitation amounts for the years 1961 - 1990 (Hijmans et al., 2005). Cumulative MAP was calculated in ArcGIS by adding grid cells of MAP in south to north longitudinal transects similar to the trajectories of storms originating in the Gulf of Alaska (Mock et al., 1998). Subset rasters of each WorldClim layer were created in ArGIS including MAP (Figure 2.2), DJF P (Figure 2.3), JJA P (Figure 2.4), Cumulative MAP (Figure 2.5), MAT (Figure 2.6), DJF T (Figure 2.7), and JJA T (Figure 2.8) that were later used in the multiple regression derivation of the isoscape, discussed below.

The statistical significance of physical parameters on  $\delta^{18}\text{O}$  surface water values was analyzed by linear and multiple regression techniques using MatLab (MathWorks, 2005). A linear regression correlation was performed in MatLab to test the strength of correlation between  $\delta^{18}\text{O}$  and temperature, precipitation, and other physiographic variables. High correlation ( $r = 1.00$ ) between  $\delta^{18}\text{O}$  and a physiographic variable indicates  $\delta^{18}\text{O}$  is strongly influenced by that variable. Weak correlation ( $r = 0.00$ ) indicates  $\delta^{18}\text{O}$  is not strongly influenced by the variable.



To test for the significance of several independent variables on the dependent variable  $\delta^{18}\text{O}$ , multiple regression was performed. In multiple linear regression, individual physiographic parameters are measured to determine the strongest controls on  $\delta^{18}\text{O}$  values. Correlation matrices of samples (n) and variables (p) were constructed with p-values <0.05 to determine the multiple regression equation of

$$Y = b_0 + b_1X_1 + b_2X_2 + b_3X_3 + \dots + b_nX_n$$

where Y is the predicted dependent variable ( $\delta^{18}\text{O}$ ),  $b_0$  to  $b_n$  are partial regression coefficients, and  $X_1$  to  $X_n$  are independent variables (Brown, 1998). Using the Raster Calculator tool in ArcGIS, the rasters of MAP, DJF P, JJA P, Cumulative MAP, MAT, DJF T, and/or JJA P were combined in the multiple regression equation, resulting in the output of an isoscape of surface water  $\delta^{18}\text{O}$  values.

## **Results and Interpretation**

### ***Isoscape of Alaskan surface waters***

#### ***Isoscape derivation***

The isotopic results of the water samples collected are listed in Appendix A and are displayed in Figure 2.9. The results of the linear correlations are shown in Table 2.2, and correlations range from the highest ( $r = 0.82$ ) to the lowest ( $r = -0.02$ ). Surface water  $\delta^{18}\text{O}$  is most strongly correlated to MAP ( $r = 0.82$ ), DJF P ( $r = 0.82$ ), MAT ( $r = 0.78$ ), DJF T ( $r = 0.77$ ), and catchment latitude ( $r = -0.68$ ).

As expected, this indicates that precipitation, temperature, and latitude have the greatest influence on  $\delta^{18}\text{O}$  values in Alaska. Interestingly, winter precipitation ( $r = 0.82$ ) is more strongly correlated with  $\delta^{18}\text{O}$  than is summer precipitation ( $r = 0.60$ ). This is explained by higher winter precipitation amounts along the Gulf of Alaska and lower

precipitation amounts in the interior of Alaska. Similarly, winter temperature ( $r = 0.77$ ) has a greater control on  $\delta^{18}\text{O}$  values than do summer temperatures ( $r = 0.15$ ), as precipitation and temperature are collinearly related.

A simple analysis of the linear correlation between  $\delta^{18}\text{O}$  and MAP does not, however, account for the variability in  $\delta^{18}\text{O}$  during rainout that occurs during Rayleigh distillation. To determine the influence of Rayleigh distillation on  $\delta^{18}\text{O}$  and to simulate the rainout process from a moisture source originating over the Gulf of Alaska, cumulative MAP was calculated along south-to-north longitudinal transects. Cumulative MAP was found to have a weaker influence on  $\delta^{18}\text{O}$  ( $r = -0.24$ ) compared to MAP ( $r = 0.82$ ). Rainout occurring during Rayleigh distillation accounts for only 24% of the variability in  $\delta^{18}\text{O}$  values in Alaska. Cumulative MAP captures the spatial distribution of MAP, whereas MAP does not, since cumulative MAP is dependent on temperature, latitude, and distance from the Pacific.

The influence of physiographic controls such as latitude and altitude from other variables in the correlation matrix was identified using the multiple linear regression analysis. The statistically best fit multiple regression equation included catchment latitude, catchment longitude, catchment altitude, MAP, cumulative MAP, DJF P, JJA P, MAT, DJF P, and JJA P coefficients ( $r^2 = 0.74$ ) (Table 2.3). However, because of the colinear relationship between many of these variables such as latitude, altitude, and temperature, the physiographic relationships between the parameters were separated during multiple linear regression analysis.

Two multiple linear regression equations were determined when the colinear physiographic parameters were separated:

$$\delta^{18}\text{O} = (0.0102247 \times \text{DJF P}) + (0.0090214 \times \text{DJF T}) - 19.6118 \quad (\text{Equation 1})$$

$$\delta^{18}\text{O} = (2.04114 \times 10^{-8} \times \text{Cum MAP}) + (0.0089869 \times \text{DJF P}) \\ + (0.0252606 \times \text{MAT}) - 20.1991 \quad (\text{Equation 2})$$

Although the  $R^2$  for Equation 2 is higher (0.71) than for Equation 1 ( $R^2 = 0.68$ ), Equation 1 is simpler because only precipitation and temperature are included. Therefore, Equation 1, incorporating DJF P and DJF T, was used in ArcGIS to derive the isoscape of Alaskan  $\delta^{18}\text{O}$  surface water values (Figure 2.10).

The isoscape modeled  $\delta^{18}\text{O}$  values that range between -13‰ and -26‰, with the highest values occurring along the Gulf of Alaska and the lowest values occurring at high elevations and in the interior of the continent (Figure 2.10). Coastal areas controlled by higher precipitation amounts and higher temperatures are characterized by more positive  $\delta^{18}\text{O}$  values near Glacier Bay up through the Kenai Peninsula. The extent of the control of precipitation and temperature is apparent in the rapid decrease of  $\delta^{18}\text{O}$  values moving from the Gulf of Alaska over the mountain ranges and into the interior of the continent. The mountain ranges in Alaska and the Yukon are visible in Figure 2.10 as low  $\delta^{18}\text{O}$  (-26‰ to -24‰) values, including from south to north the Chugach - St. Elias Mountains, the Wrangell Mountains, the Alaska Range, and the Brooks Range. The most negative  $\delta^{18}\text{O}$  values occur as expected in the Brooks Range. This high-resolution isoscape provides a more accurate tool for determining isotope-temperature-precipitation relationships in the subarctic to Arctic region, compared to past global lower resolution models.

### *Isoscape residuals*

To test the fit of the isoscape modeled  $\delta^{18}\text{O}$  values compared to the measured  $\delta^{18}\text{O}$  values, the residual  $\delta^{18}\text{O}$  values were calculated using the equation:

$$\text{Residual} = \delta^{18}\text{O}_{\text{modeled}} - \delta^{18}\text{O}_{\text{measured}}$$

The residual values are listed in Appendix C and are displayed in Figure 2.11 in 0.5‰ contoured intervals. Residual values range from -6.4‰ to +5.1‰ and average 1.2‰. The highest and lowest residual values are centered around high altitude catchment locations on the leeward (northern) side of the Wrangell and St. Elias mountain ranges. When a linear regression correlation was performed on the residual values and physiographic parameters, variability in the residuals occurred primarily because of catchment altitude ( $r = 0.20$ ). All other parameters such as distance from the Pacific and type of catchment watershed (e.g., glacial, permafrost, non-glacial), were not significant at the  $p > 0.05$  level. The inclusion of catchment altitude within the regression equation did not improve the overall  $r^2$  values. However, the results of the multiple linear regression indicate that 68% of the variability in surface water  $\delta^{18}\text{O}$  values of Alaska can be explained by winter precipitation and temperature, which are colinear with altitude.

### *Spatial variability in surface water stable isotopes*

To test whether the Alaskan surface water samples are representative of Alaskan precipitation, the  $\delta^{18}\text{O}/\delta\text{D}$  values of surface water samples were plotted to obtain a regression surface water line (SWL) (Figure 2.12). The Alaska SWL of  $\delta\text{D} = 8.0 \times \delta^{18}\text{O} + 6.8$  ( $r^2 = 0.97$ ) was compared to the Global Meteoric Water Line (GMWL) of  $\delta\text{D} = 8 \times \delta^{18}\text{O} + 10$  (Dansgaard, 1964). The similarity in the relationships suggests that the surface waters in Alaska may provide a proxy for Alaskan precipitation.

Surface water  $\delta^{18}\text{O}$  values range from -8.1 to -25.9‰, averaging -19.4‰. The  $\delta\text{D}$  values range from -63.1 to -197.8‰, averaging -147.9‰ (Figure 2.12). The highest values occur along the coast of the Gulf of Alaska, and the lowest values occur in the rainshadow of the Saint Elias Mountains in the Yukon.  $\delta^{18}\text{O}$  values become more negative moving inland toward Central Alaska. Surface waters collected in the rainshadow of the Chugach in the Copper River Valley plot below the SWL (Figure 2.12). The  $d$  values range from -13.6 to 17.0‰, averaging 7.3‰ (Appendix A).

To examine the spatial effects of MAP and MAT on  $\delta^{18}\text{O}$  values, average annual, summer, and winter temperature and precipitation values for each stream catchment were determined (Appendix B). The spatial range and average MAT and MAP are shown in Table 2.1. For the catchments sampled in this study, the spatially averaged MAT ranged from -12.7 to 4.8°C (average -2.7°C), winter temperature ranged from -29.5 to -1.9°C (average -16.3°C), and summer temperature ranged from 2.9 to 11.6°C (average 9.4°C). The spatially averaged MAP ranged from 0.158 to 1.922 m (average 0.672 m), winter precipitation ranged from 0.010 to 0.751 m (average 0.277), and summer precipitation ranged from 0.029 to 0.468 m (average 0.093 m).

#### *Temperature effect*

Decreasing temperatures in air masses drive rainout and the depletion of  $^{18}\text{O}$  during Rayleigh distillation, but the  $\delta^{18}\text{O}$ -T relationship for Alaska has not been well-established. To determine how MAT affects  $\delta^{18}\text{O}$  values in Alaska, the  $\delta^{18}\text{O}$ -T relationship was examined. As shown in Figure 2.13,  $\delta^{18}\text{O}$  values change according to the equation

$$\delta^{18}\text{O} = 0.55 \times \text{MAT} - 17.9$$

( $r^2 = 0.61$ ) indicating that for every 1°C decrease in MAT,  $\delta^{18}\text{O}$  values decrease by 0.55‰. This change is consistent with worldwide values of 0.60‰ per 1°C change in temperature (Dansgaard, 1964; Rozanski et al., 1992) and western Canadian values of 0.49‰ per 1°C change in temperature (Clark and Fritz, 1997). The most negative Alaskan  $\delta^{18}\text{O}$  values are associated with the lowest MAT values (Figure 2.13), which is an expected result of Rayleigh distillation and the continental effect. Rainout and isotopic evolution occurs quickly as air masses move over Alaska and encounter topographic highs such as the Chugach and Wrangell mountains and associated temperature lows in those regions. Sampling locations located in Central Alaska far inland from the moderating effects of the Pacific Ocean exhibit more temperature extremes compared to sampling locations located closer to marine sources along the coast. As a result of this continental effect, the  $\delta^{18}\text{O}$  values in Central Alaska are more negative than those found along the Gulf of Alaska.

#### *Cumulative precipitation amount effect*

As with MAT, the  $\delta^{18}\text{O}$  values are dependent on precipitation amount. However, simple MAP cannot explain  $\delta^{18}\text{O}$  variability across Alaska. The cumulative precipitation amount effect displays Rayleigh distillation (Figure 2.14) according to the equation

$$\delta^{18}\text{O} = -0.0325 \times \text{MAP} - 13.3$$

where cumulative MAP is in meters and the  $r^2 = 0.61$ . As an air mass moves from the moisture source region of the Pacific Ocean in the Gulf of Alaska over the continent toward the north, progressive rainout occurs during Rayleigh distillation, as indicated by the negative correlation between cumulative MAP and  $\delta^{18}\text{O}$  values. As an air mass moves farther away from its moisture source, it becomes progressively depleted in moisture, and

the  $\delta^{18}\text{O}$  values become more negative. The most positive  $\delta^{18}\text{O}$  values occur closer to the moisture source along the Pacific Coast before rainout depletes the air mass, while the most negative  $\delta^{18}\text{O}$  values occur in regions farthest from the moisture source along with the lowest MAP and highest cumulative MAP. Regions of high MAP occur along the Gulf of Alaska coast and over the coastal mountain ranges, while the zones of lower MAP occur inland in Central Alaska and near the North Slope. Regions of high cumulative MAP correspond to regions of low  $\delta^{18}\text{O}$  near the North Slope, while areas of low cumulative MAP correspond to regions of high  $\delta^{18}\text{O}$ .

#### *Altitude and latitude effect*

Because of the  $\delta^{18}\text{O}$ -T relationship,  $\delta^{18}\text{O}$  values generally decrease with increasing altitude through Rayleigh distillation processes. As altitude and latitude increase, temperature decreases. To determine how Alaskan isotope values vary with altitude and latitude, the average latitude and altitude of the sampled catchments was determined using the DEM in GIS. The highest  $\delta^{18}\text{O}$  values occur in the lowest catchment altitudes along the coast, but the very weak correlation ( $r^2 = 0.13$ ) between  $\delta^{18}\text{O}$  and altitude (Figure 2.15) indicate a nonlinear relationship and that altitude is not a factor determining  $\delta^{18}\text{O}$  variability. However, this nonlinear relationship characterizes all of the sampled catchments across Alaska and does not take into account regional  $\delta^{18}\text{O}$ -altitude trends within individual mountain ranges. When considered regionally, the  $\delta^{18}\text{O}$  values of the Chugach mountains, Wrangell mountains, and Brooks Range are more closely correlated with altitude, which will be discussed in detail in a separate paper to follow.

Catchment latitude and altitude accounts for 68% and 39%, respectively, of the variability in the  $\delta^{18}\text{O}$  values (Table 2.2), which is not surprising since air temperature decreases with increasing latitude and altitude. North American  $\delta^{18}\text{O}$  values decrease by about 0.6‰ per degree of increasing latitude because of extreme temperature changes during Rayleigh distillation (Clark and Fritz, 1997). Alaskan surface water  $\delta^{18}\text{O}$  values decrease with increasing latitude and altitude along a curvilinear gradient (Figure 2.16). The highest  $\delta^{18}\text{O}$  values occur at the lower latitudes ( $58^\circ$  to  $62^\circ\text{N}$ ) and altitudes, follow a steep trend that flattens along latitudes  $62^\circ$  to  $66^\circ\text{N}$ , and then the lowest  $\delta^{18}\text{O}$  values occur at the higher latitudes ( $66^\circ$  to  $71^\circ\text{N}$ ). Extreme temperature changes over the lower latitude mountain ranges and subsequent altitude changes suggest that rainout during Rayleigh distillation is responsible for the steep  $\delta^{18}\text{O}$ -latitude-altitude gradient. Fractionation of the air mass as rainout occurs over the high mountain ranges causes more negative  $\delta^{18}\text{O}$  precipitation values to fall over the mountains. The lower slope of the  $\delta^{18}\text{O}$ -latitude curve in the central latitudes of Alaska indicates that continued rainout and fractionation has produced more negative  $\delta^{18}\text{O}$  values. However, topographical controls are visible in the  $\delta^{18}\text{O}$ -latitude-altitude curve (Figure 2.16) as  $\delta^{18}\text{O}$  values increase with decreasing altitude and decrease with increasing altitude, following the topography from south to north.

#### *Distance from the Pacific Ocean effect*

To better visualize the effect of these mountain ranges and corresponding temperature differences on  $\delta^{18}\text{O}$  values in Alaska, a topographic profile of a south-north transect was constructed (Figure 2.17). The transect begins in Valdez in the south and extends to Prudhoe Bay to the north. The Chugach Mountains, Alaska Range, and Brooks



Range are visible in the profile. To investigate the rainout effect over the south-north transect, the  $\delta^{18}\text{O}$  values were plotted against distance from the Pacific. The value  $d$ , which is an indicator of moisture cycling, evaporation, and humidity, was also plotted against distance from the Pacific coast. Variations in  $\delta^{18}\text{O}$  appear to be dominated by latitude, distance from the Pacific, and altitude, with highest values occurring near the coasts and in lowest elevations, and the lowest values occurring inland at the highest elevations. The highest  $\delta^{18}\text{O}$  values along the coast indicate that the moisture source of the surface waters is the Gulf of Alaska, with values becoming more negative as rainout occurs over the continent and distance from the moisture source increases. The  $\delta^{18}\text{O}$  values decrease from -15‰ at the Gulf of Alaska to -25‰ in the interior at the crest of the Brooks Range.

As expected, the high  $\delta^{18}\text{O}$  values occur at the coastal moisture source, and the values gradually decrease as distance from the coast increases. Under equilibrium conditions without local evaporation or advection of vapor from outside the system, Rayleigh distillation causes a progressive decrease in  $\delta^{18}\text{O}$  values. Equilibrium conditions are confirmed because  $d$  values do not show an evaporative effect or advection of additional moisture sources. An increase in the  $d$  values could indicate recycling of moisture in the interior of the continent from sources other than the Pacific Ocean, such as the evaporation of rain, sublimation of ice, or evapotranspiration. However, when considering large rivers or catchments over  $100 \text{ km}^2$ , there is no increase or trend in  $d$  from south to north. This indicates that large rivers to the north of Fairbanks, such as the Yukon and Sagavanirktok with large catchment areas, likely do not contribute sufficient amounts of moisture that is recycled to the atmosphere to change  $d$  values in the interior

of Alaska. Rather,  $d$  values appear to be controlled by local topography and microclimates, as  $d$  values in similar regions vary greatly.

Variations in local topography are most evident in the plots of  $\delta^{18}\text{O}$ , MAP, and MAT along the south-north transect (Figure 2.18). The imprint of the Chugach Mountains, Alaska Range, and Brooks Range is apparent in the MAP plot, with MAP increasing as rainout occurs over the higher altitudes. The  $\delta^{18}\text{O}$  values decrease with increasing altitude over the Alaska Range, exhibiting continental rain-out effects in the interior of Alaska near Fairbanks. As water vapor with high  $\delta^{18}\text{O}$  values moves north from the Gulf of Alaska into Alaska, it is orographically lifted and adiabatically cooled over the Chugach Mountains and St. Elias Mountains in the southern portion of Alaska. Rayleigh distillation causes an inverse relation between  $\delta^{18}\text{O}$  and elevation, with  $\delta^{18}\text{O}$  values decreasing with increasing altitude and distance from the Pacific.

As air masses move into Alaska from the Pacific and traverse the Chugach, Wrangells, and Alaska Range, the  $\delta^{18}\text{O}$  values decrease from rainout of precipitation (Figure 2.18). As air masses move into the drier interior of Alaska near Fairbanks, the  $\delta^{18}\text{O}$  values flatten out, likely because the air masses have become depleted of moisture during rainout processes. The  $\delta^{18}\text{O}$  values decrease over the Brooks Range, driven by temperature decreases over the mountain range.

An alternative hypothesis to explain the decreasing  $\delta^{18}\text{O}$  values over the Brooks Range is that a second moisture source originates in the Arctic Ocean. If a cold air mass from the Arctic Ocean supplied moisture to the region north of the Brooks Range, low  $\delta^{18}\text{O}$  values and shifting  $d$  values would be expected from the addition of moisture from a different source. If the addition of moisture from such a source was occurring,  $d$  values

would also increase, but  $d$  values show no trend in this region (Figure 2.17). The Arctic Ocean may provide some moisture to the area, but because MAP in the region is so low, detection of changes in the values is difficult. As Pacific air masses continue to move north to the Brooks Range, the majority of the air parcels have been depleted of moisture. As a result, low rainfall amounts are typical of the region on the south side of the Brooks Range (Figure 2.18) (Mock et al., 1998). The low  $\delta^{18}\text{O}$  values and the low MAP on the north side of the Brooks Range confirm that the Arctic Ocean is not a significant source of moisture to the region (Mock et al., 1998).

### ***Implications for paleoclimatic reconstructions***

The modern surface water  $\delta^{18}\text{O}$  change with altitude and latitude by Rayleigh distillation of an air mass under near equilibrium conditions can be applied to paleoclimatic reconstructions, assuming that air masses formed under similar temperature and humidity conditions. The extent of continental ice sheets lowered sea levels during the Last Glacial Maximum (LGM) (Clark et al., 2009), creating a strong continental climate in Central Alaska. Additionally, perpetual sea ice cover (Bartlein et al., 1998) likely prevented the Arctic Ocean from providing moisture to the North Slope of Alaska. Using the modern patterns in  $\delta^{18}\text{O}$  values presented here as an analogue for past conditions, paleo-precipitation was likely sourced from the south in the Pacific Ocean, and surface water  $\delta^{18}\text{O}$  would have undergone similar to modern changes during rainout and northward transport across Alaska. The modern latitude-altitude- $\delta^{18}\text{O}$  relationship can be applied to paleoenvironmental records to determine past MAP and MAT values. To determine past  $\delta^{18}\text{O}$ -Temperature ( $\delta^{18}\text{O}$ -T) relationships, the modern  $\delta^{18}\text{O}$ -T

relationship is needed. Data from this study indicate a 0.55‰ increase in  $\delta^{18}\text{O}$  with each 1°C increase in MAT, which is useful for determining paleotemperatures of Alaska.

Correlation between  $\delta^{18}\text{O}$  and the source of surface waters (i.e., glacial, non-glacial, or permafrost) was low (Table 2.2). A recent study by (Derksen and Brown, 2012) suggests that snow cover extent in the Arctic in May and June has been low during 2008-2012, the years during which my water samples were collected. For this reason, my samples are representative of MAP, and not snowmelt or glacial runoff. This is also apparent in the closely matched SWL to the GMWL (Figure 2.12) and the low correlation ( $r = -0.24$ ) between  $\delta^{18}\text{O}$  and glacial/non-glacial/permafrost source areas in the linear regression (Table 2.2).

## **Conclusion**

An understanding of the variability in the isotopic composition of meteoric water across Alaska and the Yukon today provides a means to define the factors determining that variability and its relationship to modern climate. This then provides a tool to interpret the geologic record. The scarcity of high-resolution Arctic GNIP data requires the use of surface water  $\delta^{18}\text{O}$  as a proxy for precipitation  $\delta^{18}\text{O}$  values in Alaska. Surface water  $\delta^{18}\text{O}$  values range from -8.1 to -25.9‰ and average -19.4‰, with the highest values occurring along the coast of the Gulf of Alaska, and the lowest values occurring in the rainshadow of the Saint Elias Mountains in the Yukon.  $\delta^{18}\text{O}$  values generally become more negative with distance inland toward Central and Northern Alaska, as the result of Rayleigh distillation driving precipitation. Strong correlations between  $\delta^{18}\text{O}$ , MAT, winter precipitation, and cumulative MAP confirm that Rayleigh distillation controls  $\delta^{18}\text{O}$  values as air masses originating in the Gulf of Alaska become progressively

depleted in  $\delta^{18}\text{O}$  as they traverse the major mountain ranges northward from the coast. The modern Cumulative MAP-DJF P-MAT relationship used to derive a high-resolution isoscape of  $\delta^{18}\text{O}$  surface water values can be applied to paleoenvironmental, modern, and future records to determine isotope-precipitation-temperature values. To determine past  $\delta^{18}\text{O}$ -Temperature ( $\delta^{18}\text{O}$ -T) relationships, the modern  $\delta^{18}\text{O}$ -T relationship of 0.55‰ increase in  $\delta^{18}\text{O}$  with 1°C increase in MAT was determined, along with a 0.28‰ increase in  $\delta^{18}\text{O}$  with every 1°C increase in DJFT. This is a useful tool for determining paleotemperatures of Alaska, which is necessary not only for the interpretation of the magnitude, timing, and patterns of past response to climatic change, but also for the regional calibration of global climate models to obtain predictions of future impacts of climate change to the Arctic.

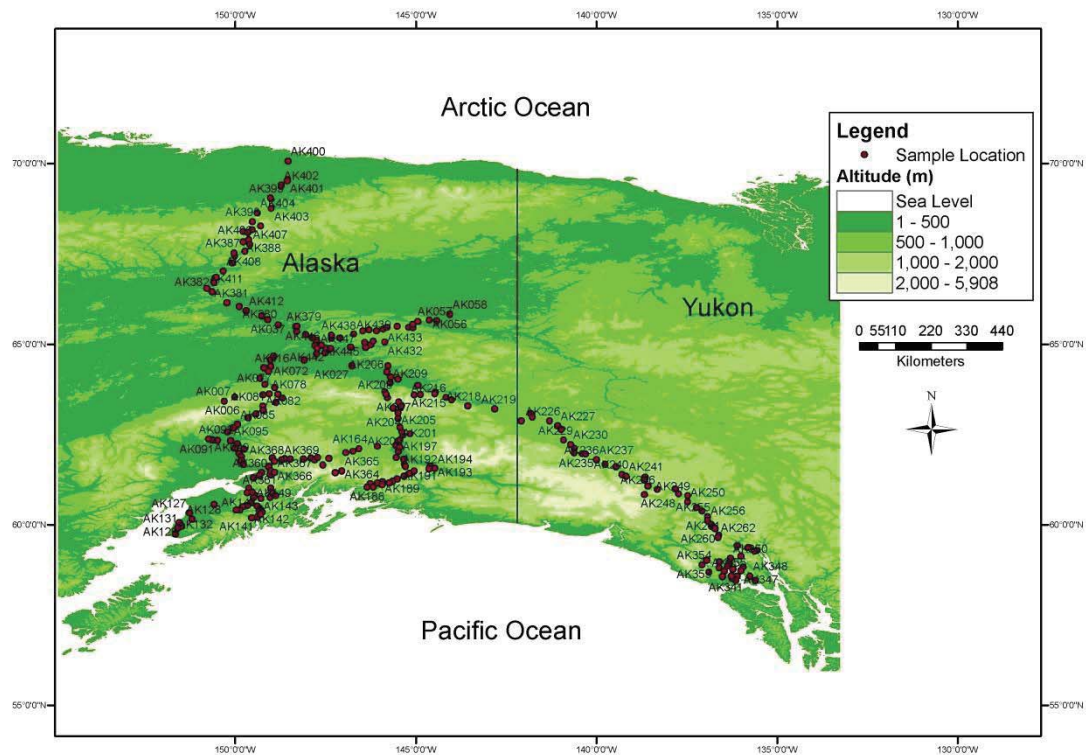


Figure 2.1. Map of Alaska sampling locations. Base map is a USGS 300-m Digital Elevation Model (DEM) (USGS, 1997).

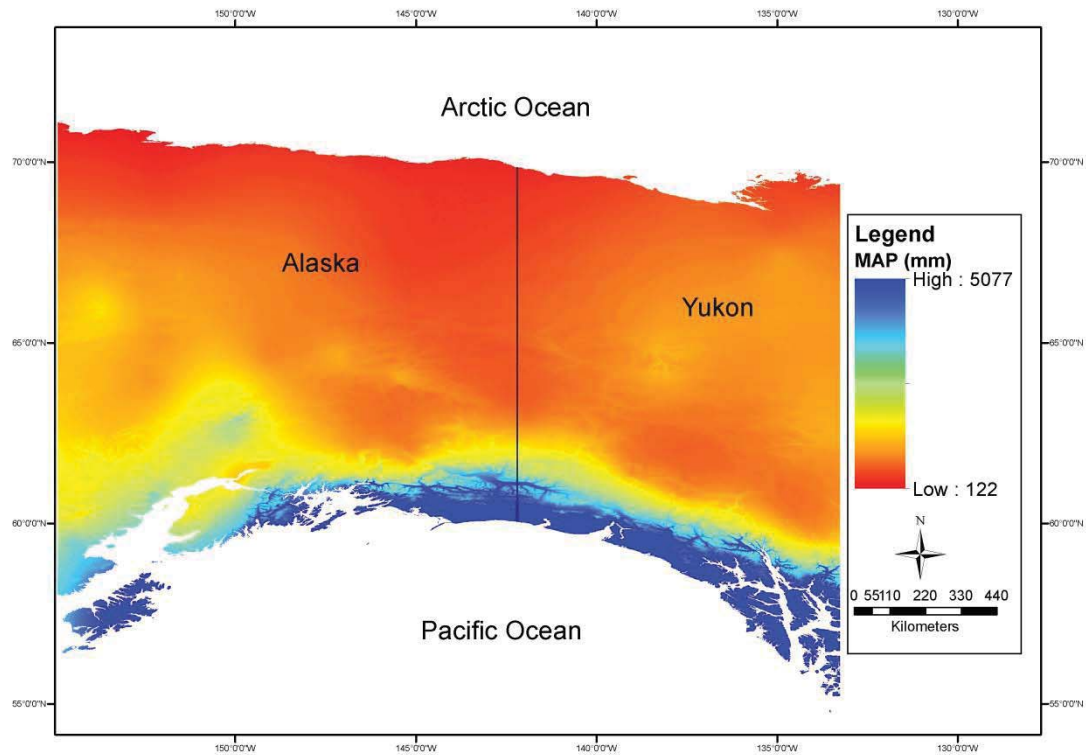


Figure 2.2. Mean annual precipitation (MAP). Map of Alaska and the Yukon showing MAP in millimeters (mm) from the WorldClim database spanning the years 1961 - 1990 (Hijmans et al., 2005). Precipitation amounts range from 5077 mm along the Gulf of Alaska to 122 mm along the North Slope.

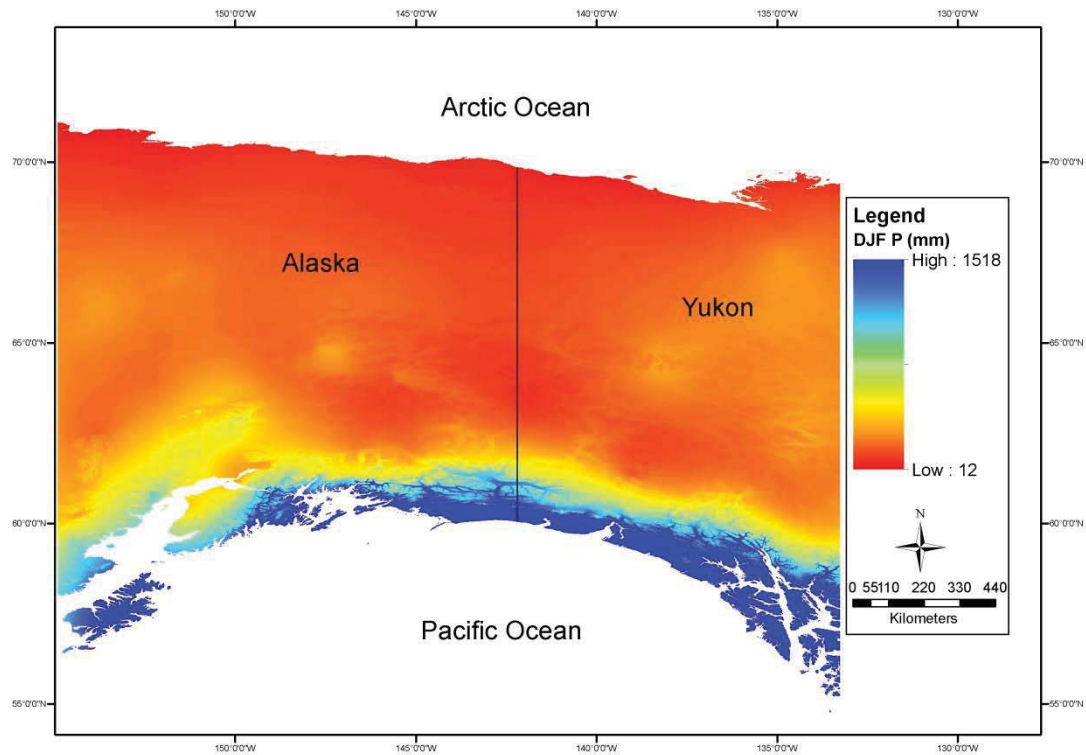


Figure 2.3. DJF precipitation. Map of Alaska and the Yukon showing precipitation in millimeters (mm) during the months of December, January, and February (DJF) from the WorldClim database spanning the years 1961 - 1990 (Hijmans et al., 2005). Precipitation amounts range from 1518 mm along the Gulf of Alaska to 12 mm along the North Slope.



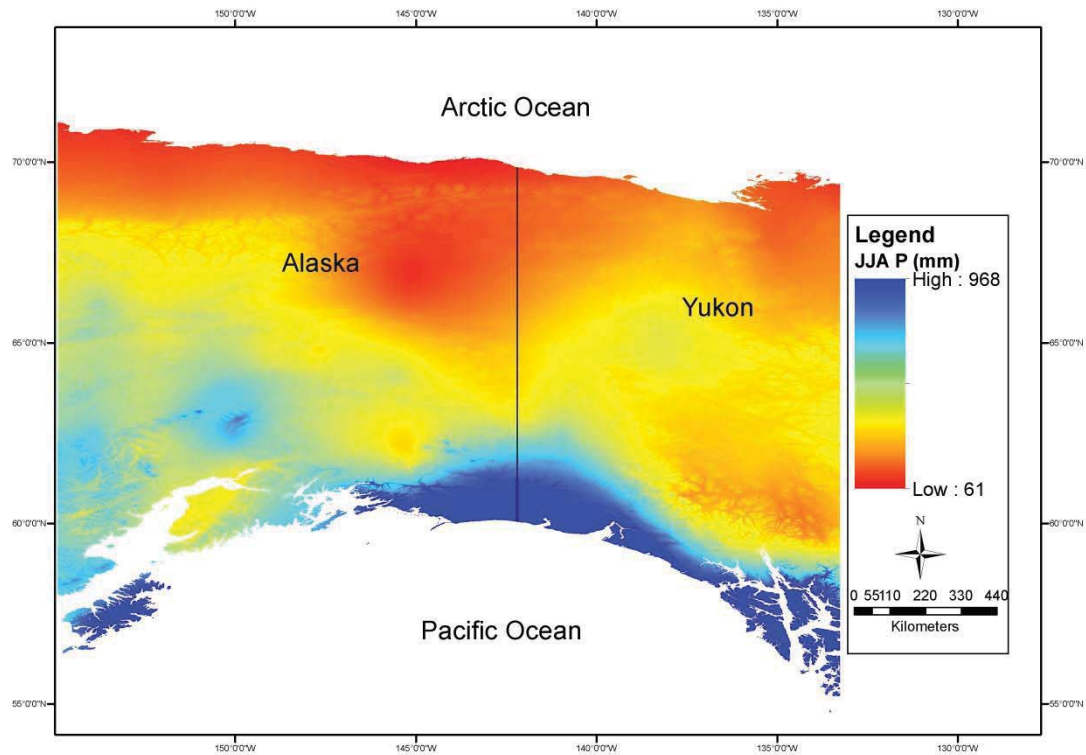


Figure 2.4. JJA precipitation. Map of Alaska and the Yukon showing precipitation in millimeters (mm) during the months of June, July, and August (JJA) from the WorldClim database spanning the years 1961 - 1990 (Hijmans et al., 2005). Precipitation amounts range from 968 mm along the Gulf of Alaska to 61 mm along the North Slope.

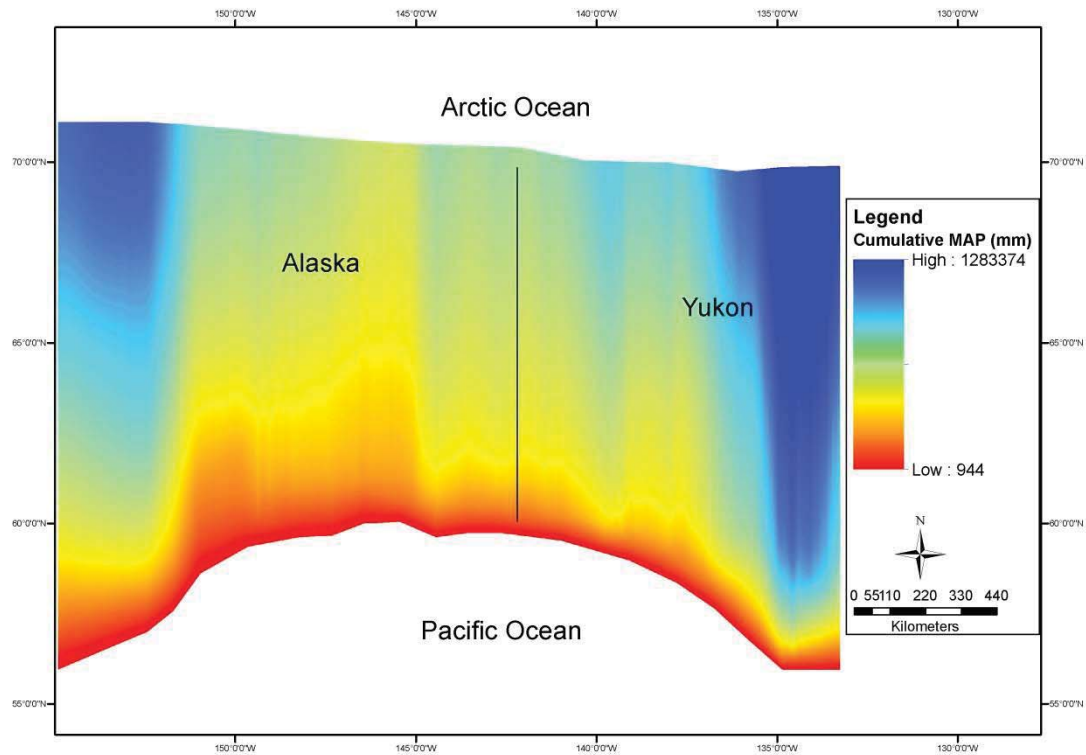


Figure 2.5. Cumulative MAP. Map of Alaska and the Yukon showing cumulative MAP in millimeters (mm). Cumulative precipitation amounts were calculated along south-to-north longitudinal transects using the WorldClim database's MAP spanning the years 1961 - 1990 (Hijmans et al., 2005). Precipitation amounts range from 944 mm along the Gulf of Alaska to 1,283,374 mm along the Arctic Ocean.

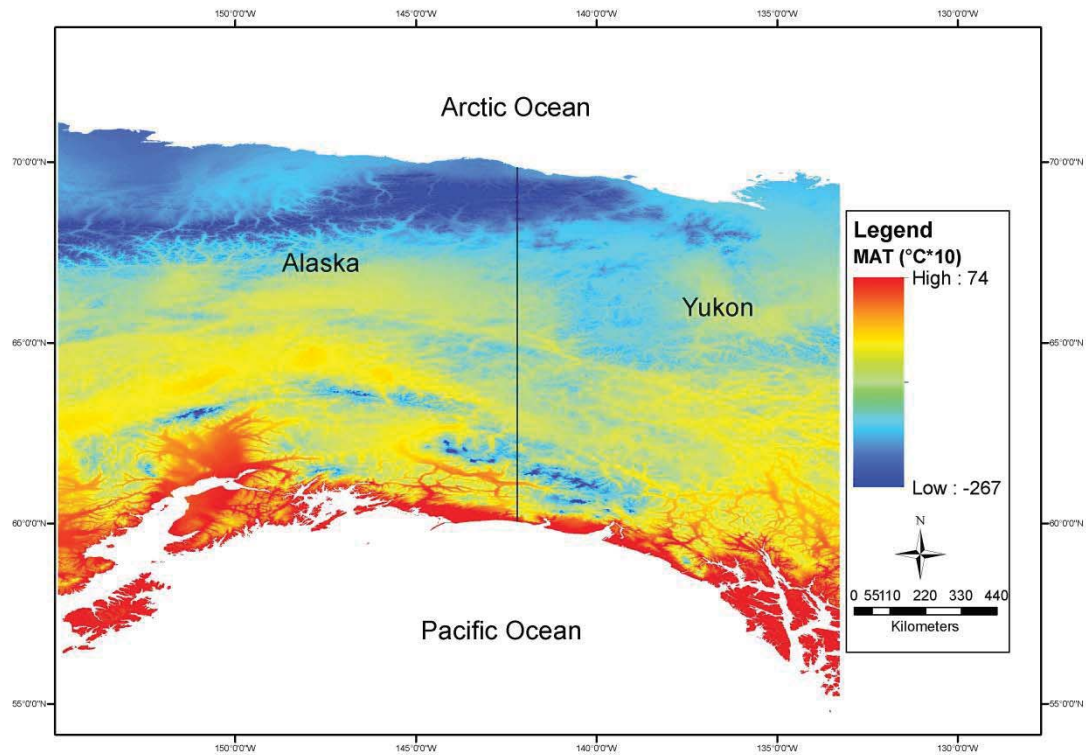


Figure 2.6. Mean Annual Temperature (MAT). Map of Alaska and the Yukon showing MAT from the WorldClim database spanning 1961 - 1990 (Hijmans et al., 2005). Plotted temperatures are reported in  $^{\circ}\text{C} \times 10$ , so MAT range from  $+7.4^{\circ}\text{C}$  to  $-26.7^{\circ}\text{C}$ .

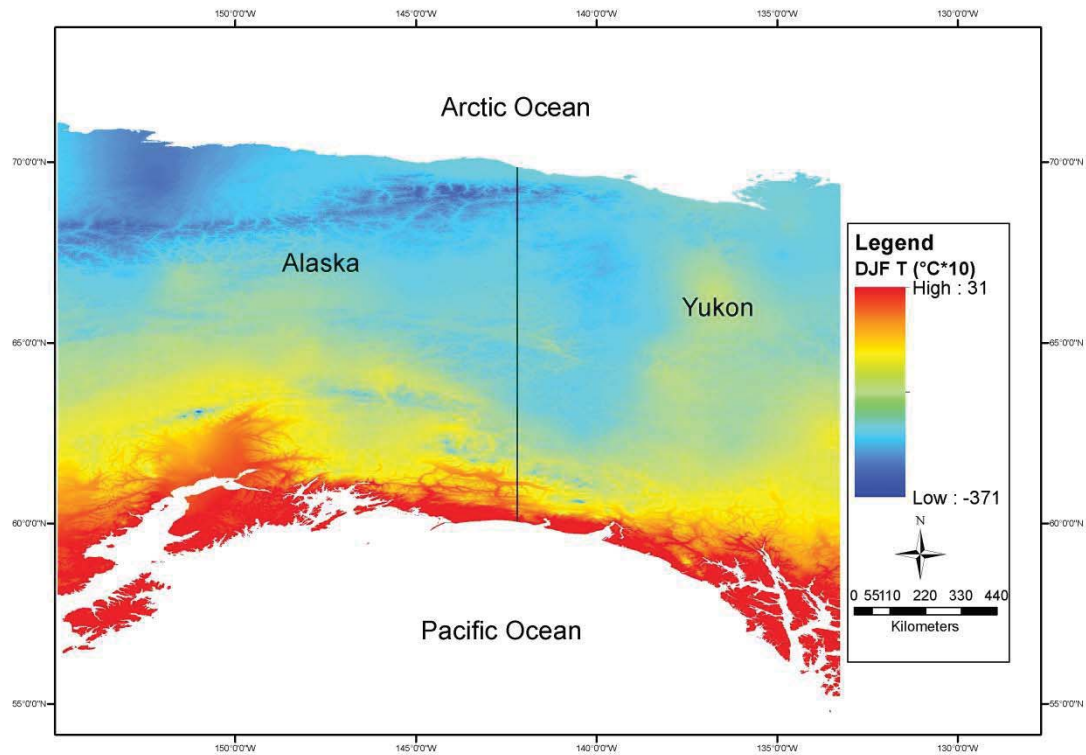


Figure 2.7. DJF temperatures. Map of Alaska and the Yukon showing average December, January, and February (DJF) temperatures from the WorldClim database spanning 1961 - 1990 (Hijmans et al., 2005). Plotted temperatures are reported in  $^{\circ}\text{C} \times 10$ , so DJF T range from  $+3.1^{\circ}\text{C}$  to  $-37.1^{\circ}\text{C}$ .

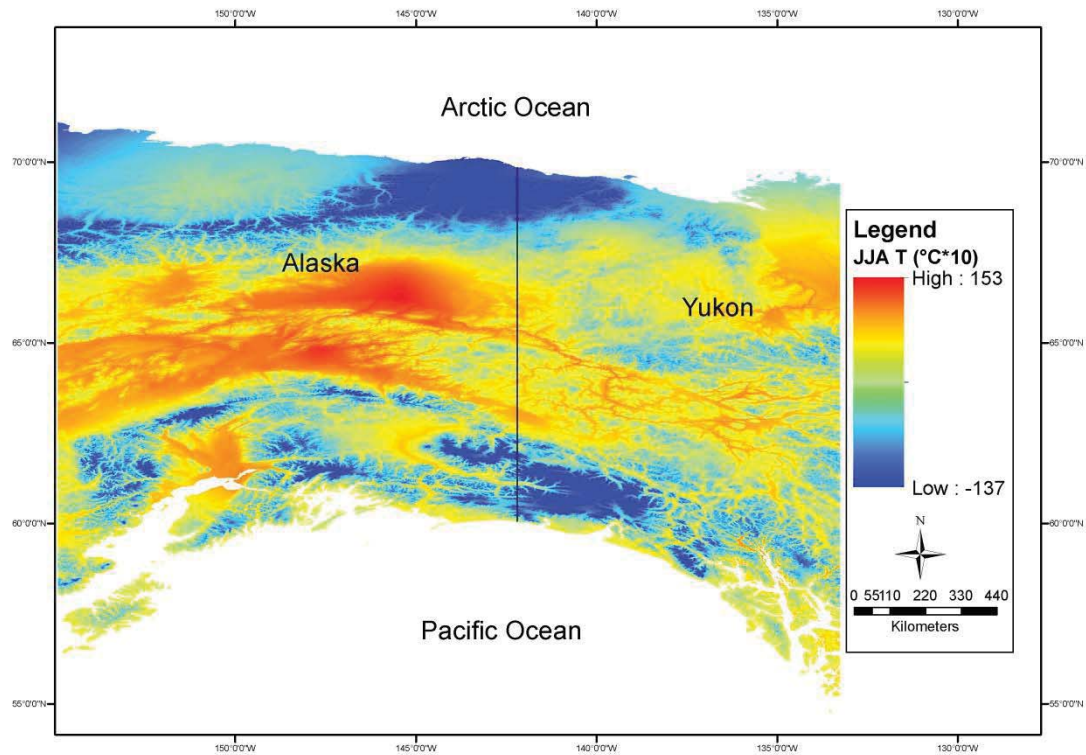


Figure 2.8. JJA temperatures. Map of Alaska and the Yukon showing average June, July, and August (JJA) temperatures from the WorldClim database spanning 1961 - 1990 (Hijmans et al., 2005). Plotted temperatures are reported in  $^{\circ}\text{C} \times 10$ , so JJA T range from  $+15.3^{\circ}\text{C}$  to  $-13.7^{\circ}\text{C}$ .



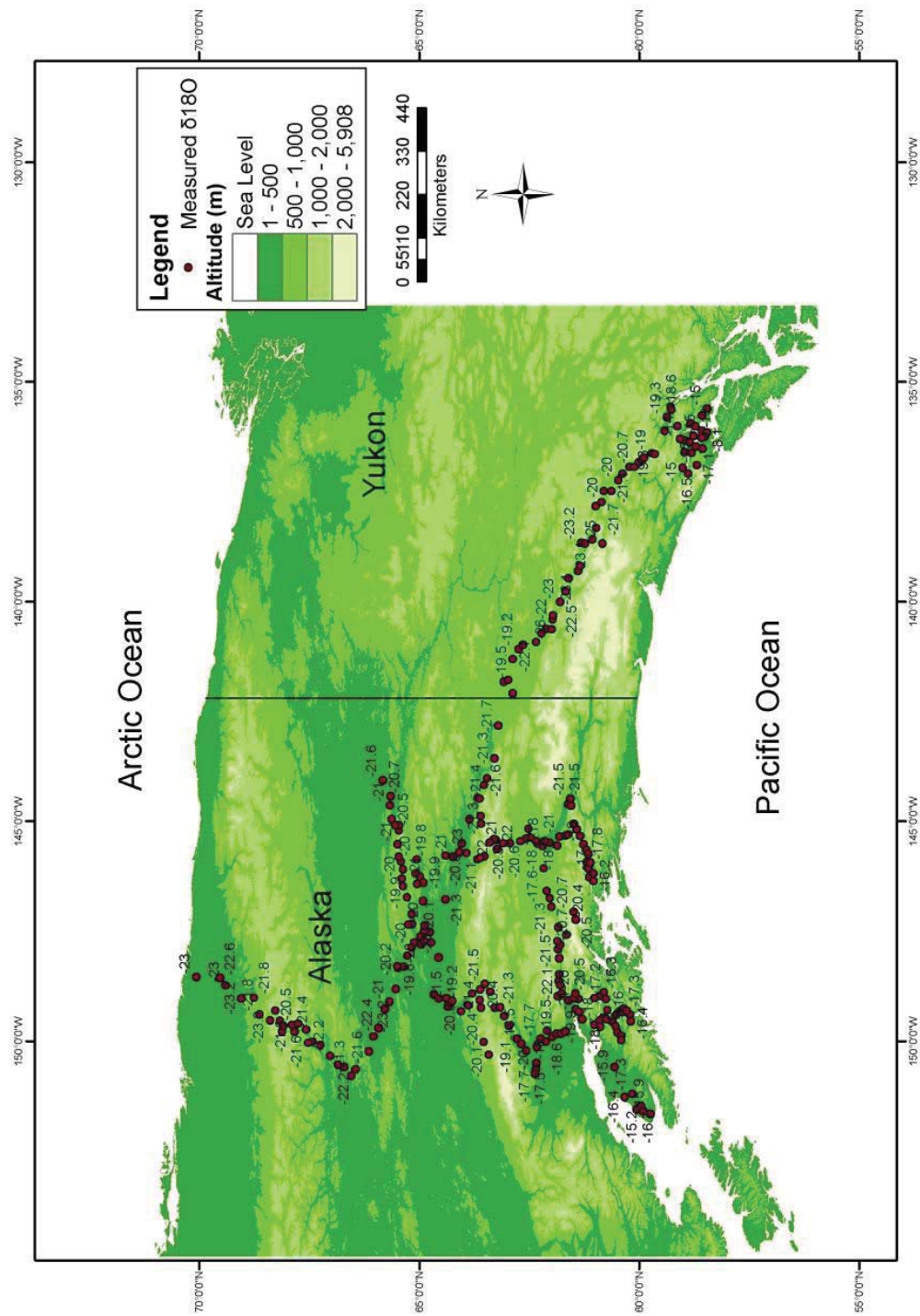


Figure 2.9.  $\delta^{18}\text{O}$  values of surface water samples. Surface water  $\delta^{18}\text{O}$  values range from -8.1‰ to -25.9‰, averaging -19.4‰. The base map is a USGS 300-m Digital Elevation Model (DEM) (USGS, 1997).

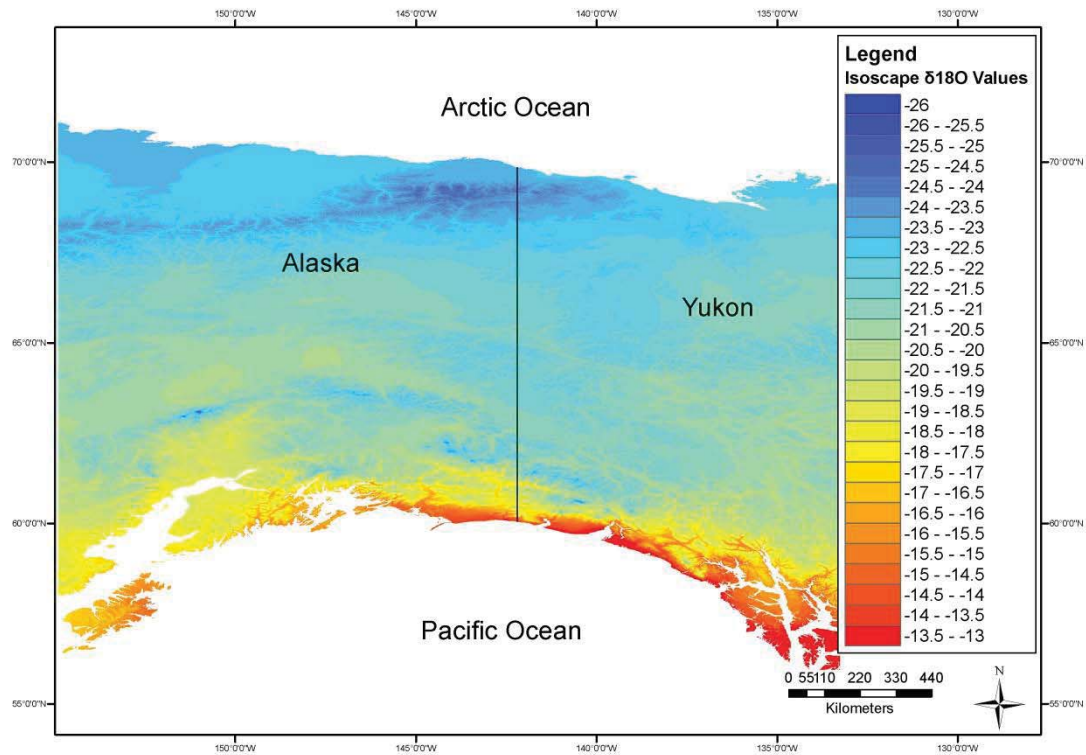


Figure 2.10. Isoscape of Alaska and the Yukon. Map showing isoscape of modeled  $\delta^{18}\text{O}$  values in surface waters. Modeled  $\delta^{18}\text{O}$  values range from -13‰ to -26‰, with the less negative values occurring along the Gulf of Alaska where temperature and precipitation amounts are higher, and the more negative values occurring at higher altitudes and in the interior where temperature and precipitation amounts are lower.

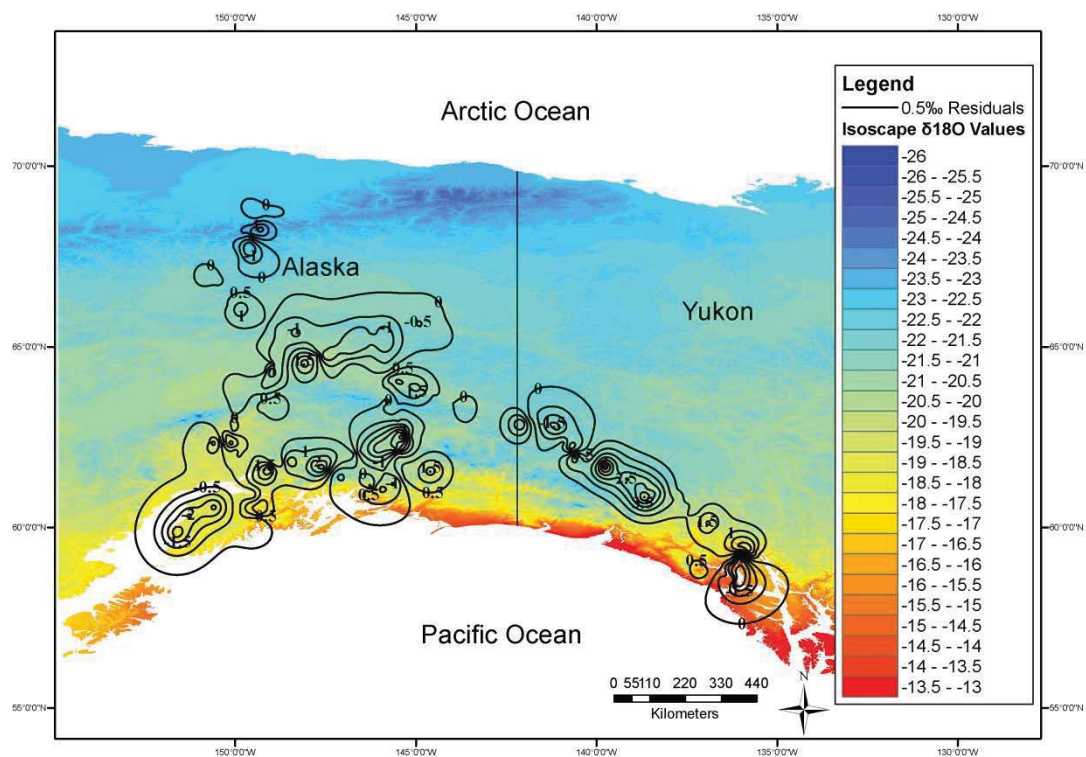


Figure 2.11. Map of isoscape residuals. Map showing the difference between measured and modeled  $\delta^{18}\text{O}$  values in surface waters across Alaska and the Yukon. Residual values are contoured in 0.5‰ contours, ranging from -2‰ on the Kenai Peninsula to +3.5‰ in the rainshadow of the Wrangells, averaging +1.2‰.



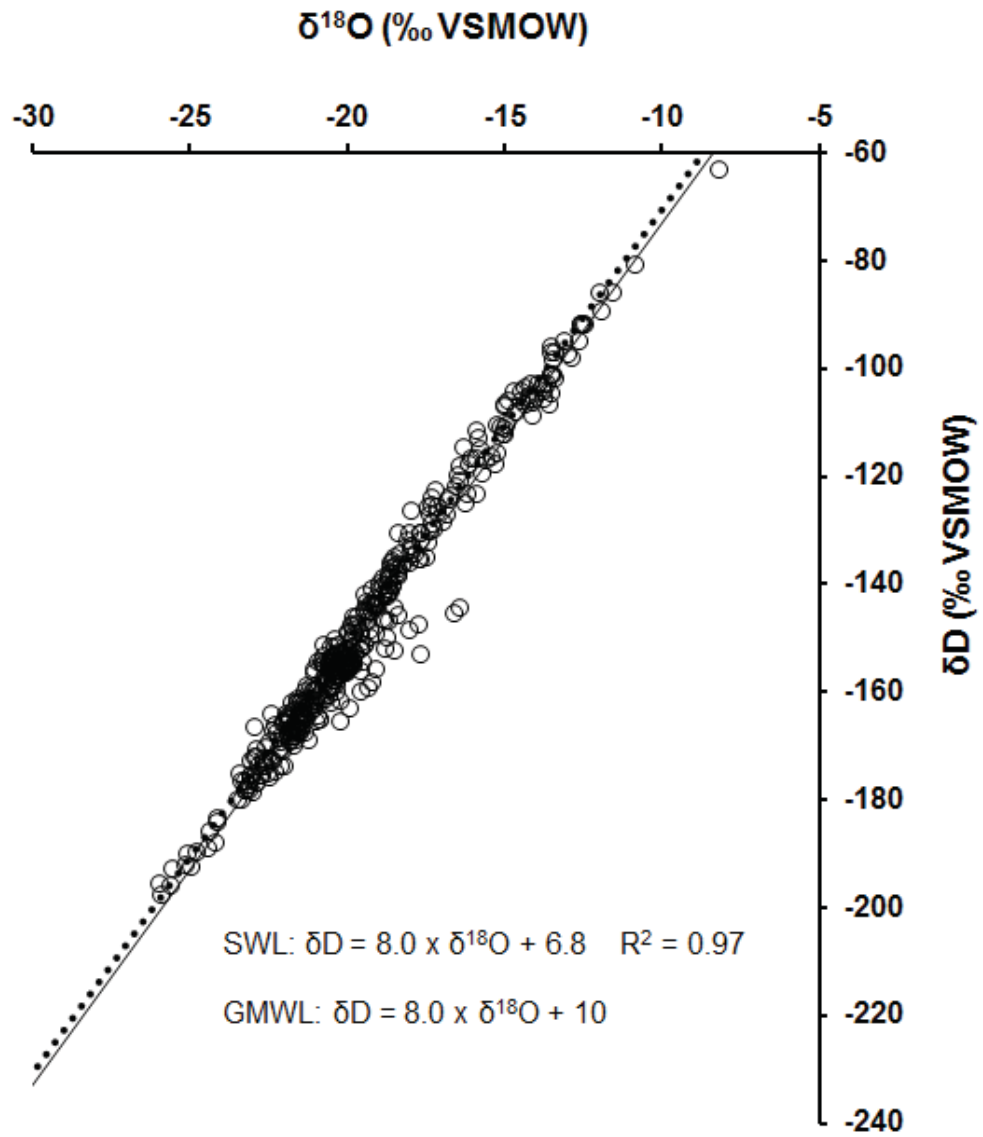


Figure 2.12.  $\delta^{18}\text{O}$  and  $\delta\text{D}$  surface water values. Plot showing  $\delta^{18}\text{O}$ ,  $\delta\text{D}$ , Surface Water Line (SWL, solid black line), and Global Meteoric Water Line (GMWL, dashed line). The SWL and GMWL are similar, suggesting surface waters can be used as proxies for precipitation  $\delta^{18}\text{O}$  values.

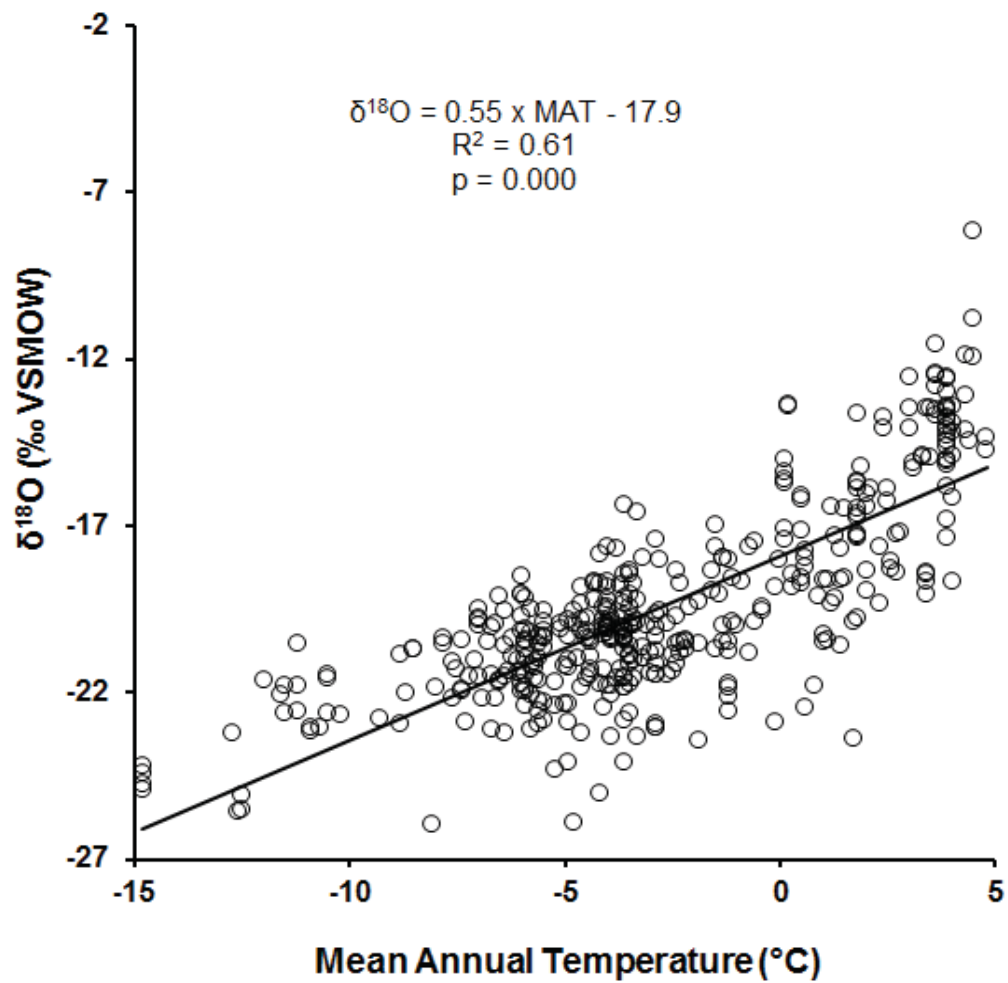


Figure 2.13. MAT and  $\delta^{18}\text{O}$  values. Mean Annual Temperature (MAT) of sampled catchments and  $\delta^{18}\text{O}$  values decrease at a rate of 0.55‰ per 1°C drop in MAT. Rayleigh distillation driven by temperature decreases over the Chugach Mountains and the Alaska Range causes rainout and the progressive depletion of  $\delta^{18}\text{O}$  values over the continent.

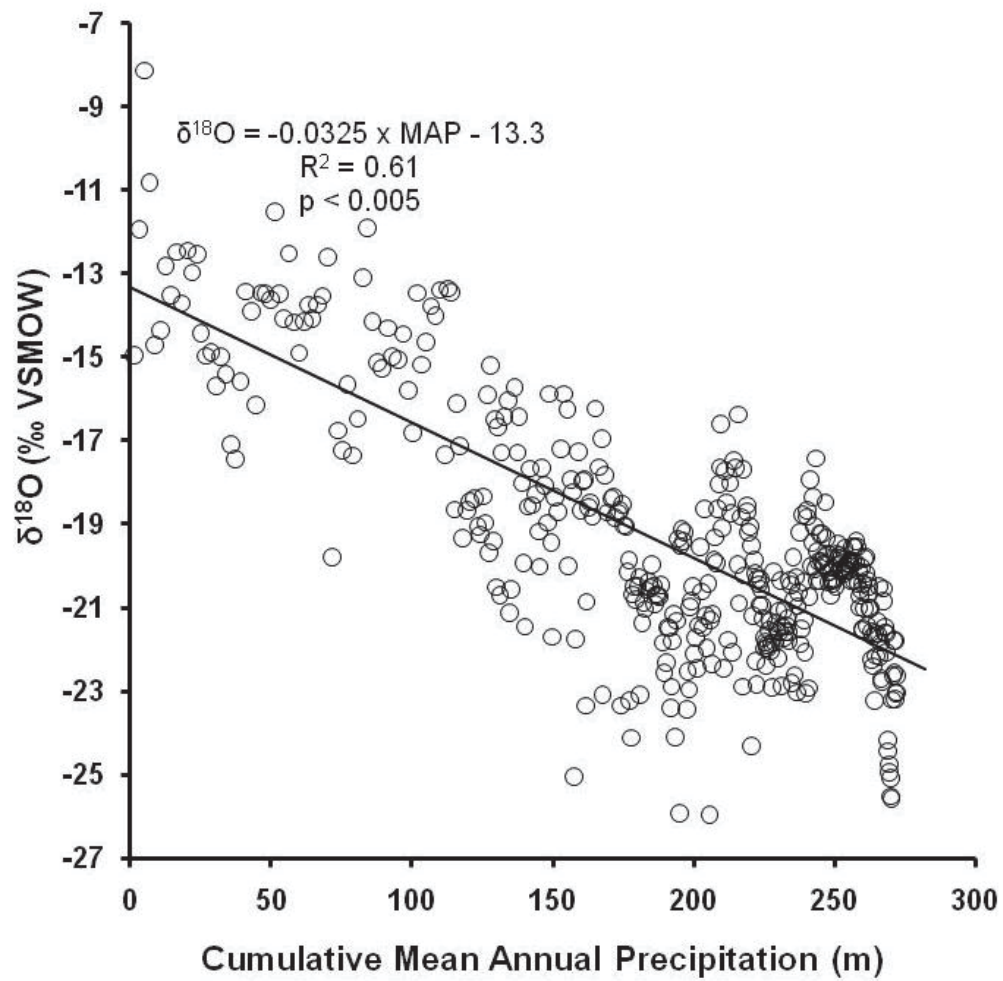


Figure 2.14.  $\delta^{18}\text{O}$  with cumulative MAP. Plot showing the change in  $\delta^{18}\text{O}$  with cumulative MAP and logarithmic relationship. The cumulative MAP is calculated starting in the south at the Gulf of Alaska (0 m) and concludes in the north at the Arctic Ocean (270 m). As air masses in the Pacific Ocean move inland, progressive loss of the heavier isotopes results in precipitation that becomes increasingly more negative with distance north.

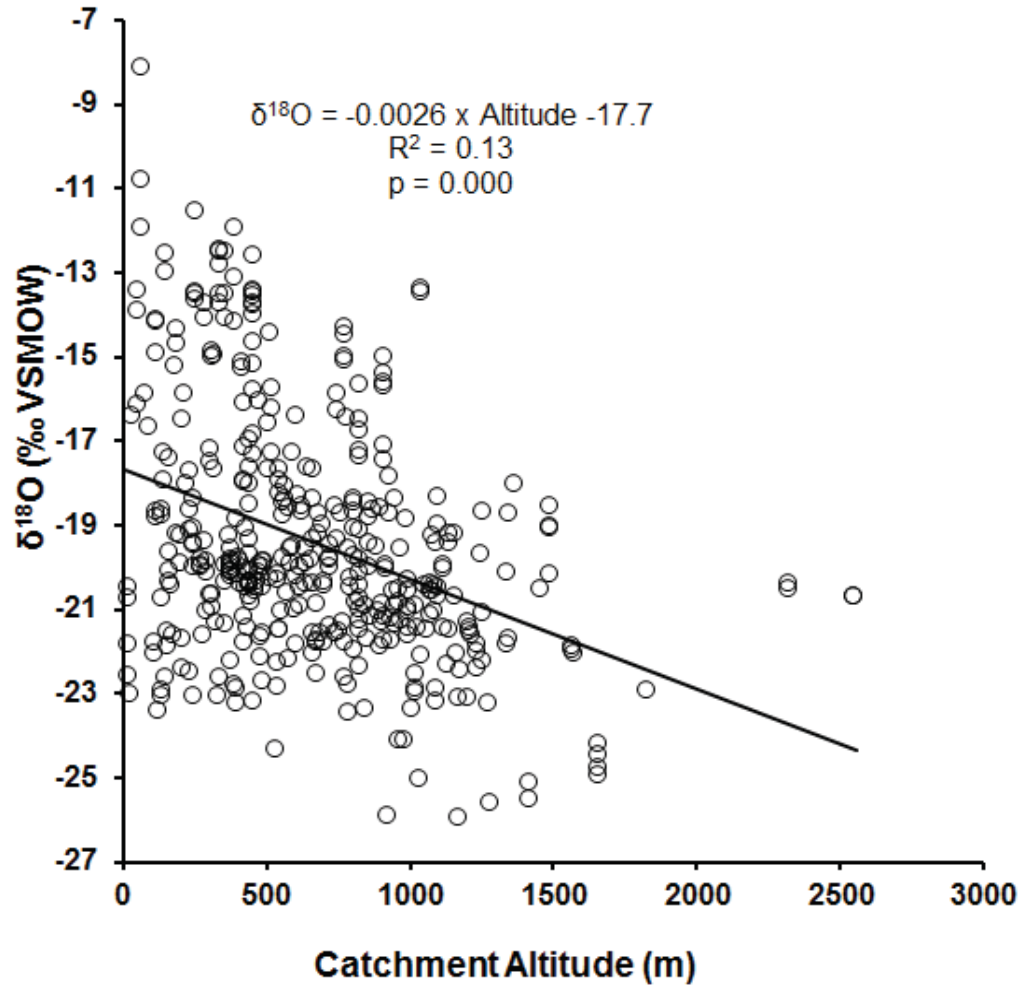


Figure 2.15.  $\delta^{18}\text{O}$  change with catchment altitude. The calculated linear relationship suggests that values of  $\delta^{18}\text{O}$  decrease by  $2.6\text{‰ km}^{-1}$ ; however, the lack of correlation ( $R^2$ ) indicates that the catchment altitude is not a controlling factor in  $\delta^{18}\text{O}$  composition.

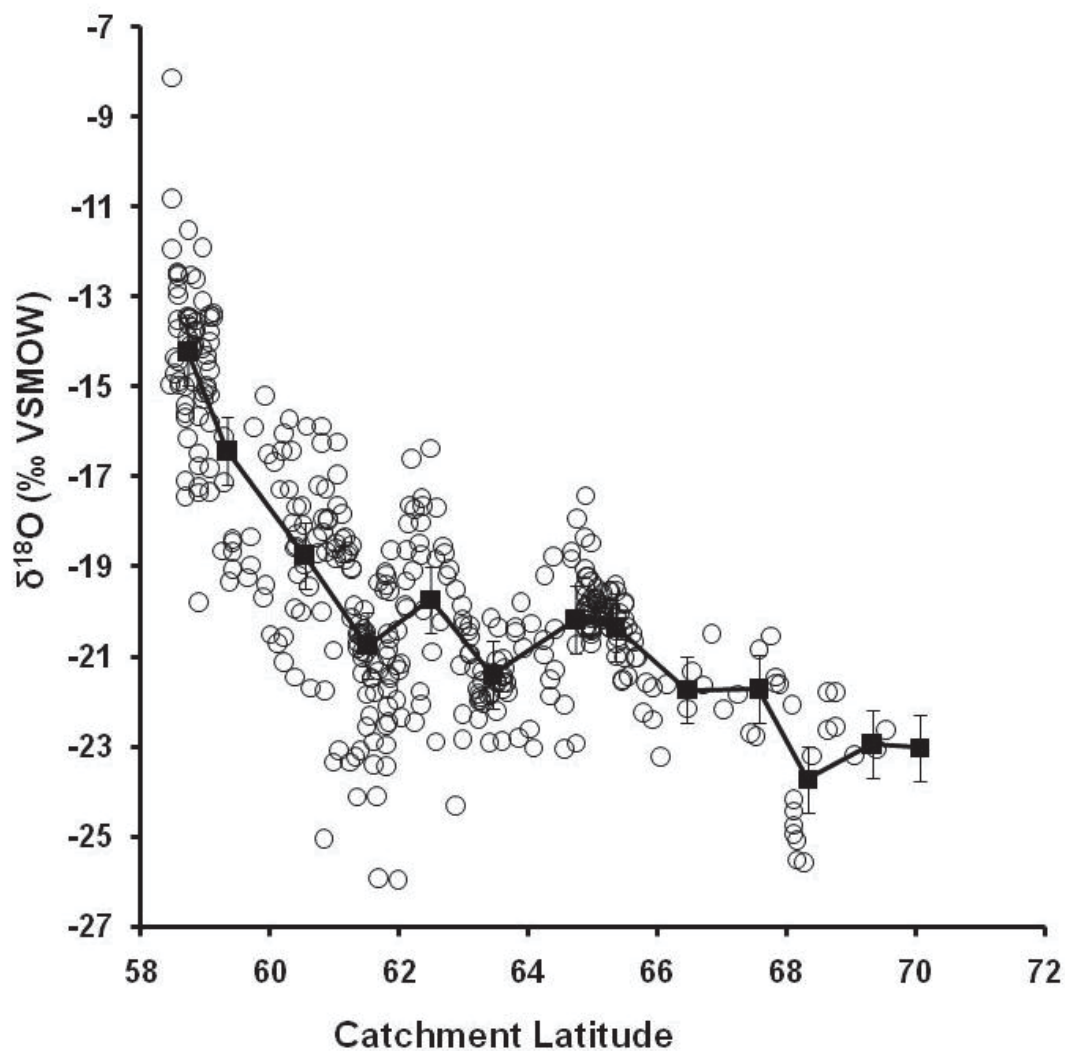


Figure 2.16.  $\delta^{18}\text{O}$  change with catchment latitude. The average  $\delta^{18}\text{O}$  values (open circles) separated into 1-degree latitudinal groups (black squares) with one  $\sigma$  error bars show a regional curvilinear decrease with latitude, indicating Rayleigh distillation during rainout over the continent controls isotopic values in Alaskan precipitation.

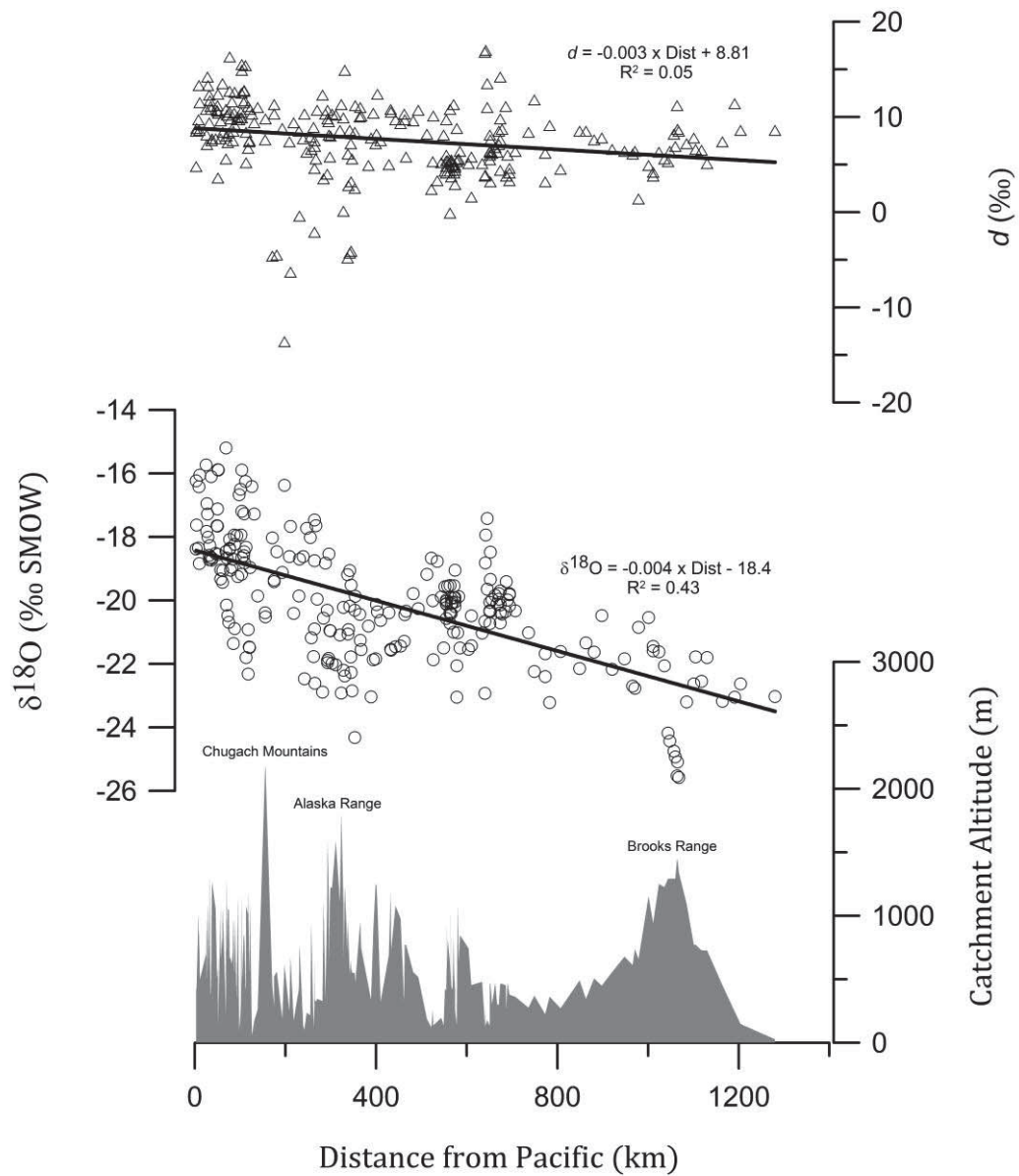


Figure 2.17. South to north transect of surface water  $\delta^{18}\text{O}$  values in Alaska. Plot showing surface water  $d$  values (triangles),  $\delta^{18}\text{O}$  values (circles), and topography (profile) from the Gulf of Alaska (left; 0 km) to the Arctic Ocean (right, 1,280 km). From south-north, the Chugach Mountains, Alaska Range, and Brooks Range are visible.  $\delta^{18}\text{O}$  values decrease at a rate of 4‰ per 1000 km distance from the Pacific, indicating increasing fractions of moisture removal from air masses as they move north across the continent.

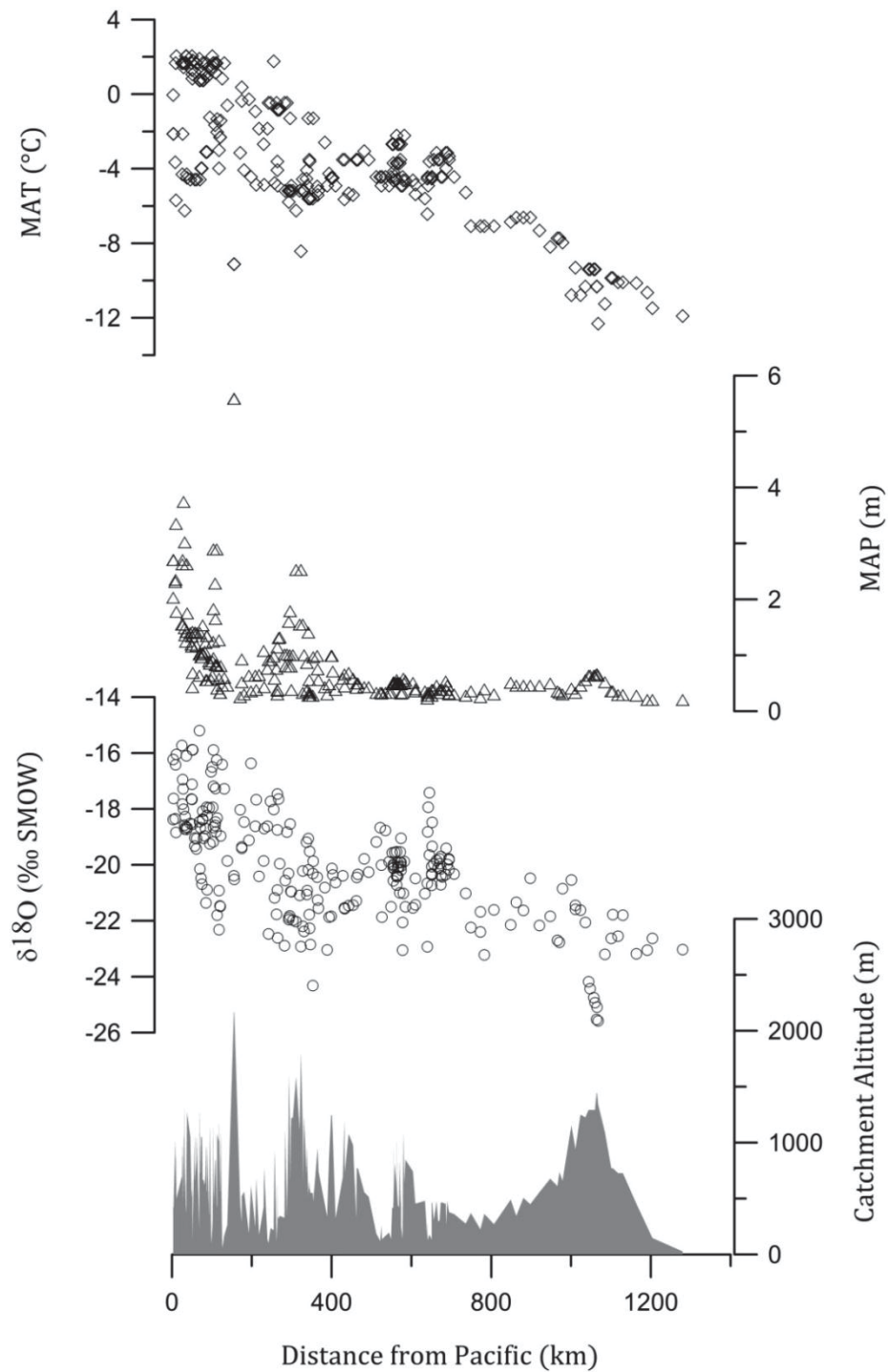


Figure 2.18. South to north transect of MAT, MAP, and  $\delta^{18}\text{O}$ . Topographic profile showing the south-north transect of Mean Annual Temperature (MAT) (diamonds), Mean Annual Precipitation (MAP) (triangles), and surface water  $\delta^{18}\text{O}$  values (circles). The progressive rainout of heavy isotopes from the south to the north during Rayleigh distillation is apparent in the decreasing  $\delta^{18}\text{O}$  values and temperatures, the high MAP over the mountains, and the low MAP values in the interior.

Table 2.1. Average temperature and precipitation for sampled catchments.

	<b>Average</b>	<b>Range</b>		<b>Average</b>	<b>Range</b>
<b>MAT (°C)</b>	-2.7	-12.7 to 4.8	<b>MAP (m)</b>	0.672	0.158 to 1.922
<b>DJF T (°C)</b>	-16.3	-29.5 to -1.9	<b>DJF P (m)</b>	0.277	0.010 to 0.751
<b>JJA T (°C)</b>	9.4	2.9 to 11.6	<b>JJA P (m)</b>	0.093	0.029 to 0.468





Table 2.3. Multiple linear regression results.

Variable	Statistical Best - Colinear	Physical Basis - Non-Colinear	Physical Basis - Non-Colinear	
		Equation 1	Equation 2	
	Coefficient	p-value	Coefficient	p-value
Sample Lat (dec. deg.)				
Sample Long (dec. deg.)				
Sample Alt (m)				
Catch Lat (dec. deg.)	-0.00145353	0.000		
Catch Long (dec. deg.)	-0.369677	0.000		
Catch Alt (m)	-0.00460049	0.000		
GI (1) NG (2) Perm (3)				
Dist from Pacific (m)				
MAP (m)	0.17242	0.000		
Cum MAP (m)	-1.46E-06	0.000		2.04114E-08
DJF P (m)	0.0118832	0.000	0.0102247	0.0089869
JJA P (m)	-0.00084363	0.000		
MAT (°C)	-0.0869074	0.000		0.0252606
DJF T (°C)	0.0348934	0.000	0.0090214	
JJA T (°C)	0.0768975	0.000		
δD (‰ VSMOW)				
d				
Intercept	-3.34501		-19.6118	-20.1991
RMSE	1.51827		1.65657	1.57856
R <sup>2</sup>	0.74		0.68	0.71
R <sup>2</sup> Adjusted	0.73		0.68	0.71
F-statistic	111.491		432.739	331.615

## CHAPTER 3

### THERMAL STRATIGRAPHY OF THE FOX PERMAFROST TUNNEL

#### **Abstract**

The persistence of old carbon in permafrost environments is problematic in establishing ages of ice formation used to constrain climatic perturbations during the late Pleistocene. Previous work in the CRREL Permafrost Tunnel has suggested that ancient preserved ice wedges formed syngenetically during Marine Isotope Stage 3 (MIS 3). However, a new method of determining the timing of ice wedge and pool ice formation using radiocarbon-dated DOC and CO<sub>2</sub> reveals that the features are much younger than previously thought and are epigenetic in origin. At least five freeze events and one melt event are apparent in the tunnel. Large ice wedges from the tunnel likely formed between 26 – 22 cal ka BP, or possibly during Heinrich event 2. The formation of these Freeze event 1 wedges was followed by secondary wedges that formed during Freeze event 2. These events were truncated by Melt event 1, which likely occurred between 22 - 18 cal ka BP, as indicated by pool ice and thaw features apparent in the tunnel. Ice wedges in Freeze event 3 likely formed between 18 - 13 cal ka BP, or possibly during Heinrich event 1, after the melt event. Inconclusive radiocarbon ages from a fourth interval of ice wedge formation, Freeze event 4, prohibit precise dating of ice wedge formation. However, the stratigraphic location of the Freeze event 4 wedges indicates that the wedges likely formed after 18 cal ka BP, possibly around 15 cal ka BP. A final freeze event, Freeze event 5, may have occurred prior to the onset of the Younger Drays cold event, but wedges from this interval were not sampled. The prevalence of inversions in

the radiocarbon ages indicates that carbon may persist for as long as 17,000 years within permafrost environments, potentially providing anomalous age dates when dating carbon in permafrost. This highlights the importance of combining stable isotope analyses with  $^{14}\text{C}$  dating of DOC within ice in permafrost environments to constrain the age of climatic perturbations in Central Alaska.

## **Introduction**

Because ice wedges form in winter by thermal contraction cracking and infilling of snow meltwater in spring (French, 2007; Lachenbruch, 1962), they have been used as potential proxies for paleoclimate and records of the isotopic value of winter precipitation in Siberia (Popp et al., 2006; Rozanski et al., 1997; Wetterich et al., 2011), Antarctica (Raffi and Stenni, 2011), and Alaska (Meyer et al., 2010b). The previous year's cracking creates zones of weakness in the ice, allowing for preferential cracking along the weakened areas, usually in the middle of the wedge (Mackay, 1975). When the ground contracts again the next winter, loess, silt, and macroscopic organic debris (macros) blow into the crack, forming an organic-rich layer, or folia, in between each cracking event (French and Shur, 2010). Spring meltwater once again flows into and refreezes as it fills the crack, recording that year's climatic information (Meyer et al., 2002). As the process continues each winter and spring, annual sub-vertical layers of spring meltwater and organic debris form a wedge shape, recording hundreds to thousands of years of climatic signals (Vasil'chuk, 2013). Cracking typically occurs near the center of the wedge, with the youngest ice near the center of the wedge progressively becoming older toward the outside of the wedge (Opel et al., 2011).

Varying environmental conditions produce two different types of ice wedges. Sediment accumulation occurring synchronously with thermal contraction of frozen ground typically produces syngenetic ice wedges, which theoretically should contain ages similar to those of the host sediment because the sediment deposition, peat accumulation, burial, or mass movement of the material occurs at the same time (French and Shur, 2010). These wedges may be up to 3 – 5 m wide near the surface and extend down to 10 m as growth occurs over long periods of continuous sedimentation with repeated frost cracking (Harry and Gozdzik, 1988). Epigenetic ice wedges, however, form within existing sediments and should have ages younger than the surrounding sediments (Mackay, 1990). Epigenetic wedge size is limited by the mean depth of frost cracking, resulting in smaller (1-1.5 m wide and up to 4 m in height) wedges (Harry and Gozdzik, 1988).

Constraining the timing of frost cracking in both epigenetic and syngenetic ice wedges using conventional radiocarbon dating of particulate organic carbon (POC) has been problematic, providing ages out of stratigraphic order (Hamilton et al., 1988) and anomalously old ages within the wedge (Griffing, 2011; Hamilton et al., 1988). Although there has been some success with Accelerator Mass Spectrometer (AMS)  $^{14}\text{C}$  dating of POC within Siberian and Alaskan ice wedges (Meyer et al., 2010a; Opel et al., 2011), age inversions are also common (Hamilton et al., 1988; Shur et al., 2004). Inactive or relict ice wedges preserved in the CRREL Permafrost Tunnel near Fairbanks, Alaska (Figure 3.1) had been assigned an age of Marine Isotope Stage (MIS) 3 based on POC  $^{14}\text{C}$  ages (Hamilton et al., 1988; Sellmann, 1967), but a significantly younger  $^{14}\text{C}$  age of  $24,884 \pm 139$   $^{14}\text{C}$  yr BP ( $29,770 \pm 230$  cal yr BP) was determined from methane extracted from an

ice wedge in the tunnel (Katayama et al., 2007), bringing into question the true age of ice wedges and timing of events in Central Alaska.

Lachniet et al. (2012) investigated this age disparity in a single wedge (50S) from the CRREL Permafrost Tunnel and found that the persistence of old carbon in the environment and the contribution of that old organic matter into an ice wedge during formation caused anomalously old ages when dating POC. The ice wedge had previously been assigned an age of MIS 3 based on  $^{14}\text{C}$  dates on POC from within the ice and sediments surrounding it (Hamilton et al., 1988), but  $^{14}\text{C}$  dating of dissolved organic carbon (DOC) and occluded  $\text{CO}_2$  gas within the ice enabled Lachniet et al. (2012) to model the age of  $\text{CO}_2$  by calculating the fraction of respired  $\text{CO}_2$  and the age of respired  $\text{CO}_2$ . The modeled ages, although younger than the  $\text{CO}_2$  age, were near the DOC ages, indicating that the DOC age can be used to approximate the timing of ice formation. Because it is only possible to contaminate the currently forming ice wedge with older, not younger, organic material, these DOC ages were used as an estimate for the timing of ice wedge formation. This DOC and  $\text{CO}_2$  dating method established a maximum limiting age of ice wedge formation, suggesting that the ice wedge formed between 28 and 22 cal ka BP during MIS 2, perhaps even during Heinrich event 2 (Lachniet et al., 2012). This new  $^{14}\text{C}$  dating improved upon previous work that had investigated oxygen ( $\delta^{18}\text{O}$ ) and hydrogen ( $\delta\text{D}$ ) stable isotopes. Radiocarbon dating of POC from the same ice wedge had suggested that it had formed during Heinrich event 3 (Griffing, 2011).

My research tests the hypothesis that ice wedge freezing and melt occurred in the Permafrost Tunnel during and after MIS 2, and it further refines the thermal event

chronology by additional  $^{14}\text{C}$  dating of carbon associated with sediments and ice. This paper uses the novel approach of using DOC and  $\text{CO}_2$   $^{14}\text{C}$  dated ice wedges to provide a new chronology of thermal events in Central Alaska during the past ca. 30,000 years.

## **Tunnel geology**

### ***Tunnel stratigraphy***

The CRREL Permafrost Tunnel in Fox, Alaska (Figure 3.1) lies within the zone of discontinuous permafrost in Central Alaska. The 120-meter long main tunnel and side winze were excavated from the frozen sediments of the Late Quaternary Goldstream Formation (Hamilton et al., 1988; Sellmann, 1967) (Figure 3.2). A general stratigraphic column with radiocarbon-dated sediment and ice was established by Sellmann (1967) and Hamilton et al. (1988) (Figure 3.3). At the base of the tunnel, the stratigraphy consists of the 1 m thick Birch Creek Schist bedrock overlain by the Fox Gravel. The Fox Gravel is 3-4 m thick, consisting of imbricated sandy gravel with angular to subangular clasts of schist, quartz, gneiss, and granite with lenses of silt and sand. These 20 cm thick by 1-2 m long lenses contain 10-cm diameter willow wood stumps and wood fragments (Hamilton et al., 1988). Tree logs dated by liquid scintillation counting rooted in the Fox Gravel indicate that deposition occurred  $43,410 \pm 240$   $^{14}\text{C}$  yr BP ( $46,320 \pm 350$  cal yr BP) (Long and Pewe, 1996). This age was similar to Hamilton et al.'s (1988)  $^{14}\text{C}$  age of  $43,300 \pm 1600$  ( $46,930 \pm 1390$  cal yr BP) of willow wood from the same location. However, both ages are near the limit for radiocarbon dating (Reimer et al., 2009) and record the possible timing of tree growth, not of deposition. Because of these potentially infinite ages, the true age of the Fox Gravel is unknown.

The Fox Gravel is unconformably overlain by a lower 4-5 m thick unit consisting of coarse and medium silt that Hamilton et al. (1988) classified as eolian in origin. Large 2-4 m wide ice wedges extend vertically 3-4 m in the lower silt unit and are truncated by a thaw unconformity. Thaw features, which were first interpreted as melt ponds (Sellmann, 1967) and later as thermokarst cave ice (Douglas et al., 2011; Kanevskiy et al., 2008; Shur et al., 2004), extend above the thaw unconformity as 2-6 m wide by 0.5-2.0 m deep lenses. An upper 8-11 m thick unit consisting of coarse and medium silt contains smaller 0.2-1 m wide wedges that extend vertically 1-2 m into the tunnel. The upper silt unit is overlain by debris fan deposits of subangular quartz and schist in silty sand (Hamilton et al., 1988). Sellmann (1967) described a separate unconformity in the upper 1-2 m consisting of reddish brown organic silt with oxidized zones above reddish brown to gray silt. This unconformity is exposed in a now-inaccessible vertical ventilation shaft at the rear of the tunnel.

### ***Tunnel $^{14}\text{C}$ ages***

Efforts to determine the timing of deposition of sediments and ice wedge formation in the tunnel have been problematic because of multiple age inversions and the persistence of old carbon in permafrost environments. Sellmann (1967) first attempted to determine the timing of tunnel sediment deposition and ice wedge formation using gas proportional counting  $^{14}\text{C}$  dating. For the current study, radiocarbon ages were calibrated to calendar years before present (cal yr BP) using the OxCal 4.2 program (Bronk Ramsey, 2009) and the IntCal09 calibration (Reimer et al., 2009). Radiocarbon ages from wood fragments, peat, bone, and fibrous plant material from tunnel sediments ranged from  $6,970 \pm 135$   $^{14}\text{C}$  yr BP ( $7,810 \pm 1200$  cal yr BP) in the ventilation shaft to  $33,700 \pm$



2500  $^{14}\text{C}$  yr BP ( $39,170 \pm 2920$  cal yr BP) in the lower silt unit (Sellmann, 1967).

Additional radiocarbon ages from willow wood and organic fragments of wood and grass rootlets from the lower silt unit led Hamilton et al. (1988) to conclude that deposition occurred between  $36,200 \pm 2500$   $^{14}\text{C}$  yr BP ( $41,460 \pm 2700$  cal yr BP) and  $30,160 \pm 160$   $^{14}\text{C}$  yr BP ( $34,780 \pm 130$  cal yr BP).

Hamilton et al. (1988) also concluded that the interval during MIS 3 was a period of ice wedge growth because radiocarbon ages from organic residue and amorphous plant organic material extracted from lower unit melted ice wedges overlapped surrounding sediments and ranged from  $31,400 \pm 2900/2100$   $^{14}\text{C}$  yr BP ( $37,270 \pm 3780$  cal yr BP) to  $32,300 \pm 2000/1600$   $^{14}\text{C}$  yr BP ( $37,610 \pm 2390$ ) (Sellmann, 1967). However, age inversions such as the older radiocarbon ages of  $32,790 \pm 560$   $^{14}\text{C}$  yr BP ( $37,525 \pm 680$  cal yr BP) and  $35,500 \pm 2400$   $^{14}\text{C}$  yr BP ( $40,760 \pm 2660$  cal yr BP) (Hamilton et al., 1988) from peat mats above the dated wedge and lower silt unit suggested that the sediments had been reworked during thaw processes (Shur et al., 2004). Additional evidence for reworking of sediments included a much younger  $^{14}\text{C}$  age of methane of  $24,880 \pm 140$   $^{14}\text{C}$  yr BP ( $29,770 \pm 230$  cal yr BP) extracted from lower unit ice wedge 50S (Katayama et al., 2007), although the details of this dating technique were not published.

These age inversions and apparent wedge growth during interstadial, not stadial, periods led Lachniet et al. (2012) to use AMS dating of wedge 50S and an adjacent ice lens from the thaw unconformity using POC, DOC, and occluded  $\text{CO}_2$  gas from within the ice. POC from within the ice ranged in age from  $28,260 \pm 180$  to  $37,040 \pm 410$  cal yr BP, similar to ages of sediments surrounding the wedge. This led to the conclusion that

the POC from the sediments and within the wedge was of similar origin, and possibly entered the wedge with melt water seeping through the active layer surface during spring thaw. This process helps explain the age inversions apparent within the tunnel as older particulate carbon was incorporated into stratigraphically lower ice wedges. In contrast to the POC ages, analyses of CO<sub>2</sub> gas and DOC from wedge 50S returned ages between 28 and 23 ka cal yr BP for the wedge and  $21,470 \pm 200$  cal yr BP for an ice lens stratigraphically above the wedge. This suggested that ice wedges in the lower silt unit of the tunnel formed during MIS 2, earlier than previously suggested.

Ice wedges in the upper silt unit are stratigraphically constrained by an age of  $12,570 \pm 390$  <sup>14</sup>C BP ( $14,880 \pm 730$  cal yr BP) from peat at the contact between the upper silt unit and the debris fan (Hamilton et al., 1988). However, reworking of sediments during deposition of this debris fan could have caused age inversions. The youngest date of  $11,000 \pm 280$  <sup>14</sup>C yr BP ( $12,900 \pm 280$  cal yr BP) from a wood log appears near the tunnel entrance and upper stratigraphic section of the tunnel (Sellmann, 1967). To complete the chronological thermal history of Central Alaskan paleoclimate, additional dating following the method of Lachniet et al. (2012) is needed to constrain the timing of the upper and lower unit ice wedges and thaw features in the tunnel.

## **Methods**

To refine the ages of thermal events in central Alaska, ice wedge and pool ice samples were collected from the CRREL Permafrost Tunnel for isotopic subsampling. Ice wedges in the tunnel contained air bubbles and fine organic matter and silt that formed vertical and parallel to folia at the center of the wedge. Folia became more angled toward the outside and base of the wedges. Wedges ranged in size from 2 cm wide up to 3 m

wide and from 1 m to over 6 m in height. Clear pool ice or lens ice was found above the large wedges in the lower silt unit.

Ice wedges and pools of various sizes and from various stratigraphic positions were identified for sampling in the main tunnel and named according to their distance in meters from the tunnel entrance on the north (N) or south (S) tunnel wall. Sample names/distances in this study differed by approximately -8 m compared to posted distances inside the tunnel because the zero point in this study started at the tunnel door entrance. Ice wedges and pools were photographed, measured, and sketched in detail to document stratigraphic position in the tunnel and distinguishing features. Sample blocks from eight ice wedges (1N, 14.9S Winze, 18N, 35S, 45S, 50S, 52.5S, and 58N) and seven ice pools (31N-Pool, 34S-Pool, 45N-Pool, 50S-Pool A, 50S-Pool L, 51S-Pool, and 70N-Pool) within both stratigraphic units in the main tunnel were collected. Ice wedges and pools were swept clean of silt and debris. Samples were cut from the wedges in approximately 30-cm-tall blocks for the width of the entire wedge using an electric chain saw and removed by cracking the block ice face with chisels. Samples from the ice pools were cut in approximately 30-cm by 30-cm blocks with an electric chain saw and removed with chisels. Green sedge *Carex aquatilis* (B. Lichvar, personal communication, October 26, 2011) material from one of the ice pools was also sampled for radiocarbon analyses. Blocks were measured, labeled, and packed into coolers for transport to the CRREL cold room at Ft. Wainwright, AK.

The cold room facility at Ft. Wainwright, AK consisted of a -5°C temperature-controlled Butcher Boy freezer. Each ice block was removed from its cooler and scraped clean of silt from the tunnel using aluminum ice scraping tools. Once cleaned of silt and

debris, each block was measured, hand-sketched in detail to show cross-cutting and other important features, and photographed. Approximately 10-cm slices of ice were cut from the wedge blocks with a chain saw, with extreme care taken while sampling to avoid contamination of the samples with modern carbon. Each slice was packaged separately and double bagged in Ziploc bags to prevent cross-contamination. Samples were packed in coolers with ice and cold packs, and shipped overnight via FedEx to the Las Vegas Isotope Science (LVIS) laboratory at the University of Nevada, Las Vegas. Samples were transferred to a freezer in the laboratory. They were later transported to the Scripps Institute of Oceanography in California and the University of Arizona, where CO<sub>2</sub> was isolated from the ice blocks via melting in an evacuated chamber.

Because of the possibility of carbonate-rich silt dissolving in water and producing CO<sub>2</sub> gas during melting, Wilson (1998) used a sublimating rather than a melting method of isolating the CO<sub>2</sub> gas from ground ice. The Tanana and Yukon Rivers were a source of carbonate loess to the Fairbanks region during the late Pleistocene, so tests to determine the presence of carbonates in residual organic material from melted wedge ice and surrounding sediments were conducted with 10% HCl solution. The organic residue and the sediments showed no reaction with the HCl, suggesting an absence of carbonate loess in the permafrost tunnel. This indicates that the loess was likely of Nenana River origin or that the calcium carbonate leached out of the loess before deposition (Beget, 1990; Muhs and Budahn, 2006). For this reason, a melting rather than sublimating method was used to extract the CO<sub>2</sub> gas from the ice wedges.

Dating of the ice blocks was conducted using a gas-extraction-by-ice-melting method. By melting the ice in an evacuated closed system, gas originally trapped within

the bubbles in the ice was extracted and measured for CO<sub>2</sub> and DOC. Using a modified method of Wilson (Wilson, 1998), an approximately 10-cm x 10-cm ice block was placed in a glass vessel, and the system was evacuated to remove atmospheric gas from the vessel. The block was left to melt over several hours and water vapor, CO<sub>2</sub>, and other atmospheric gases were separated cryogenically using an evacuated extraction line. The CO<sub>2</sub> was collected in glass ampoules and converted to graphite. The DOC was collected by evaporating the melted ice and separating the POC from the detrital silt. The CO<sub>2</sub> and DOC were analyzed for  $\delta^{13}\text{C}$  via AMS at the University of Arizona NSF Radiocarbon Facility in Tucson, Arizona. The  $\delta^{13}\text{C}$  values were reported in ‰ relative to the Vienna Pee Dee Belemnite (‰ VPDB) standard. The  $\delta^{13}\text{C}$  were used to estimate organic matter carbon sources. The OxCal 4.2 program (Bronk Ramsey, 2009) and the IntCal09 calibration (Reimer et al., 2009) were used to convert <sup>14</sup>C ages to calendar years before present (cal yr BP) (present = 1950 A.D.) and to determine age probability distributions at the 68.2% probability level. The ages were reported as median ages  $\pm$  one sigma uncertainty (Table 3.1).

## **Results**

### ***Ice wedge and pool ice stratigraphy***

Although previous research established the general sediment stratigraphy of the tunnel (Bray et al., 2006; Hamilton et al., 1988; Sellmann, 1967), the detailed thermal stratigraphy of the ice wedge and pool ice has not been established with enough detail to determine timing and extent of ice formation relevant to interpreting paleoclimate in central Alaska. This is in part due to anomalous <sup>14</sup>C ages, but also because thaw structures such as slumps, refrozen thaw pools, and debris fan deposits complicate the

stratigraphic placement of thermal events within the tunnel. In addition, not all ice wedges, ice pools, and thaw features appear in one continuous section of the tunnel, so the thermal stratigraphy must be pieced together based on relative position in the tunnel.

To better classify the relative age of the thermal events in the tunnel, the general stratigraphic sequence of host sediments, ice wedges, ice pools, thaw features, and ice wedge truncating features was documented with photographs and sketches from the main adit of the tunnel. The general sediment stratigraphy of the main adit consists of the Fox Creek Gravel at the base of the tunnel overlain by a lower silt unit, an upper silt unit above the lower silt, and a debris fan deposit that is visible in the ceiling near the tunnel entrance (Hamilton et al., 1988). Within this sediment stratigraphy, the thermal stratigraphy consists of 'freeze' and 'melt' events. Because ice wedges form as a result of freezing climatic conditions, ice wedges within the tunnel were classified as 'freeze' events. In the absence of additional evidence to the contrary, the clear ice above the ice wedges was interpreted to reflect pools of standing water that formed as a result of melting water that later refroze, thus assigning the generic term of 'pool' ice within a 'melt' event herein. The origin of the water in the pools is required to test between a 'pond' and 'thermokarst cave ice' origin, and such data will be discussed in Chapter 4. At least five distinct freeze events and one melt event that formed pools or thermokarst cave ice were identified (Figure 3.4). Freeze and melt events were enumerated according to their relative stratigraphic position in the tunnel and apparent sequence of formation, beginning with Freeze event 1 at the base of the tunnel (Wedges 28N, 35S, 45N, 45S, 50S, 58N, 60S, 67N, 70N), Freeze event 2 (35S secondary wedge), Melt event 1 (28N Pool, 31N Pool, 34S Pool, 45N Pool, 50S Pool, 51S Pool, 60S Pool, 70N Pool), Freeze

event 3 (Wedges 18N and 50N), Freeze event 4 (Wedges 14.9S, 50S, 52.5S), and Freeze event 5 (Wedges 45N, 52.5N, 60S, 64S) (Figure 3.4).

Freeze event 1 (F1) includes at least nine 1 - 2 m wide ice wedges exposed in the same apparent stratigraphic section in the lower silt unit at the base of the tunnel, about 12 – 13 m below the ground surface (bgs) (Figure 3.4). These F1 ice wedges, named because they appear to be in the lowest stratigraphic section of the tunnel and likely formed before the other wedges, consist of near vertical and parallel silt rich folia and ice bubbles (Figure 3.5A). Above F1, a small secondary wedge crosscuts the top of a single F1 wedge (35S) around 12 m bgs, suggesting it formed after F1 during Freeze event 2 (F2) (Figure 3.5A). The top of the F2 wedge lies within the lower silt unit and is truncated, along with F1 wedges, by an apparent period of thaw, or Melt event 1 (M1) (Figure 3.5B) (Figure 3.4). This M1 event appears to have occurred after F2, as evidenced by thaw features such as clear ice that appears ponded above the wedges with slumped organic-rich soil horizons that lie stratigraphically above the F2 wedge around 11 m bgs. The ice pools within M1 range in size from 0.3 m to 2.0 m wide and consist of silty to clear non-foliated ice (Figure 3.5B), which suggests that warmer conditions existed during this event, permitting liquid water to persist. This melt event was followed by a third Freeze event (F3), characterized by small 0.2 – 0.8 m wide wedges in the lowest section of the upper silt unit (Figure 3.5C). The F3 wedges appear stratigraphically above the M1 features at around 10 m bgs, suggesting that they formed after the M1 event (Figure 3.4). Narrow wedges appearing around 8 m bgs and above the F3 wedges likely formed during Freeze event 4 (F4) (Figure 3.4). These narrow wedges cut through both the M1 and F1 events, extending down the tunnel to about 13 m bgs

(Figure 3.5A and 3.5D). Ice wedges exposed in the tunnel ceiling and extending down to about 7 m bgs above the F4 wedges make up Freeze event 5 (F5) (Figure 3.4). Because the tops of these wedges extend up into the tunnel ceiling, the height of the wedge tops is unknown (Figure 3.5E).

### ***Ice wedge and pool ice $^{14}\text{C}$ dating***

Although the stratigraphic position of these freeze and thaw features constrains the relative order of formation, the determination of the timing of events is not possible without radiocarbon dating. Previous research established the age of the Permafrost Tunnel host sediments from rootlets, wood logs, and organic material frozen within the silt (Hamilton et al., 1988; Lachniet et al., 2012; Sellmann, 1967), so this study focused on determining the timing of freeze and melt events using the  $^{14}\text{C}$  ages of DOC and  $\text{CO}_2$  within the ice. The radiocarbon analyses included 19  $^{14}\text{C}$  ages of DOC and seven  $^{14}\text{C}$  ages of  $\text{CO}_2$  gas within the wedge and pool ice, and one AMS age from macro-sized sedge vegetation. The  $^{14}\text{C}$  ages of the  $\text{CO}_2$  within the ice wedges ranged from  $27,990 \pm 270$  to  $35,830 \pm 440$  cal yr BP, while the  $\text{CO}_2$  within the pool ice returned an age of  $31,140 \pm 140$  cal yr BP (Table 1). The  $^{14}\text{C}$  ages of the DOC from organic material in the ice wedge samples ranged from  $17,910 \pm 210$  to  $35,690 \pm 450$  cal yr BP and from  $21,470 \pm 200$  to  $31,890 \pm 380$  cal yr BP within the pool ice (Table 3.1). The youngest DOC ages are significantly younger than  $\text{CO}_2$  from the same subsample.

In addition to the  $^{14}\text{C}$  analyses,  $\delta^{13}\text{C}$  values were used to detect the presence of respired  $\text{CO}_2$  from ancient organic matter in the ice. The  $\delta^{13}\text{C}$  values in the wedge ice ranged from -14.4 to -21.5‰ in the  $\text{CO}_2$  samples and from -24.7 to -26.7‰ in the DOC samples (Table 3.1). The pool ice  $\text{CO}_2$   $\delta^{13}\text{C}$  value was -9.7‰, and ranged from -25.4 to -



26.1‰ in the DOC samples (Table 3.1). The  $\delta^{13}\text{C}$  values were compared to the modern value of atmospheric  $\text{CO}_2$  ( $\delta^{13}\text{C} = -6.8\text{‰}$ ) and to the value of organic material ( $\delta^{13}\text{C} = -27\text{‰}$ ). With the exception of the 34S Pool sample with a  $\delta^{13}\text{C}$  of  $-9.7\text{‰}$ , the other samples had mean  $\delta^{13}\text{C}$  values of  $-16.8\text{‰}$ , intermediate between modern atmospheric values and organic material values. These intermediate values indicate that organic material older than the age of the wedge or atmospheric  $\text{CO}_2$  likely contributed carbon to the sample, thus returning ages of respired  $\text{CO}_2$  much older than of wedge formation (Lachniet et al., 2012).

The presence of older organic material incorporated into the ice wedges during cracking events is also apparent in the  $^{14}\text{C}$  ages of the DOC and  $\text{CO}_2$  within the wedges. Under ideal cracking conditions, the age of the ice wedge material should be younger near the center of the wedge and older toward the outer edge of the wedge as the wedge continues to grow and incorporate younger and younger material. However, none of the wedges sampled exhibit this pattern. The reverse pattern of younger to older dates moving inward from the edge of the wedge to the center is apparent in the F1 wedges (Figure 3.6). Both DOC and  $\text{CO}_2$  were analyzed within the wedges in an effort to determine an age/width relationship. Within the following wedges, the number (N) of DOC and/or  $\text{CO}_2$  samples analyzed was as follows: 1N (3), 14.9S Winze (1), 18N (2), 35S (1), 50S (8), 52.5S (1), and 58N (6). Despite efforts to obtain high resolution radiocarbon ages of individual folia within each wedge, the scatter in the ages within each wedge prohibits determining when individual cracking events occurred in the wedge. The  $^{14}\text{C}$  ages of DOC within wedge 50S ranged from 25,870 cal yr BP near the outer edge to 34,550 cal yr BP near the center of the wedge. Similarly, wedge 58N also

exhibited age scatter throughout the wedge from 26,700 to 30,540 cal yr BP near the center of the wedge. This scatter in ages highlights the problematic incorporation and persistence of older organic carbon into the ice wedges, making the determination of timing of formation difficult.

### ***Timing of freeze and melt events***

The range of DOC and CO<sub>2</sub> ages from each sampled freeze and melt event were used to develop the relative timing of ice wedge growth and ice pool formation for Freeze event 1 (Wedges 35S, 45S, 50S, 58N), Freeze event 2 (35S Secondary Wedge), Melt event 1 (34S Pool, 50S Pool, 51S Pool), Freeze event 3 (Wedge 18N), Freeze event 4 (Wedges 14.9S Winze and 52.5S), and Freeze event 5 (Figure 3.7). The stratigraphic position of one sampled wedge, 1N, could not be visualized because of the tunnel portal support beams and structure that obstructed the view of the sediments surrounding the wedge. Therefore, wedge 1N was not classified in to a freeze event. However, it may represent an additional freeze event. Host sediment ages from both the lower and upper sections of the tunnel were used to constrain both the oldest and youngest possible ages of thermal event timing.

The first <sup>14</sup>C ages used to constrain the timing of Freeze event 1 are from previously reported ages of 41,020 ± 880 cal yr BP from silty peat (Hamilton et al., 1988) and 40,800 ± 410 cal yr BP from wood (Lachniet et al., 2012) in the lower host sediments surrounding the large F1 wedges in the lower silt unit (Figure 3.7). These host sediment ages are older than the <sup>14</sup>C ages of DOC within the F1 ice wedges that range from 25,870 ± 270 to 34,970 ± 460 cal yr BP (Figure 3.7). Because the host sediment ages are at least 6,000 years older than the F1 ages, and as much as 15 kyr older, the lower host sediments

were likely in place prior to the formation of the F1 and subsequent wedges (Figure 3.5A). Therefore, the freeze and melt events are likely significantly younger than 41 cal ka BP (Figure 3.7).

Further evidence for a 41 cal ka BP maximum age of the freeze and melt events is provided by the range of  $^{14}\text{C}$  ages of DOC within the F1 ice wedges, which range from  $25,870 \pm 270$  to  $34,970 \pm 460$  cal yr BP (Figure 3.7). Unless secondary cracking occurs, it is not likely that younger material enters a wedge during a cracking event, meaning the maximum limiting age for an ice wedges is likely approximated by the youngest age returned during analyses (Lachniet et al., 2012). Therefore, the maximum limiting age of the F1 wedges must be  $25,870 \pm 270$  cal yr BP (Figure 3.7). Further, the F1 ice wedges are stratigraphically constrained by thaw and pool ice features above them (Figure 3.5A). An apparent period of thaw is evident in organic-rich horizons that truncate the F1 wedges and pool ice lenses above the wedges (Figure 3.5B). Since the pool ice  $^{14}\text{C}$  ages of DOC range from  $21,470 \pm 200$  to  $31,890 \pm 380$  cal yr BP (Figure 3.7), the F1 wedges below these features must not be younger than  $21,470 \pm 200$  cal yr BP. Therefore, the F1 wedges likely formed between 25.9 – 21.5 cal ka BP (Figure 3.7).

The Freeze event 2 (F2) ice wedge is represented by a small 0.20 m wide by 0.60 m tall secondary wedge that cross-cuts the right side of wedge 35S (Figure 3.5A). Because the secondary wedge cuts through the already-formed wedge 35S in F1, it likely formed after the F1 event. The F2 event is further constrained in age by the pool ice from Melt event 1 (M1) that truncates the wedge from above (Figure 3.5B). With the pool ice  $^{14}\text{C}$  ages of DOC ranging from  $21,470 \pm 200$  to  $31,890 \pm 380$  cal yr BP (Figure 3.7), the F2 wedges below these features must not be older than  $21,470 \pm 200$  cal yr BP. The F2

event was not dated, but it likely formed after the F1 event and before the M1 event, within the range of 25.9 – 21.5 cal ka BP (Figure 3.7).

Because the pool ice features in Melt event 1 (M1) are located stratigraphically above the F1 and F2 wedges and below the F3 wedges, the M1 event likely occurred after the F1 and F2 wedges formed but before the F3 wedges formed (Figure 3.5). Unlike the wedges, the pool ice consists of non-foliated lenses of silt-rich ice grading upward to clear ice (Figure 3.5B), suggesting the pools formed under warmer conditions without ground contraction from freezing compared to the wedge ice. Additional evidence for non-frozen conditions is apparent in slump structures in the sediment around the pool ice that indicates the frozen ground thawed and was reworked during the melt event (Figure 3.5B). This reworking during thaw likely occurred during a warm period as pools were present at the surface, exposed to the atmosphere. A  $\delta^{13}\text{C}$  value of -9.7‰ from  $\text{CO}_2$  in the pool ice is close to the modern value of atmospheric  $\text{CO}_2$  ( $\delta^{13}\text{C} = -6.8\text{‰}$ ), which suggests contamination with infinite age carbon may have occurred during sampling. The old  $^{14}\text{C}$  ages of DOC within the pool ice ranging from  $21,470 \pm 200$  to  $31,890 \pm 380$  cal yr BP suggest the high  $\delta^{13}\text{C}$  values are likely not the result of water that equilibrated with the atmosphere prior to refreezing. These ages indicate the ice must be equal to or younger than 21.5 cal ka BP (Figure 3.7). Because there are no foliations within the pool ice, it is unknown whether these pools formed during a seasonally warm event or over many warm seasons. Green sedge material that appeared to be in growth position within the pool ice returned a radiocarbon age of  $26,430 \pm 280$  cal yr BP (Figure 3.5), older than the maximum limiting age of 21.5 cal ka BP for the pool ice. This older sedge material likely slumped into the pool during thaw and reworking, contributing to the uneven surface of

the top of the pool ice as the pool froze (Figure 3.5B). This period of freezing of the pool ice likely occurred before the formation of the F3 wedges, which are located stratigraphically above the M1 event, and constrain the minimum age of the pool ice (Figure 3.5C). The  $^{14}\text{C}$  ages of DOC within the F3 wedge range from  $17,910 \pm 210$  to  $18,820 \pm 140$  cal yr BP, indicating the M1 event likely formed before 17.9 cal ka BP, placing the range of possible timing from 21.5 to 17.9 cal ka BP (Figure 3.7).

A small wedge, 18N, located stratigraphically above the M1 features and below the F4 wedges was classified as Freeze event 3 (F3) (Figure 3.5C). The  $^{14}\text{C}$  ages of DOC within this F3 ice wedge range from  $17,910 \pm 210$  to  $18,820 \pm 140$  cal yr BP (Figure 3.7), suggesting the age of the ice is likely equal to or younger than 17.9 cal ka BP. This maximum limiting age combined with the M1 maximum age stratigraphically below the F3 wedge indicates that the wedge likely formed between 17.9 and 21.5 cal ka BP (Figure 3.7).

A fourth Freeze event (F4) is apparent stratigraphically above the F3 event and below the F5 event (Figures 3.5A and 3.5D). The  $^{14}\text{C}$  ages of DOC within the F4 sampled ice wedges, 14.9S Winze and 52.5S, range from  $32,030 \pm 400$  to  $35,690 \pm 450$  cal yr BP, the oldest ages returned from the sampled wedges (Figure 3.7). Because of the stratigraphic age constraints of the wedges below these F4 wedges, these 32 - 36 cal ka BP  $^{14}\text{C}$  ages from DOC are likely the result of contamination from older carbon incorporated into the wedge during cracking. Because the F4 wedges are stratigraphically constrained below by the F3 wedges with a maximum limiting age of 17.9 cal ka BP, the F4 wedges are likely younger than 17.9 cal ka BP (Figure 3.7). A  $^{14}\text{C}$  age of  $12,900 \pm 280$  cal yr BP from a wood log in the Debris Fan stratigraphically above the F4 wedges

(Sellmann, 1967) constrains the minimum age of the F4 event. Thus, the F4 event likely occurred between 17.9 - 12.9 cal ka BP (Figure 3.7).

A fifth Freeze event 5 (F5) is apparent stratigraphically above the F4 event (Figure 3.5E). These wedges are located in the uppermost section of the tunnel and were not sampled because they are only partly exposed in the tunnel ceiling. Similar to the F4 wedges, the F5 wedges are narrow but extend several meters down into the tunnel from the ceiling. It is unknown where the tops of the wedges begin stratigraphically, as indicated in Figure 3.4. Sellmann (1967) identified small wedges of this size and approximate stratigraphic position in the ventilation shaft at the rear of the tunnel, but the shaft was inaccessible during this study because of sediment collapse, instability, and safety concerns near the shaft entrance. Because of their stratigraphic position above the F4 wedges, the F5 wedges must be younger than 17.9 cal ka BP (Figure 3.7). Like the F4 wedges, the F5 wedges are also constrained above by the 12.9 cal ka BP age from a wood log in the Debris Fan near the tunnel entrance. Therefore, the likely age of the F5 event is between 17.9 - 12.9 cal ka BP (Figure 3.7).

The F5 wedges are constrained stratigraphically by the Debris Fan near the tunnel entrance and organic materials dated by Sellmann (1967). A transported willow log with an age of  $12,900 \pm 280$  cal yr BP in the Debris Fan suggests the Debris Fan is younger than 12.9 cal ka BP. The range of ages and maximum limiting ages of the five freeze events, one melt event, and lower and upper host sediments indicate the events likely occurred between 25.9 cal ka BP and 12.9 cal ka BP (Figure 3.7).

## Discussion

### *Approximate timing of freeze and melt events*

Between the time the lower and upper host sediments were emplaced around 41.0 cal ka BP and 9.5 cal ka BP, respectively, at least five intervals of freezing and one interval of melt occurred in Central Alaska. The F1 wedges, with a  $^{14}\text{C}$  maximum limiting age of  $25,870 \pm 270$  cal yr BP and a stratigraphic minimum limiting age of  $21,470 \pm 200$  cal ka BP, likely formed between 25.9 – 21.5 cal ka BP (Figure 3.7), much later than the previously reported  $37,270 \pm 3780$  to  $37,610 \pm 2390$  cal yr BP (Sellmann, 1967). Hamilton et al. (1988) and Sellmann (1967) reported ages from the organic material surrounding the wedges in the lower silt unit that were similar to their radiocarbon ages in the ice (Figure 3.4). These data were interpreted to indicate that the wedges were syngenetic, forming at the same time as sediment deposition. Further evidence from cryostructures and apparent thermokarst-cave ice was interpreted to support a syngenetic origin of the wedges (Kanevskiy et al., 2008; Shur et al., 2004). However,  $^{14}\text{C}$  ages of DOC in the lower unit wedges were up to 14,000 years younger than the surrounding sediment (Lachniet et al., 2012), suggesting the timing of sediment deposition did not occur simultaneously with the ice wedge growth. The radiocarbon ages of the DOC presented here confirm the wedges and pool ice are much younger than the surrounding sediment ages, and it is likely the wedges formed significantly after, not during, the time of sediment deposition (Figure 3.7). The younger DOC ages from the ice wedges presented here indicate the wedges are actually epigenetic, not syngenetic, in origin, and formed later than previously thought.

The timing of the freeze and melt events correspond to changes in Central Alaskan and Beringian climate as indicated by glacial moraines, sea level rise and fall, and vegetation changes that suggest climate fluctuated between cold and warm conditions between 25.9 and 12.9 cal ka BP.

*Freeze event 1 – 25.9 to 21.5 cal ka BP*

The F1 wedges, with a  $^{14}\text{C}$  maximum limiting age of  $25,870 \pm 270$  cal yr BP and a stratigraphic minimum limiting age of  $21,470 \pm 200$  cal yr BP, likely formed between 25.9 – 21.5 cal ka BP (Figure 3.7). This 25.9 – 21.5 cal ka BP interval of freezing in the Permafrost Tunnel corresponds to an interval of glacial retreat in northern and southwestern Alaska. Evidence from  $^{10}\text{Be}$  dating of terminal moraines in the Brooks Range indicates glacial stillstands occurred between 27 – 24 cal ka BP (Balascio et al., 2005), while the retreat of glaciers from their late LGM terminal positions farther south in the Alaska Range appears to have occurred around 22 – 19 cal ka BP (Briner and Kaufman, 2008). This expansion of Alaskan glaciers also corresponds to the approximately 120 m fall of sea level in the during the global LGM, which would have exposed much of the Bering land bridge (Elias and Crocker, 2008). As glaciers expanded in conjunction with sea level regression, the resulting increased aridity in the interior of the continent may have limited the availability of moisture for the growth of glaciers, contributing to their eventual retreat around 19 cal ka BP (Briner et al., 2005). Likewise, this increased aridity over the continent may have also limited the availability of moisture for the growth of ice wedges, and could have prompted the cease of ice wedge growth.

The cold conditions necessary for F1 ice wedge growth between 25.9 and 21.5 cal ka BP also correspond to intervals of high loess production as glaciers expanded.



However, loess accumulation was low because of the lack of sufficient vegetation to trap loess (Muhs et al., 2003). Despite the increased continentality from lowered sea levels, the appearance of moisture-tolerant grasses and sedges from fossil arctic ground squirrel caches within this interval indicate conditions were not entirely arid in eastern Beringia (Gaglioti et al., 2011). Further evidence present in the  $\delta^{15}\text{N}$  record of megafauna diets suggests a shift to wetter conditions began around 27 cal ka BP near Fairbanks (Fox-Dobbs et al., 2008) and around 25 cal ka BP along the North Slope (Mann et al., 2013). This shift from drier to wetter conditions could explain the appearance of the F1 wedges around 25.9 cal ka BP as sufficient moisture was available for ice wedge growth to occur. The growth of the F1 and F2 wedges during this cold and wet event starting at 25.9 cal ka BP must have ceased by  $21,470 \pm 200$  cal yr BP because the dated Melt event 1 features truncate the F1 wedges (Figure 3.5).

#### *Freeze event 2 - <25.9 to 21.5 cal ka BP*

The F2 wedges were not radiocarbon dated, but based on stratigraphic position, these wedges formed after the F1 wedges and before the F3 wedges, likely between 25.9 and 21.5 cal ka BP (Figure 3.7). Because the F2 wedges are small secondary wedges, the growth period was likely shorter compared to the F1 wedges. The F2 wedges were truncated by the Melt event 1, so the F2 wedges must have ceased formation by 21.5 cal ka BP (Figure 3.7). Radiocarbon dating and/or stable isotope analyses of the F2 wedges is necessary to estimate a more precise timing of formation.

#### *Melt event 1 – 21.5 to 17.9 cal ka BP*

The M1 pool ice features, located stratigraphically above the F1 and F2 wedges, returned a maximum limiting age of  $21,470 \pm 200$  cal yr BP and a stratigraphic minimum

limiting age of  $17,910 \pm 210$  cal yr BP. The M1 features likely formed between 21.5 – 17.9 cal ka BP (Figure 3.7), during a warmer interval. This timing of melt in the tunnel is consistent with evidence of warming in the Canadian Arctic and Yukon such as a 20 cal ka BP horse mandible (Lacelle et al., 2013) which indicates the area around the Richardson Mountains NWT was ice free during this time. A decline in the  $\delta^{15}\text{N}$  in caribou bone around 20 cal ka BP also indicates a shift in diet to more moist acidic tundra vegetation characteristic of warmer and wetter climates (Mann et al., 2013). Evidence for glacial retreat near Denali in the Alaska Range between 22 and 19 cal ka BP (Briner and Kaufman, 2008) also indicates warmer conditions existed within this interval.

The M1 pool ice maximum limiting age of  $21,470 \pm 200$  cal yr BP (Figure 3.7) is much younger than the previously reported  $37,150 \pm 3920$  cal yr BP from rootlets and organic material at the bottom of a thaw pond (Figure 3.4) (Sellmann, 1967). Green sedge material that appeared to be in growth position within the pool ice returned a radiocarbon age of  $26,430 \pm 280$  cal yr BP (Figure 3.5), which is also younger than the previously reported ages from the organic material surrounding the pool ice (Hamilton et al., 1988; Sellmann, 1967). I interpret this sedge material as an older horizon that fell into the pool at the end of the melt event, returning an age of sedge growth rather than the timing of the actual melt. The persistence of older carbon in the sediments surrounding the material is again highlighted by an oldest age of organic material of  $31,890 \pm 380$  cal yr BP from the pool ice (Figure 3.7). Old organic material must have been mobilized during the melt event, refrozen in the pool, and preserved in the refrozen pool ice. Slump structures apparent in the sediment above the pool ice (Figure 3.5B) also indicate that mass movement occurred when previously frozen ground thawed and was reworked by slope

processes. This Melt event 1 had previously been classified as a thaw unconformity (Hamilton et al., 1988), possibly representative of summer warm conditions during the LGM (Lachniet et al., 2012). The new DOC ages of the stratigraphically-constraining wedges above and below the pool ice confirm the timing of these melt features as occurring during warm intervals during the LGM. However, without stable isotopic data from the melt features, the exact timing and correlation with global warm events is not possible.

*Freeze event 3 – 17.9 to 12.9 cal ka BP*

The F3 wedges, with a maximum limiting age of  $17,910 \pm 210$  cal yr BP and a stratigraphic minimum limiting age of  $12,900 \pm 280$  cal yr BP (Figure 3.7), represent a previously undocumented interval of ice wedge growth in the tunnel that likely occurred between 17.9 and 12.9 cal ka BP. The beginning of this same interval includes the largest sea ice and glacial extent in the Arctic, sea levels as low as 120 m below modern sea levels, and the lowest global temperatures during the LGM (Miller et al., 2010). Hamilton et al. (1988) reported an age of  $34,780 \pm 130$  cal yr BP from organic wood and grass from the silty peat 1.8 m above the large ice wedges in the lower unit, but no ages of ice wedges from this stratigraphic interval in the upper silt unit were reported. An age of  $12,900 \pm 280$  cal yr BP from a wood log in the debris fan deposit near the tunnel entrance (Sellmann, 1967) provides a possible constraining age, but the log could be several thousand years older than the actual timing of the debris fan event. A reported age of  $34,780 \pm 130$  cal yr BP (Hamilton et al., 1988) from the surrounding sediments above wedge 40S, however, indicates that like the F1 and F2 wedges, the F3 wedges are

epigenetic in origin because the age of the sediment is much older than the  $^{14}\text{C}$  age of DOC within the ice wedge.

The 17.9 - 12.9 cal ka BP timing of the F3 wedges corresponds to an interval of glacial retreat in the Nenana Valley near Fairbanks (Dortch et al., 2010). This glacial retreat could have been triggered by increased continentality as sea levels reached their lowest point during the LGM (Elias and Crocker, 2008) and also may have limited moisture availability for F3 wedge growth. The formation of these wedges may have ceased at the onset of rapid warming around 16 kyr, as seen in the increase in warmer pollen species in lake sediment records from Central Alaska (Ager and Brubaker, 1985) and in the  $\delta^{15}\text{N}$  decrease in muskoxen and caribou diets (Mann et al., 2013). However, without stable isotope data from these ice wedges, the timing and correlation with other paleoclimatic records cannot be compared.

#### *Freeze event 4 - <17.9 to 12.9 cal ka BP*

The F4 wedges returned the oldest radiocarbon ages sampled in the tunnel, ranging from  $32,030 \pm 400$  cal yr BP to  $35,690 \pm 450$  cal yr BP (Figure 3.7). However, these ages are clearly a result of contamination with older carbon because they are stratigraphically constrained by younger ages (Figure 3.4). The F4 wedges are located stratigraphically above the F3 wedges with a maximum limiting age of  $17,910 \pm 210$  cal yr BP and stratigraphically below the debris fan with a minimum limiting age of  $12,900 \pm 280$  cal yr BP (Figure 3.5D), so the F4 wedges must be younger than 17.9 cal ka BP. Although the age of  $12,900 \pm 280$  cal yr BP from the wood log in the debris fan deposit could be several thousand years older than the actual timing of the debris fan event, ages from organic material in host sediments stratigraphically above the log in the tunnel

ventilation shaft provide minimum limiting ages of 9.5 cal ka BP (Sellmann, 1967). This indicates the F4 wedges likely formed between 17.9 and 12.9 cal ka BP, which correlates with the transition to warmer and wetter climatic conditions around 16 cal ka BP, similar to those discussed above during the F3 event. Stable isotopic data from these wedges could enable a better approximation of the timing and extent of the F4 event.

#### *Freeze event 5 - <17.9 to 12.9 cal ka BP*

Similar to the F3 and F4 events, the F5 event is constrained by a 12.9 cal ka BP willow log from the Debris Fan (Sellmann, 1967) (Figure 3.7). These wedges were not sampled, and the tops of these wedges were not visible because they extend above the ceiling of the tunnel. Because the F5 wedges are located stratigraphically above the F3 and F4 wedges, the F5 wedges likely formed after 17.9 cal ka BP, perhaps during the early Younger Dryas (YD). Ice wedges in Barrow formed during the YD, suggesting cool conditions occurred on the North Slope of Alaska (Meyer et al., 2010b). However, stable isotopic data from these F5 wedges would provide a better estimate of the temperature fluctuations during this interval.

#### ***Implications for dating carbon in the permafrost environments***

The several thousand year range of these radiocarbon values within these freeze and melt events highlights the need for high resolution  $^{14}\text{C}$  sampling of DOC within the ice combined with stable isotopic analyses of the ice to resolve anomalous age dating. As shown in the F4 wedges, long persistence times of carbon in permafrost environments can cause anomalously old ages, as carbon can be up to 17,000 years older than the age of the ice wedge. As seen in the Freeze and Melt events within the tunnel, carbon was

frozen, thawed and remobilized during incorporation into the ice wedge, and refrozen again during the ice wedge formation.

### ***Summary of thermal events in the Permafrost Tunnel***

Central Alaska experienced at least five distinct freeze events and at least one melt event as shown in radiocarbon dated ice wedges preserved in the CRREL Permafrost Tunnel. Large ice wedges from the lower silt unit in the tunnel formed during F1, between 25.9 - 21.5 cal ka BP or during H2, followed by the secondary wedges in the F2 event. A melt event likely occurred between 21.5 - 17.9 cal ka BP, characterized by the pool ice features. The F3 event likely occurred between 17.9 - 12.9 cal ka BP, or during H1. F4 and F5, likely occurred after 17.9 cal ka BP, but the exact timing of these events is unknown (Figure 3.7).

### **Conclusion**

A new method of using  $^{14}\text{C}$  ages of DOC and  $\text{CO}_2$  to determine the timing of ice wedge and pool ice formation revealed five freeze events and one melt event within the CRREL Permafrost Tunnel. These freeze and melt events, consisting of large ice wedges and pool ice, likely occurred between 25.9 - 21.5 cal ka BP, earlier than previously thought. Small secondary wedges formed above these F1 wedges during a Freeze event 2. These F1 and F2 wedges were truncated by the Melt event 1 that likely occurred around 21.5 - 17.9 cal ka BP, as indicated by pool ice and thaw features apparent in the tunnel. Ice wedges in Freeze event 3 likely between 17.9 - 12.9 cal ka BP, or possibly during Heinrich event 1. Inconclusive radiocarbon ages from a fourth interval of ice wedge formation, Freeze event 4, prohibit precise dating of ice wedge formation. However, the stratigraphic location of the Freeze event 4 wedges indicates the wedges likely formed

after 17.9 cal ka BP. A fifth event, Freeze event 5, also likely formed after 17.9 cal ka BP, possibly prior to the Younger Dryas. The prevalence of carbon as much as 17,000 years older than the timing of ice wedge growth is apparent in the Freeze event 4 wedges, suggesting carbon in the arctic is reworked and resequenced during changing climatic conditions, causing anomalous ages in permafrost environments. More precise dating of these thaw events is required to determine the timing of these changes. Stable isotope analyses of the ice wedges could help to constrain the timing of these events by correlating the isotopic record with ice core and ocean sediment records.

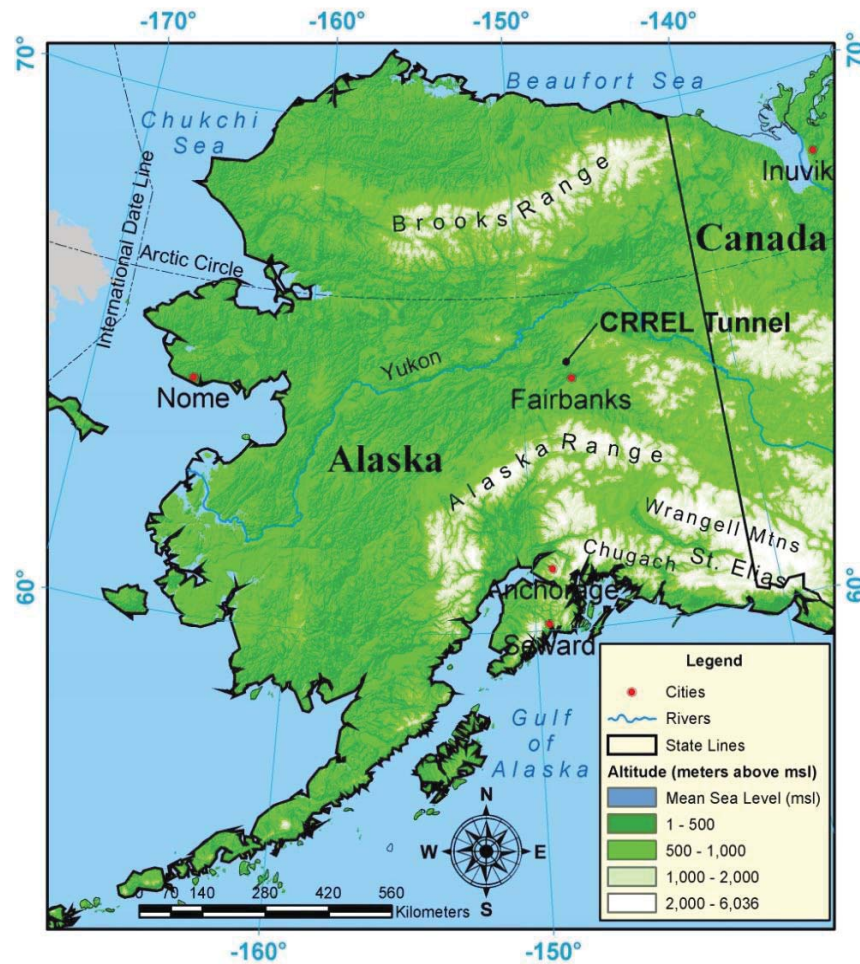


Figure 3.1. Map of USACE CRREL Permafrost Tunnel location. The USACE CRREL Permafrost Tunnel is located just north of Fairbanks, Alaska. Base map is a USGS 300-m Digital Elevation Model (DEM) (USGS, 1997).



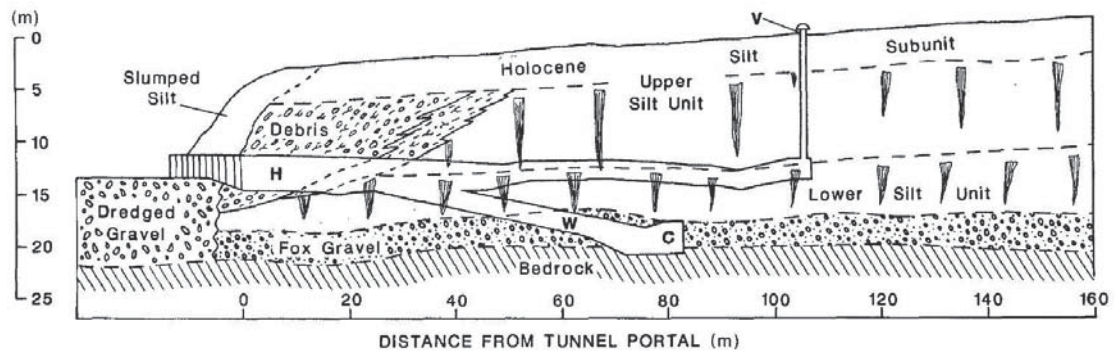


Figure 3.2. Cross-section of the CRREL Permafrost Tunnel. Cross-section showing preserved ancient ice wedges within the upper and lower silt units of the Goldstream Formation (Hamilton et al., 1988).

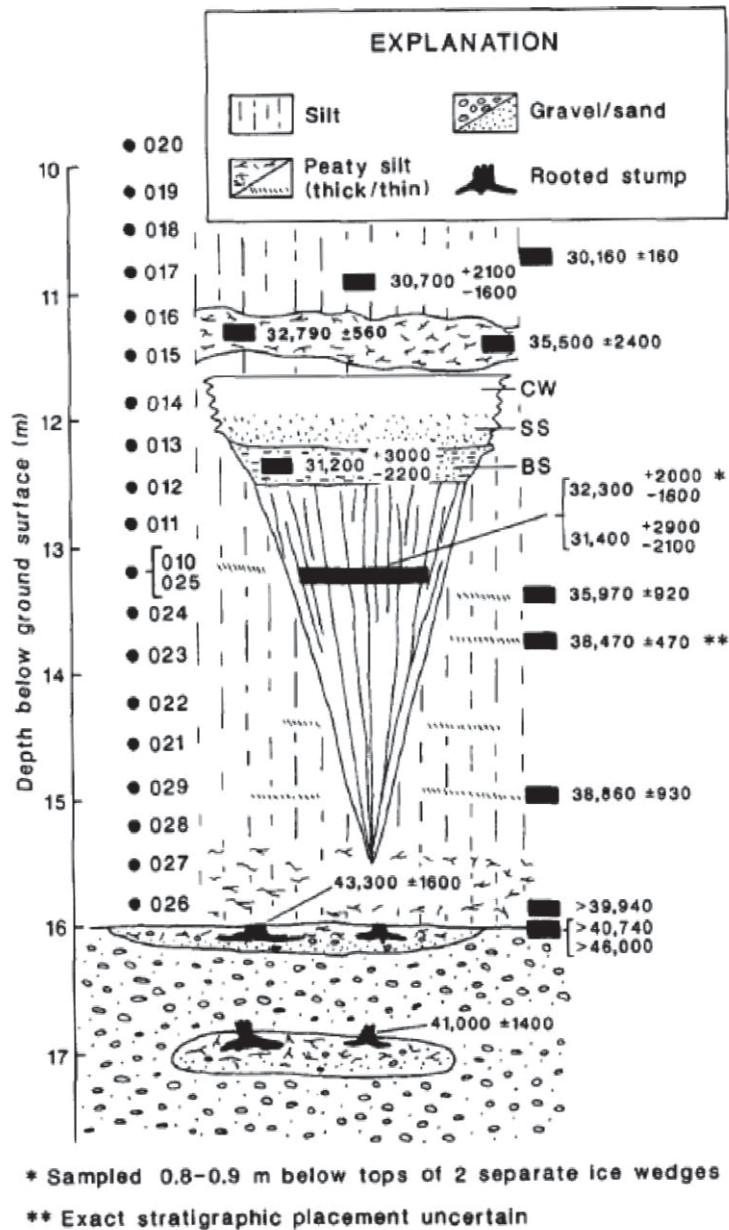


Figure 3.3. General stratigraphic section of the CRREL Permafrost Tunnel. Figure showing radiocarbon ages of willow logs, ice wedges, peaty organic material, and bottom sediment (BS) from a thaw pond within the upper and lower silt units (Hamilton et al., 1988). Ages shown are non-calibrated  $^{14}\text{C}$  ages.

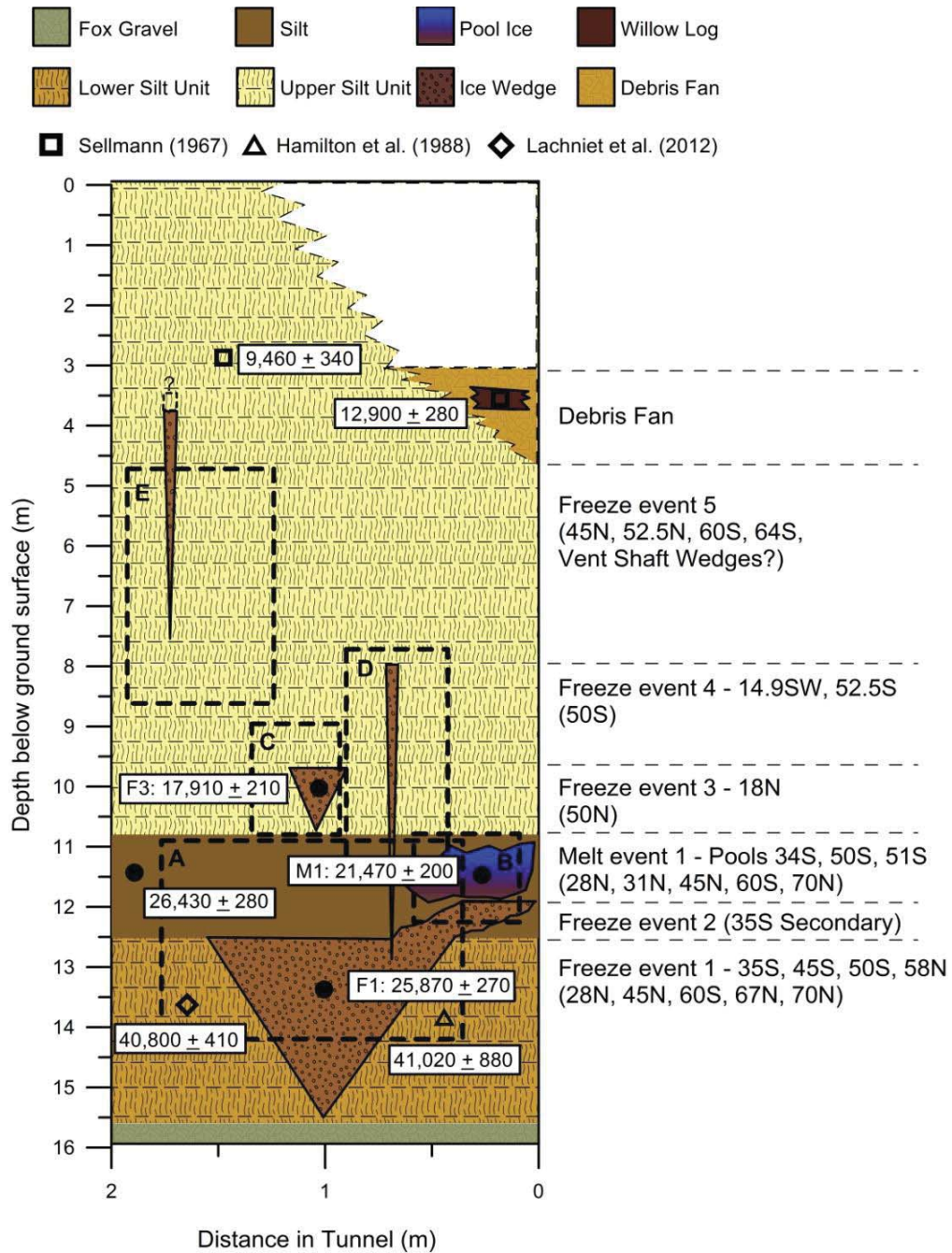


Figure 3.4. Stratigraphic placement of freeze and melt events. A generalized stratigraphic section of the CRREL Permafrost Tunnel showing the approximate stratigraphic placement of five freeze (F) events and one melt (M) event. Labeled dashed boxes correspond to photographs A-E taken in the tunnel shown in Figure 5. Filled circles mark locations of sampled organic material with the youngest  $^{14}\text{C}$  ages of DOC from a suite of ages shown in calibrated years BP. Dashed stratigraphic contact lines indicate the approximate location of the Debris Fan and absence of sediments above the Debris Fan near the tunnel portal.

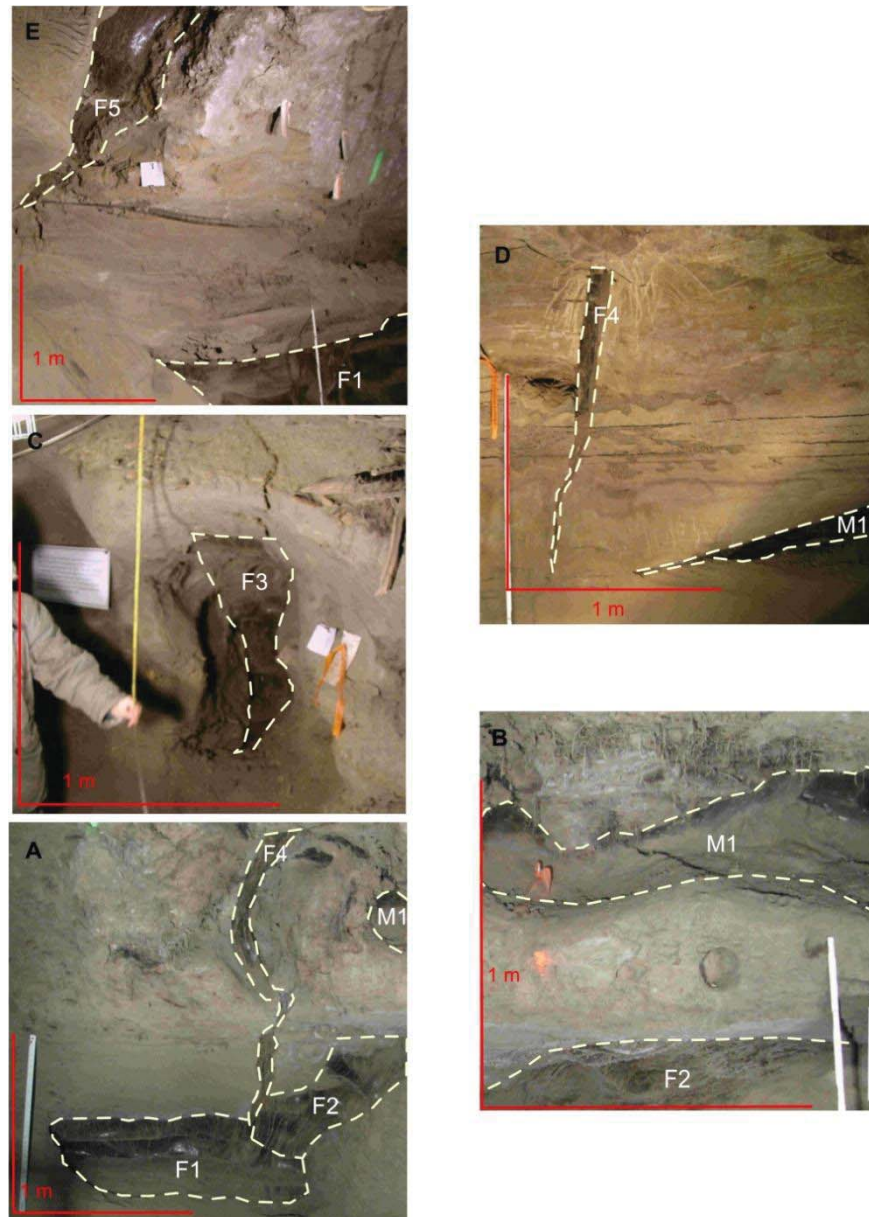


Figure 3.5. Photographs of five freeze and melt events. Photographs showing the relative position and stratigraphic placement of five freeze (F1 through F5) events and one melt (M1) event (dashed outlines) from the CRREL Permafrost Tunnel. A) Wedge 35S in F1 (0.5 m above ground level inside tunnel), the secondary wedge at 35S in F2, the 34S Pool in M1, and the F4 wedge above Wedge 35S. B) Closer view of the 34S pool in M1 (~ 1.2 m above ground level) and the 35S secondary wedge beneath it in F2. C) Wedge 18N in F3 (~1.5 m above ground level), with an approximately 1.5 m person standing beside the wedge. D) Wedge 52.5N in F4 (~ 3 m above ground level) with 50S pool ice in M1 below it. E) Wedge 64S in F5 (4 + m above ground level) extends up into the ceiling of the tunnel and lies stratigraphically above Wedge 64S in F1.



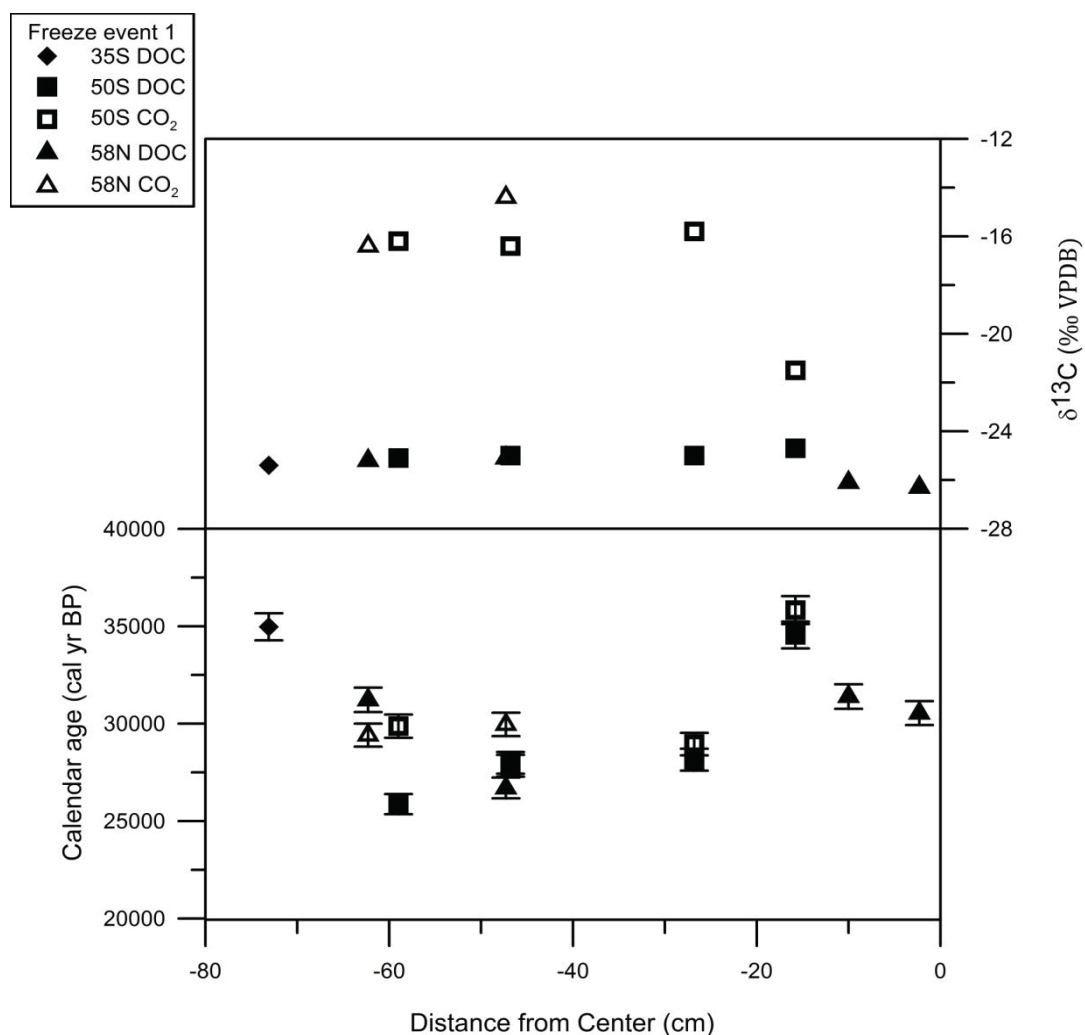


Figure 3.6. Freeze event 1 ages and  $\delta^{13}\text{C}$  values. Freeze event 1 (F1) ice wedge (35S, 45S, 50S, and 58N) radiocarbon dating sampling locations, calendar ages (in calibrated years BP), and  $\delta^{13}\text{C}$  values of DOC (closed symbols) and CO<sub>2</sub> (open symbols) from the CRREL Permafrost Tunnel. F1 ice wedges have a maximum limiting age of  $25,870 \pm 270$  cal yr BP.

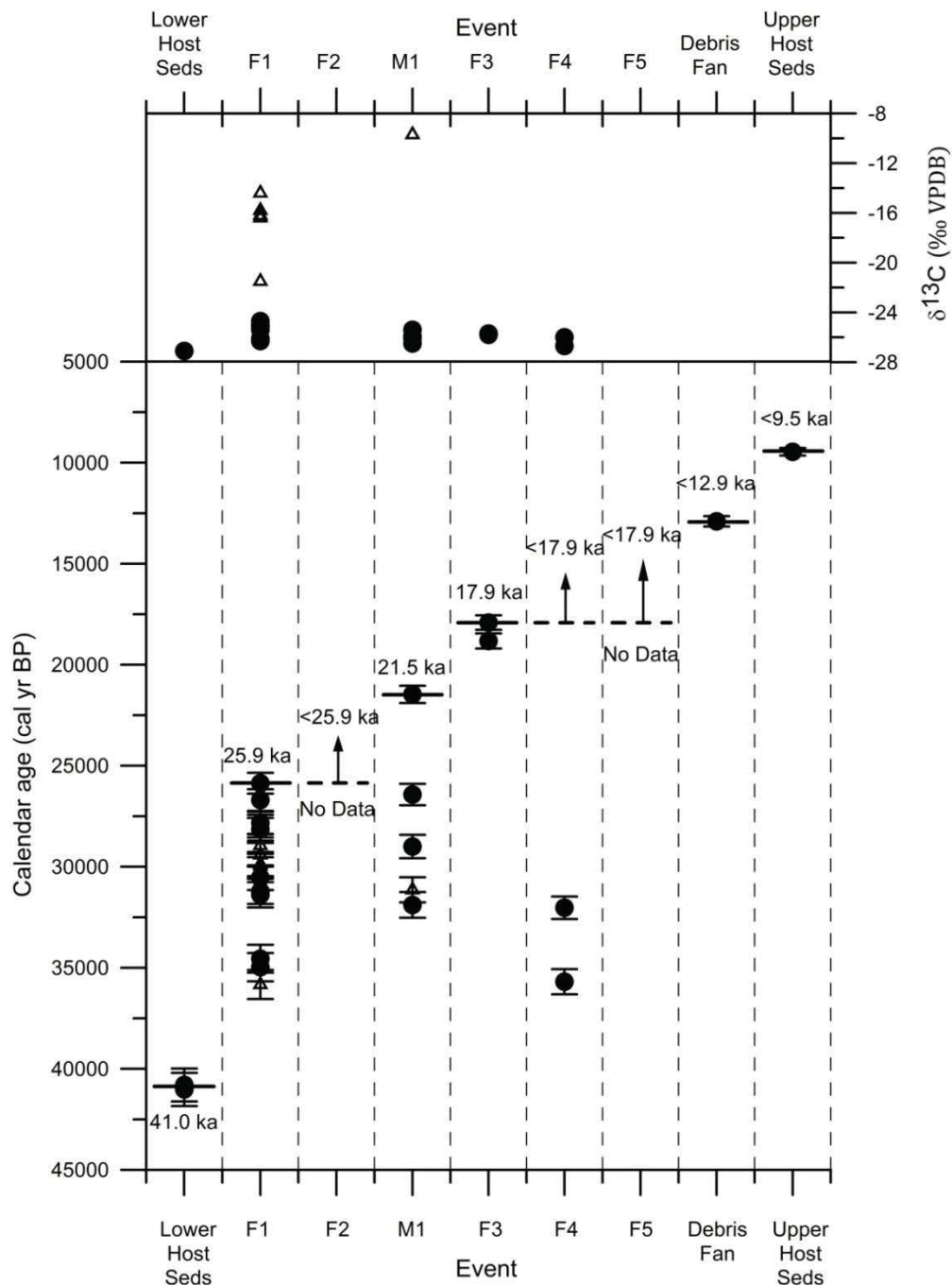


Figure 3.7. Approximate timing of freeze and melt events. The combined calendar ages and  $\delta^{13}\text{C}$  values for DOC (circles) and  $\text{CO}_2$  (triangles) from ice wedge and pool ice and stratigraphic placement suggest at least five freeze events and one melt event occurred in the CRREL Permafrost Tunnel. The limiting ages for each event are represented by thick bars while dashed bars with arrows represent the stratigraphically constrained limiting ages of events.

Table 3.1. Radiocarbon ages of DOC and CO<sub>2</sub> within wedges and pool ice.

Sample ID	Lab ID <sup>1</sup>	Material	Sampling interval from left (cm)	$\delta^{13}\text{C}$ (‰ VPDB)	<sup>14</sup> C Age and uncertainty ( <sup>14</sup> C yr BP)	Calibrated 68.2% Age Range (cal yr BP) <sup>2</sup>	Median calendar age and uncertainty (cal yr BP)
1N 0-5	AA96666	DOC	0.0-5.0	-25.2	26260 ±280	31150-30720	30920 ±210
1N 5-10	AA96660	DOC	5.0-10.0	-25.2	25400 ±240	30520-29770	30220 ±310
1N 15-20	AA96667	DOC	15.0-20.0	-25.5	26610 ±260	31290-31000	31140 ±160
14.9S Winze	AA96668	DOC	N.A.	-26.0	27840 ±280	32380-31550	32030 ±400
18N 0-5	AA96669	DOC	0.0-5.0	-25.7	14719 ±79	18030-17710	17910 ±210
18N 5-10	AA96661	DOC	5.0-10.0	-25.8	15679 ±88	18910-18700	18820 ±140
34S-Pool	AA93912	CO <sub>2</sub>	N.A.	-9.7	26610 ±240	31010-31280	31140 ±140
34S-Pool	AA93913	DOC	N.A.	-25.4	18000 ±110	21280-21610	21470 ±200
34S-Pool	AA93914	Plant	N.A.	-26.5	21990 ±160	26150-26690	26430 ±280
35S 15-20	AA96662	DOC	15.0-20.0	-25.4	30390 ±380	35230-34610	34970 ±460
50S-1	AA93902	CO <sub>2</sub>	3.0-8.5	-16.2	24980 ±200	29570-30170	29870 ±240
50S-1	AA93903	DOC	3.0-8.5	-25.1	21600 ±140	25640-26130	25870 ±270
50S-2	AA93904	CO <sub>2</sub>	20.5-23.5	-16.4	23130 ±170	27750-28210	27990 ±270
50S-2	AA93905	DOC	20.5-23.5	-25.0	23000 ±170	27610-28120	27840 ±330
50S-3	AA93906	CO <sub>2</sub>	35.5-38.5	-15.8	24120 ±190	28670-29240	28950 ±260
50S-3	AA93907	DOC	35.5-38.5	-25.0	23310 ±170	27940-28370	28150 ±210
50S-4	AA92308	CO <sub>2</sub>	46.5-56.5	-21.5	31380 ±400	35330-36390	35830 ±440
50S-4	AA92309	DOC	46.5-56.5	-24.7	29890 ±400	34400-34970	34550 ±470
50S-Pool	AA96663	DOC	N.A.	-25.9	27720 ±280	32200-31450	31890 ±380
51S-Pool	AA96670	DOC	N.A.	-26.1	24190 ±200	29300-28720	29000 ±260
52.5S	AA96664	DOC	N.A.	-26.7	31120 ±410	36270-35140	35690 ±450
58N 0-5	AA93908	CO <sub>2</sub>	0.0-5.0	-16.4	24570 ±200	29650-29140	29410 ±310
58N 0-5	AA93909	DOC	0.0-5.0	-25.2	26780 ±280	31360-31070	31220 ±160
58N 15-20	AA93910	CO <sub>2</sub>	15.0-20.0	-14.4	25140 ±210	30230-29710	29960 ±240
58N 15-20	AA93911	DOC	15.0-20.0	-25.1	22210 ±170	26950-26240	26700 ±390
58N 45-50	AA96665	DOC	45.0-50.0	-26.1	27160 ±260	31540-31210	31390 ±200
58N 60-65	AA96671	DOC	60.0-65.0	-26.3	25690 ±230	30770-30300	30540 ±250

<sup>1</sup> Samples processed and analyzed at the University of Arizona radiocarbon facility.<sup>2</sup> Ages were calibrated to calendar years before present (BP) (present = 1950 A.D.) using IntCal09 calibration curve at the 68.2% probability level.

## CHAPTER 4

### VARIABLE LATE PLEISTOCENE PALEOCLIMATE IN ALASKA FROM HIGH-RESOLUTION $\delta^{18}\text{O}$ OF PERMAFROST ICE WEDGES SUGGESTS NORTH ATLANTIC FORCING

#### **Abstract**

Radiocarbon dating of dissolved organic carbon (DOC) within ice wedges and pool ice in the CRREL Permafrost Tunnel in Fairbanks, AK has revealed timing of formation during Marine Isotope Stage II, earlier than suggested by previous workers. Results from Chapter 3 suggest that five ice wedge growth events occurred in the interval between ca. 26 and 13 cal ka BP. Because of highly variable radiocarbon ages resulting from contamination with old carbon (described in Chapter 3), in this work I attempted to further refine growth ages by correlation of wedge ice  $\delta^{18}\text{O}$  values to a record of sea surface temperature (SST) in the Bering Sea. For this correlation and to investigate the magnitude of paleoclimatic change in Central Alaska during MIS II, I analyzed  $\delta^{18}\text{O}$  at high resolution for five intervals of ice wedge growth during cooling intervals and one interval of pool ice growth during a warmer interval characterized by thaw and ground ice melt. These intervals are identified with  $\delta^{18}\text{O}$  records, displaying  $\delta^{18}\text{O}$  values ranging from -28.9‰ to -20.4‰, which range between 6.6‰ below and +1.9 ‰ above the modern snow  $\delta^{18}\text{O}$  value of -22.3‰. These  $\delta^{18}\text{O}$  values suggest most of the ice wedges formed during colder-than-modern conditions, consistent with last glacial period  $^{14}\text{C}$  ages. Using isotope-temperature relationships defined in Chapter 2, paleo-winter temperatures ranged from -41.6 to -11.2°C, while paleo-mean annual temperatures (MAT) ranged from -14.1 to 1.4°C. This range in  $\delta^{18}\text{O}$  is consistent with paleotemperature fluctuations observed in the Bering Sea SST and Greenland ice core records. Based on a visual correlation to the Bering Sea SST record within the ice age



limits identified in Chapter 3, I suggest here that Freeze event 1 likely occurred during cooling of -12.3 to -1.2°C between 26.5 - 25.3 cal ka BP, coinciding with Heinrich event 2, while Freeze event 2 occurred during cooling of -8.8 to -2.8°C between 21.0 - 20.5 cal ka BP. One warming interval, M1, when clear pool ice formed in a melt horizon above the F1 and F2 wedges, may have occurred as paleo-MAT ranged between -9.9 and -1.2°C between 19.1 - 18.8 cal ka BP. Freeze event 3 represents the lowest (coldest)  $\delta^{18}\text{O}$  values that suggest paleo-MAT ranged between -14.1 and -9.2°C which is correlated to the coldest regional climate interval when the Laurentide Ice Sheet reached its local maximum extent in the Yukon between 17.3 - 17.0 cal ka BP, coinciding with Heinrich event 1. Freeze event 4 has similar high  $\delta^{18}\text{O}$  values as a late Holocene ice wedge in the nearby Vault Creek permafrost tunnel, which was radiocarbon-dated to ca. 3.9 cal ka, and represents the warmest ice wedge forming thermal event as paleo-MAT likely ranged between -1.4 and 1.4°C. The combination of low-resolution and low-fidelity radiocarbon dating, high resolution  $\delta^{18}\text{O}$  data, and paleotemperature estimates allow for more robust age constraints, and when compared with the well-dated Bering Sea temperature record, suggest ice wedges in Central Alaska formed in response to North Atlantic DO- and H-type millennial forcing of climate.

## **Introduction**

### ***Oxygen and hydrogen isotopes in paleoclimate***

Oxygen and hydrogen isotope ratios in proxies such as ice cores, speleothems, and benthic foraminifera are useful tools in studying past climatic changes in global temperature, circulation, and precipitation patterns. Oxygen ( $\delta^{18}\text{O}$ ) and hydrogen ( $\delta\text{D}$ ) isotopes are measures of the relative abundance in the ratios of  $^{18}\text{O}/^{16}\text{O}$  and  $^2\text{H}/^1\text{H}$ ,

respectively, in relation to the standard of mean ocean water (SMOW). Isotope fractionation is temperature dependent and follows the Rayleigh distillation curve (Craig, 1961; Epstein and Mayeda, 1953). Other factors including altitude, seasonality, and latitude affect the isotopic signature of precipitation (Dansgaard, 1964).

Stable isotopes of oxygen and hydrogen in Greenland ice cores (Svensson et al., 2008), global ocean sediments (Lisiecki and Raymo, 2005), Bering Sea sediments (Schlung et al., 2013), and ground ice (Meyer et al., 2010b), among many others, have been used to estimate Pleistocene temperature and climatic variations driven by orbital and millennial forcing of climate (Jouzel et al., 2007a). In ice records, more negative oxygen and deuterium isotopic values typically represent colder conditions, while more positive isotopic values represent warmer temperatures (Jouzel et al., 2007b; Meyer et al., 2002). Greenland ice core isotopic records exhibit rapid shifts in  $\delta^{18}\text{O}$  values of up to 6‰ during warm Dansgaard-Oeschger (DO) events and cold stadials (Andersen et al., 2004), indicating temperatures shifted by as much as 12 to 15°C during these climatic fluctuations (Johnsen et al., 2001). Some of these cold stadials are coincident with Heinrich (H) events, marked in oceanic sediment records by Ice Rafted Debris (IRD) released during massive discharges of ice into the North Atlantic (Hemming, 2004), driven by millennial forcing of climate (Alley and Clark, 1999; Bond and Lotti, 1995). Bering Sea oceanic isotopic records exhibit similar millennial-scale DO- and H-type shifts that indicate sea surface temperatures (SST) fluctuated by as much as 5°C between the warm interstadials and cold stadials over the past 60 ka (Figure 4.1) (Schlung et al., 2013).

In the absence of ice cores with continuous high resolution records of past climate, ice wedges in Arctic environments have recently been used as indicators of past Late Pleistocene and Holocene climatic trends in Siberia (Vasil'chuk and Vasil'chuk, 1998), on the North Slope of Alaska (Meyer et al., 2010b), and in Central Alaska (Meyer et al., 2008). When ice wedges form, the snow meltwater that flows into the thermal contraction cracks records that year's climatic signal (Meyer et al., 2002). Low  $\delta^{18}\text{O}$  values from ice wedges near Barrow, AK indicate colder than present temperatures during the Younger Dryas (YD, ca. 12.9 to 11.5 cal ka BP) and late Pleistocene (Meyer et al., 2010b). Similarly, a  $\sim 10\text{‰}$  range in  $\delta^{18}\text{O}$  values from Late Pleistocene- to Holocene-age ice wedges preserved in the Vault Creek Tunnel near Fairbanks, AK, indicate temperatures in Central Alaska fluctuated between warmer and colder than modern conditions, although the exact timing of the fluctuations is uncertain because of conflicting radiocarbon ages (Meyer et al., 2008). Stable isotope values from bulk samples of select ice wedges in the CRREL Permafrost Tunnel (Douglas et al., 2011) indicate wedges likely formed under cooler-than-modern conditions, but poor age constraints prohibit estimating the timing of formation and the low isotopic resolution prevents determining the magnitude of  $\delta^{18}\text{O}$  change within the ice wedges.

Because DO and H events are expressed in global records, it is possible that North Atlantic forcing of climate on millennial scales is recorded in Alaska. Megafauna abundances in Central Alaska have been suggested to coincide with DO and H events (Mann et al., 2013), and radiocarbon dating of a single ice wedge from the CRREL Permafrost Tunnel near Fairbanks, Alaska (Figure 4.2) suggested that formation occurred during the Last Glacial Maximum at ca. 21 cal ka BP, or possibly slightly earlier during

Heinrich event 2 (H2) (Lachniet et al., 2012). However, the hypothesis of North Atlantic forcing of climate in Alaska has not been tested with sufficient resolution. More detailed radiocarbon dating of several ice wedges and pool ice in the Permafrost Tunnel from dating dissolved organic carbon (DOC) and carbon dioxide (CO<sub>2</sub>) of organic material within the ice indicate that at least five freeze events and one melt event occurred between 25.9 and 12.9 cal ka BP (Chapter 3). However, it is not possible to constrain the precise ages of these ice bodies with radiocarbon dating techniques.

As a complement to the attempts to age-date ice wedge formation, in the current study I analyzed the  $\delta^{18}\text{O}$  change within ice wedges and pool ice and from them, estimate the magnitude of climatic variations during the late Pleistocene in Central Alaska. Further, in an attempt to better refine the growth intervals of the ice wedges, high-resolution  $\delta^{18}\text{O}$  analyses of five wedge generations were compared and correlated to a marine sediment record from the Bering Sea as a proxy for regional changes in paleotemperature.

## **Methods**

A detailed description of the tunnel stratigraphy, ice wedge sampling techniques, and radiocarbon dating of CO<sub>2</sub> and DOC is provided in Chapter 3. Ice wedges and pools of various sizes and from various stratigraphic positions were identified for sampling in the tunnel and designated according to their distance in meters from the tunnel entrance on the north (N) or south (S) tunnel wall. Blocks of ice were cut from eight ice wedges (1N, 14.9S Winze, 18N, 35S, 45S, 50S, 52.5S, and 58N) and seven ice pools (31N-Pool, 34S-Pool, 45N-Pool, 50S-Pool A, 50S-Pool L, 51S-Pool, and 70N-Pool) using an electric chainsaw.

I subsampled each ice block in the cold room facility at Ft. Wainwright, AK for stable isotope analyses using the purpose-built Wedgenator ice milling tool. This device consists of a Dremel tool with a carbide, high-speed cutter bit attached to an aluminum meter stick secured and mounted at both ends. Using the Wedgenator tool, I milled ice samples in 2-mm swaths and collected in pre-labeled Ziploc plastic bags. To prevent contamination between each sample, the Dremel tool bit and ice wedge were brushed clean of ice shards using a small toothbrush following each sample collection. Samples were stored in plastic bags, packed in coolers with dry ice and cold packs, and shipped overnight via FedEx to the Las Vegas Isotope Science (LVIS) laboratory at the University of Nevada, Las Vegas. Samples were transferred to a freezer located in the laboratory.

Each stable isotope ice wedge sample was melted, filtered to remove particulate sedimentary material, and transferred to a five milliliter vial fitted with a two milliliter plastic insert. Two microliter aliquots were injected into a ThermoElectron high temperature conversion elemental analyzer (TC/EA) by reaction with glassy carbon at 1,450°C in a helium carrier gas stream to produce H<sub>2</sub> and CO gases. Isotopic ratios of oxygen ( $\delta^{18}\text{O}$ ) and deuterium ( $\delta\text{D}$ ) were determined on a ThermoElectron Delta V Plus isotope ratio mass spectrometer relative to two internal standards calibrated to SLAP (Standard Light Antarctic Precipitation) and VSMOW (Vienna Standard Mean Ocean Water) and reported in per mil (‰) concentrations.

## Results and interpretation

### *Ice wedge and pool ice stable isotopes*

High resolution stable isotopes were analyzed in eight ice wedges (Appendix D) and seven ice pools (Table 4.1) from the CRREL Permafrost Tunnel. The ice wedge  $\delta^{18}\text{O}$  values range from -28.9 to -20.4‰ (mean = -26.0‰), the  $\delta\text{D}$  values range from -226.5 to -163.7‰ (mean = -205.8‰), and the  $d$  values range from -7.6 to 19.0‰ (mean = 2.4‰). The pool ice  $\delta^{18}\text{O}$  values range from -26.6 to -21.8‰ (mean = -23.4‰), the  $\delta\text{D}$  values range from -209.5 to 175.6‰ (mean = -186.1‰), and the  $d$  values range from -3.2 to 3.4‰ (mean = 1.4‰). These values plot below the Global Meteoric Water Line (GMWL) along a slope of 6.4 (Figure 4.3).

The  $\delta^{18}\text{O}$  results of the ice wedges and pool ice were categorized into one of the freeze or melt events identified in Chapter 3. The approximate timing of five freeze events and one melt event were estimated in Chapter 3 using the relative stratigraphic position in the tunnel and  $^{14}\text{C}$  dating of DOC within the ice and were ordered by apparent sequence of formation, beginning with F1 at the base of the tunnel (Wedges 28N, 35S, 45N, 45S, 50S, 58N, 60S, 67N, 70N), F2 (35S secondary wedge), M1 (28N Pool, 31N Pool, 34S Pool, 45N Pool, 50S Pool, 51S Pool, 60S Pool, 70N Pool), F3 (Wedges 18N and 50N), F4 (Wedges 14.9S, 50S, 52.5S), and F5 (Wedges 45N, 52.5N, 60S, 64S). The resulting isotopic values of each sampled freeze and melt event are shown in Figure 4.4.

The isotopic values of the ice wedges form a distinctive concave shape with the highest  $\delta^{18}\text{O}$  values at the outer sides of the wedge gradually decreasing to the lowest values at the center of the wedge (Figure 4.4A-D). The F3 wedge contains the lowest  $\delta^{18}\text{O}$  value of -28.9‰ (Figure 4.4C), while the F4 wedges contain the highest  $\delta^{18}\text{O}$  value

of -20.4‰ (Figure 4.4D). The largest range in  $\delta^{18}\text{O}$  values within wedges occurs in the largest wedges, the F1 wedges, with  $\delta^{18}\text{O}$  values ranging from -27.9‰ near the center to -21.8‰ at the outside of the wedge (Figure 4.4A).

Within the isotopic profile of one the F1 wedges, though, a secondary wedge is apparent about 30 cm from the right side of wedge 35S (Figure 4.4A). The  $\delta^{18}\text{O}$  values start to deviate from the pattern seen in the other F1 wedges by increasing around -25‰ instead of following the gradually decreasing pattern toward the center of the wedge. The  $\delta^{18}\text{O}$  values increase to -24.5‰ for 20 cm, then sharply decrease to -27‰ toward the center, consistent with the pattern of the other three F1 wedges. This observation of a double isotopic excursion towards negative values is consistent with a younger wedge cross cutting the F1 wedge. This 35S secondary wedge, classified as the F2 wedge, was documented but not sampled in Chapter 3, and is visually apparent on the right side of the wedge (Figure 4.5). Because F2 cuts F1, wedge F2 must be younger than F1. Another ice wedge, 1N, shares the same  $\delta^{18}\text{O}$  values and profile as the F2 wedge at 35S, but its stratigraphic position was obscured by placement of the metal tunnel portal. Therefore, it is tentatively assigned an F2 age based on its isotopic similarity to the F2 wedge at 35S (Figure 4.4B).

### ***Origin of wedge and pool ice***

To establish whether the origin of the ice wedge ice and pool ice was meteoric precipitation, snowmelt, or ice wedge ice, the  $\delta^{18}\text{O}$ - $\delta\text{D}$  relationships in both the ice wedges and ice pools were examined. Ice with a  $\delta^{18}\text{O}$ - $\delta\text{D}$  slope lower than 6.0 indicates the ice formed by sublimation, while slopes greater than 6.0 suggest ice formed by refreezing of liquid water, as shown in the similar  $\delta^{18}\text{O}$ - $\delta\text{D}$  relationships between buried

ground ice and local meteoric precipitation in the Yukon. These slope thresholds have indicated the origin of ground ice was meteoric precipitation, as the ground ice plotted along the local meteoric line with a similar slope (Lacelle et al., 2009). A similar  $\delta^{18}\text{O}$ - $\delta\text{D}$  relationship exists here between the ice wedge values and modern snow values, as the ice wedge values plot along the local meteoric water line (LMWL) with a slope greater than 6.0, indicating the source of the wedge ice was likely snowmelt that infiltrated into the contraction cracks during ice wedge formation (Figure 4.3).

Likewise, the similar slope of the LMWL and the pool ice line (PIL) indicates the source of the pool ice was meteoric precipitation (Figure 4.3), not melted ice wedge ice, thus confirming the name "pool" ice. With the exception of the 45S Pool sample, the pool ice  $\delta^{18}\text{O}$  values are higher than the ice wedge  $\delta^{18}\text{O}$  values, indicating the source of the pool ice is likely meteoric precipitation. The lower  $\delta^{18}\text{O}$  value of the 45S sample is intermediate between the wedge ice and meteoric precipitation, suggesting the pool ice is a mixture of both sources. It is possible the 45S pool formed first before the other pools, with thawing wedge ice and/or permafrost contributing to the water in the pool. As climatic conditions warmed, meteoric precipitation contributed moisture to the pool until flash freezing froze the pool into ice. The low pool ice values of the other pools indicates the ice did not form as a result of melting ice wedge ice, as suggested by the thermokarst-cave ice hypothesis (Shur et al., 2004). The melting and refreezing of ice wedge ice to form thermokarst cave ice would likely result in heavier pool ice  $\delta^{18}\text{O}$  values plotting below the Ice Wedge Line (IWL) as kinetic fractionation processes enrich the initial water with heavier isotopes along the freezing slope (Souchez et al., 2000). Instead, the  $\delta^{18}\text{O}$ - $\delta\text{D}$  relation between the PIL and the LMWL suggests the pools collected meteoric



precipitation during warmer intervals and underwent refreezing as conditions cooled (Figure 4.3).

### ***High resolution $\delta^{18}\text{O}$ record of paleoclimate***

Sampling of ice wedges for  $\delta^{18}\text{O}$  has typically been conducted at low resolutions, with one (Douglas et al., 2011) to several (Meyer et al., 2010b) samples per decimeter-scale wedge representing  $\delta^{18}\text{O}$  values for the entire duration of formation. As a result of the low sampling resolution of previous studies, the presence of high-frequency climate variability on the time scales represented by the ice wedges remains poorly documented. Efforts to establish a  $\delta^{18}\text{O}$ -age relationship within one wedge (50S) resulted in anomalous particulate organic carbon (POC) ages and an inconclusive  $\delta^{18}\text{O}$ -age relationship within the wedge (Griffing, 2011). In addition, several decades of previous POC dating unpublished results prompted concerns of sample contamination resulting from the observation of age/depth anomalies in these and other ice wedges in the tunnel (Lawson unpublished data), prompting the efforts here to establish more rigorous sampling protocols to minimize contamination issues, and to use high resolution  $\delta^{18}\text{O}$  and DOC analyses to establish an ice wedge  $\delta^{18}\text{O}$ -age relationship. Wedge 35S in the F1 event was analyzed every 4 mm to identify possible fluctuations within the ice wedge  $\delta^{18}\text{O}$  record. Small  $\sim 0.5\text{‰}$   $\delta^{18}\text{O}$  fluctuations are observed on  $\sim 4$  mm-scales throughout the wedge (Figure 4.6). These small fluctuations may be a seasonal climatic signal, but it is more likely they are fluctuating at longer timescales, perhaps decadal.

The high-to-low  $\delta^{18}\text{O}$  values from the edges to the centers of the wedges follow the expected pattern of the ice wedge growth model. If secondary cracking had occurred within the wedges, it is expected  $\delta^{18}\text{O}$  values would fluctuate between more negative and

less negative values across shorter sections of the wedge, coinciding with younger radiocarbon ages. These fluctuating  $\delta^{18}\text{O}$  values would reflect the different climatic conditions during formation. With the exception of wedge 35S, evidence of secondary cracking events such as spikes of less negative to more negative  $\delta^{18}\text{O}$  values is not apparent in the ice wedges, as the  $\delta^{18}\text{O}$  values follow the expected high-to-low pattern with no apparent large fluctuations within the wedges (Figure 4.4).

However, the  $\delta^{18}\text{O}$  values within wedge 35S do not follow this expected pattern. Visual investigation of the tunnel face before sampling detected the presence of a possible small secondary wedge on the right side of wedge 35S and high resolution isotopic analyses revealed this secondary wedge likely formed during a secondary cracking event. The high-to-low pattern of  $\delta^{18}\text{O}$  values from the outer right edge of the wedge to the center is observed twice in wedge 35S, indicating a secondary wedge formed and cross cut the original F1 event (Figure 4.5). Compared to the main wedge 35S  $\delta^{18}\text{O}$  values ranging from -26.8 to -23.0‰, the secondary wedge  $\delta^{18}\text{O}$  values range from -25.5 to -21.8‰, approximately 1.3 to 1.2‰ higher, suggesting it formed under warmer climatic conditions compared to the F1 event.

Although a high resolution  $\delta^{18}\text{O}$ -age relationship was not possible because of the limitations of radiocarbon analyses, high resolution  $\delta^{18}\text{O}$  analyses within the wedges enabled the comparison of high-frequency climate variability within and between ice wedge events. These results provide a significantly higher resolution record of  $\delta^{18}\text{O}$  variability in Central Alaska than previously recorded in other proxies. With  $\delta^{18}\text{O}$  values ranging between -26.6 and -21.8‰, the highest of all the events sampled, the F4 event likely represents the warmest interval sampled in the tunnel. High resolution sampling of

the F3 event revealed it represented the coldest interval of those sampled in the tunnel, with  $\delta^{18}\text{O}$  values ranging between -28.9 and -26.2‰ within the wedge, and up to -7.0‰ lower compared to the warmest (F4) wedges sampled. The F1 event likely represents the next warmest interval, with  $\delta^{18}\text{O}$  values ranging from -27.9 to -21.8‰ within the wedges, up to -6.1‰ lower than the F4 wedges, and +1.0‰ higher than the F3 wedges. The F2 wedges likely formed under even warmer conditions compared to the F1 and F3 wedges, with  $\delta^{18}\text{O}$  values ranging between -26.0 and -22.7‰, up to -4.2‰ lower than the F4 wedges and +2.9‰ higher than the F3 wedge (Figure 4.5).

This high resolution analysis at 4 mm revealed a much more detailed paleoclimatic record of  $\delta^{18}\text{O}$  fluctuations compared to low resolution analyses, suggesting that high resolution sampling is necessary to capture the climatic variability within ice wedge growth intervals in Central Alaska.

#### ***Wedge $\delta^{18}\text{O}$ as a proxy for paleoclimate change***

The fluctuations of  $\delta^{18}\text{O}$  within and between the wedges allowed for comparison of paleoclimatic changes during freeze events, but to compare the magnitude of  $\delta^{18}\text{O}$  change between the freeze events and modern climatic conditions, the  $\delta^{18}\text{O}$  values of the ice wedges and pool ice were first compared to modern snow and Holocene ice wedge  $\delta^{18}\text{O}$  values (Figure 4.7). Modern snow collected in Denali National Park between 1989 and 1993 ranged in  $\delta^{18}\text{O}$  value from -27.8 to -18.2‰ ( $\delta^{18}\text{O}$  weighted mean of  $-22.3 \pm 3.5$ ‰), in  $\delta\text{D}$  value from -227.5 to -187.8‰ ( $\delta\text{D}$  weighted mean of  $-176.3 \pm 31.4$ ‰), and in  $d$  value from -11.5 to 8.7‰ (mean = -0.6‰) (USNIP, 2011). Similar to these modern snow values, a 3.9 cal ka BP ice wedge from an open pit at the Vault Creek Tunnel near

Fairbanks had a mean  $\delta^{18}\text{O}$  value of -21.8‰, and  $\delta\text{D}$  value of -172‰ (Meyer et al., 2008).

Compared to the modern snow, the Permafrost Tunnel ice wedges generally have lower than modern  $\delta^{18}\text{O}$  values, and range between -6.6 below and +1.9‰ above modern snow values (Figure 4.7). Assuming climatic conditions during the last glacial period were similar to modern conditions and because  $\delta^{18}\text{O}$  values decrease with decreasing temperature,  $\delta^{18}\text{O}$  values lower than modern values are interpreted to indicate climatic conditions were colder than modern. Likewise,  $\delta^{18}\text{O}$  values higher than modern values are interpreted to indicate climatic conditions were warmer than modern.

Although the use of  $\delta^{18}\text{O}$  values within the wedges is useful for comparison to modern values, combining the  $\delta^{18}\text{O}$  values with  $^{14}\text{C}$  ages allows for a better age refinement of the timing and magnitude of freeze and melt events in the tunnel. For example, the Vault Creek ice wedge (Meyer et al., 2008) not only provides a constraining age of 3.9 cal ka BP for the timing of formation of the events in the Permafrost Tunnel, but it also closely matches the F4 wedge isotopic values ( $\delta^{18}\text{O} = -21.9$  to  $-20.4$ ‰) (Figure 4.7). Because the F4 wedge  $\delta^{18}\text{O}$  values closely match those of the Holocene age Vault Creek ice wedge, it is likely the F4 wedges formed around 3.9 cal ka BP. The F4 wedge  $\delta^{18}\text{O}$  values are the highest of those sampled in the tunnel and range between +0.4 and +1.9‰ above modern values, likely representing the warmest ice wedge forming thermal event (Figure 4.7).

Compared to the warmest thermal event in the tunnel, the F1 wedge  $\delta^{18}\text{O}$  values range from -5.6 below to +0.5‰ above modern values, suggesting the F1 event formed under colder conditions compared to modern climate, intermediate between the coldest

and warmest conditions observed in the tunnel ice wedge record. The large wedge width and 6.1‰ magnitude of change in the  $\delta^{18}\text{O}$  values suggests the interval of formation likely occurred over a cooling period between 25.9 - 21.5 cal ka BP, based on the constraining maximum and minimum limiting ages discussed in Chapter 3 (Figure 4.7).

The next interval of ice wedge growth, F2, likely occurred between 25.9 and 21.5 cal ka BP, based on maximum and minimum limiting ages discussed in Chapter 3. The F2 wedge  $\delta^{18}\text{O}$  values range from -3.7 to -0.4‰ below modern values, representing a 3.3‰ magnitude of change within the event, suggesting it formed during a cooling when conditions were warmer than the F1 and F3 events, but still colder than modern climate (Figure 4.7).

The pool ice M1  $\delta^{18}\text{O}$  values range between -4.3 below and +0.5‰ above modern snow values, indicating the pools formed under both colder and warmer than modern conditions. Although the  $\delta^{18}\text{O}$  values range from -26.6 to -21.8‰, the median  $\delta^{18}\text{O}$  value of the pool ice samples ( $\delta^{18}\text{O} = -23.1\text{‰}$ ), is close to the modern value of snow, suggesting the pool ice formed under similar to modern conditions. However, maximum and minimum limiting ages between 21.5 and 17.9 cal ka BP (Chapter 3) constrain the timing of the M1 event, suggesting the pools may have formed during warm seasonal conditions similar to modern conditions rather than cold seasonal conditions (Figure 4.7).

Conversely, the F3 wedge  $\delta^{18}\text{O}$  values range from -6.6 to -3.9‰ below modern values, indicating it formed during the coldest conditions of those sampled in the tunnel. The 3.3‰ magnitude of  $\delta^{18}\text{O}$  change within the wedge likely occurred between 17.9 - 12.9 cal ka BP based on maximum and minimum limiting ages discussed in Chapter 3 (Figure 4.7). This combined use of high resolution  $\delta^{18}\text{O}$  records and  $^{14}\text{C}$  ages of DOC

within ice wedge ice provides a proxy for paleoclimate change in Central Alaska that suggests climatic conditions were -5.6 below to -0.5‰ above modern conditions likely beginning around 25.9 cal ka BP, warmed to about -3.7 to -0.4‰ below modern conditions, warmed perhaps seasonally to -4.3 below to +0.5‰ above modern conditions around 21.5 cal ka BP, cooled to -6.6 to -3.9‰ below modern conditions around 17.9 cal ka BP, and then eventually warmed to modern conditions around 3.9 cal ka BP (Figure 4.7).

### ***Paleotemperature reconstruction of freeze and melt events***

The high resolution ice wedge and pool ice  $\delta^{18}\text{O}$  values were used to reconstruct the range of temperature fluctuations between modern and past conditions over which the freeze and melt events formed. To estimate the magnitude of fluctuation between modern and past temperatures, two different  $\delta^{18}\text{O}$ -T equations were used to predict the possible range under which the ice wedges and pool ice formed. The first  $\delta^{18}\text{O}$ -T equation was determined from the spatial isoscape derived in Chapter 2 using winter temperatures and spatially-derived surface water  $\delta^{18}\text{O}$  values, resulting in the equation  $\delta^{18}\text{O} = 0.28 \times \text{DJFT} - 14.9$  ( $R^2 = 0.59$ ) (Equation 1). The second  $\delta^{18}\text{O}$ -T equation was obtained from the simpler MAT isoscape derived in Chapter 2 from spatially-derived surface water  $\delta^{18}\text{O}$  values and mean annual air temperature (MAT), resulting in the equation  $\delta^{18}\text{O} = 0.55 \times \text{MAT} - 17.9$  ( $R^2 = 0.61$ ) (Equation 2). The minimum and maximum  $\delta^{18}\text{O}$  values from each freeze and melt event were then used to calculate the  $\delta^{18}\text{O}$  difference from modern  $\delta^{18}\text{O}$  Denali snow values of -22.3‰ (USNIP, 2011). The range of values within each freeze and melt event were then used to calculate the gradient of  $\delta^{18}\text{O}$  change with temperature change. If Equation 1 is correct,  $\delta^{18}\text{O}$  values decrease by 1‰ for every 3.6°C of winter

(DJF) temperature decrease. If Equation 2 is correct,  $\delta^{18}\text{O}$  values decrease by 1‰ with every 1.8°C of mean annual temperature (MAT) decrease. The paleotemperature was then calculated by subtracting the modern DJF T or MAT from the isoscape-derived paleotemperatures.

The first equation suggests winter temperatures formed when temperatures likely ranged between -41.6 and -11.2°C, which is consistent with modern winter temperatures of -18°C measured in Fox, AK (NCDC, 2010). The second equation suggests mean annual temperatures formed when temperatures likely fluctuated between -14.1 and 1.4°C, which is consistent with modern MAT of -2.1°C measured in Fox, AK (NCDC, 2010) (Table 4.3).

The  $\delta^{18}\text{O}$  in the wedges does not appear to show warming out of cold events, only cooling out of warm events, suggesting climatic conditions became too warm for wedges to continue forming. The F1 wedges appear to have formed when paleo-winter temperatures ranged from -38.0 to -16.2°C (Equation 1), or when paleo-MAT ranged from -12.3 to -1.2°C (Equation 2). The F2 wedges appear to have formed under slightly warmer conditions, when paleo-winter temperatures ranged from -31.2 to -19.4°C (Equation 1), or when paleo-MAT ranged from -8.8 to -2.8°C (Equation 2). The pool ice appears to have formed when paleo-winter temperatures ranged from -33.4 to -16.2°C (Equation 1), perhaps at times slightly warmer than modern winter temperatures. The paleo-MAT may have ranged from -9.9 to -1.2°C (Equation 2) during pool ice formation, also possibly slightly warmer than modern MAT. The F3 wedge formed during the coldest interval, when paleo-winter temperatures likely ranged from -41.6 to -31.9°C (Equation 1) and when paleo-MAT ranged from -14.1 to -9.2°C (Equation 2). This cold

interval represents a period that was likely as much as  $-23.6^{\circ}\text{C}$  colder than modern winter temperatures (Equation 1) and as much as  $-12.0^{\circ}\text{C}$  colder than modern MAT (Equation 2). The F4 wedges formed when paleo-winter temperatures were likely  $-16.6$  to  $-11.2^{\circ}\text{C}$  (Equation 1) and paleo-MAT ranged from  $-1.4$  to  $1.4^{\circ}\text{C}$  (Equation 2). These paleotemperatures for the F4 wedges are consistent with modern winter temperatures of  $-18^{\circ}\text{C}$  and MAT of  $-2.1^{\circ}\text{C}$  (Table 4.2).

While the Bering Sea SST record suggests that temperatures fluctuated by as much as  $5^{\circ}\text{C}$  between DO- and H-type events (Schlung et al., 2013), the Greenland ice core GICC05 record suggests temperatures fluctuated by as much as  $12 - 15^{\circ}\text{C}$  during the last glacial period (Johnsen et al., 2001). This range of temperature fluctuation suggests the isoscape-derived paleotemperature equations may be accurate estimates of Central Alaskan paleotemperatures because the range of temperatures ( $\sim 15.5^{\circ}\text{C}$  for paleo-MAT) is near the range of Greenland temperatures during millennial fluctuations. This similar magnitude of paleotemperature shift suggests Central Alaskan paleotemperatures were possibly controlled by North Atlantic millennial forcings. A similar magnitude shift of  $\delta^{18}\text{O}$  values between the freeze events and the Bering Sea sediment record could confirm this hypothesis of millennial-scale forcing of climate within Central Alaska.

## **Discussion**

### ***Approximate timing of freeze and melt events***

The high-resolution ( $\sim 4$  mm interval) record of ice wedge  $\delta^{18}\text{O}$  values combined with radiocarbon ages from organic material within the ice suggests formation was episodic, likely began around 25.9 cal ka BP and ceased around 3.6 cal ka BP. The range of isotopic values within the wedges and between the different freeze events also allows



for a tentative correlation with high resolution  $\delta^{18}\text{O}$  records. To better approximate the timing of ice wedge growth and pool ice formation, the  $\delta^{18}\text{O}$  values of the radiocarbon dated freeze and melt events were visually correlated with the planktonic Bering Sea IODP U1340 (Schlung et al., 2013)  $\delta^{18}\text{O}$  record which is tied to the Greenland GICC05 ice core record for referenced time intervals (Svensson et al., 2008). While the GICC05 data provides a proxy of Greenland snow  $\delta^{18}\text{O}$  values affected by global climate teleconnections, the U1340 site data provides the geographically nearest, highest resolution, and most comprehensive record of sea surface temperature (SST) data to date for the region. For this correlation, it was assumed the paleoclimatic conditions and perturbations in the Bering Sea were similar to those experienced in Central Alaska during the time period in which the freeze and melt events occurred. This assumption, therefore, provides only a tentative correlation between the freeze and melt events and the Bering Sea U1340 ocean sediment record and a tentative chronology of thermal events from radiocarbon dated ice wedges from the Permafrost Tunnel (Figure 4.8). The minimum and maximum limiting ages were used to determine the range and likely timing of the event, and the U1340 records were used to estimate the most likely correlated age based on the magnitude of  $\delta^{18}\text{O}$  fluctuations (Table 4.3).

The Bering Sea SST record exhibits millennial-scale forcing of DO- and H-type events at ca.1200-year intervals (Schlung et al., 2013) (Figure 4.8). Similarly, the ice wedge and pool ice values follow this same trend. The high resolution  $\delta^{18}\text{O}$  analyses of the F1 wedges revealed the decrease in  $\delta^{18}\text{O}$  values from the onset of wedge formation to the ceasing of wedge formation followed a gradual decline (Figure 4.6), suggesting the wedges did not form during rapid climatic shifts but instead during gradual shifts in

climate. The tentative correlation with the Bering Sea record indicates this shift occurred over ca. 1200 years, which is consistent with the timescale of forcing of DO- and H-type events in the North Atlantic (Figure 4.8). This tentative correlation combined with the apparent similar magnitude shift in paleotemperatures between the freeze events and Bering Sea records suggests that Central Alaskan climate was likely controlled by the effect of millennial-scale events in the North Atlantic.

Evidence for this millennial forcing is apparent in the ice wedge  $\delta^{18}\text{O}$  record exhibiting high values at the edges of the wedge decreasing to low values at the center of the wedge (Figure 4.4), which is consistent with the concave pattern of high  $\delta^{18}\text{O}$  values decreasing to low  $\delta^{18}\text{O}$  values observed in both Alaskan (Meyer et al., 2010b) and modern Antarctic wedges (Raffi and Stenni, 2011). This pattern of decreasing  $\delta^{18}\text{O}$  values is also similar to the decreasing  $\delta^{18}\text{O}$  pattern observed in the U1340 Bering Sea record, suggesting cooling initiated Central Alaskan ice wedge growth and rapid warming truncated ice wedge growth (Figure 4.8).

The timing of the decrease in  $\delta^{18}\text{O}$  values by as much as 6.6‰ within the wedges (Figure 4.4) correlates with the decrease in  $\delta^{18}\text{O}$  values observed during cooling over the last glacial period apparent in the Bering Sea U1340 sediment record (Schlung et al., 2013), pollen and vegetation records indicating shifts in warm and cold tolerant species (Ager and Brubaker, 1985), and glacial moraine ages indicative of glacial still-stands (Briner et al., 2005). Between the time of emplacement of the lower host sediments around 41.0 cal ka BP and the growth of Holocene ice wedges around 3.9 cal ka BP, respectively, at least four intervals of freezing and one interval of melt occurred in Central Alaska.

### *Freeze event 1*

The 6.1‰ magnitude decrease in  $\delta^{18}\text{O}$  values to -5.6 below and +0.5‰ above modern snow values combined with  $^{14}\text{C}$  ages of DOC within the F1 wedges suggests they likely formed during cooler than modern conditions, possibly when paleo-winter temperatures ranged from -38.0 to -16.2°C and paleo-MAT ranged from -12.3 to -1.2°C. Based on the apparent correlation between cooling trends in the wedge and in Bering Sea SST, F1 is tentatively assigned a formation age between 26.5 - 25.3 cal ka BP, coinciding with H2 (Figure 4.8). The  $\delta^{18}\text{O}$  values are consistent with  $\delta^{18}\text{O}$  values from wedges within the same F1 interval in the tunnel obtained during low-resolution sampling (Douglas et al., 2011), and also with  $\delta^{18}\text{O}$  values of Zone C ice wedges from the Vault Creek Tunnel near Fairbanks (Meyer et al., 2008). The timing of formation of these wedges is younger than previously reported (Hamilton et al., 1988; Sellmann, 1967), and is consistent with the possible timing during H2 first suggested by Lachniet et al. (2012). If the wedge  $\delta^{18}\text{O}$  decrease corresponds to the correlative age, it would represent a duration of ice wedge formation over ca. 1200 years. At widths of up to 1.6 m, the F1 wedges were the widest present in the tunnel, indicating they may have formed over the longest cooling interval, or during periods of slope stability. Evidence of mass movement such as slumping and debris flows apparent in the tunnel suggest periods of thaw and coincident mass movement of slope material may have limited or truncated ice wedge growth (Figure 4.5). However, evidence of slope instability is not as prevalent around the F1 wedges compared to the M1-F4 events, suggesting slope stability and/or cool conditions may have promoted wedge growth.

Further evidence for cooling in Central Alaska during the growth of the F1 wedges during this ca. 26.5 – 25.3 cal ka BP interval is apparent in the records of Alaskan glacial advance. The  $^{10}\text{Be}$  dating of terminal moraines in the Brooks Range indicates glacial advance occurred between 27 – 24 cal ka BP (Balascio et al., 2005), corresponding to the approximately 120 m fall of sea levels in the Bering Sea (Elias and Crocker, 2008). As ice sheets expanded and sea level regressed, the resulting increased aridity in the interior of the continent may have limited the availability of moisture for the growth of glaciers, contributing to their eventual retreat (Briner et al., 2005). This increased aridity over the continent may have also limited the availability of moisture for the growth of ice wedges, and may have prompted the cease of ice wedge growth ca. 25.3 cal ka BP. However, the appearance of moisture-tolerant grasses and sedges from fossil arctic ground squirrel caches (Gaglioti et al., 2011) combined with  $\delta^{15}\text{N}$  records of megafauna diets (Fox-Dobbs et al., 2008) suggests climatic conditions underwent a shift ca. 27 cal ka BP near Fairbanks and ca. 25 cal ka BP along the North Slope (Mann et al., 2013). This shift from drier to wetter conditions combined with cooling during H2 could explain the initiation of growth of the F1 wedges ca. 26.5 cal ka BP as sufficient moisture and cooling was available for ice wedge growth to occur. Additional evidence for Heinrich event cooling in the Arctic includes ice rafted debris found in the Fram Strait (Darby et al., 2002), indicating ice export occurred from the Laurentide Ice Sheet (LIS) through the M'Clure Strait in northern Canada into the Arctic Ocean ca. 26,450 cal yr BP (Stokes et al., 2005), which is consistent with the estimation of the timing of the initiation of F1 wedge growth.

### *Freeze event 2*

Based on the 3.3‰ magnitude decrease in  $\delta^{18}\text{O}$  values and the apparent correlation between cooling trends in the wedge and in Bering Sea SST, F2 is tentatively assigned a formation age between ca. 21.0 - 20.5 cal ka BP (Figure 4.8). With  $\delta^{18}\text{O}$  values ranging from -26.1 to -22.7‰ (Figure 4.4B), the initiation of growth of the F2 wedges appears to have occurred at temperatures cooler than the initiation of the F1 wedge growth, likely when paleo-winter temperatures ranged from -31.2 to -19.4°C and paleo-MAT ranged from -8.8 to -2.8°C. The magnitude of cooling observed in the F2 wedges corresponds to the magnitude of  $\delta^{18}\text{O}$  change in the U1340 record, although this cooling does not correspond to a specific H event (Figure 4.8). Higher  $\delta^{18}\text{O}$  values at the edges of the F2 wedge also can be interpreted as the wedge ceasing formation during warmer conditions compared to the F1 event. This may have occurred during a shift to warmer and wetter climates ca. 20 cal ka BP, as indicated by the decline in the  $\delta^{15}\text{N}$  in caribou bone which suggests a shift in diet to more moist acidic tundra vegetation (Mann et al., 2013). An additional indicator of warmer conditions includes evidence of glacial still-stands near Denali in the Alaska Range ca. 22 and 19 cal ka BP (Briner and Kaufman, 2008).

### *Melt event 1*

The 4.8‰ range in  $\delta^{18}\text{O}$  values between -4.3 below and +0.5‰ above modern snow values suggests the pools formed under conditions slightly cooler to warmer than modern conditions, possibly when paleo-winter temperatures ranged from -33.4 to -16.2°C and paleo-MAT ranged from -9.9 to -1.2°C. The apparent correlation between warming trends in the pool ice and in Bering Sea SST tentatively suggests an M1

formation age between ca. 19.1 - 18.8 cal ka BP (Figure 4.8). The  $\delta^{18}\text{O}$  values are also consistent with  $\delta^{18}\text{O}$  values obtained during low-resolution sampling of pool ice within the tunnel (Douglas et al., 2011). In addition, the pool ice  $\delta^{18}\text{O}$ - $\delta\text{D}$  slope is similar to the slope of the local meteoric water line (LMWL), indicating the source of the pool ice is meteoric precipitation (Figure 4.3). This meteoric origin of pool ice is consistent with warming during the 19.1 - 18.8 cal ka BP interval, suggesting climatic conditions were likely too warm for thermal contraction cracking and ice wedge formation to occur.

This interval of likely formation over only 300 years occurred much earlier than the ca. 31 cal ka BP age of pool ice formation previously reported (Hamilton et al., 1988; Sellmann, 1967), and is consistent with warming in the Canadian Arctic and Yukon. A horse mandible with an age of ca. 19.7 cal ka BP (Lacelle et al., 2013) indicates the area around the Richardson Mountains NWT was ice free during this time. Glacial retreat near Denali in the Alaska Range was likely complete by ca. 19 cal ka BP (Briner and Kaufman, 2008) indicating warmer conditions prevailed in the region. However, these warm conditions may have been short lived, as evidence from the NWT indicates cold conditions returned to the area ca. 18.5 cal ka BP as the Laurentide Ice Sheet (LIS) reached its maximum extent (Lacelle et al., 2013).

### *Freeze event 3*

A -6.6 to -3.9‰ decrease in F3 ice wedge  $\delta^{18}\text{O}$  values compared to modern snow values suggests Central Alaska experienced colder than modern conditions, with paleo-winter temperatures likely ranging from -41.6 to -31.9°C and paleo-MAT ranging from -14.1 to -9.2°C. Based on the apparent correlation between cooling trends in the wedge and in Bering Sea SST, F3 is tentatively assigned a formation age between ca. 17.3 and

17.0 cal ka BP, coinciding with H1 (Figure 4.8). This F3 wedge also corresponds to a wedge with low  $\delta^{18}\text{O}$  values between -29.3 and -23.6‰ in the Vault Creek Tunnel near Fairbanks (Meyer et al., 2008) that suggests they both formed under similar conditions and likely at the same time interval.

The H1 cold event that occurred from ca. 16.5 kyr to 17.5 kyr marks the end of the LGM (Figure 4.8). This interval also corresponds to the largest sea ice and glacial extent in the Arctic, sea levels as low as 120 m below modern sea levels, and the lowest global temperatures during the LGM (Miller et al., 2010). The timing of the F3 wedges is consistent with terminal moraine ages that suggest glacial still-stands in the Nenana Valley near Fairbanks (Dortch et al., 2010) and near the Delta River Valley began ca. 17 cal ka BP (Matmon et al., 2010). Glacial retreat from LLGM positions could have been triggered by increased continentality as sea levels reached their lowest point during the LGM (Elias and Crocker, 2008) and also may have limited moisture availability for F3 wedge growth. The rapid warming observed in the U1340 record ca. 16 kyr is also accompanied by an increase in warmer pollen species in lake sediment records from Central Alaska (Ager and Brubaker, 1985), and the  $\delta^{15}\text{N}$  decrease in muskoxen and caribou diets that signals wetter and warmer conditions (Mann et al., 2013).

Toward ca. 14 cal ka BP, loess accumulation began to increase (Muhs et al., 2003) as vegetation began to change to a shrub-birch tundra which was a better trap of loess (Ager and Brubaker, 1985). This transition to a shrub-birch tundra is also reflected in the  $\delta^{15}\text{N}$  values in caribou and muskoxen bones that suggest a shift in diet to more moist acidic tundra vegetation (Mann et al., 2013). Although ice wedges in Barrow, AK dating to ca. 14.3 - 12.9 cal ka BP provide evidence for a YD cold event in Alaska

(Meyer et al., 2010b), YD-age wedges do not appear to be present in Central Alaska. The U1340 record indicates the magnitude of cooling during the YD was small, so it is possible that the cooling was not cold enough or long enough to initiate ice wedge cracking.

The appearance of wetter and warmer vegetation is also consistent with the resubmergence of the Bering Strait by ca. 13.4 - 13.2 cal ka BP (England and Furze, 2008), as ice sheets melted and sea levels rose, producing a warmer and wetter climate for Central Alaska. A wood willow log with an age of 12.9 cal ka BP in the Debris Fan above the F4 wedges indicates conditions were suitably warm and wet for willow trees to grow near the tunnel.

#### *Freeze event 4*

The closely matching  $\delta^{18}\text{O}$  values between the F4 wedges and the Vault Creek ice wedge indicates the F4 wedges likely formed around 3.9 cal ka BP when temperatures were warmer than modern conditions (Figure 4.8), with paleo-winter temperatures ranging from -16.6 to -11.2°C and paleo-MAT ranging from -1.4 to 1.4°C. The presence of the Debris Fan above the wedges provides further indication conditions were warm enough for mass movement of slope sediments. It appears likely the Debris Fan sheared off sections of the F4 wedges, creating the appearance of two separate F4 and F5 wedges. However, F5 wedges were not analyzed for  $\delta^{18}\text{O}$  values, so this hypothesis cannot be tested. The likely shearing off of the F4 wedges by the Debris Fan indicates mass movement of unfrozen or thawed sediments occurred during a warm interval, after the formation of the F4 wedges around 3.9 cal ka BP.



### *Freeze event 5*

Ice wedges within F5 were not sampled for stable isotopes, so no correlation was made between the F5 wedges and the U1340 record. Based on the likely age of the F4 event, it is possible the F5 wedges are synonymous with the F4 wedges or formed after 3.9 cal ka BP. High resolution isotopic data from the F5 wedges would be needed to estimate the timing of the formation.

### ***Summary of Central Alaskan paleoclimate***

Central Alaska experienced five distinct climatic perturbations as shown in radiocarbon dated and isotopically distinct ice wedges and pool ice preserved in the CRREL Permafrost Tunnel. The F1 cold event likely occurred between ca. 26.5 - 25.3 cal ka BP, apparent as a 6‰ decrease in  $\delta^{18}\text{O}$  values as paleo-winter temperatures ranged from -38.0 to -16.2°C and paleo-MAT ranged from -12.3 to -1.2°C, likely occurring during H2. A second cold interval, F2, characterized by a decrease of 3.3‰ in  $\delta^{18}\text{O}$  values, likely occurred between ca. 21.0 - 20.5 cal ka BP. A warm interval, M1, likely occurred between ca. 19.1 - 18.8 cal ka BP, with increases of up to 4.8‰ in  $\delta^{18}\text{O}$  values and paleo-winter temperatures ranging from -33.4 to -16.2°C and paleo-MAT ranging from -9.9 to -1.2°C. A third freeze event, F3, likely occurred between ca. 17.3 - 17.0 cal ka BP, coinciding with H1, and recorded a decrease in  $\delta^{18}\text{O}$  values of 2.7‰ representing the lowest and coldest of the events sampled as paleo-winter temperatures ranged from -41.6 to -31.9°C and paleo-MAT ranged from -14.1 to -9.2°C. The F4 event likely occurred ca. 3.9 cal ka BP and occurred as  $\delta^{18}\text{O}$  values were between -4.3 below and +0.5‰ above to modern values and paleo-winter temperatures ranged from -16.6 to -11.2°C and paleo-MAT ranged from -1.4 to 1.4°C (Table 4.3).

## Conclusion

If this correlation in wedge ages and climatic perturbations in other records is correct, ice wedge growth began ca. 26.5 cal ka BP, likely in response to H2 cooling, as recorded in the decreasing  $\delta^{18}\text{O}$  values in the ice as paleo-winter temperatures ranged from -38.0 to -16.2°C and paleo-MAT ranged from -12.3 to -1.2°C. Four intervals of cooling (ca. 26.5 - 25.3 cal ka BP, ca. 21.0 - 20.5 cal ka BP, ca. 17.3 - 17.0 cal ka BP, and ca. 3.9 cal ka BP) and one interval of warming (ca. 19.1 to 18.8 cal ka BP) were recorded in the ice wedges and pool ice, with two of the cooling intervals likely occurring in response to Heinrich events. High resolution  $\delta^{18}\text{O}$  values in ice wedges combined with  $^{14}\text{C}$  ages of DOC within the ice were visually correlated with Bering Sea ocean sediment records. It was found that between H2 and 3.9 cal ka BP, Central Alaskan  $\delta^{18}\text{O}$  values fluctuated by as much as -6.6‰ below to +1.9‰ above modern values and paleo-winter temperatures ranged between -41.6 and -11.2°C while paleo-MAT ranged between -14.1 and 1.4°C. These freeze event temperature and  $\delta^{18}\text{O}$  fluctuations are consistent in timing and magnitude with DO- and H-type events observed in the Bering Sea SST and Greenland ice core records, suggesting possible North Atlantic millennial-scale forcing of climate in Central Alaska. Although the persistence and incorporation of old organic matter into ice wedges and permafrost during formation and the resulting possibly anomalous ages causes difficulty in accurately dating ice growth, the results here indicate this method of combining high resolution isotopic analyses with  $^{14}\text{C}$  dating of DOC within the ice provides better chronological control on paleoclimate records in permafrost when combined with the Bering Sea SST record.

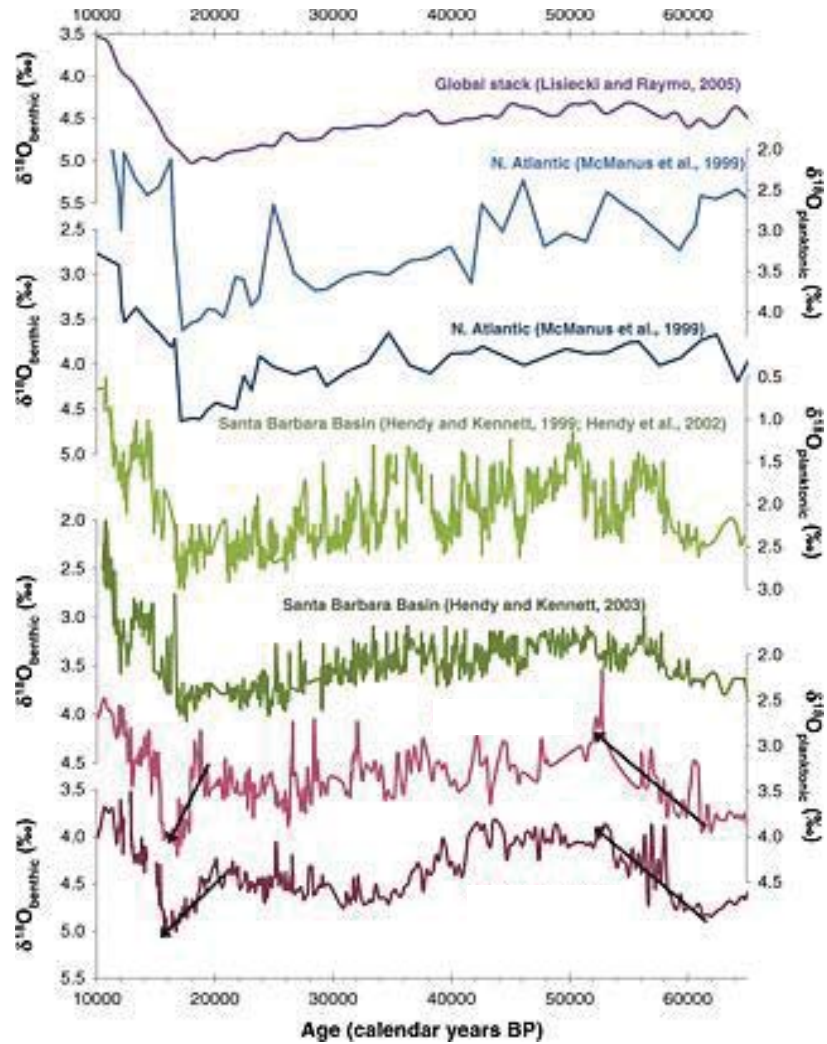


Figure 4.1. Bering Sea U1340  $\delta^{18}\text{O}$  records. Benthic and planktonic  $\delta^{18}\text{O}$  records from the North Atlantic, the Santa Barbara Basin, and Integrated Ocean Drilling Program site U1340 in the Bering Sea follow the same general pattern as Lisiecki and Raymo's (2005) Global Stack record over the past 60 kyr (Schlung et al., 2013). The high-resolution pattern of the U1340 data indicates these millennial-scale events were not confined to the North Atlantic.

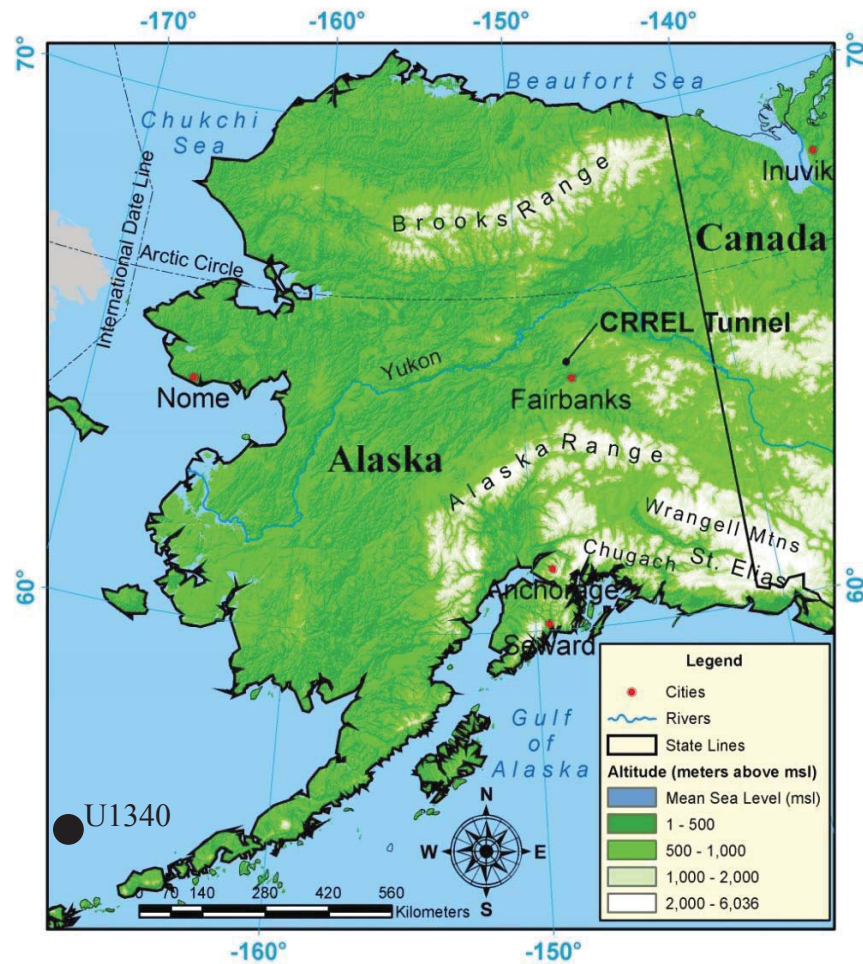


Figure 4.2. CRREL Permafrost Tunnel location map. The tunnel is located just north of Fairbanks, Alaska. The Bering Sea IODP Site U1340 provides ocean sediment records of past sea surface temperature (SST). Base map is a USGS 300-m Digital Elevation Model (DEM) (USGS, 1997).

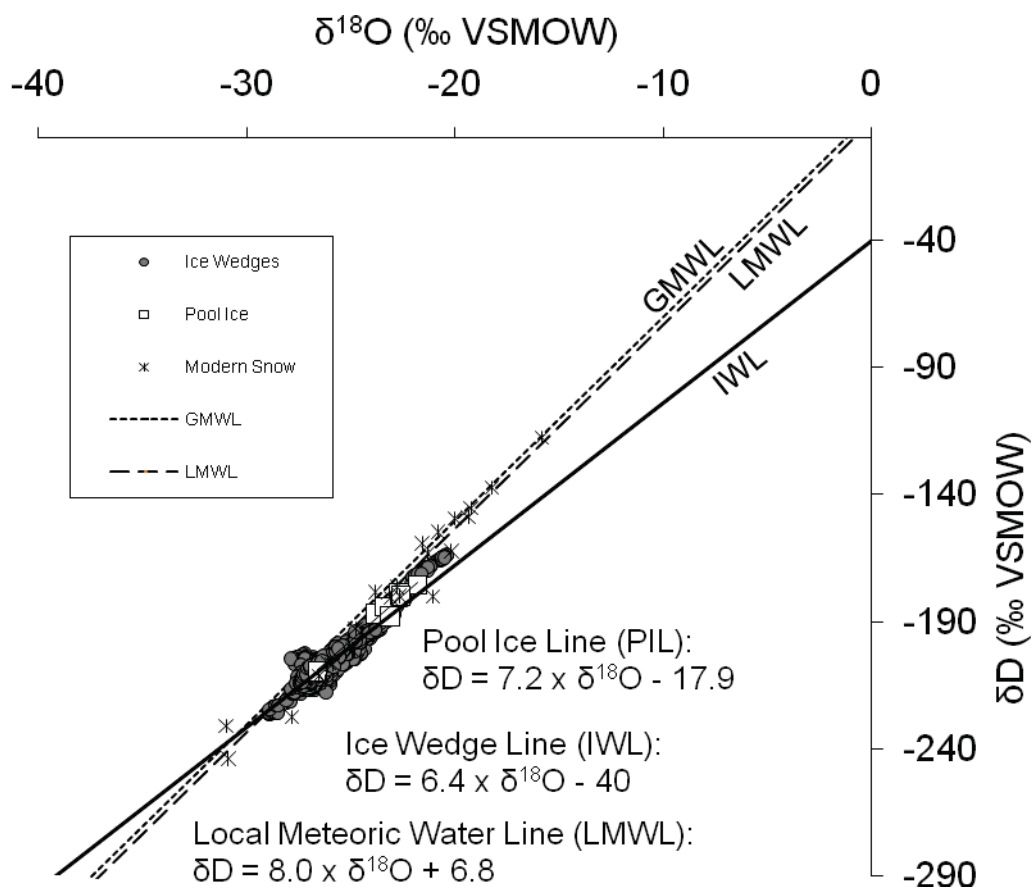


Figure 4.3.  $\delta^{18}\text{O}$  and  $\delta\text{D}$  values from ice wedges and pool ice. Ice wedge and pool ice values plot below the Global Meteoric Water Line (GMWL) and the Local Meteoric Water Line (LMWL) with a trend of  $\delta\text{D} = 6.4 \times \delta^{18}\text{O} - 40$ . Ice wedge and pool ice values plot below modern snow values, indicating the wedge ice consists of melted snow. The similar slopes of the LMWL (8.0) and the PIL (7.2) indicate the pool ice originated as meteoric precipitation. Modern snow  $\delta^{18}\text{O}$  and  $\delta\text{D}$  values for Denali National Park were obtained from USNIP (2011).

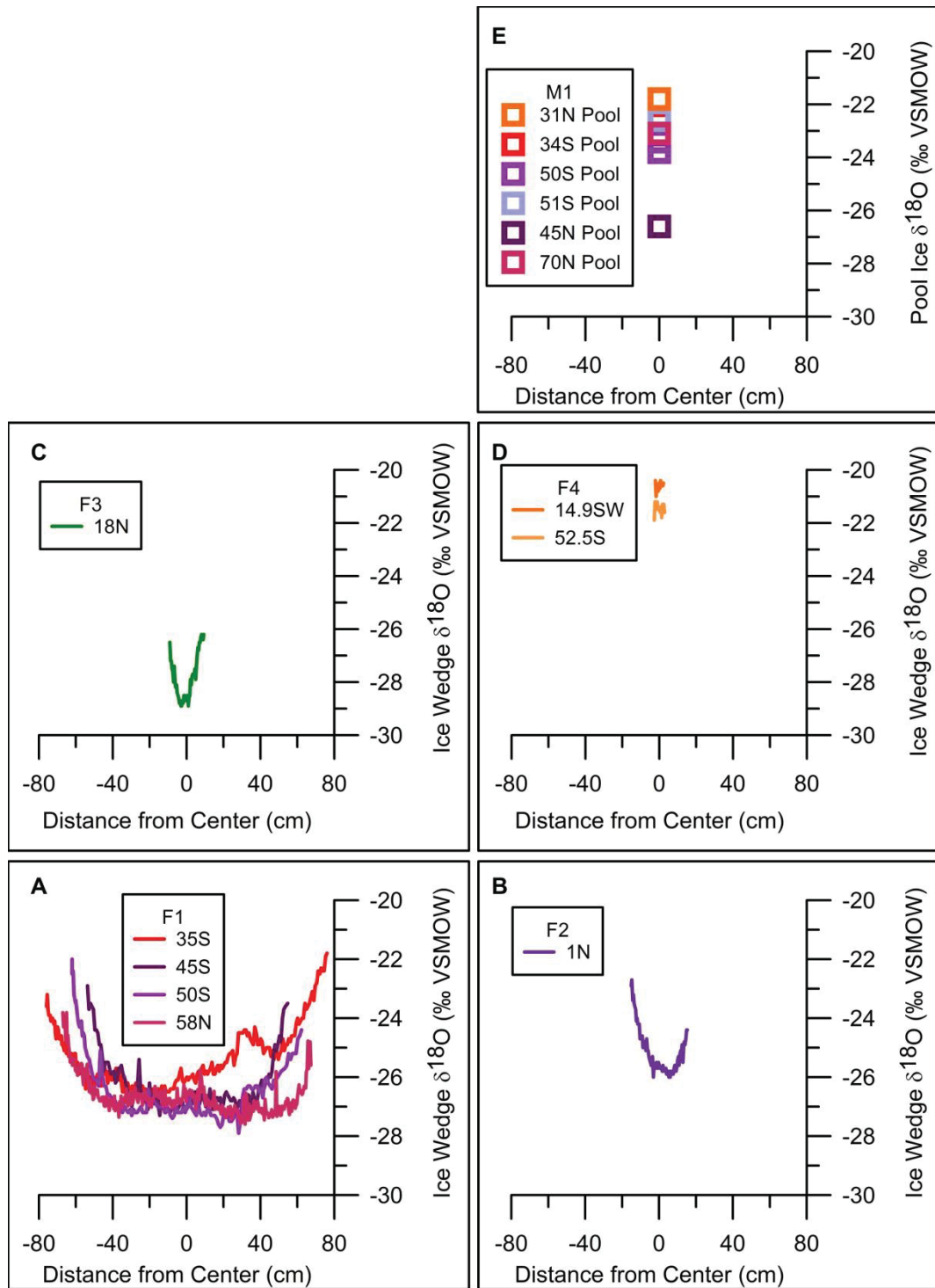


Figure 4.4.  $\delta^{18}\text{O}$  values from four freeze events and one melt event. Ice wedge and pool ice  $\delta^{18}\text{O}$  values of four freeze events (F1 - F4) and one melt event (M1) from the CRREL Permafrost Tunnel.



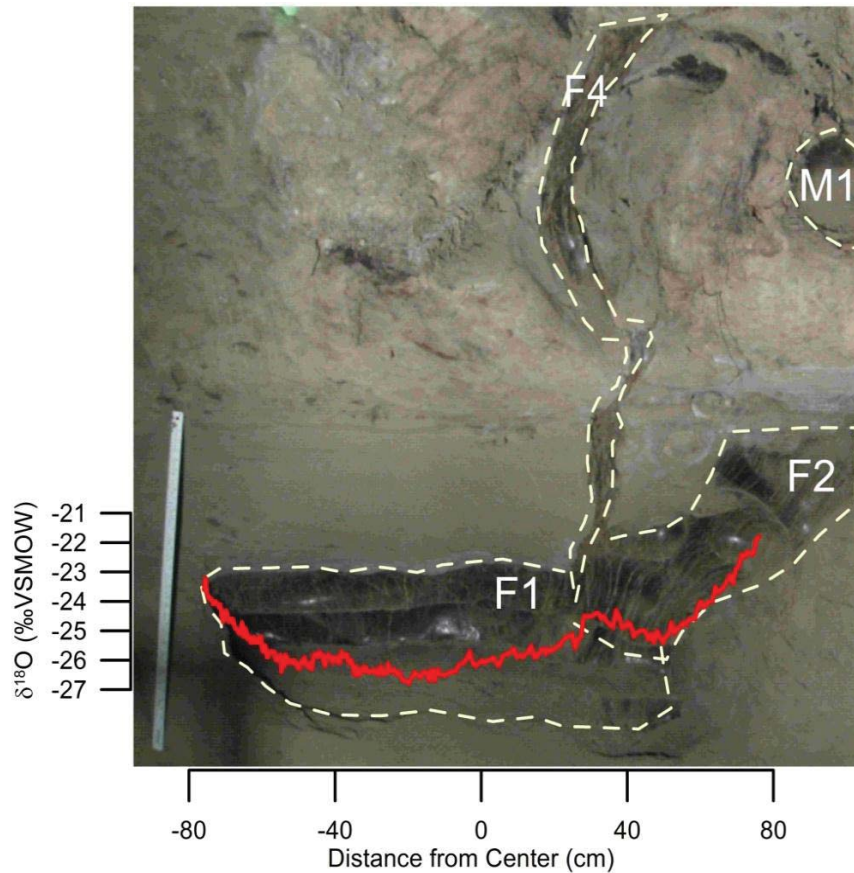


Figure 4.5. Freeze event 1 ice wedge 35S  $\delta^{18}\text{O}$  values. Freeze event 1 (F1) ice wedge (35S)  $\delta^{18}\text{O}$  values with secondary ice wedge apparent as isotopic deviation on right side of wedge. The secondary wedge is classified as F2 because it cross cuts the F1 wedge and therefore formed after the F1 wedge. The F2 wedge also has higher  $\delta^{18}\text{O}$  values, suggesting it formed under warmer climatic conditions compared to the F1 wedge. The pool ice in melt event 1 (M1) and wedge ice in freeze event 4 (F4) are also visible. Note meter stick for scale on left side of wedge.

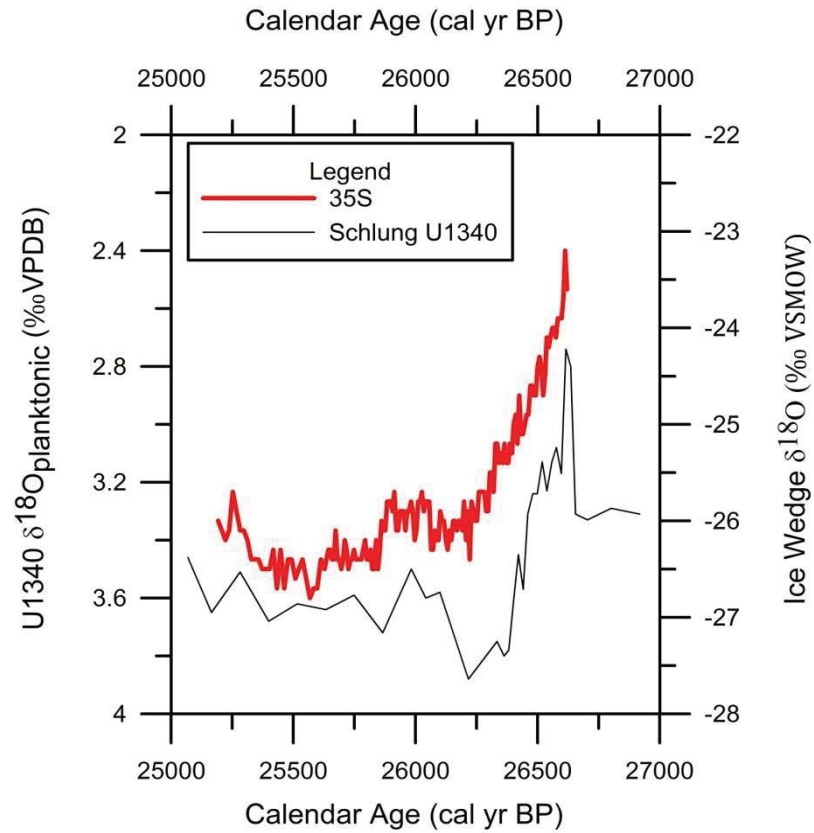


Figure 4.6. Wedge 35S high resolution  $\delta^{18}\text{O}$  record. The high resolution  $\delta^{18}\text{O}$  record for wedge 35S reveals small  $\sim 0.5\text{‰}$  fluctuations within the wedge that are similar to the larger fluctuations observed in the Bering Sea U1340 planktonic record (Schlung et al., 2013). However, the capability of radiocarbon dating prohibits correlating the wedge fluctuations with climate proxy data at such high resolution.



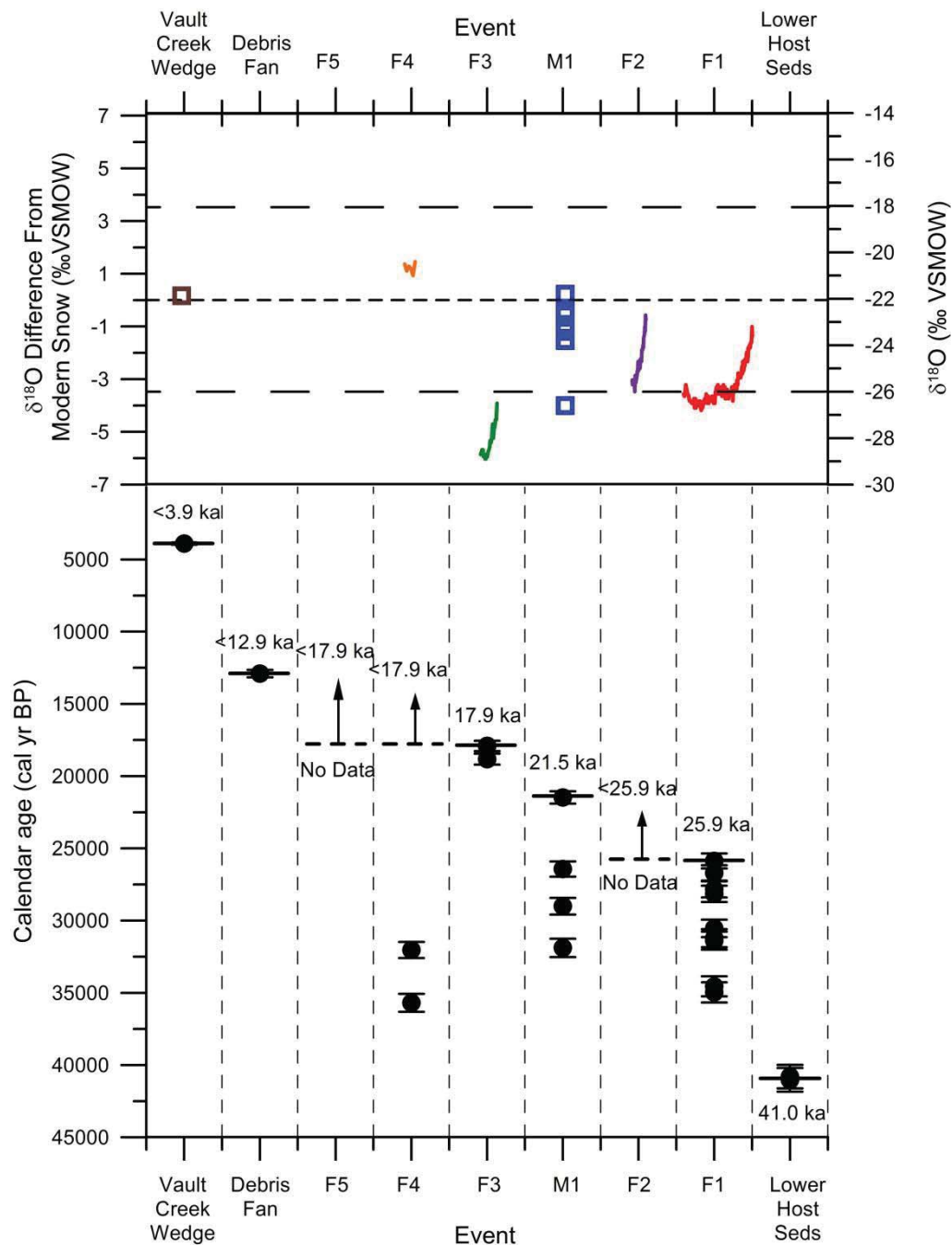


Figure 4.7. Freeze and melt events with  $\delta^{18}\text{O}$  values. Radiocarbon maximum limiting ages revealed at least five freeze events and one melt event in the CRREL Permafrost Tunnel. The  $\delta^{18}\text{O}$  values of tunnel ice wedges and pool ice values range between -28.9 and -20.5‰. The Holocene-aged ice wedge  $\delta^{18}\text{O}$  value of -21.8‰ from the Vault Creek Tunnel is consistent with mean modern Denali National Park snow  $\delta^{18}\text{O}$  values of -22.3‰ (small dashed line)  $\pm$  3.5‰ (large dashed line). The  $\delta^{18}\text{O}$  difference between modern snow and freeze and melt events ranges between -6.6 and +1.9‰.

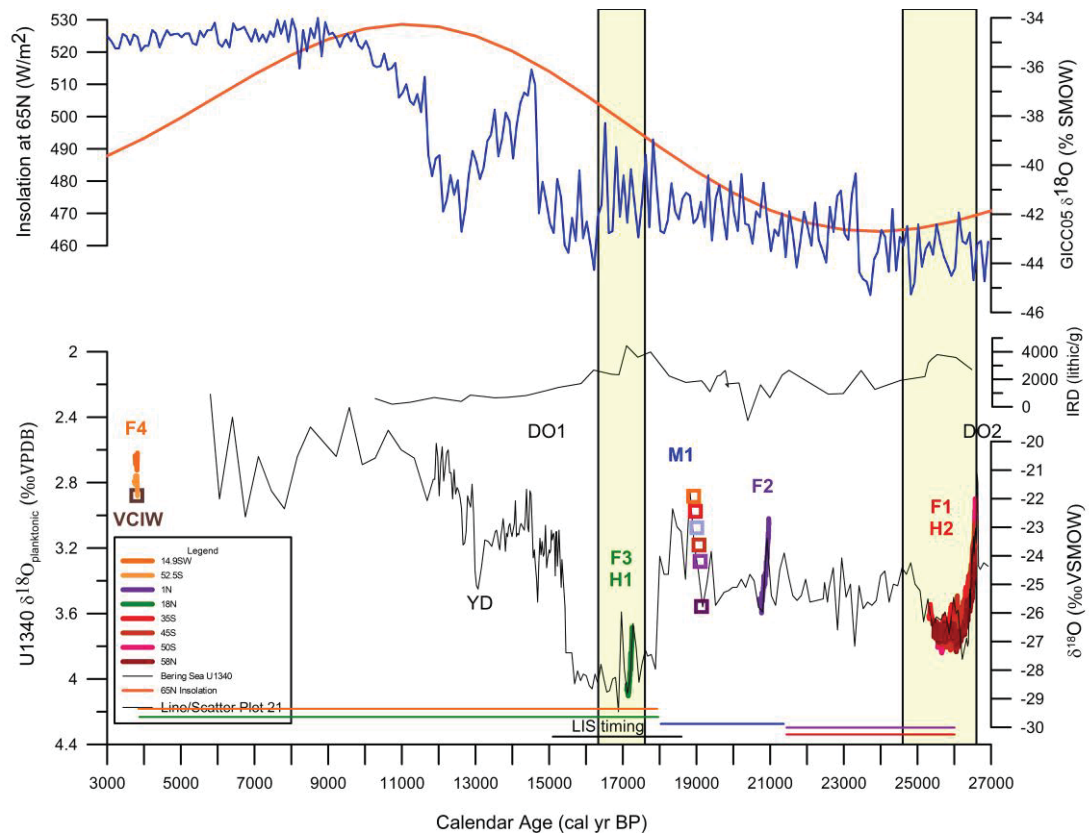


Figure 4.8. Tentative correlation of  $\delta^{18}\text{O}$  with Bering Sea SST record. The tentative correlation of  $\delta^{18}\text{O}$  for the four freeze events (F1 - F4) and one melt (M1) event with the Bering Sea U1340 record (Schlung et al., 2013), the IRD record (Bond et al., 1995), and the GICC05 record (Svensson et al., 2008). Colored bars corresponding to the colored F/M events show the large range of possible timing of formation for each F/M event estimated by  $^{14}\text{C}$  ages and stratigraphic position in the CRREL Permafrost Tunnel. The F1 (red) ice wedges (35S, 45S, 50S, and 58N) likely formed between 26.5 - 25.3 cal ka BP, or during Heinrich event 2 (yellow shaded bar). The F2 (purple) wedge (1N) likely formed between 21.0 - 20.5 cal ka BP. The M1 (squares) pool ice likely formed between 19.1 - 18.8 cal ka BP. The F3 (green) wedge (18N) likely formed between 17.3 - 17.0 cal ka BP, or during Heinrich event 1 (yellow shaded bar). The F4 (orange) wedges (14.9S Winze, 52.5S) likely formed around 3.6 cal ka BP, constrained in age by the isotopically similar Vault Creek Ice Wedge (VCIW). The timing of the Laurentide Ice Sheet (LIS) growth is indicated by a black bar, and the Dansgaard-Oeschger (DO) events 1 and 2 are shown. The long cold interval during the Last Glacial Maximum and onset of deglaciation after the Last Glacial Maximum (LGM) follows the insolation curve at 65°N latitude (Berger and Loutre, 1991) (orange curve).

Table 4.1. Pool ice stable isotope values.

<b>Sample ID</b>	<b><math>\delta^{18}\text{O}</math> (‰ VSMOW)</b>	<b><math>\delta\text{D}</math> (‰ VSMOW)</b>	<b>dx</b>
31N-Pool	-21.8	-175.6	-1.1
34S-Pool	-22.7	-178.7	2.5
45N-Pool	-26.6	-209.5	3.1
50S-Pool A	-23.8	-186.9	3.4
50S-Pool L	-23.4	-184.1	3.4
51S-Pool	-22.6	-179.7	1.4
70N-Pool	-23.1	-187.9	-3.2

Table 4.2.  $\delta^{18}\text{O}$  values and approximate paleotemperatures.

Freeze Melt Event	Wedge	Wedge $\delta^{18}\text{O}$ <sup>1</sup>		Wedge $\delta^{18}\text{O}$ from modern <sup>2</sup>		Tentative U1340 Correlated Age <sup>3</sup>	H Event	Equation 1: Isoscape DJFT Paleotemp (°C)		Paleo- DJFT (°C) <sup>4</sup>		Equation 2: Isoscape MAT Paleotemp (°C)		Paleo- MAT (°C)	
		Min	Max	Min	Max			DJFT = $\delta^{18}\text{O}/0.28$ ( $R^2 = 0.59$ )		Min	Max	MAT = $\delta^{18}\text{O}/0.55$ ( $R^2 = 0.61$ )		Min	Max
F4	14.9S Winze	-21.9	-20.4	0.4	1.9	3.9	N/A	1.4	6.8	-16.6	-11.2	0.7	3.5	-1.4	1.4
	52.5S														
F3	18N	-28.9	-26.2	-6.6	-3.9	17.3 - 17.0	H1	-23.6	-13.9	-41.6	-31.9	-12.0	-7.1	-14.1	-9.2
	31N-Pool	-21.8	-21.8	0.5	0.5			1.8	1.8	-16.2	-16.2	0.9	0.9	-1.2	-1.2
	34S-Pool	-22.7	-22.7	-0.4	-0.4			-1.4	-1.4	-19.4	-19.4	-0.7	-0.7	-2.8	-2.8
	45N-Pool	-26.6	-26.6	-4.3	-4.3			-15.4	-15.4	-33.4	-33.4	-7.8	-7.8	-9.9	-9.9
M1	50S-PoolA	-23.8	-23.8	-1.5	-1.5	19.1 - 18.8	N/A	-5.4	-5.4	-23.4	-23.4	-2.7	-2.7	-4.8	-4.8
	50S-PoolL	-23.4	-23.4	-1.1	-1.1			-3.9	-3.9	-21.9	-21.9	-2.0	-2.0	-4.1	-4.1
	51S-Pool	-22.6	-22.6	-0.3	-0.3			-1.1	-1.1	-19.1	-19.1	-0.5	-0.5	-2.6	-2.6
	70N-Pool	-23.1	-23.1	-0.8	-0.8			-2.9	-2.9	-20.9	-20.9	-1.5	-1.5	-3.6	-3.6
F2	1N	-26.0	-22.7	-3.7	-0.4	21.0 - 20.5	N/A	-13.2	-1.4	-31.2	-19.4	-6.7	-0.7	-8.8	-2.8
	35S														
F1	45S	-27.9	-21.8	-5.6	0.5	26.5 - 25.3	H2	-20.0	1.8	-38.0	-16.2	-10.2	0.9	-12.3	-1.2
	50S														
	58N														

<sup>1</sup> All  $\delta^{18}\text{O}$  values reported in ‰ VSMOW.

<sup>2</sup> Modern winter  $\delta^{18}\text{O}$  value from Denali National Park = -22.3‰ (USNIP, 2011)

<sup>3</sup> All  $^{14}\text{C}$  ages were calibrated to calendar years before present (cal yr BP) (present = 1950 A.D) using IntCal09 calibration curve at the 68.2% probability level, and are reported in calendar years before present (cal ka BP).

<sup>4</sup> Paleo-DJFT T (°C) = the Isoscape DJFT paleotemp - modern DJFT from Fox, AK, which averages -18°C (NCDC, 2010).

<sup>5</sup> Paleo-MAT (°C) = the Isoscape MAT paleotemp - modern MAT from Fox, AK, which averages -2.1°C (NCDC, 2010).

Table 4.3.  $\delta^{18}\text{O}$  values and approximate correlated ages of sampled ice wedges.

Freeze Melt Event	Wedge	$\delta^{18}\text{O}$				Range			$^{14}\text{C}$		Tentative U1340		$\delta^{18}\text{O}$ Difference from Modern Snow	
		Min	Max	Mean		$\delta^{18}\text{O}^1$			Age <sup>2</sup>	Error	Age <sup>3</sup>	Event	H	
		$\delta^{18}\text{O}^1$	$\delta^{18}\text{O}^1$	$\delta^{18}\text{O}^1$										(‰ VSMOW) <sup>4</sup>
F4	14.9S Winze	-21.0	-20.4	-20.6	0.6				32030	±400	14.5 - 14.3	N/A	0.4	1.9
	52.5S	-21.9	-21.2	-21.5	0.7				35690	±450				
F3	18N	-28.9	-26.2	-27.8	2.7				17910	±210	17.3 - 17.0	H1	-6.6	-3.9
M1	31N-Pool	-21.8	-21.8	-21.8	N/A				N/A					
	34S-Pool	-22.7	-22.7	-22.7	N/A				21470	±200				
	45N-Pool	-26.6	-26.6	-26.6	N/A				N/A					
	50S-PoolA	-23.8	-23.8	-23.8	N/A				31890	±380	19.1 - 18.8	N/A	-4.3	0.5
	50S-PoolL	-23.4	-23.4	-23.4	N/A				N/A					
F2	51S-Pool	-22.6	-22.6	-22.6	N/A				29000	±260				
	70N-Pool	-23.1	-23.1	-23.1	N/A				N/A					
	1N	-26.0	-22.7	-25.1	3.3				30220	±310	21.0 - 20.5	N/A	-3.7	-0.4
	35S	-26.8	-21.8	-25.4	5.0				34970	±460				
F1	45S	-27.3	-22.9	-26.2	4.4				N/A		26.5 - 25.3	H2	-5.6	0.5
	50S	-27.9	-22.0	-26.3	5.9				25870	±270				
	58N	-27.6	-23.8	-26.7	3.8				26700	±390				

<sup>1</sup> All  $\delta^{18}\text{O}$  values reported in ‰ VSMOW.

<sup>2</sup> All  $^{14}\text{C}$  ages were calibrated to calendar years before present (cal yr BP) (present = 1950 A.D) using IntCal09 calibration curve at the 68.2% probability level.

<sup>3</sup> Reported in calibrated thousand calendar years before present (cal ka BP).

<sup>4</sup> Mean modern Denali National Park snow value is  $-22.3 \pm 3.5\text{‰}$ .

## Appendix A: Surface water sampling data

Sample ID	$\delta^{18}\text{O}$ (‰ SMOW)	$\delta\text{D}$ (‰ SMOW)	$d$	Sample Date	Sample Latitude	Sample Longitude	Sample Alt (m)	GI (G) Non (N) Perm (P)	Creek Name
AK001	-20.71	-151.4	14.2	8/6/2008	64.94915	-147.68190	213	P	Goldstream Creek
AK002	-19.65	-146.2	11.0	8/6/2008	64.86903	-147.81925	146	P	Pond Farmers Loop
AK003	-22.93	-166.6	16.8	8/6/2008	64.73972	-147.98578	244	P	Fox Spring
AK004	-17.42	-125.8	13.5	8/7/2009	64.83355	-147.64540	155	P	Chena River
AK005	-17.94	-126.5	17.0	8/7/2009	64.78956	-147.71464	174	P	Tanana River
AK006	-21.84	-167.5	7.2	7/3/2009	63.43249	-150.30830	1149	G	Toklat River
AK007	-20.13	-152.9	8.2	7/3/2009	63.43227	-150.30678	1154	G	Eielson #1
AK008	-20.36	-150.5	12.4	7/3/2009	63.52151	-150.04333	920	G	Eielson #2
AK009	-20.05	-155.5	4.9	7/4/2009	65.14243	-147.42030	219	P	Captain Creek
AK010	-20.07	-155.6	5.0	7/4/2009	65.15611	-147.34235	230	P	Chatanika Creek
AK011	-20.10	-155.3	5.5	7/4/2009	65.17451	-147.28357	241	P	Kokomo Creek
AK012	-20.10	-155.4	5.4	7/4/2009	65.20431	-147.22688	260	P	Crooked Creek
AK013	-19.53	-156.3	-0.1	7/4/2009	65.21278	-147.19708	245	P	Belle Creek
AK014	-21.96	-165.8	9.8	7/5/2009	63.25217	-145.43394	1213	G	Phelan River
AK015	-21.89	-164.4	10.7	7/5/2009	63.23166	-145.47708	1099	G	College Creek
AK016	-21.98	-165.5	10.3	7/5/2009	63.22945	-145.62840	945	G	McCallum Creek
AK017	-21.83	-165.1	9.5	7/5/2009	63.24178	-145.67413	877	N	Unnamed Spring
AK018	-22.38	-164.1	14.9	7/5/2009	63.27522	-145.65884	844	N	Unnamed Creek
AK019	-22.03	-166.1	10.2	7/5/2009	63.37391	-145.73116	777	G	Miller Creek
AK020	-22.92	-172.1	11.3	7/5/2009	63.40277	-145.73566	769	G	Castner Creek
AK021	-22.20	-167.7	9.9	7/5/2009	63.49509	-145.85971	725	N	Upper Suzy Q Creek
AK022	-21.78	-167.1	7.2	7/5/2009	63.67733	-145.88490	549	N	Donnelly Creek
AK024	-22.61	-174.0	6.9	7/6/2009	64.05367	-145.43317	336	N	Clearwater River
AK025	-23.04	-176.5	7.8	7/6/2009	64.15628	-145.84885	308	G	Tanana River
AK026	-20.63	-157.5	7.5	7/6/2009	64.26177	-146.10823	300	N	Shaw Creek
AK027	-21.29	-160.0	10.3	7/6/2009	64.47042	-146.93086	228	N	Salcha River
AK028	-20.39	-153.3	9.8	7/7/2009	64.94740	-147.67459	215	P	Goldstream Creek
AK029	-19.97	-153.6	6.2	7/7/2009	64.94486	-147.79881	214	P	Big El Dorado Creek
AK030	-20.11	-154.6	6.3	7/7/2009	65.10150	-147.74963	185	P	Willow Creek
AK031	-19.99	-153.9	6.0	7/7/2009	65.14951	-147.86188	272	P	Washington Creek
AK032	-19.84	-152.0	6.8	7/7/2009	65.15916	-147.91362	304	P	Cushman Creek
AK033	-20.35	-151.7	11.1	7/7/2009	65.27734	-148.13147	219	P	Globe Creek
AK034	-19.41	-151.5	3.8	7/7/2009	65.32811	-148.31245	153	P	Tatalina River
AK035	-19.79	-154.2	4.1	7/7/2009	65.47114	-148.26834	199	P	Tolovana River
AK036	-20.33	-156.3	6.4	7/7/2009	65.51673	-148.80309	201	P	Lost Creek
AK037	-21.02	-159.8	8.4	7/7/2009	65.66551	-149.09686	164	P	Hess Creek
AK038	-22.24	-166.2	11.8	7/7/2009	65.73690	-149.29343	197	P	Unnamed Creek
AK039	-21.68	-170.2	3.2	7/7/2009	65.87878	-149.72064	91	P	Yukon River
AK040	-19.82	-155.3	3.3	7/7/2009	65.46545	-148.34135	191	P	Tolovana River
AK041	-19.54	-152.2	4.1	7/8/2009	65.26733	-146.72548	368	P	U.S. Creek
AK042	-19.55	-151.0	5.4	7/8/2009	65.28986	-146.47977	436	P	Sourdough Creek
AK043	-20.57	-154.9	9.7	7/8/2009	65.29047	-146.38197	449	P	Faith Creek
AK044	-20.41	-158.0	5.3	7/8/2009	65.35357	-146.16273	595	P	Idaho Creek
AK045	-20.12	-155.0	6.0	7/8/2009	65.35400	-146.12164	636	P	Unnamed Spring
AK046	-21.00	-156.6	11.3	7/8/2009	65.36054	-146.08932	659	P	Montana Creek
AK047	-20.72	-155.0	10.8	7/8/2009	65.36777	-146.07158	674	P	Unnamed Spring
AK048	-20.03	-155.5	4.8	7/8/2009	65.41107	-145.88774	740	P	Twelvemile Creek
AK049	-20.39	-158.2	5.0	7/8/2009	64.41113	-145.88753	738	P	Reed Creek
AK050	-20.42	-159.1	4.3	7/8/2009	65.40044	-145.74062	621	P	North Fork 12 Mile Ck
AK051	-21.02	-162.6	5.5	7/8/2009	65.43953	-145.52754	715	P	Ptarmigan Creek
AK052	-21.50	-165.6	6.4	7/8/2009	65.55009	-145.17642	486	P	Mammoth Creek
AK053	-21.54	-167.3	5.1	7/8/2009	65.57117	-144.88445	336	P	Boulder Creek



Sample ID	$\delta^{18}\text{O}$ (‰ SMOW)	$\delta\text{D}$ (‰ SMOW)	$d$	Sample Date	Sample Latitude	Sample Longitude	Sample Alt (m)	GI (G) Non (N) Perm (P)	Creek Name
AK054	-21.43	-165.7	5.8	7/8/2009	65.57213	-144.80103	293	P	Crooked Creek
AK055	-20.49	-162.3	1.6	7/8/2009	65.59093	-144.70314	271	P	Albert Creek
AK056	-21.03	-163.1	5.1	7/8/2009	65.61884	-144.48416	241	P	Quartz Creek
AK057	-20.66	-161.5	3.8	7/8/2009	65.64067	-144.42215	213	P	Birch Creek
AK058	-21.59	-167.6	5.1	7/8/2009	65.82542	-144.06052	184	P	Yukon River
AK059	-20.07	-155.7	4.8	7/8/2009	64.83084	-147.84874	202	P	Chena River
AK060	-20.49	-156.2	7.7	7/1/2009	64.95728	-146.23825	266	P	Chena River
AK061	-19.99	-156.4	3.5	7/1/2009	65.05055	-146.04962	380	P	Chena Hot Springs
AK062	-21.87	-164.9	10.1	7/2/2009	64.34371	-149.21217	157	G	Nenana River
AK065	-21.57	-162.0	10.5	7/2/2009	63.65623	-148.83611	556	G	Nenana River
AK066	-21.46	-162.0	9.7	7/5/2009	63.74038	-149.29222	787	P	Savage River
AK067	-20.73	-157.8	8.1	7/12/2009	64.96404	-147.62553	247	P	Fox Spring
AK068	-20.43	-154.7	8.7	7/12/2009	64.96409	-147.62524	252	P	Unnamed Creek
AK069	-19.34	-147.1	7.6	7/19/2009	64.70893	-148.50883	231	P	Bonanza Creek
AK070	-18.82	-146.7	3.9	7/19/2009	64.66523	-148.94447	124	P	Little Goldstream Ck
AK071	-23.05	-175.6	8.8	7/19/2009	64.56499	-148.09364	116	P	Tanana River
AK072	-18.77	-146.9	3.3	7/19/2009	64.45837	-149.05109	135	P	Fish Creek
AK073	-19.18	-145.3	8.2	7/19/2009	64.31264	-149.05824	174	P	Julius Creek
AK074	-20.26	-151.3	10.7	7/19/2009	64.13432	-149.25461	270	P	Bear Creek
AK075	-19.79	-148.7	9.6	7/19/2009	63.91357	-149.08372	413	P	Panguingue Creek
AK076	-20.45	-153.9	9.7	7/19/2009	63.80489	-148.95302	526	N	Bison Gulch
AK077	-20.34	-156.9	5.8	7/19/2009	63.78028	-148.90945	458	N	Fox Creek
AK078	-21.44	-162.2	9.3	7/19/2009	63.72766	-148.88785	488	G	Riley Creek
AK079	-21.54	-161.6	10.8	7/19/2009	63.56559	-148.81711	625	G	Carlo Creek
AK080	-21.87	-164.5	10.4	7/19/2009	63.38611	-148.90869	662	N	Jack River
AK081	-21.55	-162.3	10.1	7/19/2009	63.25109	-149.25548	673	N	Middle Fork Chulitna
AK082	-21.26	-159.1	11.0	7/19/2009	63.14523	-149.42184	549	N	East Fork Chulitna
AK083	-20.44	-153.5	10.0	7/19/2009	63.06409	-149.54472	479	N	Honolulu Creek
AK084	-19.87	-147.7	11.2	7/19/2009	62.97603	-149.63133	537	N	Granite Creek
AK085	-19.06	-143.9	8.6	7/19/2009	62.71241	-150.20486	216	N	Byers Creek
AK086	-18.54	-140.2	8.1	7/19/2009	62.62703	-150.22778	184	N	Troublesome Creek
AK087	-18.83	-140.3	10.3	7/19/2009	62.56539	-150.23244	163	G	Chulitna River
AK088	-22.89	-170.8	12.3	7/19/2009	62.56539	-150.23232	179	N	Creek nr Chulitna
AK089	-18.02	-136.2	7.9	7/19/2009	62.31623	-150.44473	151	N	Moose Creek
AK090	-17.47	-135.2	4.6	7/19/2009	62.34756	-150.62399	268	N	Kroto Creek
AK091	-17.65	-135.6	5.6	7/19/2009	62.35429	-150.66357	322	N	Twentymile Creek
AK092	-19.96	-148.9	10.7	7/19/2009	62.37360	-150.73772	351	N	Peters Creek
AK093	-22.47	-169.4	10.3	7/19/2009	62.17551	-150.17906	87	G	Susitna River
AK094	-17.73	-135.6	6.3	7/19/2009	62.20237	-150.06735	114	N	Answer Creek
AK095	-21.77	-165.3	8.9	7/19/2009	62.32298	-150.12265	110	G	Talkeetna River
AK096	-18.62	-141.2	7.7	7/19/2009	62.10439	-150.06026	74	N	Montana Creek
AK097	-19.86	-150.4	8.5	7/19/2009	61.99631	-150.05347	69	G	Sheep Creek
AK098	-20.41	-153.9	9.4	7/19/2009	61.92387	-150.07106	65	G	Kashwitna River
AK099	-18.62	-141.5	7.4	7/19/2009	61.80999	-150.09818	41	N	Little Willow Creek
AK100	-19.12	-144.2	8.8	7/19/2009	61.76761	-150.06702	50	N	Willow Creek
AK101	-19.36	-143.6	11.3	7/19/2009	61.62678	-149.80122	81	G	Little Susitna River

Sample ID	$\delta^{18}\text{O}$ (‰ SMOW)	$\delta\text{D}$ (‰ SMOW)	$d$	Sample Date	Sample Latitude	Sample Longitude	Sample Alt (m)	GI (G) Non (N) Perm (P)	Creek Name
AK102	-23.41	-175.4	11.9	7/20/2009	61.60843	-149.07463	66	G	Matanuska River
AK103	-22.56	-170.4	10.1	7/20/2009	61.56388	-149.04321	47	N	Bodenburg Creek
AK104	-20.74	-153.4	12.5	7/20/2009	61.50356	-149.03217	26	G	Knik River
AK105	-21.03	-155.9	12.3	7/20/2009	61.48824	-149.09949	19	N	Goat Creek
AK106	-20.26	-152.8	9.3	7/20/2009	61.40889	-149.13455	270	N	Eklutna Creek
AK108	-20.48	-154.2	9.7	7/20/2009	61.40859	-149.13518	268	N	Eklutna Spring
AK109	-20.58	-155.6	9.1	7/20/2009	61.44992	-149.36981	47	N	Eklutna River
AK110	-20.80	-154.5	11.9	7/20/2009	61.40385	-149.45717	95	G	Peters Creek
AK111	-19.86	-147.9	11.0	7/20/2009	61.31023	-149.58092	82	G	Eagle River
AK112	-18.82	-138.9	11.7	7/20/2009	61.01678	-149.73120	6	N	McHugh Creek
AK113	-18.47	-135.1	12.7	7/20/2009	60.98436	-149.57614	15	N	Falls Creek
AK114	-18.59	-137.2	11.5	7/20/2009	60.93855	-149.16716	7	G	Glacier Creek
AK115	-17.27	-125.4	12.8	7/20/2009	60.84558	-148.99020	10	G	Twentymile River
AK117	-15.89	-111.6	15.5	7/20/2009	60.79255	-148.90379	21	N	Unnamed Ck Portage
AK118	-16.25	-114.6	15.4	7/20/2009	60.79721	-148.91209	21	G	Portage River
AK119	-17.19	-122.6	14.9	7/20/2009	60.81707	-148.98875	16	G	Placer River
AK120	-18.36	-130.6	16.3	7/20/2009	60.72739	-149.28680	202	G	Granite Creek
AK121	-19.43	-142.0	13.5	7/20/2009	60.59944	-149.54126	395	N	Quartz Creek
AK122	-18.97	-140.2	11.6	7/20/2009	60.49027	-149.69809	168	N	Crescent Creek
AK123	-17.65	-130.6	10.7	7/20/2009	60.49269	-149.80975	131	G	Kenai River
AK124	-18.55	-136.0	12.4	7/20/2009	60.48267	-149.88094	131	N	Cooper Creek
AK125	-17.66	-130.8	10.6	7/20/2009	60.48180	-149.97417	107	N	Russian River
AK126	-15.88	-123.5	3.6	7/20/2009	60.53677	-150.75499	49	N	Moose River
AK127	-16.41	-121.0	10.3	7/20/2009	60.31691	-151.25851	12	G	Kasilof River
AK128	-17.28	-128.9	9.4	7/20/2009	60.30209	-151.27180	24	N	Crooked Creek
AK129	-16.67	-123.7	9.7	7/20/2009	60.04828	-151.66420	5	N	Ninilchik River
AK130	-16.50	-122.1	9.9	7/20/2009	60.03293	-151.70050	3	N	Deep Creek
AK131	-15.20	-115.9	5.6	7/20/2009	59.85183	-151.79167	25	N	Stariski Creek
AK132	-15.89	-116.7	10.4	7/20/2009	59.77202	-151.83664	16	N	Anchor River
AK134	-18.08	-132.0	12.7	7/21/2009	60.50128	-149.43198	148	N	Moose Creek
AK136	-19.18	-141.0	12.5	7/21/2009	60.43028	-149.37103	147	G	Falls Creek
AK137	-18.27	-134.5	11.7	7/21/2009	60.40463	-149.36412	137	G	Plarmigan Creek
AK138	-18.58	-136.3	12.3	7/21/2009	60.38046	-149.35196	151	N	Rocky Creek
AK139	-18.01	-130.8	13.3	7/21/2009	60.35668	-149.3499	151	G	Victor Creek
AK140	-15.73	-115.1	10.8	7/21/2009	60.31042	-149.36029	146	N	Snow River Hotel Ck
AK141	-16.05	-116.9	11.5	7/21/2009	60.17855	-149.39507	52	N	Salmon Creek
AK142	-16.42	-118.1	13.3	7/21/2009	60.15305	-149.43539	24	G	Resurrection River
AK143	-17.28	-124.1	14.2	7/21/2009	60.33298	-149.35313	136	G	Snow River
AK144	-17.94	-133.2	10.4	7/21/2009	60.81405	-149.43311	99	G	Sixmile Creek
AK145	-18.23	-136.6	9.2	7/21/2009	60.84936	-149.43658	79	N	Old Woman Creek
AK146	-17.96	-133.9	9.7	7/21/2009	60.90108	-149.44057	41	N	Sunset Creek
AK147	-17.94	-133.0	10.5	7/21/2009	60.91873	-149.62161	42	N	Bear Creek
AK148	-18.66	-139.4	9.9	7/21/2009	60.92101	-149.64557	7	N	Resurrection Creek
AK149	-18.70	-142.1	7.5	7/21/2009	60.77958	-149.42966	136	N	Canyon Creek
AK150	-19.55	-149.4	7.0	7/22/2009	61.68217	-149.04825	109	N	Moose Creek
AK151	-19.53	-148.9	7.3	7/22/2009	61.71047	-148.89923	157	N	Eska Creek



Sample ID	$\delta^{18}\text{O}$ (‰ SMOW)	$\delta\text{D}$ (‰ SMOW)	$d$	Sample Date	Sample Latitude	Sample Longitude	Sample Alt (m)	GI (G) Non (N) Perm (P)	Creek Name
AK152	-21.72	-162.1	11.6	7/22/2009	61.73241	-148.75227	173	G	Kings River
AK153	-22.11	-169.3	7.5	7/22/2009	61.78578	-148.45395	270	G	Chickaloon River
AK155	-20.49	-159.4	4.5	7/22/2009	61.81225	-148.15416	619	N	Unnamed Creek
AK156	-20.83	-161.2	5.4	7/22/2009	61.81218	-148.1539	618	N	Purinton Creek
AK157	-21.42	-166.0	5.4	7/22/2009	61.79113	-147.93637	423	G	Hicks Creek
AK158	-23.43	-180.1	7.3	7/22/2009	61.79480	-147.78917	468	G	E. Fork Matanuska
AK159	-24.11	-183.5	9.4	7/22/2009	61.77723	-147.77139	485	G	Matanuska River
AK160	-21.47	-167.8	3.9	7/22/2009	61.80237	-147.68547	569	G	Caribou Creek
AK161	-22.45	-176.0	3.6	7/22/2009	61.83595	-147.40619	983	N	Camp Creek
AK162	-21.31	-167.8	2.7	7/22/2009	61.98957	-146.94591	740	G	Little Nelchina River
AK163	-22.35	-172.9	5.9	7/22/2009	62.02241	-146.71231	714	P	Cash Creek
AK164	-19.32	-159.5	-4.9	7/22/2009	62.04917	-146.54341	676	P	Mendeltna Creek
AK165	-17.63	-153.0	-12.0	7/22/2009	62.10064	-145.96858	577	P	Tolsona River
AK166	-16.59	-145.7	-13.0	7/22/2009	62.10981	-145.55855	454	P	Moose Creek
AK167	-21.15	-163.8	5.4	7/22/2009	62.05426	-145.42822	362	G	Tazlina River
AK168	-20.62	-159.6	5.3	7/22/2009	61.95238	-145.29568	322	G	Klutina River
AK169	-20.98	-165.6	2.3	7/22/2009	61.81709	-145.21571	436	P	Willow Creek
AK170	-21.32	-165.2	5.4	7/22/2009	61.66749	-145.17683	467	N	Squirrel Creek
AK171	-21.15	-161.5	7.7	7/22/2009	61.66280	-145.18222	465	G	Tonsina River
AK172	-20.89	-154.5	12.6	7/22/2009	61.43344	-145.11954	530	G	Tiekel River
AK173	-21.36	-162.4	8.5	7/22/2009	61.40210	-145.18575	485	N	Squaw Creek
AK174	-20.48	-156.5	7.3	7/22/2009	61.36262	-145.28093	420	N	Unnamed Creek
AK175	-20.69	-157.2	8.3	7/22/2009	61.33337	-145.31133	413	N	Boulder Creek
AK176	-20.15	-153.2	8.0	7/22/2009	61.25877	-145.28337	357	G	Stuart Creek
AK177	-19.06	-144.1	8.4	7/22/2009	61.24120	-145.34518	382	G	Tsaina River
AK178	-19.04	-144.6	7.7	7/22/2009	61.20230	-145.53729	506	G	Unnamed Creek
AK179	-18.52	-140.5	7.7	7/22/2009	61.19786	-145.55394	502	G	Unnamed Creek
AK180	-18.67	-141.7	7.7	7/22/2009	61.18798	-145.62111	539	G	Unnamed Creek
AK181	-18.35	-137.1	9.7	7/22/2009	61.16689	-145.70457	651	G	Worthington Glacier
AK182	-18.72	-140.4	9.4	7/22/2009	61.11223	-145.81183	199	G	Sheep Creek
AK183	-18.73	-142.3	7.5	7/22/2009	61.09639	-145.86697	143	G	Lowe River
AK184	-18.84	-142.2	8.6	7/22/2009	61.10996	-146.23705	24	G	Valdez Glacier Ck
AK185	-18.38	-138.6	8.5	7/23/2009	61.11731	-146.26784	2	N	Old Valdez Creek
AK186	-17.63	-132.2	8.8	7/23/2009	61.08268	-146.24074	16	G	Abercrombie Creek
AK187	-16.23	-125.1	4.8	7/23/2009	61.08278	-146.32869	16	N	Allison Creek
AK188	-16.95	-128.5	7.1	7/23/2009	61.08471	-146.26524	8	N	Unnamed Creek
AK189	-17.83	-134.5	8.1	7/23/2009	61.06737	-145.90666	141	N	Horsetail Falls
AK190	-20.92	-160.7	6.7	7/23/2009	61.47974	-145.15350	555	N	Little Tonsina River
AK191	-21.80	-169.2	5.2	7/23/2009	61.63125	-144.58655	333	N	Unnamed Creek
AK192	-22.32	-167.4	11.1	7/23/2009	61.62149	-144.54776	350	N	Liberty Creek
AK193	-21.49	-164.4	7.5	7/23/2009	61.58195	-144.43880	227	N	Fivemile Creek
AK194	-21.47	-164.4	7.4	7/23/2009	61.52508	-144.41426	166	G	Copper River
AK195	-18.03	-148.8	-4.6	7/23/2009	62.15200	-145.47720	488	N	Dry Creek
AK196	-18.47	-152.3	-4.5	7/23/2009	62.26484	-145.41107	468	N	Bear Creek
AK197	-18.75	-152.1	-2.1	7/23/2009	62.26943	-145.38470	430	G	Gulkana River
AK198	-20.90	-159.6	7.5	7/23/2009	62.30141	-145.30669	446	G	Gakona River

Sample ID	$\delta^{18}\text{O}$ (‰ SMOW)	$\delta\text{D}$ (‰ SMOW)	$d$	Sample Date	Sample Latitude	Sample Longitude	Sample Alt (m)	GI (G) Non (N) Perm (P)	Creek Name
AK199	-16.37	-144.6	-13.6	7/23/2009	62.41645	-145.39064	569	P	Poplar Grove Creek
AK200	-17.67	-147.7	-6.3	7/23/2009	62.52903	-145.51567	591	P	Sourdough Creek
AK201	-18.70	-150.0	-0.4	7/23/2009	62.69657	-145.44893	738	P	Haggard Creek
AK202	-21.18	-162.9	6.6	7/23/2009	62.93793	-145.51103	806	P	Huffman Creek
AK203	-20.31	-158.5	4.0	7/23/2009	63.10123	-145.49184	994	N	Gulkana River
AK204	-20.56	-160.9	3.5	7/23/2009	63.10197	-145.49065	1000	N	Fish Creek
AK205	-20.95	-161.8	5.8	7/23/2009	63.17017	-145.53220	997	N	Gunn Creek
AK206	-20.96	-159.7	8.0	7/23/2009	63.26352	-145.68427	846	G	Delta River
AK207	-21.09	-160.1	8.6	7/23/2009	63.52431	-145.85420	666	G	Gunnysack Creek
AK208	-21.06	-162.4	6.1	7/23/2009	63.61320	-145.86426	645	G	Bear Creek
AK209	-20.81	-161.6	4.9	7/23/2009	64.02341	-145.72508	370	N	Jarvis Creek
AK211	-22.81	-174.0	8.5	7/25/2009	63.81767	-144.91299	413	G	Gerstle River
AK212	-22.88	-172.4	10.7	7/25/2009	63.78733	-144.79355	405	G	Little Gerstle River
AK213	-21.73	-166.8	7.1	7/25/2009	63.70271	-144.63985	432	G	Johnson River
AK214	-21.57	-166.7	5.9	7/25/2009	63.68709	-144.46362	419	N	Sears Creek
AK215	-21.25	-164.8	5.2	7/25/2009	63.69219	-144.36964	426	N	Berry Creek
AK216	-21.59	-166.9	5.8	7/25/2009	63.61501	-143.98630	471	G	Bear Creek
AK217	-21.37	-163.2	7.8	7/25/2009	63.49591	-143.83548	490	G	Robertson River
AK218	-21.31	-164.1	6.4	7/25/2009	63.38248	-143.59595	524	N	Yerrick Creek
AK219	-21.72	-168.3	5.5	7/25/2009	63.32602	-142.83548	505	G	Tok River
AK220	-20.92	-164.6	2.8	7/25/2009	63.05262	-141.85347	529	P	Beaver Creek
AK221	-20.31	-160.0	2.5	7/25/2009	63.03939	-141.82590	538	P	Unnamed Creek
AK222	-22.85	-177.2	5.6	7/25/2009	63.00670	-141.80682	530	P	Chisana River
AK223	-22.27	-175.0	3.2	7/25/2009	62.98022	-141.83081	530	P	Fish Camp Creek
AK224	-24.32	-186.2	8.4	7/25/2009	62.97808	-141.95702	529	P	Nebesna River
AK225	-20.18	-165.7	-4.3	7/25/2009	62.96846	-141.90370	549	P	Moose Creek
AK226	-19.52	-160.2	-4.1	7/25/2009	62.85360	-141.45978	549	P	Gardiner Creek
AK227	-19.19	-158.3	-4.8	7/25/2009	62.66324	-141.05751	561	P	Despert Creek
AK228	-20.22	-161.7	0.1	7/25/2009	62.63874	-141.02905	567	P	Scottie Creek
AK229	-22.06	-173.8	2.7	7/26/2009	62.36431	-140.86577	677	P	Beaver Creek
AK230	-19.09	-156.0	-3.2	7/26/2009	62.30365	-140.79019	728	P	Enger Creek
AK231	-19.93	-163.1	-3.7	7/26/2009	62.09578	-140.66533	711	P	Little Sanpete Ck
AK232	-25.96	-195.6	12.1	7/26/2009	61.98795	-140.55595	719	G	White River
AK233	-21.97	-173.9	1.9	7/26/2009	61.96674	-140.41576	681	P	Koidern River # 2
AK235	-21.20	-169.0	0.6	7/26/2009	61.90079	-140.22586	691	P	Long's Creek
AK236	-22.97	-178.7	5.0	7/26/2009	61.80164	-140.03987	738	P	Edith Creek
AK237	-22.53	-175.2	5.1	7/26/2009	61.75084	-139.93402	757	P	Unnamed Creek
AK238	-25.91	-197.8	9.5	7/26/2009	61.67883	-139.75565	713	G	Donjek River
AK239	-22.89	-176.9	6.2	7/26/2009	61.59202	-139.42776	731	P	Swede Johnson Ck
AK240	-23.09	-178.4	6.3	7/26/2009	61.43131	-139.21974	846	P	Burwash Creek
AK241	-24.12	-184.2	8.7	7/26/2009	61.37603	-139.14381	871	G	Duke River
AK242	-23.21	-178.6	7.1	7/26/2009	61.32566	-138.93303	823	P	Copper Joe Creek
AK243	-23.34	-180.3	6.4	7/26/2009	61.22456	-138.74745	857	G	Bock's Creek
AK244	-23.09	-177.4	7.3	7/26/2009	61.08337	-138.53712	804	G	Williscroft Creek
AK245	-25.04	-190.1	10.2	7/26/2009	61.00101	-138.51224	788	G	Slim's River
AK246	-23.34	-176.7	10.1	7/26/2009	61.02085	-138.34546	873	G	Silver Creek

Sample ID	$\delta^{18}\text{O}$ (‰ SMOW)	$\delta\text{D}$ (‰ SMOW)	$d$	Sample Date	Sample Latitude	Sample Longitude	Sample Alt (m)	GI (G) Non (N) Perm (P)	Creek Name
AK247	-20.85	-165.3	1.6	7/26/2009	60.92214	-137.88292	860	P	Jarvis River
AK248	-21.75	-167.4	6.6	7/26/2009	60.79580	-137.67152	643	P	Bear Creek
AK249	-20.00	-156.3	3.7	7/26/2009	60.74763	-137.50658	595	G	Dezadeash River
AK250	-21.70	-163.5	10.1	7/26/2009	60.67650	-137.35931	844	G	Quill Creek
AK251	-20.02	-156.5	3.6	7/26/2009	60.59215	-137.23055	741	P	Kathleen River
AK252	-21.45	-164.3	7.4	7/26/2009	60.36809	-137.05537	716	P	Unnamed Creek
AK253	-19.93	-155.9	3.5	7/26/2009	60.35572	-137.04941	710	P	Flying Squirrel Ck
AK254	-20.56	-156.6	7.9	7/26/2009	60.28748	-137.00026	703	P	Klukshu Creek
AK255	-21.12	-159.4	9.6	7/26/2009	60.22655	-136.96057	700	P	Vand Creek
AK256	-20.69	-158.2	7.3	7/26/2009	60.11139	-136.92891	724	P	Takhanne River
AK257	-20.51	-155.7	8.3	7/26/2009	59.99199	-136.84454	840	G	Blanchard River
AK258	-19.42	-145.2	10.1	7/26/2009	59.92426	-136.79791	885	G	Stanley Creek
AK259	-19.69	-147.7	9.8	7/26/2009	59.84274	-136.65341	891	G	Goat Creek
AK260	-18.97	-141.0	10.8	7/26/2009	59.78709	-136.59395	891	G	Mule Creek
AK261	-18.33	-138.3	8.4	7/26/2009	59.72360	-136.60350	1011	G	Nadahini River
AK262	-19.25	-144.0	10.0	7/26/2009	59.64341	-136.47055	882	N	Clear Creek
AK264	-17.12	-125.7	11.2	7/27/2009	59.31414	-135.54715	9	N	Shakuseyi Creek
AK265	-16.10	-118.0	10.8	7/27/2009	59.29470	-135.50644	13	N	Unnamed Creek
AK266	-18.65	-138.1	11.1	7/27/2009	59.26652	-135.62334	22	G	Chilkat River
AK267	-19.33	-145.1	9.6	7/27/2009	59.37389	-135.83524	34	G	Unnamed Creek
AK268	-18.67	-139.1	10.2	7/27/2009	59.41271	-135.9989	63	G	Klehini River
AK269	-18.46	-136.9	10.8	7/27/2009	59.42227	-136.06059	101	N	Muncaster Creek
AK270	-18.39	-136.6	10.5	7/27/2009	59.42807	-136.13203	136	G	Little Boulder Creek
AK271	-19.05	-142.6	9.8	7/27/2009	59.43324	-136.19450	157	G	Big Boulder Creek
AK272	-13.49	-104.6	3.3	2007	58.72881	-135.99354	9	G	Sandy Cove
AK273	-13.49	-101.2	6.7	2007	58.75705	-136.17255	9	G	Sebree
AK274	-13.74	-104.4	5.5	2007	58.85659	-136.01394	4	G	Adams West
AK275	-12.82	-98.2	4.4	2007	58.59204	-136.48361	3	G	Geikie West
AK276	-12.97	-97.3	6.4	2007	58.60746	-136.11449	7	G	Johnson Cove
AK277	-13.43	-98.5	8.9	2007	58.73908	-136.48839	6	G	Sun Dew
AK278	-14.16	-105.9	7.4	2007	58.80346	-136.62263	3	G	Skidmore
AK279	-13.74	-103.1	6.8	2007	58.83011	-136.40022	7	G	Tidal
AK280	-13.09	-95.1	9.6	2007	58.93049	-136.19279	7	G	Wachusett East
AK281	-16.81	-127.1	7.4	2007	59.05747	-136.17349	21	G	Riggs
AK282	-13.78	-103.8	6.4	2007	59.07863	-136.37173	15	G	Lower Muir
AK283	-15.00	-112.4	7.6	2007	59.04486	-137.00810	26	G	Upper Tarr
AK284	-14.30	-107.0	7.5	2007	58.97356	-136.95698	10	G	Lower Tarr
AK285	-15.66	-130.4	-5.1	2007	58.92108	-137.03089	17	G	Topeka
AK286	-15.12	-111.0	10.0	2007	58.90891	-136.58426	8	G	Queen
AK287	-11.94	-86.2	9.3	2007	58.42030	-136.05686	5	G	Ripple
AK288	-13.35	-101.9	4.9	2007	59.03734	-136.10950	9	G	Mc Bride Glacier
AK289	-15.69	-119.6	6.0	2007	58.84772	-136.81961	28	G	Reid Glacier
AK290	-15.06	-112.5	8.0	2008	59.04486	-137.00810	26	G	Upper Tarr
AK291	-17.35	-127.3	11.6	2008	58.92108	-137.03089	17	G	Topeka
AK292	-13.63	-102.9	6.1	2008	58.72881	-135.99354	9	G	Sandy Cove
AK293	-14.08	-108.8	3.8	2008	58.75705	-136.17255	9	G	Sebree



Sample ID	$\delta^{18}\text{O}$ (‰ SMOW)	$\delta\text{D}$ (‰ SMOW)	$d$	Sample Date	Sample Latitude	Sample Longitude	Sample Alt (m)	GI (G) Non (N) Perm (P)	Creek Name
AK294	-13.70	-105.7	3.9	2008	58.66449	-136.32772	8	G	Geikie East
AK295	-13.52	-95.9	12.2	2008	58.59204	-136.48361	3	G	Geikie West
AK296	-12.54	-92.0	8.4	2008	58.60746	-136.11449	7	G	Johnson Cove
AK297	-17.43	-132.3	7.1	2008	58.87382	-136.82546	12	G	Reid Inlet
AK298	-14.08	-106.6	6.0	2008	58.85659	-136.01394	4	G	Adams West
AK299	-14.00	-105.7	6.3	2008	59.07863	-136.37173	15	G	Lower Muir
AK300	-8.13	-63.1	2.0	2008	58.42030	-136.05686	5	G	Ripple
AK301	-13.91	-103.0	8.3	2008	58.73908	-136.48839	6	G	Sun Dew
AK302	-14.90	-110.5	8.8	2008	58.80346	-136.62263	3	G	Skidmore
AK303	-13.53	-106.8	1.5	2008	58.83011	-136.40022	7	G	Tidal
AK304	-15.27	-117.9	4.3	2008	58.90891	-136.58426	8	G	Queen Inlet
AK305	-15.00	-111.3	8.6	2008	58.84772	-136.81961	28	G	Reid Glacier
AK306	-14.14	-103.1	10.0	2008	58.98943	-136.42084	9	G	Wachusett West
AK307	-11.91	-89.6	5.6	2008	58.93049	-136.19279	7	G	Wachusett East
AK308	-13.46	-101.4	6.3	2008	59.05747	-136.17349	21	G	Riggs
AK309	-13.44	-101.2	6.3	2008	59.03734	-136.10950	9	G	McBride Glacier
AK310	-17.33	-130.3	8.4	2008	59.09244	-136.35234	1000	G	Upper Muir
AK311	-14.14	-105.0	8.1	2008	58.80346	-136.62263	3	G	Skidmore
AK312	-16.15	-123.5	5.7	2008	58.73908	-136.48839	6	G	Sun Dew
AK313	-12.48	-91.9	7.9	2008	58.59204	-136.48361	3	G	Geikie West
AK314	-12.45	-91.9	7.7	2008	58.66449	-136.32772	8	G	Geikie East
AK315	-11.53	-86.0	6.2	2008	58.72881	-135.99354	9	G	Sandy Cove
AK316	-12.60	-95.0	5.8	2008	58.83011	-136.40022	7	G	Tidal Inlet
AK317	-14.45	-106.2	9.4	2008	59.04486	-137.00810	26	G	Tarr Inlet Upper
AK319	-15.59	-117.0	7.7	2008	58.87382	-136.82546	12	G	Reid Inlet
AK320	-15.40	-116.4	6.7	2008	58.84772	-136.81961	28	G	Reid Glacier
AK321	-12.51	-92.0	8.1	2008	58.75705	-136.17255	9	G	Sebree
AK322	-10.80	-80.7	5.7	2008	58.42030	-136.05686	5	G	Ripple
AK340	-14.70	-104.3	13.3	7/21/2009	58.50975	-136.19615	5	G	GB South
AK341	-14.34	-103.8	10.9	7/21/2009	58.52257	-136.23092	5	G	GB South
AK342	-14.97	-106.7	13.1	7/21/2009	58.57850	-136.21680	5	G	North Fingers Bay
AK343	-14.87	-106.2	12.8	7/21/2009	58.60278	-136.22978	5	G	North Fingers Bay
AK344	-14.64	-108.3	8.8	7/22/2009	59.06653	-136.28347	1000	G	Upper Muir
AK345	-15.18	-110.6	10.8	7/23/2009	59.06647	-136.28602	1000	G	Lower Luffy Falls
AK346	-14.96	-107.1	12.5	7/25/2009	58.44440	-135.59852	10	N	Falls Creek
AK347	-13.47	-97.1	10.6	7/26/2009	58.47262	-135.84822	9	G	Bartlett River
AK348	-14.43	-104.3	11.1	7/26/2009	58.47717	-135.84262	10	G	Bartlett River
AK349	-13.40	-97.1	10.0	7/29/2009	59.09243	-136.35233	1000	G	Upper Muir
AK350	-15.80	-112.9	13.5	7/29/2009	59.05550	-136.31217	1000	N	Upper Muir
AK351	-19.79	-146.2	12.1	7/30/2009	58.86000	-137.10840	25	G	Johns Hopkins
AK352	-16.75	-124.6	9.4	7/30/2009	58.86159	-137.10068	25	G	Johns Hopkins
AK353	-17.22	-130.1	7.7	7/30/2009	58.89958	-136.97612	25	N	Johns Hopkins
AK354	-16.48	-120.1	11.7	7/30/2009	58.92527	-136.96733	25	G	Johns Hopkins
AK355	-17.08	-126.9	9.7	7/30/2009	58.86087	-136.80365	28	N	Reid Inlet
AK360	-21.84	-165.9	8.8	8/1/2009	61.52720	-148.96442	25	N	Unnamed Creek
AK361	-20.46	-152.0	11.8	8/1/2009	61.50705	-148.99508	25	G	Knik River

Sample ID	$\delta^{18}\text{O}$ (‰ SMOW)	$\delta\text{D}$ (‰ SMOW)	$d$	Sample Date	Sample Latitude	Sample Longitude	Sample Alt (m)	GI (G) Non (N) Perm (P)	Creek Name
AK362	-20.52	-154.4	9.8	8/1/2009	61.44202	-147.19075	25	G	Unnamed Creek
AK363	-20.39	-155.5	7.6	8/1/2009	61.43477	-147.16792	25	G	Unnamed Creek
AK364	-20.69	-155.5	10.0	8/1/2009	61.47150	-147.09715	25	N	Unnamed Creek
AK365	-20.71	-155.3	10.4	8/1/2009	61.50740	-147.00058	25	N	Unnamed Creek
AK366	-20.47	-155.3	8.5	8/1/2009	61.48830	-148.90038	200	N	Goat Creek
AK367	-19.97	-149.3	10.5	8/1/2009	61.47662	-148.83988	200	G	Eklutna River
AK368	-19.20	-143.8	9.7	8/1/2009	61.78392	-148.72065	1006	N	Independence Str
AK369	-19.41	-145.0	10.3	8/1/2009	61.71083	-148.76800	322	G	Little Susitna River
AK379	-20.17	-156.8	4.6	5/25/2010	65.47112	-148.26765	199	P	Tolovana River
AK380	-23.22	-176.7	9.1	5/25/2010	66.03249	-150.13049	149	P	Ft. Hamlin Creek
AK381	-21.61	-168.4	4.5	5/25/2010	66.11613	-150.16544	178	P	No Name Creek
AK382	-22.15	-168.7	8.5	5/25/2010	66.44104	-150.63025	385	P	Kanuti River
AK383	-21.84	-168.3	6.4	5/26/2010	67.25451	-150.17728	337	P	Slate Creek
AK384	-22.70	-175.5	6.1	5/26/2010	67.43797	-150.07936	377	P	Mid Fork Koyukuk
AK385	-22.77	-175.7	6.4	5/26/2010	67.46088	-150.03490	386	P	Hammond Creek
AK386	-20.85	-165.4	1.4	5/26/2010	67.59699	-149.78664	434	P	Discovery Creek
AK387	-21.59	-168.9	3.8	5/26/2010	67.81100	-149.82208	542	P	Snowden Mountain
AK388	-21.45	-167.4	4.2	5/26/2010	67.81100	-149.82208	560	P	Snowden Mountain
AK389	-24.18	-188.1	5.3	5/26/2010	68.08245	-149.56352	997	P	Dietrich River
AK390	-24.43	-189.0	6.4	5/26/2010	68.08784	-149.55476	1012	P	Unnamed Creek
AK391	-24.93	-192.5	6.9	5/27/2010	68.11838	-149.54794	1171	P	Unnamed Creek
AK392	-24.75	-189.8	8.2	5/27/2010	68.11327	-149.53685	1096	P	Chandalar River
AK393	-25.53	-193.0	11.2	5/27/2010	68.13359	-149.47490	1369	P	Unnamed Creek
AK394	-25.09	-192.1	8.7	5/27/2010	68.13769	-149.44194	1171	P	Atigun River
AK395	-25.58	-196.2	8.5	5/27/2010	68.28412	-149.37256	885	P	Trevor Creek
AK396	-22.55	-173.9	6.5	5/28/2010	68.72224	-149.02057	641	P	Slope Mountain Ck
AK397	-22.63	-173.3	7.8	5/28/2010	68.61945	-149.31883	885	P	Imnaviat Creek
AK398	-23.20	-178.5	7.2	5/29/2010	68.46376	-149.54353	868	P	Galbraith Aufeis
AK399	-23.18	-178.0	7.4	5/30/2010	69.14781	-148.84343	301	P	Happy Valley
AK400	-23.03	-175.6	8.6	5/31/2010	70.19651	-148.40875	22	P	Sagavanirktok R
AK401	-22.63	-172.4	8.6	5/31/2010	69.50210	-148.57324	173	P	Unnamed Creek
AK402	-23.05	-173.0	11.4	5/31/2010	69.39773	-148.73222	231	P	Unnamed Creek
AK403	-21.80	-169.3	5.1	5/31/2010	68.86742	-148.84950	416	P	Unnamed Creek
AK404	-21.78	-167.7	6.6	6/1/2010	68.64706	-149.41144	744	P	Kuparuk River
AK405	-22.06	-170.9	5.6	6/1/2010	68.03195	-149.67055	774	P	Unnamed Creek
AK406	-21.62	-166.6	6.3	6/1/2010	67.93430	-149.82001	613	P	Nutirik River
AK407	-20.54	-159.4	4.9	6/1/2010	67.73730	-149.75484	491	P	Unnamed Creek
AK408	-22.17	-170.8	6.6	6/1/2010	67.01910	-150.28860	339	P	South Fork Koyukuk
AK409	-20.48	-156.0	7.8	6/1/2010	66.83723	-150.60399	309	P	Jim River 1
AK410	-21.63	-165.5	7.6	6/1/2010	66.67610	-150.66025	278	P	N. Fork Bonanza Ck
AK411	-21.34	-162.2	8.5	6/1/2010	66.53843	-150.79440	265	P	Fish Creek
AK412	-22.40	-173.0	6.2	6/1/2010	65.87791	-149.71649	91	P	Yukon River
AK413	-18.48	-144.6	3.2	6/27/2010	64.70866	-148.50938	189	P	Bonanza Creek
AK414	-18.67	-147.0	2.4	6/27/2010	64.66493	-148.94537	139	P	Little Goldstream Ck
AK415	-22.06	-171.2	5.3	6/27/2010	64.56497	-149.09349	121	P	Tanana River
AK416	-21.50	-163.9	8.1	6/27/2010	64.54890	-149.11700	120	P	Nenana River

Sample ID	$\delta^{18}\text{O}$ (‰ SMOW)	$\delta\text{D}$ (‰ SMOW)	$d$	Sample Date	Sample Latitude	Sample Longitude	Sample Alt (m)	GI (G) Non (N) Perm (P)	Creek Name
AK417	-19.70	-153.2	4.4	6/27/2010	64.94734	-147.67352	221	P	Goldstream Creek
AK418	-19.96	-152.6	7.1	6/27/2010	64.94480	-147.79878	218	P	Big El Dorado Ck
AK419	-20.06	-154.5	6.0	6/27/2010	64.96423	-147.62523	260	P	Fox Stream
AK420	-20.32	-156.1	6.4	6/27/2010	64.96423	-147.62523	260	P	Fox Spring
AK421	-19.57	-152.3	4.3	6/27/2010	65.15605	-147.34209	235	P	Chatanika Creek
AK422	-19.88	-153.4	5.6	6/27/2010	65.21250	-147.19733	270	P	Belle Creek
AK423	-19.24	-150.2	3.7	6/28/2010	64.89229	-147.48895	177	P	Steele Creek
AK424	-18.36	-145.9	1.0	6/28/2010	64.89222	-147.4128	187	P	Hopper Creek
AK425	-19.44	-151.4	4.2	6/28/2010	64.88554	-147.2498	164	P	Little Chena River
AK426	-19.22	-148.8	4.9	6/28/2010	64.87509	-146.78056	188	P	Flat Creek
AK427	-20.37	-156.4	6.6	6/28/2010	64.90022	-146.43375	235	P	Fourmile Creek
AK428	-19.87	-154.8	4.2	6/28/2010	64.90166	-146.35684	239	P	North Fork Chena
AK429	-19.73	-152.9	5.0	6/28/2010	65.02516	-146.21513	296	P	Angel Creek
AK430	-19.82	-154.9	3.7	6/28/2010	65.05537	-146.18137	312	P	West Fork Chena
AK431	-19.80	-155.3	3.2	6/28/2010	65.05361	-146.0589	373	P	Chena HS Stream
AK432	-19.47	-154.4	1.3	6/28/2010	65.05361	-146.0589	373	P	Chena HS Pool
AK433	-19.76	-154.5	3.6	6/28/2010	65.05361	-146.0589	373	P	Monument Creek
AK434	-19.91	-154.6	4.7	8/15/2011	65.14268	-147.41911	220	P	Captain Creek
AK435	-20.19	-157.1	4.4	8/15/2011	65.15588	-147.34216	232	P	Chatanika Creek
AK436	-19.93	-155.7	3.7	8/15/2011	65.17446	-147.28398	241	P	Kokomo Creek
AK437	-19.99	-155.8	4.1	8/15/2011	65.20435	-147.22673	261	P	Crooked Creek
AK438	-20.37	-158.2	4.8	8/15/2011	65.21223	-147.19812	277	P	Belle Creek
AK439	-19.92	-155.3	4.1	8/15/2011	65.26764	-146.72496	368	P	U.S. Creek
AK440	-20.36	-157.4	5.5	8/15/2011	64.96402	-147.62515	251	P	Fox Spring
AK441	-20.33	-156.4	6.3	8/15/2011	64.96402	-147.62515	250	P	Fox Stream
AK442	-19.89	-154.0	5.2	8/15/2011	64.89228	-147.48897	185	P	Steele Creek
AK443	-19.05	-149.5	2.9	8/15/2011	64.89227	-147.41283	193	P	Hopper Creek
AK444	-20.01	-154.7	5.3	8/15/2011	64.88532	-147.24817	168	P	Little Chena River
AK445	-20.14	-153.5	7.6	8/15/2011	64.94769	-147.6757	221	P	Goldstream Creek
AK446	-19.79	-149.9	8.5	8/15/2011	64.94525	-147.80031	222	P	Big El Dorado Creek
AK447	-20.34	-155.6	7.1	8/15/2011	64.84189	-147.81122	137	P	Chena River



## Appendix B: Surface water temperature and precipitation data

Sample ID	Catch Lat	Catch Long	Catch Alt (m)	Dist from Pacific (m)	G(1), P(2), N(3)	MAP (mm)	Cum MAP (mm)	DJF P (mm)	JJA P (mm)	MAT (°C*10)	DJF T (°C*10)	JJA T (°C*10)
AK001	64.97	-147.61	442.8	674000	2	319	415901	61	140	-36	-227	146
AK002	64.888	-147.727	163.3	645000	2	316	415278	59	135	-29	-217	150
AK003	64.739	-147.749	132	640000	2	323	408463	61	137	-29	-215	150
AK004	64.888	-147.727	163.3	645000	2	316	415278	59	135	-29	-217	150
AK005	64.762	-147.518	140.2	642000	2	335	407821	72	139	-32	-224	149
AK006	63.424	-150.31	1335	399000	1	546	364797	90	239	-46	-174	99
AK007	63.424	-150.31	1335	401000	1	546	364797	90	239	-46	-174	99
AK008	63.531	-150.012	1069	403000	1	497	362989	80	231	-62	-187	82
AK009	65.159	-147.336	377.3	574000	2	316	415606	62	138	-40	-233	145
AK010	65.159	-147.336	377.3	569000	2	316	415606	62	138	-40	-233	145
AK011	65.169	-147.114	470.2	566000	2	304	404471	54	143	-51	-241	135
AK012	65.159	-147.336	377.3	555000	2	316	415606	62	138	-40	-233	145
AK013	65.251	-147.338	632.9	563000	2	296	418897	51	143	-55	-242	130
AK014	63.261	-145.422	1563	293000	1	246	310083	26	155	-74	-230	88
AK015	63.261	-145.422	1563	293000	1	246	310083	26	155	-74	-230	88
AK016	63.232	-145.624	1236	303000	1	253	305343	26	153	-59	-219	104
AK017	63.232	-145.624	1236	295000	3	253	305343	26	153	-59	-219	104
AK018	63.232	-145.624	1236	331000	3	253	305343	26	153	-59	-219	104
AK019	63.301	-145.407	1574	311000	1	248	310737	26	158	-87	-239	76
AK020	63.398	-145.47	1822	323000	1	246	311943	26	159	-88	-241	76
AK021	63.514	-145.789	1251	328000	3	244	319105	23	159	-76	-233	89
AK022	63.676	-145.864	697.8	344000	3	280	320622	29	166	-40	-203	125
AK024	64.026	-145.503	339.8	265000	3	362	335833	50	176	-35	-208	133
AK025	64.083	-145.703	328.7	389000	1	318	332498	34	174	-29	-195	138
AK026	64.235	-145.802	312.2	410000	3	312	342031	37	169	-32	-203	139
AK027	64.411	-146.774	321.9	462000	3	330	363377	53	161	-37	-219	139
AK028	64.97	-147.61	442.8	674000	2	319	415901	61	140	-36	-227	146
AK029	64.955	-147.8	272.9	656000	2	309	418377	50	147	-34	-218	144
AK030	65.117	-147.747	291.5	667000	2	305	422952	52	141	-36	-223	146
AK031	65.172	-147.865	487	690000	2	300	426521	47	147	-41	-226	140
AK032	65.172	-147.865	487	663000	2	300	426521	47	147	-41	-226	140
AK033	65.268	-148.054	465.3	686000	2	292	433940	44	148	-45	-228	137
AK034	65.352	-148.305	243.8	687000	2	291	445783	44	144	-41	-226	142
AK035	65.498	-148.289	399.5	694000	2	288	449088	44	143	-45	-230	139
AK036	65.53	-148.819	356.8	707000	2	291	452627	42	149	-49	-233	135
AK037	65.676	-149.107	290	736000	2	295	477371	42	150	-49	-234	137
AK038	65.778	-149.272	377.3	749000	2	298	476565	42	154	-56	-239	130
AK039	65.928	-149.702	208.3	773000	2	311	479083	44	155	-52	-238	136
AK040	65.483	-148.334	373.4	694000	2	288	450647	43	146	-46	-231	138
AK041	65.275	-146.727	580.5	572000	2	289	392089	53	135	-48	-241	140
AK042	65.361	-146.472	787.7	558000	2	265	380647	43	133	-64	-252	125
AK043	65.397	-146.297	944.3	555000	2	262	385089	42	129	-64	-253	126
AK044	65.366	-146.096	822.5	566000	2	252	384575	41	126	-59	-250	131
AK045	65.366	-146.096	822.5	555000	2	252	384575	41	126	-59	-250	131
AK046	65.366	-146.096	822.5	571000	2	252	384575	41	126	-59	-250	131
AK047	65.366	-146.096	822.5	563000	2	252	384575	41	126	-59	-250	131
AK048	65.411	-145.909	912.2	555000	2	244	386737	38	123	-67	-256	125
AK049	64.41	-145.773	662.3	428000	2	294	351528	35	160	-44	-217	131
AK050	65.464	-145.8	1086	563000	2	233	382235	35	120	-74	-262	118
AK051	65.491	-145.526	1087	580000	2	224	385030	34	114	-71	-262	122
AK052	65.46	-145.201	825.5	585000	2	218	392925	34	111	-72	-264	122
AK053	65.449	-145.083	752.9	604000	2	219	401893	34	111	-70	-262	124
AK054	65.551	-145.09	434.3	610000	2	223	404668	36	104	-61	-259	137

Sample ID	Catch Lat	Catch Long	Catch Alt (m)	Dist from Pacific (m)	G(1), P(2), N(3)	MAP (mm)	Cum MAP (mm)	DJF P (mm)	JJA P (mm)	MAT (°C*10)	DJF T (°C*10)	JJA T (°C*10)
AK055	65.623	-144.955	460.7	610000	2	219	437143	37	100	-59	-258	140
AK056	65.664	-144.627	554.2	634000	2	216	499534	36	97	-61	-261	137
AK057	65.645	-144.425	301.8	640000	2	218	518606	36	97	-55	-257	144
AK058	65.827	-144.061	176.7	651000	2	207	504633	33	92	-57	-259	142
AK059	64.888	-147.727	163.3	645000	2	316	415278	59	135	-29	-217	150
AK060	64.982	-146.255	483.6	620000	2	287	370388	47	142	-44	-233	140
AK061	65.059	-145.864	723.4	522000	2	248	368871	34	136	-70	-251	116
AK062	64.345	-149.214	151.9	526000	1	341	425895	47	178	-36	-210	140
AK065	63.612	-148.822	687.8	433000	1	394	379183	56	202	-36	-168	105
AK066	63.597	-149.237	1056	443000	2	429	390459	64	213	-59	-185	84
AK067	64.739	-147.749	132	651000	2	323	408463	61	137	-29	-215	150
AK068	64.97	-147.61	442.8	678000	2	319	415901	61	140	-36	-227	146
AK069	64.97	-147.61	442.8	652000	2	319	415901	61	140	-36	-227	146
AK070	64.666	-148.945	116.2	641000	2	296	432529	42	158	-40	-221	138
AK071	64.565	-148.095	135	578000	2	314	409452	48	151	-29	-208	145
AK072	64.391	-149.02	135.8	535000	2	322	433858	45	171	-37	-212	140
AK073	64.256	-149.084	187.5	512000	2	348	423795	48	183	-36	-206	139
AK074	64.049	-149.314	513.2	493000	2	390	417080	54	202	-41	-191	118
AK075	63.885	-149.186	556.2	482000	2	395	403646	55	205	-39	-179	112
AK076	63.796	-148.916	701.8	463000	3	378	394449	52	203	-39	-174	107
AK077	63.796	-148.916	701.8	466000	3	378	394449	52	203	-39	-174	107
AK078	63.623	-149.069	1024	454000	1	406	396174	60	208	-67	-194	77
AK079	63.507	-148.703	1208	432000	1	387	377036	56	200	-64	-193	79
AK080	63.39	-148.872	895.2	394000	3	422	371072	64	203	-36	-164	102
AK081	63.283	-149.24	736.8	367000	3	499	373550	81	216	-34	-156	102
AK082	63.168	-149.235	966.9	365000	3	471	366367	76	217	-57	-174	78
AK083	63.072	-149.429	1053	364000	3	541	366928	99	235	-22	-139	109
AK084	62.965	-149.651	492	354000	3	678	338097	119	257	-11	-125	119
AK085	62.781	-149.946	429.4	342000	3	753	311538	124	261	-14	-125	113
AK086	62.681	-150.059	621.6	296000	3	716	304386	126	260	-11	-123	117
AK087	62.566	-150.223	398.4	288000	1	706	301109	125	256	-1	-120	129
AK088	62.566	-150.223	398.4	282000	3	706	301109	125	256	-1	-120	129
AK089	62.333	-150.498	219.7	255000	3	658	291413	119	234	0	-126	130
AK090	62.348	-150.625	303.4	264000	3	644	295577	119	230	-6	-132	126
AK091	62.354	-150.664	319.1	267000	3	643	296454	118	229	-7	-133	125
AK092	62.374	-150.737	359	270000	3	635	300477	117	227	-10	-138	123
AK093	62.237	-149.952	232.3	242000	1	636	265586	108	237	6	-108	129
AK094	62.237	-149.952	232.3	247000	3	636	265586	108	237	6	-108	129
AK095	62.325	-150.127	106.5	262000	1	687	276195	120	248	8	-112	135
AK096	62.126	-150.006	135.6	239000	3	609	257491	103	226	10	-106	134
AK097	62.091	-149.758	384.7	230000	1	563	264266	96	216	-6	-111	112
AK098	61.976	-149.896	167.3	218000	1	542	250500	89	208	11	-102	131
AK099	61.876	-149.835	230.9	209000	3	504	245123	82	197	11	-100	128
AK100	61.787	-149.833	229.5	193000	3	483	239654	80	190	9	-100	126
AK101	61.678	-149.781	285.4	175000	1	460	236803	76	180	12	-97	127
AK102	61.607	-149.079	124.5	181000	1	415	277557	73	157	17	-96	132
AK103	61.497	-149.02	17.21	173000	3	511	277732	129	187	-12	-107	96
AK104	61.497	-149.02	17.21	166000	1	511	277732	129	187	-12	-107	96



Sample ID	Catch Lat	Catch Long	Catch Alt (m)	Dist from Pacific (m)	G(1), P(2), N(3)	MAP (mm)	Cum MAP (mm)	DJF P (mm)	JJA P (mm)	MAT (°C*10)	DJF T (°C*10)	JJA T (°C*10)
AK105	61.438	-149.025	993.6	163000	3	609	273827	136	200	-34	-123	74
AK106	61.388	-149.038	792.1	154000	3	598	269821	133	174	10	-94	119
AK108	61.388	-149.038	792.1	154000	3	598	269821	133	174	10	-94	119
AK109	61.442	-149.281	462	157000	3	481	258489	94	167	14	-93	125
AK110	61.369	-149.331	811.6	149000	1	579	262283	129	182	-7	-100	99
AK111	61.298	-149.501	292.5	139000	1	513	237335	110	164	17	-89	129
AK112	61.017	-149.626	860	110000	3	621	208876	148	169	3	-90	108
AK113	61.017	-149.626	860	109000	3	621	208876	148	169	3	-90	108
AK114	61.015	-149.017	895.7	108000	1	845	239677	272	196	14	-76	114
AK115	60.864	-148.972	589.6	109000	1	1145	214445	346	205	27	-62	123
AK117	60.801	-148.886	746.6	104000	3	1190	198573	350	208	25	-62	119
AK118	60.801	-148.886	746.6	112000	1	1190	198573	350	208	25	-62	119
AK119	60.754	-149.037	303.3	104000	1	1221	208132	362	206	28	-58	122
AK120	60.73	-149.287	660.8	77000	1	953	199057	296	190	20	-66	116
AK121	60.605	-149.571	854.9	61000	3	802	178546	211	186	-4	-84	91
AK122	60.535	-149.666	693.9	82000	3	818	167184	218	166	20	-68	117
AK123	60.491	-149.804	543.4	49000	1	767	158148	197	159	23	-66	120
AK124	60.409	-149.874	737.5	51000	3	786	150747	201	174	5	-76	98
AK125	60.405	-149.975	506.2	50000	3	744	147186	188	163	14	-72	109
AK126	60.564	-150.583	77.12	51000	3	570	173670	121	149	18	-81	119
AK127	60.329	-151.274	30.6	126000	1	502	228030	102	139	12	-89	112
AK128	60.157	-151.2	139.6	131000	3	549	197020	121	142	13	-79	108
AK129	60.064	-151.553	86.48	98000	3	586	284173	136	144	18	-71	111
AK130	59.962	-151.499	209.7	101000	3	614	262715	146	147	15	-68	105
AK131	59.913	-151.592	181.7	69000	3	630	284687	153	148	19	-63	109
AK132	59.749	-151.664	213	52000	3	691	290812	173	156	21	-54	108
AK134	60.516	-149.396	563.6	77000	3	1045	185487	304	187	26	-57	119
AK136	60.436	-149.305	1155	103000	1	1069	167253	300	197	13	-64	103
AK137	60.413	-149.308	608.9	33000	1	1160	165313	343	200	26	-53	116
AK138	60.382	-149.338	577.9	32000	3	1074	167958	308	198	15	-62	104
AK139	60.348	-149.258	1362	29000	1	1066	152424	261	208	-12	-82	77
AK140	60.296	-149.3	515.9	25000	3	1177	150065	333	203	18	-57	105
AK141	60.213	-149.4	474.1	11000	3	1171	144412	331	202	20	-53	107
AK142	60.192	-149.553	779.4	9000	1	1097	133693	303	192	20	-56	107
AK143	60.296	-149.3	515.9	28000	1	1177	150065	333	203	18	-57	105
AK144	60.826	-149.461	546.6	87000	1	781	204680	206	179	6	-81	106
AK145	60.826	-149.461	546.6	88000	3	781	204680	206	179	6	-81	106
AK146	60.903	-149.536	418.1	93000	3	703	205518	173	186	-13	-97	87
AK147	60.903	-149.536	418.1	102000	3	703	205518	173	186	-13	-97	87
AK148	60.879	-149.675	623.3	104000	3	677	197767	164	180	-9	-95	91
AK149	60.742	-149.498	679.4	84000	3	798	192780	211	179	5	-81	103
AK150	61.853	-148.983	965.8	197000	3	523	290506	105	197	-28	-127	86
AK151	61.762	-148.917	883.9	180000	3	504	280969	99	182	-4	-107	109
AK152	61.828	-148.627	850.5	208000	1	528	282105	108	186	-12	-118	103
AK153	61.824	-148.476	1042	216000	1	539	287624	113	187	-12	-120	105
AK155	61.818	-148.113	960.1	213000	3	549	285635	116	191	-23	-134	97
AK156	61.818	-148.113	960.1	219000	3	549	285635	116	191	-23	-134	97
AK157	61.851	-147.905	1206	238000	1	529	285519	111	190	-30	-145	92

Sample ID	Catch Lat	Catch Long	Catch Alt (m)	Dist from Pacific (m)	G(1), P(2), N(3)	MAP (mm)	Cum MAP (mm)	DJF P (mm)	JJA P (mm)	MAT (°C*10)	DJF T (°C*10)	JJA T (°C*10)
AK158	61.801	-147.806	788	227000	1	569	283507	123	191	-19	-136	103
AK159	61.66	-147.576	962.5	230000	1	560	275486	121	196	-36	-150	86
AK160	61.865	-147.716	1135	230000	1	498	288588	100	190	-44	-160	82
AK161	61.841	-147.412	1175	216000	3	482	283440	99	187	-41	-164	89
AK162	61.994	-146.942	900.1	194000	1	406	277706	74	174	-41	-185	102
AK163	62.031	-146.745	821.2	202000	2	353	276499	60	166	-49	-199	100
AK164	62.106	-146.574	747.5	208000	2	339	275697	55	161	-46	-200	105
AK165	62.166	-146.062	642	192000	2	335	275727	59	152	-40	-195	112
AK166	62.198	-145.565	506.1	202000	2	291	277618	51	132	-33	-194	121
AK167	62.034	-145.486	424	157000	1	322	270415	63	134	-29	-188	122
AK168	61.86	-145.552	572.9	145000	1	357	266713	71	144	-35	-188	112
AK169	61.812	-145.341	599.7	130000	2	355	264654	66	153	-47	-194	99
AK170	61.677	-145.32	765.9	108000	3	405	262164	80	162	-44	-187	98
AK171	61.616	-145.294	863.2	109000	1	420	260331	88	157	-35	-182	107
AK172	61.424	-145.171	948.6	88000	1	547	256061	127	184	-25	-164	109
AK173	61.424	-145.171	948.6	85000	3	547	256061	127	184	-25	-164	109
AK174	61.349	-145.333	1095	73000	3	601	239934	150	201	-22	-154	107
AK175	61.349	-145.333	1095	75000	3	601	239934	150	201	-22	-154	107
AK176	61.27	-145.522	1487	70000	1	606	229753	127	219	-60	-174	63
AK177	61.27	-145.522	1487	62000	1	606	229753	127	219	-60	-174	63
AK178	61.27	-145.522	1487	57000	1	606	229753	127	219	-60	-174	63
AK179	61.27	-145.522	1487	46000	1	606	229753	127	219	-60	-174	63
AK180	61.211	-145.643	1255	38000	1	677	219852	150	222	-43	-159	78
AK181	61.162	-145.737	950	8000	1	820	217954	192	235	-24	-139	92
AK182	61.19	-145.933	1343	32000	1	805	222667	199	235	-23	-135	93
AK183	61.113	-145.941	929.9	37000	1	849	212745	168	231	-42	-149	74
AK184	61.164	-146.064	983.8	10000	1	700	215438	156	225	-46	-155	72
AK185	61.132	-146.27	565.5	3000	3	1490	212953	412	301	27	-59	118
AK186	61.042	-146.18	442.1	4000	1	985	198873	242	255	-15	-116	91
AK187	61.042	-146.357	515.9	3000	3	1215	192459	316	276	5	-87	102
AK188	61.042	-146.18	442.1	27000	3	985	198873	242	255	-15	-116	91
AK189	61.113	-145.941	929.9	26000	3	849	212745	168	231	-42	-149	74
AK190	61.491	-145.046	1022	118000	3	515	271253	108	191	-44	-175	90
AK191	61.615	-144.601	419.8	113000	3	536	358026	107	197	-39	-172	95
AK192	61.547	-144.645	1133	118000	3	546	348515	110	208	-50	-176	81
AK193	61.57	-144.481	542.4	121000	3	597	366540	125	207	-29	-161	104
AK194	61.57	-144.481	542.4	120000	1	597	366540	125	207	-29	-161	104
AK195	62.146	-145.444	443.6	171000	3	298	271520	52	131	-28	-189	125
AK196	62.32	-145.506	559.1	181000	3	273	281516	42	133	-35	-197	121
AK197	62.341	-145.444	557.3	264000	1	271	278287	42	132	-34	-196	122
AK198	62.516	-145.162	613.9	264000	1	273	300246	40	137	-35	-196	121
AK199	62.483	-145.363	605.9	198000	2	263	287596	39	134	-36	-198	121
AK200	62.575	-145.4	664.5	211000	2	262	289709	37	137	-38	-201	120
AK201	62.7	-145.449	759.7	231000	2	254	289618	33	141	-43	-205	116
AK202	62.943	-145.49	907	257000	2	252	300548	30	147	-50	-211	111
AK203	63.098	-145.49	994.8	292000	3	251	305344	28	151	-56	-216	106
AK204	63.098	-145.49	994.8	284000	3	251	305344	28	151	-56	-216	106
AK205	63.098	-145.49	994.8	298000	3	251	305344	28	151	-56	-216	106

Sample ID	Catch Lat	Catch Long	Catch Alt (m)	Dist from Pacific (m)	G(1), P(2), N(3)	MAP (mm)	Cum MAP (mm)	DJF P (mm)	JJA P (mm)	MAT (°C*10)	DJF T (°C*10)	JJA T (°C*10)
AK206	64.235	-145.802	312.2	299000	1	312	342031	37	169	-32	-203	139
AK207	63.514	-145.789	1251	320000	1	244	319105	23	159	-76	-233	89
AK208	63.609	-145.833	890.8	338000	1	267	318554	25	161	-57	-218	108
AK209	63.92	-145.716	446.8	383000	3	301	329595	30	173	-30	-193	135
AK211	63.857	-144.952	386.8	399000	1	315	382138	43	157	-36	-210	133
AK212	63.594	-145.045	1093	410000	1	249	347438	27	153	-73	-233	94
AK213	63.6	-144.876	677.5	399000	1	292	394033	37	155	-42	-211	124
AK214	63.668	-144.455	485.1	424000	3	293	461124	41	149	-38	-211	130
AK215	63.624	-144.474	822.1	421000	3	275	454232	36	149	-49	-218	119
AK216	63.522	-144.164	660.6	413000	1	284	444462	37	148	-45	-215	122
AK217	63.455	-144.01	717.4	394000	1	274	434568	32	150	-63	-227	104
AK218	63.289	-143.57	1199	383000	3	268	411288	32	156	-75	-237	91
AK219	63.202	-142.821	932.4	366000	1	252	433700	28	146	-60	-243	114
AK220	63.082	-141.821	841.7	339000	2	244	412654	21	149	-62	-262	124
AK221	62.987	-141.775	536.4	353000	2	259	409211	24	151	-55	-256	131
AK222	62.987	-141.775	536.4	347000	2	259	409211	24	151	-55	-256	131
AK223	62.987	-141.775	536.4	345000	2	259	409211	24	151	-55	-256	131
AK224	62.879	-142.084	529.4	353000	2	278	410170	30	154	-52	-247	129
AK225	62.987	-141.775	536.4	342000	2	259	409211	24	151	-55	-256	131
AK226	62.876	-141.303	590.7	345000	2	302	422396	29	173	-58	-257	126
AK227	62.742	-141.073	681	337000	2	329	413202	33	186	-59	-257	123
AK228	62.646	-140.98	605.6	328000	2	348	412093	36	194	-58	-254	123
AK229	62.345	-140.913	662.2	306000	2	407	403802	45	217	-58	-246	117
AK230	62.222	-140.722	825	301000	2	412	410550	52	213	-65	-249	108
AK231	62.115	-140.61	918.4	279000	2	426	414650	58	213	-66	-246	103
AK232	61.986	-140.619	1167	265000	1	437	408133	60	221	-81	-242	78
AK233	61.963	-140.399	807.3	260000	2	451	421859	67	213	-60	-237	106
AK235	61.961	-140.299	934.6	257000	2	445	432243	67	208	-58	-238	108
AK236	61.802	-140.005	1019	241000	2	442	450259	66	205	-56	-228	103
AK237	61.802	-140.005	1019	252000	2	442	450259	66	205	-56	-228	103
AK238	61.678	-139.762	923.6	257000	1	438	469731	64	201	-48	-217	108
AK239	61.611	-139.462	1021	254000	2	375	459393	49	185	-49	-214	105
AK240	61.398	-139.295	1167	243000	2	388	447558	55	195	-67	-213	77
AK241	61.347	-139.18	979.3	202000	1	361	412412	46	182	-49	-204	97
AK242	61.321	-138.656	1273	241000	2	310	392484	41	156	-46	-202	98
AK243	61.24	-138.679	840.8	238000	1	345	393151	50	160	-33	-191	110
AK244	61.071	-138.581	1203	227000	1	387	383327	63	174	-58	-198	77
AK245	60.838	-138.677	1033	219000	1	505	372817	90	191	-42	-181	88
AK246	60.98	-138.319	1009	230000	1	373	387025	66	155	-39	-187	97
AK247	60.985	-137.828	904.8	246000	2	306	391710	61	123	-35	-191	105
AK248	60.853	-137.731	907.4	249000	2	324	382255	70	121	-35	-188	103
AK249	60.803	-137.476	853.9	254000	1	313	393909	74	108	-31	-187	110
AK250	60.631	-137.476	1346	254000	1	411	386972	95	155	-65	-189	62
AK251	60.477	-137.238	1115	249000	2	443	420549	115	130	-37	-172	92
AK252	60.379	-137.074	1114	194000	2	496	435132	140	124	-26	-162	102
AK253	60.379	-137.074	1114	191000	2	496	435132	140	124	-26	-162	102
AK254	60.222	-136.928	1071	190000	2	567	455345	167	129	-24	-153	100
AK255	60.222	-136.928	1071	175000	2	567	455345	167	129	-24	-153	100



Sample ID	Catch Lat	Catch Long	Catch Alt (m)	Dist from Pacific (m)	G(1), P(2), N(3)	MAP (mm)	Cum MAP (mm)	DJF P (mm)	JJA P (mm)	MAT (°C*10)	DJF T (°C*10)	JJA T (°C*10)
AK256	60.119	-136.92	1158	155000	2	664	450629	201	132	-15	-143	106
AK257	60.008	-136.83	1454	144000	1	673	460534	214	138	-19	-139	99
AK258	59.93	-136.757	1091	125000	1	698	461448	221	142	-21	-137	94
AK259	59.895	-136.718	1245	123000	1	723	466339	219	146	-24	-138	90
AK260	59.709	-136.616	1096	122000	1	853	476630	268	150	-16	-123	93
AK261	59.709	-136.616	1096	113000	1	853	476630	268	150	-16	-123	93
AK262	59.649	-136.637	1079	95000	3	882	466302	271	158	-19	-122	89
AK264	59.289	-135.572	423.7	50000	3	977	576880	278	156	5	-90	102
AK265	59.289	-135.572	423.7	36000	3	977	576880	278	156	5	-90	102
AK266	59.268	-135.626	867.1	35000	1	1247	559229	386	159	40	-49	131
AK267	59.368	-135.799	658.7	57000	1	1114	551890	358	148	23	-72	120
AK268	59.424	-136.111	808	71000	1	1235	525153	444	154	34	-62	133
AK269	59.424	-136.111	808	69000	3	1235	525153	444	154	34	-62	133
AK270	59.424	-136.111	808	77000	1	1235	525153	444	154	34	-62	133
AK271	59.424	-136.111	808	79000	1	1235	525153	444	154	34	-62	133
AK272	58.735	-136.006	250.3	1000	1	1235	432358	444	154	34	-62	133
AK273	58.772	-136.227	353.6	1000	1	1538	404889	488	247	30	-42	110
AK274	58.833	-135.934	285.9	1000	1	1375	458298	413	222	24	-51	107
AK275	58.567	-136.515	337.4	24000	1	1973	316313	565	305	36	-30	109
AK276	58.573	-136.111	150.6	1000	1	1696	380107	485	284	39	-28	113
AK277	58.723	-136.462	53.77	1000	1	1867	358825	557	278	40	-31	116
AK278	58.811	-136.607	115.1	1000	1	1867	347019	557	278	40	-31	116
AK279	58.86	-136.376	452.3	1000	1	1764	401813	533	247	39	-38	119
AK280	58.959	-136.322	390.6	1000	1	1714	426053	526	230	43	-37	126
AK281	59.07	-136.297	451.4	1000	1	1630	449092	514	208	39	-44	126
AK282	59.07	-136.297	451.4	1000	1	1630	449092	514	208	39	-44	126
AK283	59.014	-136.952	773.5	1000	1	1741	314157	567	261	39	-44	123
AK284	59.014	-136.952	773.5	1000	1	1741	314157	567	261	39	-44	123
AK285	58.891	-137.083	826	1000	1	1609	254406	534	275	18	-58	100
AK286	58.977	-136.596	414.3	1000	1	1729	387205	535	234	31	-49	116
AK287	58.473	-136.144	62.19	1000	1	1867	351323	507	309	45	-21	115
AK288	59.131	-136.001	1040	1000	1	1112	497288	345	182	2	-84	94
AK289	58.69	-136.889	909.5	1000	1	1725	265538	486	281	1	-68	79
AK290	59.014	-136.952	773.5	1000	1	1741	314157	567	261	39	-44	123
AK291	58.891	-137.083	826	1000	1	1609	254406	534	275	18	-58	100
AK292	58.735	-136.006	250.3	1000	1	1609	432358	534	275	18	-58	100
AK293	58.772	-136.227	353.6	1000	1	1538	404889	488	247	30	-42	110
AK294	58.567	-136.515	337.4	1000	1	1973	316313	565	305	36	-30	109
AK295	58.567	-136.515	337.4	17000	1	1973	316313	565	305	36	-30	109
AK296	58.573	-136.11	150.6	1000	1	1696	380107	485	284	39	-28	113
AK297	58.69	-136.889	909.5	1000	1	1725	265538	486	281	1	-68	79
AK298	58.833	-135.934	285.9	1000	1	1375	458298	413	222	24	-51	107
AK299	59.07	-136.297	451.4	1000	1	1630	449092	514	208	39	-44	126
AK300	58.473	-136.144	62.19	1000	1	1867	351323	507	309	45	-21	115
AK301	58.723	-136.462	53.77	1000	1	1867	358825	557	278	40	-31	116
AK302	58.811	-136.607	115.1	1000	1	1867	347019	557	278	40	-31	116
AK303	58.86	-136.376	452.3	1000	1	1764	401813	533	247	39	-38	119
AK304	58.977	-136.596	414.3	1000	1	1729	387205	535	234	31	-49	116

Sample ID	Catch Lat	Catch Long	Catch Alt (m)	Dist from Pacific (m)	G(1), P(2), N(3)	MAP (mm)	Cum MAP (mm)	DJF P (mm)	JJA P (mm)	MAT (°C*10)	DJF T (°C*10)	JJA T (°C*10)
AK305	58.69	-136.889	909.5	1000	1	1725	265538	486	281	1	-68	79
AK306	58.959	-136.322	390.6	22000	1	1714	426053	526	230	43	-37	126
AK307	58.959	-136.322	390.6	18000	1	1714	426053	526	230	43	-37	126
AK308	59.07	-136.297	451.4	1000	1	1630	449092	514	208	39	-44	126
AK309	59.131	-136.001	1040	1000	1	1112	497288	345	182	2	-84	94
AK310	59.07	-136.297	451.4	41000	1	1630	449092	514	208	39	-44	126
AK311	58.811	-136.607	115.1	1000	1	1630	347019	514	208	39	-44	126
AK312	58.723	-136.462	53.77	1000	1	1867	358825	557	278	40	-31	116
AK313	58.567	-136.515	337.4	19000	1	1973	316313	565	305	36	-30	109
AK314	58.567	-136.515	337.4	1000	1	1973	316313	565	305	36	-30	109
AK315	58.735	-136.006	250.3	1000	1	1973	432358	565	305	36	-30	109
AK316	58.86	-136.376	452.3	1000	1	1764	401813	533	247	39	-38	119
AK317	59.014	-136.952	773.5	1000	1	1741	314157	567	261	39	-44	123
AK319	58.69	-136.889	909.5	1000	1	1725	265538	486	281	1	-68	79
AK320	58.69	-136.889	909.5	1000	1	1725	265538	486	281	1	-68	79
AK321	58.772	-136.227	353.6	1000	1	1538	404889	488	247	30	-42	110
AK322	58.473	-136.144	62.19	1000	1	1867	351323	507	309	45	-21	115
AK340	58.524	-136.247	187.3	1000	1	1909	348037	536	309	48	-19	119
AK341	58.524	-136.247	187.3	1000	1	1909	348037	536	309	48	-19	119
AK342	58.587	-136.263	310.7	1000	1	1772	357526	508	284	33	-34	107
AK343	58.587	-136.263	310.7	1000	1	1772	357526	508	284	33	-34	107
AK344	59.07	-136.297	451.4	24000	1	1630	449092	514	208	39	-44	126
AK345	59.07	-136.297	451.4	25000	1	1630	449092	514	208	39	-44	126
AK346	58.458	-135.596	317	25000	3	1383	457690	359	273	35	-35	111
AK347	58.735	-136.006	250.3	32000	1	1383	432358	359	273	35	-35	111
AK348	58.581	-135.747	513.3	32000	1	1439	445136	388	267	44	-28	120
AK349	59.07	-136.297	451.4	24000	1	1630	449092	514	208	39	-44	126
AK350	59.07	-136.297	451.4	24000	3	1630	449092	514	208	39	-44	126
AK351	58.891	-137.083	826	1000	1	1609	254406	534	275	18	-58	100
AK352	58.891	-137.083	826	10000	1	1609	254406	534	275	18	-58	100
AK353	58.891	-137.083	826	14000	3	1609	254406	534	275	18	-58	100
AK354	58.891	-137.083	826	15000	1	1609	254406	534	275	18	-58	100
AK355	58.69	-136.889	909.5	1000	3	1725	265538	486	281	1	-68	79
AK360	61.497	-149.02	17.21	178000	3	511	277732	129	187	-12	-107	96
AK361	61.497	-149.02	17.21	166000	1	511	277732	129	187	-12	-107	96
AK362	61.448	-147.236	2321	156000	1	546	255205	114	212	-78	-178	42
AK363	61.448	-147.236	2321	155000	1	546	255205	114	212	-78	-178	42
AK364	61.493	-147.055	2548	162000	3	530	252032	106	213	-85	-186	37
AK365	61.493	-147.055	2548	172000	3	530	252032	106	213	-85	-186	37
AK366	61.454	-148.916	613.2	163000	3	612	261478	139	190	-13	-108	95
AK367	61.454	-148.916	613.2	178000	1	612	261478	139	190	-13	-108	95
AK368	61.801	-148.719	1133	198000	3	542	283191	111	199	-40	-138	75
AK369	61.801	-148.719	1133	175000	1	542	283191	111	199	-40	-138	75
AK379	65.498	-148.289	399.5	694000	2	288	449088	44	143	-45	-230	139
AK380	66.045	-149.886	394.4	783000	2	316	481227	44	160	-64	-245	123
AK381	66.15	-150.239	278	807000	2	321	493564	46	156	-56	-240	133
AK382	66.455	-150.645	481	849000	2	325	512466	49	155	-66	-245	123
AK383	67.246	-150.097	603.7	948000	2	289	527576	43	138	-80	-258	112

Sample ID	Catch Lat	Catch Long	Catch Alt (m)	Dist from Pacific (m)	G(1), P(2), N(3)	MAP (mm)	Cum MAP (mm)	DJF P (mm)	JJA P (mm)	MAT (°C*10)	DJF T (°C*10)	JJA T (°C*10)
AK384	67.447	-150.017	485.1	966000	2	281	531320	41	142	-102	-273	89
AK385	67.527	-150.033	782.6	971000	2	278	534760	41	136	-93	-269	100
AK386	67.575	-149.732	672	979000	2	275	537458	40	133	-88	-265	105
AK387	67.835	-149.78	994	1011000	2	265	543382	38	132	-105	-278	87
AK388	67.835	-149.78	994	1011000	2	265	543382	38	132	-105	-278	87
AK389	68.112	-149.78	1654	1044000	2	257	551941	36	140	-148	-308	43
AK390	68.112	-149.78	1654	1048000	2	257	551941	36	140	-148	-308	43
AK391	68.112	-149.78	1654	1060000	2	257	551941	36	140	-148	-308	43
AK392	68.112	-149.78	1654	1057000	2	257	551941	36	140	-148	-308	43
AK393	68.16	-149.538	1415	1064000	2	251	560983	36	130	-125	-293	68
AK394	68.16	-149.538	1415	1065000	2	251	560983	36	130	-125	-293	68
AK395	68.272	-149.301	1277	1068000	2	245	566749	33	127	-126	-293	67
AK396	68.753	-149.006	672.1	1118000	2	219	573717	31	108	-112	-285	83
AK397	68.632	-149.392	773.9	1101000	2	226	587614	31	113	-115	-289	80
AK398	68.389	-149.528	1092	1085000	2	239	568024	33	125	-127	-295	66
AK399	69.046	-149.028	452.2	1164000	2	205	588346	28	100	-109	-286	86
AK400	70.064	-148.546	26.6	1280000	2	158	582459	20	76	-109	-287	84
AK401	69.532	-148.567	146.3	1204000	2	176	570486	24	84	-105	-284	89
AK402	69.399	-148.731	245.5	1191000	2	185	574126	26	89	-107	-284	87
AK403	68.753	-149.006	672.1	1130000	2	219	573717	31	108	-112	-285	83
AK404	68.632	-149.392	773.9	1105000	2	226	587614	31	113	-115	-289	80
AK405	68.084	-149.657	1165	1036000	2	255	554772	36	129	-116	-287	77
AK406	67.89	-149.626	1215	1024000	2	263	550417	37	136	-120	-288	72
AK407	67.76	-149.597	1075	1001000	2	267	548784	38	136	-112	-281	80
AK408	67.023	-150.333	580.5	921000	2	302	529136	45	141	-69	-251	122
AK409	66.843	-150.541	429.2	898000	2	313	524760	48	146	-68	-248	124
AK410	66.703	-150.583	480.3	881000	2	317	521006	48	149	-65	-245	125
AK411	66.54	-150.79	359.1	863000	2	325	519019	50	151	-60	-241	130
AK412	65.928	-149.702	208.3	773000	2	311	479083	44	155	-52	-238	136
AK413	64.97	-147.61	442.8	652000	2	319	415901	61	140	-36	-227	146
AK414	64.666	-148.945	116.2	522000	2	296	432529	42	158	-40	-221	138
AK415	64.561	-149.023	110.3	578000	2	297	440013	42	159	-39	-220	138
AK416	64.345	-149.214	151.9	549000	2	341	425895	47	178	-36	-210	140
AK417	64.97	-147.61	442.8	674000	2	319	415901	61	140	-36	-227	146
AK418	64.955	-147.8	272.9	671000	2	309	418377	50	147	-34	-218	144
AK419	64.97	-147.61	442.8	651000	2	319	415901	61	140	-36	-227	146
AK420	64.97	-147.61	442.8	651000	2	319	415901	61	140	-36	-227	146
AK421	65.159	-147.336	377.3	552000	2	316	415606	62	138	-40	-233	145
AK422	65.251	-147.338	632.9	582000	2	296	418897	51	143	-55	-242	130
AK423	64.896	-147.489	197.3	544000	2	331	413026	71	137	-33	-227	149
AK424	64.883	-147.373	246.7	574000	2	333	406652	70	141	-35	-228	148
AK425	64.883	-147.373	246.7	525000	2	333	406652	70	141	-35	-228	148
AK426	64.919	-146.814	370.8	528000	2	321	385346	58	148	-43	-233	141
AK427	64.908	-146.396	406.5	489000	2	301	362879	51	145	-39	-228	145
AK428	64.908	-146.396	406.5	503000	2	301	362879	51	145	-39	-228	145
AK429	65.042	-146.419	804.2	517000	2	277	368722	43	143	-60	-244	124
AK430	65.085	-146.176	653.1	514000	2	283	379267	45	137	-49	-238	138
AK431	65.059	-145.864	723.4	519000	2	248	368871	34	136	-70	-251	116



Sample ID	Catch Lat	Catch Long	Catch Alt (m)	Dist from Pacific (m)	G(1), P(2), N(3)	MAP (mm)	Cum MAP (mm)	DJF P (mm)	JJA P (mm)	MAT (°C*10)	DJF T (°C*10)	JJA T (°C*10)
AK432	65.059	-145.864	723.4	517000	2	248	368871	34	136	-70	-251	116
AK433	65.059	-145.864	723.4	514000	2	248	368871	34	136	-70	-251	116
AK434	65.159	-147.336	377.3	574000	2	316	415606	62	138	-40	-233	145
AK435	65.159	-147.336	377.3	574000	2	316	415606	62	138	-40	-233	145
AK436	65.169	-147.114	470.2	566000	2	304	404471	54	143	-51	-241	135
AK437	65.159	-147.336	377.3	555000	2	316	415606	62	138	-40	-233	145
AK438	65.251	-147.338	632.9	563000	2	296	418897	51	143	-55	-242	130
AK439	65.275	-146.727	580.5	572000	2	289	392089	53	135	-48	-241	140
AK440	64.97	-147.61	442.8	651000	2	319	415901	61	140	-36	-227	146
AK441	64.97	-147.61	442.8	651000	2	319	415901	61	140	-36	-227	146
AK442	64.896	-147.489	197.3	544000	2	331	413026	71	137	-33	-227	149
AK443	64.883	-147.373	246.7	574000	2	333	406652	70	141	-35	-228	148
AK444	64.883	-147.373	246.7	525000	2	333	406652	70	141	-35	-228	148
AK445	64.97	-147.61	442.8	674000	2	319	415901	61	140	-36	-227	146
AK446	64.955	-147.8	272.9	671000	2	309	418377	50	147	-34	-218	144
AK447	64.888	-147.727	163.3	645000	2	316	415278	59	135	-29	-217	150

### Appendix C: Isoscape residuals

Sample ID	$\delta^{18}\text{O}$ (‰ VSMOW)	Isoscape $\delta^{18}\text{O}$ (‰ VSMOW)	Isoscape Residual (‰ VSMOW)
AK001	-20.7	-20.6	0.2
AK002	-19.6	-20.4	-0.7
AK003	-22.9	-20.4	2.6
AK004	-17.4	-20.4	-3.0
AK005	-17.9	-20.4	-2.4
AK006	-21.8	-20.5	1.3
AK007	-20.1	-20.5	-0.4
AK008	-20.4	-21.0	-0.7
AK009	-20.1	-20.6	-0.6
AK010	-20.1	-20.6	-0.6
AK011	-20.1	-21.0	-0.9
AK012	-20.1	-20.6	-0.5
AK013	-19.5	-21.1	-1.6
AK014	-22.0	-21.8	0.1
AK015	-21.9	-21.8	0.1
AK016	-22.0	-21.4	0.5
AK017	-21.8	-21.4	0.4
AK018	-22.4	-21.4	0.9
AK019	-22.0	-22.2	-0.1
AK020	-22.9	-22.2	0.7
AK021	-22.2	-21.9	0.3
AK022	-21.8	-20.9	0.8
AK024	-22.6	-20.6	2.0
AK025	-23.0	-20.6	2.4
AK026	-20.6	-20.7	0.0
AK027	-21.3	-20.7	0.6
AK028	-20.4	-20.6	-0.2
AK029	-20.0	-20.6	-0.6
AK030	-20.1	-20.6	-0.5
AK031	-20.0	-20.8	-0.8
AK032	-19.8	-20.8	-1.0
AK033	-20.4	-20.9	-0.6
AK034	-19.4	-20.8	-1.4
AK035	-19.8	-20.9	-1.1
AK036	-20.3	-21.1	-0.7
AK037	-21.0	-21.0	0.0
AK038	-22.2	-21.2	1.0
AK039	-21.7	-21.1	0.6
AK040	-19.8	-21.0	-1.1
AK041	-19.5	-20.9	-1.4
AK042	-19.6	-21.4	-1.9
AK043	-20.6	-21.4	-0.9
AK044	-20.4	-21.3	-0.9
AK045	-20.1	-21.3	-1.2
AK046	-21.0	-21.3	-0.3
AK047	-20.7	-21.3	-0.6



Sample ID	$\delta^{18}\text{O}$ (‰ VSMOW)	Isoscape $\delta^{18}\text{O}$ (‰ VSMOW)	Isoscape Residual (‰ VSMOW)
AK048	-20.0	-21.5	-1.5
AK049	-20.4	-21.0	-0.6
AK050	-20.4	-21.7	-1.3
AK051	-21.0	-21.7	-0.7
AK052	-21.5	-21.7	-0.2
AK053	-21.5	-21.7	-0.1
AK054	-21.4	-21.4	0.0
AK055	-20.5	-21.3	-0.9
AK056	-21.0	-21.4	-0.4
AK057	-20.7	-21.3	-0.6
AK058	-21.6	-21.3	0.3
AK059	-20.1	-20.4	-0.3
AK060	-20.5	-20.9	-0.4
AK061	-20.0	-21.7	-1.7
AK062	-21.9	-20.7	1.2
AK065	-21.6	-20.6	1.0
AK066	-21.5	-21.1	0.4
AK067	-20.7	-20.4	0.4
AK068	-20.4	-20.6	-0.1
AK069	-19.3	-20.6	-1.2
AK070	-18.8	-20.8	-2.0
AK071	-23.0	-20.5	2.6
AK072	-18.8	-20.7	-1.9
AK073	-19.2	-20.7	-1.5
AK074	-20.3	-20.7	-0.5
AK075	-19.8	-20.7	-0.9
AK076	-20.4	-20.7	-0.3
AK077	-20.3	-20.7	-0.4
AK078	-21.4	-21.3	0.1
AK079	-21.5	-21.3	0.2
AK080	-21.9	-20.5	1.3
AK081	-21.5	-20.3	1.2
AK082	-21.3	-20.9	0.3
AK083	-20.4	-19.9	0.6
AK084	-19.9	-19.4	0.5
AK085	-19.1	-19.4	-0.4
AK086	-18.5	-19.3	-0.8
AK087	-18.8	-19.1	-0.3
AK088	-22.9	-19.1	3.8
AK089	-18.0	-19.1	-1.1
AK090	-17.5	-19.3	-1.8
AK091	-17.7	-19.3	-1.7

Sample ID	$\delta^{18}\text{O}$ (‰ VSMOW)	Isoscape $\delta^{18}\text{O}$ (‰ VSMOW)	Isoscape Residual (‰ VSMOW)
AK092	-20.0	-19.4	0.6
AK093	-22.5	-19.1	3.4
AK094	-17.7	-19.1	-1.3
AK095	-21.8	-18.9	2.9
AK096	-18.6	-19.0	-0.4
AK097	-19.9	-19.5	0.4
AK098	-20.4	-19.1	1.3
AK099	-18.6	-19.2	-0.6
AK100	-19.1	-19.2	-0.1
AK101	-19.4	-19.2	0.1
AK102	-23.4	-19.1	4.3
AK103	-22.6	-19.3	3.2
AK104	-20.7	-19.3	1.4
AK105	-21.0	-19.8	1.2
AK106	-20.3	-18.7	1.5
AK108	-20.5	-18.7	1.7
AK109	-20.6	-19.0	1.6
AK110	-20.8	-19.2	1.6
AK111	-19.9	-18.8	1.1
AK112	-18.8	-18.8	0.0
AK113	-18.5	-18.8	-0.3
AK114	-18.6	-17.4	1.2
AK115	-17.3	-16.4	0.9
AK117	-15.9	-16.4	-0.5
AK118	-16.3	-16.4	-0.2
AK119	-17.2	-16.2	1.0
AK120	-18.4	-17.0	1.3
AK121	-19.4	-18.4	1.0
AK122	-19.0	-17.7	1.2
AK123	-17.7	-17.8	-0.2
AK124	-18.5	-18.3	0.3
AK125	-17.7	-18.2	-0.5
AK126	-15.9	-18.7	-2.8
AK127	-16.4	-19.0	-2.6
AK128	-17.3	-18.8	-1.5
AK129	-16.7	-18.5	-1.8
AK130	-16.5	-18.5	-2.0
AK131	-15.2	-18.3	-3.1
AK132	-15.9	-18.1	-2.2
AK134	-18.1	-16.8	1.3
AK136	-19.2	-17.2	2.0
AK137	-18.3	-16.5	1.8

Sample ID	$\delta^{18}\text{O}$ (‰ VSMOW)	Isoscape $\delta^{18}\text{O}$ (‰ VSMOW)	Isoscape Residual (‰ VSMOW)
AK138	-18.6	-17.0	1.5
AK139	-18.0	-18.2	-0.1
AK140	-15.7	-16.7	-1.0
AK141	-16.0	-16.7	-0.7
AK142	-16.4	-17.0	-0.6
AK143	-17.3	-16.7	0.5
AK144	-17.9	-18.2	-0.3
AK145	-18.2	-18.2	0.0
AK146	-18.0	-19.0	-1.0
AK147	-17.9	-19.0	-1.0
AK148	-18.7	-18.9	-0.3
AK149	-18.7	-18.2	0.5
AK150	-19.5	-20.0	-0.4
AK151	-19.5	-19.4	0.1
AK152	-21.7	-19.5	2.2
AK153	-22.1	-19.5	2.6
AK155	-20.5	-19.7	0.8
AK156	-20.8	-19.7	1.1
AK157	-21.4	-20.0	1.5
AK158	-23.4	-19.6	3.9
AK159	-24.1	-20.0	4.1
AK160	-21.5	-20.4	1.1
AK161	-22.5	-20.3	2.1
AK162	-21.3	-20.6	0.7
AK163	-22.4	-20.9	1.5
AK164	-19.3	-20.9	-1.5
AK165	-17.6	-20.7	-3.0
AK166	-16.6	-20.6	-4.0
AK167	-21.2	-20.4	0.8
AK168	-20.6	-20.4	0.2
AK169	-21.0	-20.8	0.2
AK170	-21.3	-20.6	0.7
AK171	-21.2	-20.3	0.9
AK172	-20.9	-19.7	1.2
AK173	-21.4	-19.7	1.7
AK174	-20.5	-19.4	1.1
AK175	-20.7	-19.4	1.3
AK176	-20.1	-20.6	-0.4
AK177	-19.1	-20.6	-1.5
AK178	-19.0	-20.6	-1.5
AK179	-18.5	-20.6	-2.0
AK180	-18.7	-19.9	-1.3

Sample ID	$\delta^{18}\text{O}$ (‰ VSMOW)	Isoscape $\delta^{18}\text{O}$ (‰ VSMOW)	Isoscape Residual (‰ VSMOW)
AK181	-18.3	-19.1	-0.7
AK182	-18.7	-19.0	-0.3
AK183	-18.7	-19.7	-1.0
AK184	-18.8	-20.0	-1.1
AK185	-18.4	-15.8	2.6
AK186	-17.6	-18.4	-0.8
AK187	-16.2	-17.2	-1.0
AK188	-17.0	-18.4	-1.4
AK189	-17.8	-19.7	-1.9
AK190	-20.9	-20.3	0.6
AK191	-21.8	-20.2	1.6
AK192	-22.3	-20.5	1.8
AK193	-21.5	-19.8	1.7
AK194	-21.5	-19.8	1.7
AK195	-18.0	-20.4	-2.4
AK196	-18.5	-20.7	-2.2
AK197	-18.7	-20.7	-1.9
AK198	-20.9	-20.7	0.2
AK199	-16.4	-20.8	-4.4
AK200	-17.7	-20.8	-3.1
AK201	-18.7	-21.0	-2.3
AK202	-21.2	-21.2	0.0
AK203	-20.3	-21.4	-1.0
AK204	-20.6	-21.4	-0.8
AK205	-21.0	-21.4	-0.4
AK206	-21.0	-20.7	0.3
AK207	-21.1	-21.9	-0.8
AK208	-21.1	-21.4	-0.3
AK209	-20.8	-20.7	0.1
AK211	-22.8	-20.7	2.1
AK212	-22.9	-21.8	1.1
AK213	-21.7	-20.9	0.8
AK214	-21.6	-20.8	0.8
AK215	-21.3	-21.1	0.1
AK216	-21.6	-21.0	0.6
AK217	-21.4	-21.5	-0.1
AK218	-21.3	-21.8	-0.5
AK219	-21.7	-21.5	0.3
AK220	-20.9	-21.6	-0.6
AK221	-20.3	-21.4	-1.1
AK222	-22.8	-21.4	1.5
AK223	-22.3	-21.4	0.9

Sample ID	$\delta^{18}\text{O}$ (‰ VSMOW)	Isoscape $\delta^{18}\text{O}$ (‰ VSMOW)	Isoscape Residual (‰ VSMOW)
AK224	-24.3	-21.2	3.1
AK225	-20.2	-21.4	-1.2
AK226	-19.5	-21.4	-1.9
AK227	-19.2	-21.4	-2.2
AK228	-20.2	-21.3	-1.1
AK229	-22.1	-21.3	0.8
AK230	-19.1	-21.4	-2.3
AK231	-19.9	-21.3	-1.4
AK232	-26.0	-21.7	4.3
AK233	-22.0	-21.1	0.9
AK235	-21.2	-21.1	0.1
AK236	-23.0	-21.0	2.0
AK237	-22.5	-21.0	1.5
AK238	-25.9	-20.8	5.1
AK239	-22.9	-21.0	1.9
AK240	-23.1	-21.4	1.7
AK241	-24.1	-21.0	3.1
AK242	-23.2	-21.0	2.2
AK243	-23.3	-20.6	2.8
AK244	-23.1	-21.1	2.0
AK245	-25.0	-20.4	4.6
AK246	-23.3	-20.6	2.8
AK247	-20.9	-20.5	0.3
AK248	-21.7	-20.4	1.3
AK249	-20.0	-20.3	-0.3
AK250	-21.7	-21.0	0.7
AK251	-20.0	-20.1	-0.1
AK252	-21.5	-19.6	1.9
AK253	-19.9	-19.6	0.3
AK254	-20.6	-19.3	1.3
AK255	-21.1	-19.3	1.8
AK256	-20.7	-18.8	1.9
AK257	-20.5	-18.7	1.8
AK258	-19.4	-18.7	0.7
AK259	-19.7	-18.8	0.9
AK260	-19.0	-18.2	0.8
AK261	-18.3	-18.2	0.1
AK262	-19.3	-18.2	1.0
AK264	-17.1	-17.6	-0.4
AK265	-16.1	-17.6	-1.5
AK266	-18.6	-15.7	2.9
AK267	-19.3	-16.4	2.9

Sample ID	$\delta^{18}\text{O}$ (‰ VSMOW)	Isoscape $\delta^{18}\text{O}$ (‰ VSMOW)	Isoscape Residual (‰ VSMOW)
AK268	-18.7	-15.3	3.3
AK269	-18.5	-15.3	3.1
AK270	-18.4	-15.3	3.0
AK271	-19.1	-15.3	3.7
AK272	-13.5	-15.3	-1.9
AK273	-13.5	-15.0	-1.6
AK274	-13.7	-15.9	-2.1
AK275	-12.8	-14.2	-1.4
AK276	-13.0	-14.8	-1.9
AK277	-13.4	-14.2	-0.7
AK278	-14.2	-14.2	0.0
AK279	-13.7	-14.4	-0.7
AK280	-13.1	-14.4	-1.3
AK281	-16.8	-14.6	2.2
AK282	-13.8	-14.6	-0.8
AK283	-15.0	-14.1	0.9
AK284	-14.3	-14.1	0.2
AK285	-15.7	-14.9	0.7
AK286	-15.1	-14.6	0.5
AK287	-11.9	-14.5	-2.6
AK288	-13.4	-17.0	-3.7
AK289	-15.7	-15.8	-0.1
AK290	-15.1	-14.1	1.0
AK291	-17.4	-14.9	2.4
AK292	-13.6	-14.9	-1.3
AK293	-14.1	-15.0	-1.0
AK294	-13.7	-14.2	-0.5
AK295	-13.5	-14.2	-0.7
AK296	-12.5	-14.8	-2.3
AK297	-17.4	-15.8	1.6
AK298	-14.1	-15.9	-1.8
AK299	-14.0	-14.6	-0.6
AK300	-8.1	-14.5	-6.4
AK301	-13.9	-14.2	-0.3
AK302	-14.9	-14.2	0.7
AK303	-13.5	-14.4	-0.9
AK304	-15.3	-14.6	0.7
AK305	-15.0	-15.8	-0.8
AK306	-14.1	-14.4	-0.2
AK307	-11.9	-14.4	-2.5
AK308	-13.5	-14.6	-1.1
AK309	-13.4	-17.0	-3.6

Sample ID	$\delta^{18}\text{O}$ (‰ VSMOW)	Isoscape $\delta^{18}\text{O}$ (‰ VSMOW)	Isoscape Residual (‰ VSMOW)
AK310	-17.3	-14.6	2.7
AK311	-14.1	-14.6	-0.5
AK312	-16.1	-14.2	2.0
AK313	-12.5	-14.2	-1.7
AK314	-12.4	-14.2	-1.8
AK315	-11.5	-14.2	-2.7
AK316	-12.6	-14.4	-1.8
AK317	-14.4	-14.1	0.3
AK319	-15.6	-15.8	-0.2
AK320	-15.4	-15.8	-0.4
AK321	-12.5	-15.0	-2.5
AK322	-10.8	-14.5	-3.7
AK340	-14.7	-14.2	0.5
AK341	-14.3	-14.2	0.2
AK342	-15.0	-14.8	0.2
AK343	-14.9	-14.8	0.1
AK344	-14.6	-14.6	0.1
AK345	-15.2	-14.6	0.6
AK346	-15.0	-16.1	-1.1
AK347	-13.5	-16.1	-2.6
AK348	-14.4	-15.6	-1.2
AK349	-13.4	-14.6	-1.2
AK350	-15.8	-14.6	1.2
AK351	-19.8	-14.9	4.9
AK352	-16.8	-14.9	1.8
AK353	-17.2	-14.9	2.3
AK354	-16.5	-14.9	1.5
AK355	-17.1	-15.8	1.3
AK360	-21.8	-19.3	2.5
AK361	-20.5	-19.3	1.1
AK362	-20.5	-21.1	-0.6
AK363	-20.4	-21.1	-0.8
AK364	-20.7	-21.4	-0.7
AK365	-20.7	-21.4	-0.7
AK366	-20.5	-19.3	1.2
AK367	-20.0	-19.3	0.7
AK368	-19.2	-20.2	-1.0
AK369	-19.4	-20.2	-0.8
AK379	-20.2	-20.9	-0.8
AK380	-23.2	-21.4	1.8
AK381	-21.6	-21.2	0.4
AK382	-22.2	-21.4	0.7

Sample ID	$\delta^{18}\text{O}$ (‰ VSMOW)	Isoscape $\delta^{18}\text{O}$ (‰ VSMOW)	Isoscape Residual (‰ VSMOW)
AK383	-21.8	-21.8	0.0
AK384	-22.7	-22.4	0.3
AK385	-22.8	-22.2	0.6
AK386	-20.8	-22.1	-1.2
AK387	-21.6	-22.5	-0.9
AK388	-21.4	-22.5	-1.0
AK389	-24.2	-23.6	0.6
AK390	-24.4	-23.6	0.8
AK391	-24.9	-23.6	1.3
AK392	-24.7	-23.6	1.1
AK393	-25.5	-23.0	2.5
AK394	-25.1	-23.0	2.1
AK395	-25.6	-23.1	2.5
AK396	-22.5	-22.7	-0.2
AK397	-22.6	-22.8	-0.2
AK398	-23.2	-23.1	0.1
AK399	-23.2	-22.7	0.5
AK400	-23.0	-22.8	0.3
AK401	-22.6	-22.6	0.0
AK402	-23.0	-22.7	0.4
AK403	-21.8	-22.7	-0.9
AK404	-21.8	-22.8	-1.0
AK405	-22.1	-22.8	-0.7
AK406	-21.6	-22.9	-1.3
AK407	-20.5	-22.7	-2.1
AK408	-22.2	-21.5	0.6
AK409	-20.5	-21.5	-1.0
AK410	-21.6	-21.4	0.2
AK411	-21.3	-21.3	0.1
AK412	-22.4	-21.1	1.3
AK413	-18.5	-20.6	-2.1
AK414	-18.7	-20.8	-2.1
AK415	-22.1	-20.8	1.3
AK416	-21.5	-20.7	0.8
AK417	-19.7	-20.6	-0.9
AK418	-20.0	-20.6	-0.6
AK419	-20.1	-20.6	-0.5
AK420	-20.3	-20.6	-0.2
AK421	-19.6	-20.6	-1.1
AK422	-19.9	-21.1	-1.2
AK423	-19.2	-20.4	-1.1
AK424	-18.4	-20.4	-2.1



Sample ID	$\delta^{18}\text{O}$ (‰ VSMOW)	Isoscape $\delta^{18}\text{O}$ (‰ VSMOW)	Isoscape Residual (‰ VSMOW)
AK425	-19.4	-20.4	-1.0
AK426	-19.2	-20.8	-1.5
AK427	-20.4	-20.7	-0.3
AK428	-19.9	-20.7	-0.8
AK429	-19.7	-21.3	-1.6
AK430	-19.8	-21.0	-1.2
AK431	-19.8	-21.7	-1.9
AK432	-19.5	-21.7	-2.2
AK433	-19.8	-21.7	-1.9
AK434	-19.9	-20.6	-0.7
AK435	-20.2	-20.6	-0.5
AK436	-19.9	-21.0	-1.1
AK437	-20.0	-20.6	-0.7
AK438	-20.4	-21.1	-0.7
AK439	-19.9	-20.9	-1.0
AK440	-20.4	-20.6	-0.2
AK441	-20.3	-20.6	-0.2
AK442	-19.9	-20.4	-0.5
AK443	-19.1	-20.4	-1.4
AK444	-20.0	-20.4	-0.4
AK445	-20.1	-20.6	-0.4
AK446	-19.8	-20.6	-0.8
AK447	-20.3	-20.4	-0.1

## Appendix D: Ice wedge stable isotope values

Sample ID	Distance from Left Edge (cm)	Distance from Center (cm)	$\delta^{18}\text{O}$ (‰ VSMOW)	$\delta\text{D}$ (‰ VSMOW)	dx
1N-1	0.2	-15.1	-22.9	-183.3	0.3
1N-3	0.6	-14.7	-22.7	-182.8	-0.9
1N-5	1.0	-14.3	-23.4	-185.4	1.8
1N-7	1.4	-13.9	-23.2	-184.5	1.5
1N-9	1.8	-13.5	-23.5	-185.1	3.2
1N-11	2.2	-13.1	-23.6	-187.2	1.7
1N-13	2.6	-12.7	-23.7	-188.3	1.0
1N-15	3.0	-12.3	-24.1	-190.6	2.3
1N-17	3.4	-11.9	-24.0	-191.4	0.8
1N-19	3.8	-11.5	-24.2	-194.1	-0.7
1N-21	4.2	-11.1	-24.2	-194.7	-1.0
1N-23	4.6	-10.7	-24.2	-193.0	0.7
1N-25	5.0	-10.3	-24.7	-195.7	1.6
1N-27	5.4	-9.9	-24.6	-196.8	-0.2
1N-29	5.8	-9.5	-24.7	-199.0	-1.6
1N-31	6.2	-9.1	-24.6	-199.9	-3.5
1N-33	6.6	-8.7	-25.0	-200.7	-0.8
1N-35	7.0	-8.3	-24.8	-199.7	-1.6
1N-37	7.4	-7.9	-24.8	-197.8	0.9
1N-39	7.8	-7.5	-24.8	-200.5	-2.0
1N-41	8.2	-7.1	-25.1	-202.0	-1.0
1N-43	8.6	-6.7	-24.7	-199.0	-1.2
1N-45	9.0	-6.3	-25.1	-202.2	-1.0
1N-47	9.4	-5.9	-25.1	-202.5	-1.6
1N-49	9.8	-5.5	-25.3	-203.4	-1.2
1N-51	10.2	-5.1	-25.4	-204.7	-1.2
1N-53	10.6	-4.7	-25.5	-206.4	-2.2
1N-55	11.0	-4.3	-25.6	-203.6	1.2
1N-57	11.4	-3.9	-25.5	-205.5	-1.2
1N-59	11.8	-3.5	-25.3	-206.3	-4.1
1N-61	12.2	-3.1	-26.0	-206.0	1.6
1N-63	12.6	-2.7	-25.6	-207.3	-2.3
1N-65	13.0	-2.3	-25.6	-206.6	-1.7
1N-67	13.4	-1.9	-25.7	-206.7	-1.4
1N-69	13.8	-1.5	-25.5	-207.2	-3.2
1N-71	14.2	-1.1	-25.6	-207.8	-2.8
1N-73	14.6	-0.7	-25.7	-208.2	-2.5
1N-75	15.0	-0.3	-25.5	-206.7	-2.4
1N-77	15.4	0.1	-25.6	-208.2	-3.6
1N-79	15.8	0.5	-25.7	-208.0	-2.7
1N-81	16.2	0.9	-25.7	-209.5	-3.8
1N-83	16.6	1.3	-25.7	-207.6	-2.3
1N-85	17.0	1.7	-25.8	-207.2	-0.6
1N-87	17.4	2.1	-25.6	-208.2	-3.8
1N-89	17.8	2.5	-25.8	-208.8	-2.3
1N-91	18.2	2.9	-25.7	-209.3	-3.9

Sample ID	Distance from Left Edge (cm)	Distance from Center (cm)	$\delta^{18}\text{O}$ (‰ VSMOW)	$\delta\text{D}$ (‰ VSMOW)	dx
1N-93	18.6	3.3	-25.8	-210.0	-3.3
1N-95	19.0	3.7	-25.7	-208.1	-2.8
1N-97	19.4	4.1	-25.9	-209.0	-1.9
1N-99	19.8	4.5	-25.8	-208.1	-1.6
1N-101	20.2	4.9	-25.8	-209.4	-3.3
1N-103	20.6	5.3	-26.0	-210.6	-2.5
1N-105	21.0	5.7	-25.8	-208.0	-1.9
1N-107	21.4	6.1	-26.0	-208.9	-1.0
1N-109	21.8	6.5	-25.8	-208.4	-1.7
1N-111	22.2	6.9	-25.9	-208.3	-0.8
1N-113	22.6	7.3	-25.8	-206.9	-0.4
1N-115	23.0	7.7	-25.9	-207.1	0.4
1N-117	23.4	8.1	-25.7	-207.4	-1.8
1N-119	23.8	8.5	-25.6	-206.2	-1.1
1N-121	24.2	8.9	-25.8	-208.3	-2.1
1N-123	24.6	9.3	-25.8	-207.0	-0.7
1N-125	25.0	9.7	-25.6	-206.3	-1.7
1N-127	25.4	10.1	-25.4	-206.2	-2.7
1N-129	25.8	10.5	-25.3	-204.3	-1.5
1N-131	26.2	10.9	-25.6	-205.4	-0.8
1N-133	26.6	11.3	-25.2	-203.1	-1.4
1N-135	27.0	11.7	-25.1	-202.0	-0.9
1N-137	27.4	12.1	-25.3	-203.0	-0.6
1N-139	27.8	12.5	-24.9	-201.3	-2.4
1N-141	28.2	12.9	-25.5	-204.1	-0.3
1N-143	28.6	13.3	-25.0	-202.3	-2.2
1N-145	29.0	13.7	-24.8	-199.2	-1.1
1N-147	29.4	14.1	-24.9	-200.5	-1.6
1N-149	29.8	14.5	-24.7	-199.5	-2.2
1N-151	30.2	14.9	-24.4	-197.3	-2.0
1N-153	30.6	15.3	-24.4	-198.4	-3.5
14.9SW-001	0.2	-2.1	-20.4	-163.8	-0.5
14.9SW-003	0.6	-1.7	-21.0	-166.3	1.7
14.9SW-005	1.0	-1.3	-20.7	-165.6	0.3
14.9SW-007	1.4	-0.9	-20.6	-164.3	0.8
14.9SW-009	1.8	-0.5	-20.8	-165.7	0.5
14.9SW-011	2.2	-0.1	-20.5	-164.8	-0.4
14.9SW-013	2.6	0.3	-20.7	-165.1	0.3
14.9SW-015	3.0	0.7	-20.4	-163.7	-0.6
14.9SW-017	3.4	1.1	-20.5	-164.2	0.0
14.9SW-019	3.8	1.5	-20.6	-165.5	-0.4
14.9SW-021	4.2	1.9	-20.6	-164.3	0.7
14.9SW-023	4.6	2.3	-20.5	-164.7	-0.9

Sample ID	Distance from Left Edge (cm)	Distance from Center (cm)	$\delta^{18}\text{O}$ (‰ VSMOW)	$\delta\text{D}$ (‰ VSMOW)	dx
18N-001	0.2	-9.1	-26.5	-209.9	1.8
18N-003	0.6	-8.7	-27.2	-213.2	4.3
18N-005	1.0	-8.3	-27.2	-214.3	3.2
18N-007	1.4	-7.9	-27.5	-215.7	4.6
18N-009	1.8	-7.5	-27.6	-216.7	3.8
18N-011	2.2	-7.1	-28.0	-219.6	4.6
18N-013	2.6	-6.7	-27.4	-218.0	0.9
18N-015	3.0	-6.3	-28.0	-220.3	3.4
18N-017	3.4	-5.9	-28.2	-221.5	4.1
18N-019	3.8	-5.5	-28.1	-221.5	3.2
18N-021	4.2	-5.1	-28.4	-223.4	3.6
18N-023	4.6	-4.7	-28.5	-223.9	4.0
18N-025	5.0	-4.3	-28.6	-223.3	5.9
18N-027	5.4	-3.9	-28.8	-225.0	5.7
18N-029	5.8	-3.5	-28.7	-225.3	3.9
18N-031	6.2	-3.1	-28.9	-226.5	5.0
18N-033	6.6	-2.7	-28.9	-225.7	5.8
18N-035	7.0	-2.3	-28.7	-225.3	3.9
18N-037	7.4	-1.9	-28.8	-225.0	5.2
18N-039	7.8	-1.5	-28.5	-225.1	3.2
18N-041	8.2	-1.1	-28.5	-224.6	3.6
18N-043	8.6	-0.7	-28.6	-226.0	2.8
18N-045	9.0	-0.3	-28.7	-225.3	4.3
18N-047	9.4	0.1	-28.5	-224.6	3.7
18N-049	9.8	0.5	-28.5	-225.6	2.7
18N-051	10.2	0.9	-28.9	-224.4	6.8
18N-053	10.6	1.3	-28.6	-222.9	6.0
18N-055	11.0	1.7	-28.5	-222.8	5.5
18N-057	11.4	2.1	-27.9	-221.0	2.0
18N-059	11.8	2.5	-28.1	-220.7	3.9
18N-061	12.2	2.9	-27.8	-218.0	4.6
18N-063	12.6	3.3	-27.7	-218.2	3.8
18N-065	13.0	3.7	-27.7	-217.9	3.6
18N-067	13.4	4.1	-27.7	-217.5	4.3
18N-069	13.8	4.5	-27.5	-215.8	4.2
18N-071	14.2	4.9	-27.9	-216.4	6.5
18N-073	14.6	5.3	-27.4	-214.0	5.5
18N-075	15.0	5.7	-27.0	-213.0	3.0
18N-077	15.4	6.1	-26.7	-209.6	4.1
18N-079	15.8	6.5	-26.8	-211.1	3.3
18N-081	16.2	6.9	-26.5	-208.8	3.2
18N-083	16.6	7.3	-26.5	-209.6	2.5
18N-085	17.0	7.7	-26.3	-206.5	3.8

Sample ID	Distance from Left Edge (cm)	Distance from Center (cm)	$\delta^{18}\text{O}$ (‰ VSMOW)	$\delta\text{D}$ (‰ VSMOW)	dx
18N-087	17.4	8.1	-26.2	-205.2	4.5
18N-089	17.8	8.5	-26.3	-206.2	4.4
18N-091	18.2	8.9	-26.4	-207.7	3.5
18N-093	18.6	9.3	-26.2	-205.9	3.4
21.5N	N/A	N/A	-23.9	-188.4	3.1
35S-1	0.2	-75.9	-23.6	-193.2	-4.1
35S-3	0.6	-75.5	-23.2	-189.7	-4.0
35S-5	1.0	-75.1	-23.7	-193.4	-4.0
35S-7	1.4	-74.7	-23.9	-194.2	-3.1
35S-9	1.8	-74.3	-23.9	-194.3	-2.8
35S-11	2.2	-73.9	-23.9	-194.3	-3.2
35S-13	2.6	-73.5	-24.1	-193.5	-0.7
35S-15	3.0	-73.1	-24.0	-194.9	-2.9
35S-17	3.4	-72.7	-24.0	-195.7	-4.1
35S-19	3.8	-72.3	-24.1	-195.7	-2.7
35S-21	4.2	-71.9	-24.2	-196.7	-3.3
35S-23	4.6	-71.5	-24.1	-196.3	-3.3
35S-25	5.0	-71.1	-24.5	-198.2	-2.3
35S-27	5.4	-70.7	-24.7	-199.7	-1.8
35S-29	5.8	-70.3	-24.4	-197.9	-2.7
35S-31	6.2	-69.9	-24.3	-197.7	-3.3
35S-33	6.6	-69.5	-24.4	-198.4	-2.9
35S-35	7.0	-69.1	-24.7	-199.5	-2.1
35S-37	7.4	-68.7	-24.7	-199.9	-2.5
35S-39	7.8	-68.3	-24.6	-199.2	-2.1
35S-41	8.2	-67.9	-24.6	-198.5	-1.9
35S-43	8.6	-67.5	-24.9	-199.9	-1.0
35S-45	9.0	-67.1	-24.9	-201.1	-2.3
35S-47	9.4	-66.7	-25.0	-203.2	-3.1
35S-49	9.8	-66.3	-25.1	-203.5	-2.4
35S-51	10.2	-65.9	-25.1	-202.8	-1.9
35S-53	10.6	-65.5	-24.7	-201.0	-3.1
35S-55	11.0	-65.1	-25.2	-202.7	-1.1
35S-57	11.4	-64.7	-24.9	-202.5	-3.5
35S-59	11.8	-64.3	-25.0	-202.0	-1.7
35S-61	12.2	-63.9	-25.3	-203.8	-1.5
35S-63	12.6	-63.5	-25.2	-203.6	-2.1
35S-65	13.0	-63.1	-25.4	-205.4	-2.3
35S-67	13.4	-62.7	-25.4	-207.3	-4.2
35S-69	13.8	-62.3	-25.2	-205.0	-3.3
35S-71	14.2	-61.9	-25.4	-204.5	-1.4
35S-73	14.6	-61.5	-25.3	-206.2	-3.7
35S-75	15.0	-61.1	-25.4	-205.4	-1.8

Sample ID	Distance from Left Edge (cm)	Distance from Center (cm)	$\delta^{18}\text{O}$ (‰ VSMOW)	$\delta\text{D}$ (‰ VSMOW)	dx
35S-77	15.4	-60.7	-25.2	-203.8	-2.0
35S-79	15.8	-60.3	-25.2	-204.3	-2.6
35S-81	16.2	-59.9	-25.7	-206.2	-0.6
35S-83	16.6	-59.5	-25.5	-206.4	-2.6
35S-85	17.0	-59.1	-25.5	-206.7	-2.9
35S-87	17.4	-58.7	-25.9	-208.3	-1.2
35S-89	17.8	-58.3	-25.9	-207.8	-0.5
35S-91	18.2	-57.9	-25.7	-205.8	-0.1
35S-93	18.6	-57.5	-25.7	-207.6	-1.6
35S-95	19.0	-57.1	-25.7	-207.0	-1.2
35S-97	19.4	-56.7	-25.7	-206.7	-1.2
35S-99	19.8	-56.3	-26.0	-209.0	-1.4
35S-101	20.2	-55.9	-26.0	-208.3	-0.1
35S-103	20.6	-55.5	-25.9	-208.9	-1.8
35S-105	21.0	-55.1	-25.8	-207.6	-1.4
35S-107	21.4	-54.7	-26.4	-210.5	0.8
35S-109	21.8	-54.3	-25.9	-208.3	-1.0
35S-111	22.2	-53.9	-26.2	-210.7	-0.9
35S-113	22.6	-53.5	-25.8	-207.3	-0.5
35S-115	23.0	-53.1	-26.1	-209.4	-0.7
35S-117	23.4	-52.7	-26.0	-210.7	-2.8
35S-119	23.8	-52.3	-26.0	-210.0	-2.3
35S-121	24.2	-51.9	-26.1	-209.8	-1.0
35S-123	24.6	-51.5	-26.0	-209.3	-1.3
35S-125	25.0	-51.1	-26.0	-209.7	-1.9
35S-127	25.4	-50.7	-26.2	-211.0	-1.1
35S-129	25.8	-50.3	-26.1	-210.4	-1.8
35S-131	26.2	-49.9	-26.3	-210.3	0.4
35S-133	26.6	-49.5	-26.2	-210.0	-0.7
35S-135	27.0	-49.1	-26.0	-210.3	-2.2
35S-137	27.4	-48.7	-26.0	-209.1	-1.2
35S-139	27.8	-48.3	-25.9	-207.8	-0.4
35S-141	28.2	-47.9	-26.2	-209.0	0.5
35S-143	28.6	-47.5	-26.2	-210.5	-0.9
35S-145	29.0	-47.1	-26.1	-208.7	-0.2
35S-147	29.4	-46.7	-26.3	-211.6	-1.0
35S-149	29.8	-46.3	-26.3	-210.3	0.1
35S-151	30.2	-45.9	-25.8	-207.5	-1.1
35S-153	30.6	-45.5	-25.8	-208.5	-1.9
35S-155	31.0	-45.1	-25.8	-207.9	-1.2
35S-157	31.4	-44.7	-25.9	-208.1	-0.8
35S-159	31.8	-44.3	-25.7	-207.3	-1.7
35S-161	32.2	-43.9	-25.8	-206.6	0.1

Sample ID	Distance from Left Edge (cm)	Distance from Center (cm)	$\delta^{18}\text{O}$ (‰ VSMOW)	$\delta\text{D}$ (‰ VSMOW)	dx
35S-163	32.6	-43.5	-25.8	-208.2	-1.7
35S-165	33.0	-43.1	-26.1	-209.6	-0.9
35S-167	33.4	-42.7	-26.2	-210.8	-1.5
35S-169	33.8	-42.3	-25.9	-207.2	-0.2
35S-171	34.2	-41.9	-25.8	-208.1	-1.9
35S-173	34.6	-41.5	-25.9	-208.4	-1.3
35S-175	35.0	-41.1	-25.9	-208.9	-1.8
35S-177	35.4	-40.7	-26.1	-209.3	-0.6
35S-179	35.8	-40.3	-25.9	-208.1	-1.1
35S-181	36.2	-39.9	-25.9	-207.9	-0.4
35S-183	36.6	-39.5	-25.9	-208.2	-0.9
35S-185	37.0	-39.1	-26.1	-209.3	-0.5
35S-187	37.4	-38.7	-26.1	-211.9	-3.4
35S-189	37.8	-38.3	-25.7	-208.0	-2.3
35S-191	38.2	-37.9	-25.9	-208.5	-1.1
35S-193	38.6	-37.5	-25.8	-208.4	-2.0
35S-195	39.0	-37.1	-25.8	-209.1	-2.7
35S-197	39.4	-36.7	-25.8	-206.8	-0.7
35S-199	39.8	-36.3	-26.1	-209.4	-0.7
35S-201	40.2	-35.9	-26.1	-210.2	-1.4
35S-203	40.6	-35.5	-26.0	-210.1	-2.2
35S-205	41.0	-35.1	-26.3	-212.5	-1.8
35S-207	41.4	-34.7	-26.5	-214.8	-2.7
35S-209	41.8	-34.3	-26.2	-212.5	-2.6
35S-211	42.2	-33.9	-26.5	-213.1	-1.3
35S-213	42.6	-33.5	-26.5	-213.4	-1.3
35S-215	43.0	-33.1	-26.3	-211.9	-1.2
35S-217	43.4	-32.7	-26.4	-212.3	-1.4
35S-219	43.8	-32.3	-26.4	-212.5	-1.6
35S-221	44.2	-31.9	-26.2	-210.5	-0.8
35S-223	44.6	-31.5	-26.3	-211.2	-1.2
35S-225	45.0	-31.1	-26.4	-211.4	-0.4
35S-227	45.4	-30.7	-26.4	-215.9	-4.6
35S-229	45.8	-30.3	-26.4	-213.3	-2.1
35S-231	46.2	-29.9	-26.4	-212.3	-1.3
35S-233	46.6	-29.5	-26.3	-213.2	-2.5
35S-235	47.0	-29.1	-26.4	-212.1	-1.2
35S-237	47.4	-28.7	-26.4	-212.1	-1.1
35S-239	47.8	-28.3	-26.5	-212.7	-0.7
35S-241	48.2	-27.9	-26.3	-211.7	-1.3
35S-243	48.6	-27.5	-26.2	-212.1	-2.3
35S-245	49.0	-27.1	-26.4	-212.2	-1.4
35S-247	49.4	-26.7	-26.5	-215.0	-3.2



Sample ID	Distance from Left Edge (cm)	Distance from Center (cm)	$\delta^{18}\text{O}$ (‰ VSMOW)	$\delta\text{D}$ (‰ VSMOW)	dx
35S-249	49.8	-26.3	-26.4	-212.9	-1.6
35S-251	50.2	-25.9	-26.4	-213.6	-2.7
35S-253	50.6	-25.5	-26.1	-211.4	-2.5
35S-255	51.0	-25.1	-26.4	-212.0	-1.2
35S-257	51.4	-24.7	-26.4	-212.4	-1.6
35S-259	51.8	-24.3	-26.3	-213.3	-3.0
35S-261	52.2	-23.9	-26.3	-212.4	-1.8
35S-263	52.6	-23.5	-26.4	-212.2	-0.9
35S-265	53.0	-23.1	-26.5	-214.0	-1.9
35S-269	53.8	-22.3	-26.4	-213.7	-2.4
35S-273	54.6	-21.5	-26.7	-214.2	-0.8
35S-277	55.4	-20.7	-26.7	-214.5	-0.9
35S-281	56.2	-19.9	-26.8	-213.7	0.4
35S-285	57.0	-19.1	-26.6	-212.9	-0.4
35S-289	57.8	-18.3	-26.4	-213.0	-1.7
35S-293	58.6	-17.5	-26.5	-214.1	-1.7
35S-297	59.4	-16.7	-26.6	-213.4	-0.8
35S-301	60.2	-15.9	-26.4	-213.3	-1.9
35S-305	61.0	-15.1	-26.4	-214.1	-2.7
35S-309	61.8	-14.3	-26.7	-216.6	-3.0
35S-313	62.6	-13.5	-26.3	-213.3	-2.8
35S-317	63.4	-12.7	-26.7	-213.8	-0.5
35S-321	64.2	-11.9	-26.3	-212.5	-1.8
35S-325	65.0	-11.1	-26.5	-213.4	-1.7
35S-329	65.8	-10.3	-26.5	-214.6	-2.2
35S-333	66.6	-9.5	-26.5	-213.1	-0.7
35S-337	67.4	-8.7	-26.4	-211.5	-0.1
35S-341	68.2	-7.9	-26.4	-213.4	-2.5
35S-345	69.0	-7.1	-26.4	-213.3	-2.4
35S-349	69.8	-6.3	-26.2	-211.6	-1.8
35S-353	70.6	-5.5	-26.1	-208.5	0.0
35S-357	71.4	-4.7	-26.1	-209.0	-0.3
35S-361	72.2	-3.9	-25.9	-207.7	-0.7
35S-365	73.0	-3.1	-25.7	-207.4	-1.6
35S-369	73.8	-2.3	-26.1	-214.5	-5.3
35S-373	74.6	-1.5	-26.2	-213.6	-4.1
35S-377	75.4	-0.7	-26.1	-212.4	-3.3
35S-381	76.2	0.1	-26.0	-209.2	-1.3
35S-385	77.0	0.9	-26.1	-213.0	-4.5
35S-389	77.8	1.7	-26.0	-214.6	-6.2
35S-393	78.6	2.5	-26.0	-213.3	-5.5
35S-397	79.4	3.3	-25.9	-209.4	-2.5
35S-401	80.2	4.1	-26.1	-210.1	-1.5

Sample ID	Distance from Left Edge (cm)	Distance from Center (cm)	$\delta^{18}\text{O}$ (‰ VSMOW)	$\delta\text{D}$ (‰ VSMOW)	dx
35S-405	81.0	4.9	-26.2	-213.5	-3.8
35S-409	81.8	5.7	-25.9	-211.6	-4.4
35S-413	82.6	6.5	-25.8	-210.6	-4.1
35S-417	83.4	7.3	-25.8	-206.0	0.3
35S-421	84.2	8.1	-25.7	-205.0	0.6
35S-425	85.0	8.9	-25.6	-204.9	0.3
35S-429	85.8	9.7	-25.9	-208.8	-1.3
35S-433	86.6	10.5	-25.8	-207.3	-0.6
35S-437	87.4	11.3	-25.9	-206.3	0.5
35S-441	88.2	12.1	-25.8	-204.9	1.2
35S-445	89.0	12.9	-25.7	-206.3	-0.8
35S-449	89.8	13.7	-25.5	-204.7	-0.6
35S-453	90.6	14.5	-25.9	-206.7	0.8
35S-457	91.4	15.3	-25.9	-205.4	1.7
35S-461	92.2	16.1	-25.7	-205.4	0.2
35S-465	93.0	16.9	-25.6	-205.8	-0.6
35S-469	93.8	17.7	-25.8	-204.2	2.3
35S-473	94.6	18.5	-25.6	-206.6	-1.5
35S-477	95.4	19.3	-25.7	-206.1	-0.2
35S-481	96.2	20.1	-25.6	-204.8	-0.1
35S-485	97.0	20.9	-25.5	-207.2	-3.4
35S-489	97.8	21.7	-25.5	-205.4	-1.4
35S-493	98.6	22.5	-25.3	-203.6	-1.2
35S-497	99.4	23.3	-25.2	-203.0	-1.3
35S-501	100.2	24.1	-25.2	-206.0	-4.1
35S-505	101.0	24.9	-25.1	-202.0	-1.1
35S-509	101.8	25.7	-25.6	-208.8	-3.6
35S-513	102.6	26.5	-25.3	-204.0	-1.7
35S-517	103.4	27.3	-25.2	-203.5	-2.3
35S-521	104.2	28.1	-24.5	-200.5	-4.4
35S-525	105.0	28.9	-24.5	-199.7	-3.6
35S-529	105.8	29.7	-24.5	-200.5	-4.8
35S-533	106.6	30.5	-24.5	-199.9	-3.6
35S-537	107.4	31.3	-24.4	-199.3	-4.5
35S-541	108.2	32.1	-24.4	-200.8	-6.0
35S-545	109.0	32.9	-24.6	-202.1	-5.6
35S-549	109.8	33.7	-24.5	-202.4	-6.0
35S-553	110.6	34.5	-24.7	-201.3	-4.0
35S-557	111.4	35.3	-24.8	-201.1	-2.8
35S-561	112.2	36.1	-24.9	-201.4	-2.5
35S-565	113.0	36.9	-24.3	-200.7	-6.2
35S-569	113.8	37.7	-24.5	-202.1	-5.8
35S-573	114.6	38.5	-24.9	-202.9	-3.5

Sample ID	Distance from Left Edge (cm)	Distance from Center (cm)	$\delta^{18}\text{O}$ (‰ VSMOW)	$\delta\text{D}$ (‰ VSMOW)	dx
35S-577	115.4	39.3	-24.9	-203.6	-4.8
35S-581	116.2	40.1	-24.7	-202.3	-4.7
35S-585	117.0	40.9	-24.8	-204.7	-6.3
35S-589	117.8	41.7	-25.2	-205.5	-4.1
35S-593	118.6	42.5	-25.1	-203.8	-3.4
35S-597	119.4	43.3	-25.0	-201.4	-1.7
35S-601	120.2	44.1	-25.0	-204.2	-4.0
35S-605	121.0	44.9	-25.0	-201.7	-1.6
35S-609	121.8	45.7	-25.3	-205.1	-2.3
35S-613	122.6	46.5	-25.1	-202.5	-1.8
35S-617	123.4	47.3	-25.4	-203.5	-0.7
35S-621	124.2	48.1	-25.0	-201.1	-0.8
35S-625	125.0	48.9	-25.2	-202.7	-1.1
35S-629	125.8	49.7	-25.4	-206.1	-3.2
35S-633	126.6	50.5	-25.2	-203.6	-2.3
35S-637	127.4	51.3	-25.1	-201.7	-0.9
35S-641	128.2	52.1	-24.7	-200.7	-3.4
35S-645	129.0	52.9	-25.1	-202.1	-1.3
35S-649	129.8	53.7	-24.9	-200.6	-1.2
35S-653	130.6	54.5	-24.9	-202.6	-3.6
35S-657	131.4	55.3	-24.7	-200.5	-2.5
35S-661	132.2	56.1	-24.8	-200.4	-1.6
35S-665	133.0	56.9	-24.6	-197.7	-1.1
35S-669	133.8	57.7	-24.6	-200.5	-3.7
35S-673	134.6	58.5	-24.6	-198.6	-2.1
35S-677	135.4	59.3	-24.2	-195.6	-1.9
35S-681	136.2	60.1	-24.0	-194.3	-2.4
35S-685	137.0	60.9	-24.2	-196.7	-3.2
35S-689	137.8	61.7	-24.1	-195.1	-2.3
35S-693	138.6	62.5	-24.0	-192.2	-0.4
35S-697	139.4	63.3	-24.0	-193.8	-2.1
35S-701	140.2	64.1	-23.5	-190.7	-2.7
35S-705	141.0	64.9	-23.7	-191.0	-1.2
35S-709	141.8	65.7	-23.6	-189.5	-0.6
35S-713	142.6	66.5	-23.5	-188.5	-0.5
35S-717	143.4	67.3	-23.3	-187.9	-1.5
35S-721	144.2	68.1	-23.1	-187.7	-3.0
35S-725	145.0	68.9	-23.4	-190.5	-3.4
35S-729	145.8	69.7	-22.9	-185.5	-2.0
35S-733	146.6	70.5	-22.8	-184.0	-1.7
35S-737	147.4	71.3	-22.4	-181.6	-2.6
35S-741	148.2	72.1	-22.5	-181.1	-0.8
35S-745	149.0	72.9	-22.3	-179.8	-1.3

Sample ID	Distance from Left Edge (cm)	Distance from Center (cm)	$\delta^{18}\text{O}$ (‰ VSMOW)	$\delta\text{D}$ (‰ VSMOW)	dx
35S-749	149.8	73.7	-22.4	-179.3	-0.4
35S-753	150.6	74.5	-22.4	-179.7	-0.3
35S-757	151.4	75.3	-21.9	-176.5	-1.1
35S-761	152.2	76.1	-21.8	-175.8	-1.4
45S-5	1.0	-53.7	-22.9	-187.1	-4.2
45S-9	1.8	-52.9	-23.7	-192.9	-3.4
45S-13	2.6	-52.1	-23.5	-191.4	-3.5
45S-17	3.4	-51.3	-23.6	-189.9	-1.4
45S-21	4.2	-50.5	-23.7	-190.4	-0.8
45S-25	5.0	-49.7	-24.4	-196.2	-1.3
45S-29	5.8	-48.9	-24.4	-196.4	-1.0
45S-33	6.6	-48.1	-24.5	-197.8	-2.0
45S-37	7.4	-47.3	-24.9	-199.2	0.1
45S-41	8.2	-46.5	-24.9	-204.5	-5.2
45S-45	9.0	-45.7	-25.3	-202.7	-0.6
45S-49	9.8	-44.9	-25.8	-205.8	0.4
45S-53	10.6	-44.1	-25.5	-205.0	-0.6
45S-57	11.4	-43.3	-25.5	-204.6	-0.5
45S-61	12.2	-42.5	-25.5	-204.0	0.0
45S-65	13.0	-41.7	-25.7	-205.8	0.1
45S-69	13.8	-40.9	-25.9	-210.4	-2.9
45S-73	14.6	-40.1	-25.9	-206.8	0.1
45S-77	15.4	-39.3	-25.8	-206.5	-0.1
45S-81	16.2	-38.5	-26.2	-212.8	-3.4
45S-85	17.0	-37.7	-26.1	-206.8	1.7
45S-89	17.8	-36.9	-25.7	-205.2	0.5
45S-93	18.6	-36.1	-25.7	-206.4	-0.7
45S-97	19.4	-35.3	-25.6	-205.5	-0.8
45S-101	20.2	-34.5	-25.9	-209.2	-1.7
45S-105	21.0	-33.7	-26.0	-208.7	-0.8
45S-109	21.8	-32.9	-26.2	-208.1	1.5
45S-113	22.6	-32.1	-26.4	-208.5	2.7
45S-117	23.4	-31.3	-26.7	-209.5	4.5
45S-121	24.2	-30.5	-26.7	-209.4	4.3
45S-125	25.0	-29.7	-27.0	-208.9	7.4
45S-129	25.8	-28.9	-26.6	-215.8	-2.8
45S-133	26.6	-28.1	-26.6	-215.1	-2.6
45S-137	27.4	-27.3	-26.5	-211.9	0.1
45S-141	28.2	-26.5	-26.2	-217.5	-7.6
45S-145	29.0	-25.7	-25.4	-206.4	-3.0
45S-149	29.8	-24.9	-26.5	-214.2	-1.8
45S-153	30.6	-24.1	-26.6	-212.4	0.5
45S-157	31.4	-23.3	-26.5	-213.1	-0.8

Sample ID	Distance from Left Edge (cm)	Distance from Center (cm)	$\delta^{18}\text{O}$ (‰ VSMOW)	$\delta\text{D}$ (‰ VSMOW)	dx
45S-161	32.2	-22.5	-26.7	-213.7	0.1
45S-165	33.0	-21.7	-26.9	-215.1	0.0
45S-169	33.8	-20.9	-27.1	-216.6	0.6
45S-173	34.6	-20.1	-26.2	-211.3	-2.0
45S-177	35.4	-19.3	-26.7	-211.0	2.8
45S-181	36.2	-18.5	-26.6	-211.5	0.9
45S-185	37.0	-17.7	-26.9	-213.5	1.8
45S-189	37.8	-16.9	-26.9	-215.3	-0.1
45S-193	38.6	-16.1	-26.5	-208.5	3.6
45S-197	39.4	-15.3	-27.0	-211.4	4.9
45S-201	40.2	-14.5	-27.3	-213.7	4.9
45S-205	41.0	-13.7	-26.7	-210.2	3.6
45S-209	41.8	-12.9	-26.8	-213.2	0.8
45S-213	42.6	-12.1	-27.0	-214.1	1.8
45S-217	43.4	-11.3	-27.2	-216.5	0.8
45S-221	44.2	-10.5	-27.0	-216.8	-0.8
45S-225	45.0	-9.7	-27.1	-216.3	0.9
45S-229	45.8	-8.9	-27.2	-216.6	1.2
45S-233	46.6	-8.1	-27.1	-215.5	1.3
45S-237	47.4	-7.3	-27.1	-216.8	-0.3
45S-241	48.2	-6.5	-26.9	-215.0	0.2
45S-245	49.0	-5.7	-27.1	-216.8	-0.3
45S-249	49.8	-4.9	-27.1	-216.9	-0.3
45S-253	50.6	-4.1	-27.0	-216.5	-0.4
45S-257	51.4	-3.3	-26.9	-215.9	-0.9
45S-261	52.2	-2.5	-26.8	-214.3	0.1
45S-265	53.0	-1.7	-27.0	-214.7	1.2
45S-269	53.8	-0.9	-27.0	-213.7	2.5
45S-273	54.6	-0.1	-27.1	-214.5	1.9
45S-277	55.4	0.7	-27.0	-215.0	0.8
45S-281	56.2	1.5	-26.9	-212.7	2.4
45S-285	57.0	2.3	-26.9	-215.2	0.4
45S-289	57.8	3.1	-26.9	-216.2	-0.7
45S-293	58.6	3.9	-26.6	-213.2	-0.4
45S-297	59.4	4.7	-26.5	-212.2	-0.3
45S-301	60.2	5.5	-26.7	-214.8	-0.9
45S-305	61.0	6.3	-27.0	-215.1	1.1
45S-309	61.8	7.1	-26.9	-215.4	-0.1
45S-313	62.6	7.9	-26.6	-212.5	0.4
45S-317	63.4	8.7	-26.6	-213.5	-1.0
45S-321	64.2	9.5	-26.8	-213.8	0.5
45S-325	65.0	10.3	-27.0	-215.5	0.2
45S-329	65.8	11.1	-26.8	-215.8	-1.6

Sample ID	Distance from Left Edge (cm)	Distance from Center (cm)	$\delta^{18}\text{O}$ (‰ VSMOW)	$\delta\text{D}$ (‰ VSMOW)	dx
45S-333	66.6	11.9	-26.8	-215.7	-1.0
45S-337	67.4	12.7	-26.4	-212.8	-1.7
45S-341	68.2	13.5	-26.9	-215.2	0.0
45S-345	69.0	14.3	-27.1	-215.9	0.6
45S-349	69.8	15.1	-26.7	-215.0	-1.6
45S-353	70.6	15.9	-26.7	-215.2	-1.7
45S-357	71.4	16.7	-26.7	-214.8	-0.9
45S-361	72.2	17.5	-26.8	-213.4	1.3
45S-365	73.0	18.3	-26.7	-212.5	0.8
45S-369	73.8	19.1	-27.1	-213.7	3.3
45S-373	74.6	19.9	-26.9	-210.6	4.5
45S-377	75.4	20.7	-26.6	-212.1	1.0
45S-381	76.2	21.5	-26.5	-208.9	2.9
45S-385	77.0	22.3	-26.6	-211.0	2.1
45S-389	77.8	23.1	-26.7	-211.6	1.7
45S-393	78.6	23.9	-26.8	-211.1	3.0
45S-397	79.4	24.7	-26.8	-211.7	3.0
45S-401	80.2	25.5	-26.7	-210.9	2.6
45S-405	81.0	26.3	-26.8	-212.4	2.2
45S-409	81.8	27.1	-27.0	-215.5	0.7
45S-413	82.6	27.9	-27.0	-214.7	1.4
45S-417	83.4	28.7	-26.8	-212.5	1.6
45S-421	84.2	29.5	-26.9	-214.2	1.4
45S-425	85.0	30.3	-26.9	-213.5	1.9
45S-429	85.8	31.1	-26.7	-210.8	2.5
45S-433	86.6	31.9	-26.9	-212.5	2.7
45S-437	87.4	32.7	-26.6	-212.1	1.1
45S-441	88.2	33.5	-26.6	-212.8	0.1
45S-445	89.0	34.3	-26.7	-212.1	1.1
45S-449	89.8	35.1	-27.2	-214.5	2.9
45S-453	90.6	35.9	-26.5	-210.9	1.3
45S-457	91.4	36.7	-26.7	-211.1	2.3
45S-461	92.2	37.5	-26.7	-211.2	2.3
45S-465	93.0	38.3	-26.8	-211.3	2.7
45S-469	93.8	39.1	-26.4	-209.3	1.6
45S-473	94.6	39.9	-26.3	-210.8	0.0
45S-477	95.4	40.7	-26.1	-207.9	1.2
45S-481	96.2	41.5	-26.5	-209.1	2.6
45S-485	97.0	42.3	-26.3	-208.5	2.1
45S-489	97.8	43.1	-26.1	-208.6	0.2
45S-493	98.6	43.9	-26.1	-206.0	2.8
45S-497	99.4	44.7	-25.9	-204.7	2.4
45S-501	100.2	45.5	-26.0	-204.4	3.6



Sample ID	Distance from Left Edge (cm)	Distance from Center (cm)	$\delta^{18}\text{O}$ (‰ VSMOW)	$\delta\text{D}$ (‰ VSMOW)	dx
45S-505	101.0	46.3	-25.8	-204.3	1.9
45S-509	101.8	47.1	-25.2	-197.7	4.0
45S-513	102.6	47.9	-24.9	-198.4	1.1
45S-517	103.4	48.7	-25.1	-198.0	2.5
45S-521	104.2	49.5	-24.9	-199.1	0.0
45S-525	105.0	50.3	-24.6	-197.1	-0.4
45S-529	105.8	51.1	-24.8	-201.5	-2.8
45S-533	106.6	51.9	-24.0	-192.5	-0.2
45S-537	107.4	52.7	-23.7	-190.0	-0.4
45S-541	108.2	53.5	-23.6	-190.4	-1.9
45S-547	109.4	54.7	-23.5	-189.1	-1.1
50S-1A	0.3	-62.0	-22.1	-175.0	1.7
50S-1B	0.3	-62.0	-22.0	-172.2	3.7
50S-1	0.3	-62.0	-22.5	-180.3	-0.3
50S-2	0.8	-61.5	-22.4	-180.5	-1.5
50S-3	1.3	-61.0	-23.2	-186.4	-1.0
50S-4	1.8	-60.5	-23.4	-186.9	0.7
50S-5	2.3	-60.0	-23.5	-186.7	1.3
50S-5	2.3	-60.0	-23.4	-185.9	1.6
50S-6	3.3	-59.0	-24.0	-188.8	3.2
50S-7	3.8	-58.5	-24.2	-191.3	2.3
50S-8	4.3	-58.0	-24.3	-191.4	3.3
50S-9	4.8	-57.5	-24.3	-193.9	0.7
50S-10	5.3	-57.0	-24.1	-194.5	-1.6
50S-11	5.8	-56.5	-24.6	-196.0	0.5
50S-12	6.3	-56.0	-24.5	-194.9	1.3
50S-13	6.8	-55.5	-24.6	-198.1	-0.9
50S-14	7.3	-55.0	-25.0	-198.9	0.7
50S-15	7.8	-54.5	-25.1	-197.0	3.9
50S-16	8.5	-53.8	-25.3	-199.5	3.0
50S-17	9.5	-52.8	-25.4	-200.0	3.4
50S-18	10.5	-51.8	-25.7	-202.6	2.7
50S-19	11.5	-50.8	-26.0	-203.0	4.7
50S-20	12.5	-49.8	-26.1	-205.8	3.0
50S-21	13.5	-48.8	-26.1	-205.9	2.6
50S-22	14.5	-47.8	-26.3	-205.9	4.4
50S-23	15.5	-46.8	-25.1	-202.7	-1.6
50S-24	16.5	-45.8	-25.9	-202.3	4.7
50S-25	17.5	-44.8	-26.3	-203.5	6.6
50S-26	18.5	-43.8	-26.3	-206.8	3.5
50S-27	19.5	-42.8	-26.6	-206.2	6.5
50S-28	20.5	-41.8	-26.6	-207.4	5.6
50S-29	21.5	-40.8	-26.7	-206.0	7.5



Sample ID	Distance from Left Edge (cm)	Distance from Center (cm)	$\delta^{18}\text{O}$ (‰ VSMOW)	$\delta\text{D}$ (‰ VSMOW)	dx
50S-30	22.5	-39.8	-26.9	-207.2	7.9
50S-31	23.5	-38.8	-26.8	-207.1	7.3
50S-32	24.5	-37.8	-27.0	-208.3	7.3
50S-33	25.5	-36.8	-26.9	-207.9	7.3
50S-34	26.5	-35.8	-27.1	-207.4	9.2
50S-35	27.5	-34.8	-27.2	-206.8	10.8
50S-36	28.5	-33.8	-27.0	-208.1	8.3
50S-37	29.5	-32.8	-27.1	-209.8	7.1
50S-38	30.5	-31.8	-27.2	-209.0	8.4
50S-39	31.5	-30.8	-27.1	-207.2	9.7
50S-40	32.5	-29.8	-27.3	-208.1	10.1
50S-41	33.5	-28.8	-27.1	-207.1	9.9
50S-42	34.5	-27.8	-27.2	-208.2	9.0
50S-43	35.5	-26.8	-27.2	-207.7	9.8
50S-44	36.5	-25.8	-27.1	-209.1	7.7
50S-45	37.5	-24.8	-27.0	-210.0	6.3
50S-46	38.5	-23.8	-27.2	-206.9	10.9
50S-47	39.5	-22.8	-27.2	-208.1	9.2
50S-48	40.5	-21.8	-27.2	-206.9	10.6
50S-49	41.5	-20.8	-26.4	-205.7	5.7
50S-50	42.5	-19.8	-26.8	-206.9	7.6
50S-52	44.5	-17.8	-26.8	-204.0	10.5
50S-53	45.5	-16.8	-26.9	-205.7	9.7
50S-54	46.5	-15.8	-27.0	-206.0	9.7
50S-55	47.5	-14.8	-27.0	-207.5	8.2
50S-56	48.5	-13.8	-27.0	-206.5	9.9
50S-57	49.5	-12.8	-27.0	-206.6	9.4
50S-58	50.5	-11.8	-27.2	-206.5	11.0
50S-59	51.5	-10.8	-27.0	-205.4	10.5
50S-60	52.5	-9.8	-27.1	-207.1	9.5
50S-61	53.5	-8.8	-27.3	-207.3	11.2
50S-62	54.5	-7.8	-27.4	-206.7	12.2
50S-63	55.5	-6.8	-27.3	-206.0	12.2
50S-64	56.5	-5.8	-27.0	-205.0	11.1
50S-65	57.5	-4.8	-27.2	-206.8	10.8
50S-66	58.5	-3.8	-27.2	-205.1	12.4
50S-67	59.5	-2.8	-27.2	-206.7	11.3
50S-68	60.5	-1.8	-27.0	-205.6	10.7
50S-69	61.5	-0.8	-27.2	-207.7	10.3
50S-70	62.5	0.3	-27.0	-204.9	11.4
50S-71	63.5	1.3	-26.6	-204.9	7.9
50S-72	64.5	2.3	-27.0	-206.4	9.3
50S-73	65.5	3.3	-27.1	-205.6	11.5

Sample ID	Distance from Left Edge (cm)	Distance from Center (cm)	$\delta^{18}\text{O}$ (‰ VSMOW)	$\delta\text{D}$ (‰ VSMOW)	dx
50S-74	66.5	4.3	-27.2	-206.9	11.0
50S-75	67.5	5.3	-27.3	-204.1	14.4
50S-76	68.5	6.3	-26.8	-205.0	9.6
50S-77	69.5	7.3	-27.2	-205.3	12.3
50S-78	70.5	8.3	-27.3	-203.6	14.4
50S-79	71.5	9.3	-27.2	-204.7	13.2
50S-80	72.5	10.3	-27.3	-204.4	13.8
50S-81	73.5	11.3	-27.1	-204.5	12.1
50S-82	74.5	12.3	-27.1	-204.6	12.4
50S-83	75.5	13.3	-27.3	-205.3	12.8
50S-84	76.5	14.3	-27.3	-204.8	13.7
50S-85	77.5	15.3	-27.3	-204.6	13.7
50S-86	78.5	16.3	-27.4	-203.2	15.6
50S-87	79.5	17.3	-27.6	-204.8	16.3
50S-88	80.5	18.3	-27.7	-206.8	15.1
50S-89	81.5	19.3	-27.6	-203.9	17.2
50S-90	82.5	20.3	-27.2	-202.3	15.0
50S-91	83.5	21.3	-27.3	-204.0	14.5
50S-92	84.5	22.3	-27.3	-203.0	15.1
50S-93	85.5	23.3	-27.5	-203.8	15.8
50S-94	86.5	24.3	-27.5	-204.7	15.2
50S-95	87.5	25.3	-27.4	-204.8	14.7
50S-96	88.5	26.3	-27.2	-203.6	13.8
50S-97	89.5	27.3	-27.2	-204.4	13.0
50S-98	90.5	28.3	-27.9	-204.5	19.0
50S-99	91.5	29.3	-27.4	-206.7	12.1
50S-100	92.5	30.3	-26.7	-207.9	5.6
50S-101	93.5	31.3	-26.4	-207.6	3.4
50S-102	94.5	32.3	-26.4	-205.6	5.6
50S-103	95.5	33.3	-26.3	-205.1	5.2
50S-104	96.5	34.3	-26.3	-207.1	3.6
50S-105	97.5	35.3	-26.4	-207.1	4.4
50S-106	98.5	36.3	-26.4	-206.1	5.2
50S-107	99.5	37.3	-26.3	-207.2	3.6
50S-108	100.5	38.3	-26.3	-205.3	5.2
50S-109	101.5	39.3	-26.5	-204.9	7.2
50S-110	102.5	40.3	-26.4	-205.2	6.1
50S-111	103.5	41.3	-26.7	-205.5	8.0
50S-112	104.5	42.3	-26.1	-205.0	4.0
50S-113	105.5	43.3	-26.0	-205.2	3.0
50S-114	106.5	44.3	-26.2	-204.8	4.9
50S-115	107.5	45.3	-26.3	-205.0	5.4
50S-116	108.5	46.3	-26.4	-205.1	6.4

Sample ID	Distance from Left Edge (cm)	Distance from Center (cm)	$\delta^{18}\text{O}$ (‰ VSMOW)	$\delta\text{D}$ (‰ VSMOW)	dx
50S-117	109.5	47.3	-26.1	-202.8	6.1
50S-118	110.5	48.3	-26.1	-203.7	5.2
50S-119	111.5	49.3	-26.0	-202.0	5.9
50S-120	112.5	50.3	-25.9	-202.3	5.1
50S-121	113.5	51.3	-25.8	-201.9	4.9
50S-123	115.5	53.3	-25.7	-199.0	6.7
50S-124	116.5	54.3	-25.6	-198.2	6.5
50S-125	117.5	55.3	-25.2	-202.8	-0.9
50S-126	118.5	56.3	-25.4	-201.0	2.2
50S-127	119.5	57.3	-25.2	-199.7	1.7
50S-129	121.5	59.3	-25.2	-197.7	3.9
50S-130	122.5	60.3	-24.7	-197.5	0.3
50S-131	123.5	61.3	-24.6	-195.7	0.8
50S-132	124.5	62.3	-24.4	-194.8	0.5
52.5S-001	0.2	-2.7	-21.9	-171.4	3.8
52.5S-003	0.6	-2.3	-21.2	-168.4	1.2
52.5S-005	1.0	-1.9	-21.4	-169.3	1.6
52.5S-007	1.4	-1.5	-21.4	-169.6	1.3
52.5S-009	1.8	-1.1	-21.2	-168.3	1.1
52.5S-011	2.2	-0.7	-21.5	-169.1	2.6
52.5S-013	2.6	-0.3	-21.4	-168.9	2.1
52.5S-015	3.0	0.1	-21.4	-168.8	2.0
52.5S-017	3.4	0.5	-21.6	-170.0	2.8
52.5S-019	3.8	0.9	-21.4	-169.4	2.1
52.5S-021	4.2	1.3	-21.8	-171.2	3.0
52.5S-023	4.6	1.7	-21.3	-169.8	1.0
52.5S-027	5.4	2.5	-21.3	-168.4	1.8
52.5S-029	5.8	2.9	-21.6	-171.1	1.9
58N-001	0.2	-67.1	-23.8	-192.8	-2.3
58N-003	0.6	-66.7	-24.3	-195.1	-0.7
58N-005	1.0	-66.3	-24.3	-194.8	-0.7
58N-007	1.4	-65.9	-24.1	-194.0	-1.2
58N-009	1.8	-65.5	-24.8	-197.5	0.7
58N-011	2.2	-65.1	-23.8	-193.0	-2.6
58N-013	2.6	-64.7	-24.9	-197.1	1.9
58N-015	3.0	-64.3	-24.6	-197.0	-0.4
58N-017	3.4	-63.9	-25.0	-198.7	1.1
58N-019	3.8	-63.5	-25.2	-199.5	1.7
58N-021	4.2	-63.1	-25.5	-203.3	0.6
58N-023	4.6	-62.7	-25.5	-201.4	2.5
58N-025	5.0	-62.3	-25.3	-200.9	1.8
58N-027	5.4	-61.9	-25.6	-203.7	1.1
58N-029	5.8	-61.5	-25.4	-201.5	1.7

Sample ID	Distance from Left Edge (cm)	Distance from Center (cm)	$\delta^{18}\text{O}$ (‰ VSMOW)	$\delta\text{D}$ (‰ VSMOW)	dx
58N-031	6.2	-61.1	-25.4	-201.6	1.9
58N-033	6.6	-60.7	-25.4	-201.8	1.1
58N-035	7.0	-60.3	-25.8	-202.3	3.9
58N-037	7.4	-59.9	-25.8	-203.4	3.1
58N-039	7.8	-59.5	-25.7	-202.9	2.7
58N-041	8.2	-59.1	-25.9	-203.4	4.2
58N-043	8.6	-58.7	-25.8	-204.6	2.0
58N-045	9.0	-58.3	-25.8	-203.4	2.9
58N-047	9.4	-57.9	-25.6	-202.5	2.0
58N-049	9.8	-57.5	-25.7	-203.7	1.5
58N-051	10.2	-57.1	-25.5	-204.0	0.3
58N-053	10.6	-56.7	-25.6	-202.5	2.0
58N-055	11.0	-56.3	-26.0	-205.7	2.3
58N-057	11.4	-55.9	-26.3	-206.7	3.4
58N-059	11.8	-55.5	-25.9	-204.3	2.7
58N-061	12.2	-55.1	-25.7	-203.8	1.9
58N-063	12.6	-54.7	-26.0	-204.9	2.7
58N-065	13.0	-54.3	-25.8	-204.7	1.3
58N-067	13.4	-53.9	-25.6	-203.7	0.8
58N-069	13.8	-53.5	-26.1	-205.7	3.1
58N-073	14.6	-52.7	-26.5	-206.6	5.4
58N-075	15.0	-52.3	-26.1	-205.8	2.9
58N-079	15.8	-51.5	-26.6	-206.1	6.4
58N-081	16.2	-51.1	-26.3	-205.4	5.0
58N-083	16.6	-50.7	-26.8	-207.2	6.8
58N-085	17.0	-50.3	-26.7	-207.1	6.7
58N-087	17.4	-49.9	-26.3	-207.4	2.9
58N-089	17.8	-49.5	-26.5	-208.1	3.5
58N-091	18.2	-49.1	-26.5	-207.6	4.4
58N-093	18.6	-48.7	-26.6	-207.9	4.9
58N-095	19.0	-48.3	-26.4	-207.4	4.1
58N-097	19.4	-47.9	-26.7	-208.2	5.3
58N-099	19.8	-47.5	-26.7	-208.2	5.5
58N-101	20.2	-47.1	-26.8	-210.5	4.0
58N-103	20.6	-46.7	-26.8	-209.3	5.1
58N-105	21.0	-46.3	-26.8	-208.9	5.6
58N-107	21.4	-45.9	-26.7	-207.9	5.6
58N-109	21.8	-45.5	-26.7	-209.2	4.8
58N-111	22.2	-45.1	-26.7	-208.3	5.0
58N-113	22.6	-44.7	-27.0	-209.3	6.5
58N-115	23.0	-44.3	-27.0	-210.2	5.7
58N-117	23.4	-43.9	-27.0	-209.9	5.9
58N-119	23.8	-43.5	-26.7	-207.5	5.7

Sample ID	Distance from Left Edge (cm)	Distance from Center (cm)	$\delta^{18}\text{O}$ (‰ VSMOW)	$\delta\text{D}$ (‰ VSMOW)	dx
58N-121	24.2	-43.1	-26.7	-208.4	5.0
58N-123	24.6	-42.7	-26.8	-209.3	5.4
58N-125	25.0	-42.3	-26.9	-209.5	5.9
58N-127	25.4	-41.9	-27.1	-210.0	7.1
58N-129	25.8	-41.5	-26.9	-209.0	6.1
58N-131	26.2	-41.1	-26.7	-207.2	6.7
58N-133	26.6	-40.7	-27.0	-208.5	7.1
58N-135	27.0	-40.3	-26.9	-209.1	6.3
58N-137	27.4	-39.9	-26.8	-208.2	6.1
58N-139	27.8	-39.5	-27.1	-209.0	7.6
58N-141	28.2	-39.1	-26.6	-209.2	4.0
58N-143	28.6	-38.7	-27.1	-210.7	6.4
58N-145	29.0	-38.3	-27.0	-209.5	6.3
58N-147	29.4	-37.9	-26.9	-210.1	5.4
58N-149	29.8	-37.5	-27.1	-210.7	5.9
58N-151	30.2	-37.1	-26.9	-209.9	5.3
58N-153	30.6	-36.7	-27.4	-209.6	9.2
58N-155	31.0	-36.3	-26.8	-208.2	6.5
58N-157	31.4	-35.9	-27.0	-209.7	6.4
58N-159	31.8	-35.5	-26.6	-208.4	4.7
58N-161	32.2	-35.1	-27.0	-210.8	5.4
58N-163	32.6	-34.7	-26.8	-209.1	5.4
58N-165	33.0	-34.3	-26.8	-209.0	5.4
58N-167	33.4	-33.9	-26.9	-209.5	5.6
58N-169	33.8	-33.5	-26.7	-207.1	6.2
58N-171	34.2	-33.1	-26.9	-208.9	5.9
58N-173	34.6	-32.7	-26.4	-207.1	4.0
58N-175	35.0	-32.3	-26.7	-207.9	5.4
58N-177	35.4	-31.9	-27.0	-209.8	6.0
58N-179	35.8	-31.5	-26.8	-208.5	5.6
58N-181	36.2	-31.1	-26.6	-208.2	4.5
58N-183	36.6	-30.7	-26.5	-207.2	5.1
58N-185	37.0	-30.3	-26.9	-207.5	8.0
58N-187	37.4	-29.9	-26.5	-206.5	5.3
58N-189	37.8	-29.5	-26.6	-206.2	6.3
58N-191	38.2	-29.1	-26.9	-207.4	7.7
58N-193	38.6	-28.7	-26.7	-206.5	6.9
58N-195	39.0	-28.3	-26.7	-207.3	6.1
58N-197	39.4	-27.9	-26.4	-205.6	5.2
58N-199	39.8	-27.5	-26.6	-206.4	6.4
58N-201	40.2	-27.1	-26.6	-207.0	5.4
58N-203	40.6	-26.7	-26.8	-207.2	7.0
58N-205	41.0	-26.3	-26.9	-207.4	7.5

Sample ID	Distance from Left Edge (cm)	Distance from Center (cm)	$\delta^{18}\text{O}$ (‰ VSMOW)	$\delta\text{D}$ (‰ VSMOW)	dx
58N-207	41.4	-25.9	-26.7	-206.9	6.6
58N-209	41.8	-25.5	-26.6	-207.0	5.6
58N-211	42.2	-25.1	-26.7	-206.3	7.2
58N-213	42.6	-24.7	-26.6	-206.7	6.0
58N-215	43.0	-24.3	-26.6	-206.1	6.6
58N-217	43.4	-23.9	-27.0	-207.4	8.2
58N-219	43.8	-23.5	-26.6	-206.6	5.9
58N-221	44.2	-23.1	-26.7	-208.0	5.6
58N-223	44.6	-22.7	-26.5	-207.3	4.3
58N-225	45.0	-22.3	-26.5	-206.5	5.6
58N-227	45.4	-21.9	-26.7	-207.3	6.4
58N-229	45.8	-21.5	-26.8	-206.9	7.6
58N-231	46.2	-21.1	-26.7	-206.6	6.7
58N-233	46.6	-20.7	-26.7	-207.3	6.6
58N-235	47.0	-20.3	-27.0	-207.7	7.8
58N-237	47.4	-19.9	-26.7	-207.3	6.5
58N-239	47.8	-19.5	-26.8	-207.2	7.0
58N-241	48.2	-19.1	-27.0	-208.9	7.2
58N-243	48.6	-18.7	-26.8	-207.6	6.7
58N-245	49.0	-18.3	-26.8	-207.6	6.9
58N-247	49.4	-17.9	-26.7	-207.6	5.9
58N-249	49.8	-17.5	-26.7	-207.6	5.5
58N-251	50.2	-17.1	-26.3	-205.3	5.1
58N-253	50.6	-16.7	-26.6	-207.9	5.2
58N-255	51.0	-16.3	-26.4	-205.4	5.7
58N-257	51.4	-15.9	-26.6	-207.5	5.6
58N-259	51.8	-15.5	-26.6	-207.4	5.6
58N-261	52.2	-15.1	-26.7	-207.4	6.1
58N-263	52.6	-14.7	-26.5	-206.6	5.7
58N-265	53.0	-14.3	-26.7	-207.4	6.4
58N-267	53.4	-13.9	-26.5	-206.0	5.6
58N-269	53.8	-13.5	-26.9	-206.9	8.1
58N-271	54.2	-13.1	-26.6	-206.5	6.6
58N-273	54.6	-12.7	-27.0	-207.6	8.3
58N-275	55.0	-12.3	-26.7	-207.3	6.1
58N-277	55.4	-11.9	-26.4	-206.0	5.0
58N-279	55.8	-11.5	-26.7	-207.6	5.9
58N-281	56.2	-11.1	-26.7	-209.0	4.7
58N-283	56.6	-10.7	-27.0	-208.9	6.9
58N-285	57.0	-10.3	-26.7	-208.3	5.6
58N-287	57.4	-9.9	-26.8	-208.5	6.1
58N-289	57.8	-9.5	-26.7	-207.8	6.0
58N-291	58.2	-9.1	-26.7	-207.6	6.1



Sample ID	Distance from Left Edge (cm)	Distance from Center (cm)	$\delta^{18}\text{O}$ (‰ VSMOW)	$\delta\text{D}$ (‰ VSMOW)	dx
58N-293	58.6	-8.7	-26.9	-207.9	7.5
58N-295	59.0	-8.3	-26.8	-207.9	6.5
58N-297	59.4	-7.9	-27.1	-208.0	8.4
58N-299	59.8	-7.5	-26.8	-208.4	6.1
58N-301	60.2	-7.1	-26.9	-208.7	6.8
58N-303	60.6	-6.7	-26.8	-207.4	7.0
58N-305	61.0	-6.3	-27.0	-208.0	7.9
58N-307	61.4	-5.9	-26.9	-208.2	7.0
58N-309	61.8	-5.5	-26.9	-208.2	6.7
58N-311	62.2	-5.1	-26.4	-205.6	5.4
58N-313	62.6	-4.7	-26.8	-209.0	5.5
58N-315	63.0	-4.3	-26.9	-209.0	6.0
58N-317	63.4	-3.9	-26.8	-207.7	7.0
58N-319	63.8	-3.5	-26.7	-207.3	6.6
58N-321	64.2	-3.1	-26.9	-209.0	6.1
58N-323	64.6	-2.7	-26.8	-207.8	6.7
58N-325	65.0	-2.3	-26.7	-208.3	5.4
58N-327	65.4	-1.9	-26.6	-207.4	5.8
58N-329	65.8	-1.5	-26.3	-205.4	4.7
58N-331	66.2	-1.1	-26.7	-207.4	6.2
58N-333	66.6	-0.7	-26.4	-205.0	6.0
58N-335	67.0	-0.3	-26.8	-207.9	6.7
58N-337	67.4	0.1	-26.6	-206.9	6.1
58N-339	67.8	0.5	-26.5	-206.2	5.8
58N-341	68.2	0.9	-26.6	-207.9	4.9
58N-343	68.6	1.3	-26.6	-207.1	5.5
58N-345	69.0	1.7	-26.4	-206.1	5.3
58N-347	69.4	2.1	-26.6	-208.2	4.2
58N-349	69.8	2.5	-26.6	-207.7	5.3
58N-351	70.2	2.9	-26.5	-208.2	3.5
58N-353	70.6	3.3	-26.7	-208.7	4.6
58N-355	71.0	3.7	-26.6	-208.1	4.5
58N-357	71.4	4.1	-26.8	-208.6	5.6
58N-359	71.8	4.5	-26.6	-207.8	5.3
58N-361	72.2	4.9	-27.1	-212.1	4.5
58N-363	72.6	5.3	-26.7	-208.9	4.4
58N-365	73.0	5.7	-26.8	-209.7	4.9
58N-368	73.4	6.1	-26.4	-208.4	2.9
58N-369	73.8	6.5	-26.8	-208.5	5.6
58N-372	74.2	6.9	-26.8	-208.4	5.5
58N-374	74.6	7.3	-25.8	-201.6	4.5
58N-376	75.0	7.7	-25.9	-203.6	3.2
58N-378	75.4	8.1	-26.1	-205.6	3.2



Sample ID	Distance from Left Edge (cm)	Distance from Center (cm)	$\delta^{18}\text{O}$ (‰ VSMOW)	$\delta\text{D}$ (‰ VSMOW)	dx
58N-380	75.8	8.5	-26.4	-207.7	3.1
58N-382	76.2	8.9	-26.5	-207.3	4.7
58N-384	76.6	9.3	-26.3	-204.0	6.6
58N-387	77.4	10.1	-27.0	-209.5	6.1
58N-390	77.8	10.5	-26.6	-207.4	5.5
58N-391	78.2	10.9	-26.9	-209.8	5.3
58N-393	78.6	11.3	-26.9	-210.6	4.2
58N-395	79.0	11.7	-26.8	-208.2	6.0
58N-397	79.4	12.1	-27.0	-209.8	6.2
58N-399	79.8	12.5	-26.9	-209.0	5.9
58N-401	80.2	12.9	-26.9	-209.0	5.8
58N-403	80.6	13.3	-27.0	-209.6	6.2
58N-405	81.0	13.7	-26.9	-211.0	3.9
58N-407	81.4	14.1	-26.8	-208.5	5.8
58N-409	81.8	14.5	-26.8	-208.6	5.8
58N-411	82.2	14.9	-26.5	-208.6	3.2
58N-413	82.6	15.3	-27.1	-212.1	4.7
58N-415	83.0	15.7	-26.8	-209.5	4.9
58N-417	83.4	16.1	-27.0	-210.7	5.4
58N-419	83.8	16.5	-26.9	-210.1	5.4
58N-421	84.2	16.9	-27.1	-211.3	5.5
58N-423	84.6	17.3	-27.0	-210.6	5.4
58N-425	85.0	17.7	-27.1	-210.1	6.7
58N-427	85.4	18.1	-27.1	-210.2	6.6
58N-429	85.8	18.5	-27.3	-211.2	6.8
58N-431	86.2	18.9	-27.2	-211.0	6.6
58N-433	86.6	19.3	-27.0	-211.9	3.8
58N-435	87.0	19.7	-27.1	-211.2	5.8
58N-437	87.4	20.1	-27.2	-211.4	6.1
58N-439	87.8	20.5	-27.1	-211.2	5.4
58N-441	88.2	20.9	-27.4	-212.6	6.2
58N-443	88.6	21.3	-27.4	-211.3	7.7
58N-445	89.0	21.7	-27.3	-211.5	6.4
58N-447	89.4	22.1	-27.2	-211.8	6.1
58N-449	89.8	22.5	-27.0	-211.0	5.2
58N-451	90.2	22.9	-27.3	-211.6	6.6
58N-453	90.6	23.3	-27.0	-211.5	4.6
58N-455	91.0	23.7	-27.0	-210.8	5.2
58N-457	91.4	24.1	-27.1	-210.9	6.0
58N-459	91.8	24.5	-27.4	-213.1	6.3
58N-461	92.2	24.9	-27.3	-215.0	3.3
58N-463	92.6	25.3	-27.2	-212.8	5.0
58N-465	93.0	25.7	-27.1	-211.8	5.0

Sample ID	Distance from Left Edge (cm)	Distance from Center (cm)	$\delta^{18}\text{O}$ (‰ VSMOW)	$\delta\text{D}$ (‰ VSMOW)	dx
58N-467	93.4	26.1	-27.0	-213.6	2.1
58N-469	93.8	26.5	-27.1	-213.3	3.8
58N-471	94.2	26.9	-27.2	-213.7	3.5
58N-473	94.6	27.3	-27.2	-213.1	4.2
58N-475	95.0	27.7	-27.1	-213.2	3.6
58N-477	95.4	28.1	-27.4	-210.0	9.2
58N-479	95.8	28.5	-27.3	-211.7	6.5
58N-481	96.2	28.9	-27.6	-211.5	8.9
58N-483	96.6	29.3	-27.4	-212.2	6.9
58N-485	97.0	29.7	-27.6	-213.7	6.7
58N-487	97.4	30.1	-27.3	-212.3	6.3
58N-489	97.8	30.5	-27.3	-211.8	6.8
58N-491	98.2	30.9	-26.7	-209.6	3.7
58N-493	98.6	31.3	-27.3	-212.1	6.1
58N-495	99.0	31.7	-27.6	-214.1	6.7
58N-497	99.4	32.1	-26.5	-209.2	3.2
58N-499	99.8	32.5	-26.7	-209.8	3.4
58N-501	100.2	32.9	-27.2	-212.1	5.7
58N-503	100.6	33.3	-27.5	-214.0	5.6
58N-505	101.0	33.7	-26.9	-211.4	3.9
58N-507	101.4	34.1	-27.5	-214.0	5.6
58N-509	101.8	34.5	-27.3	-211.4	7.3
58N-511	102.2	34.9	-27.3	-212.2	5.9
58N-513	102.6	35.3	-27.0	-212.2	3.8
58N-515	103.0	35.7	-27.1	-212.1	4.6
58N-517	103.4	36.1	-27.2	-212.1	5.2
58N-519	103.8	36.5	-26.8	-210.7	3.7
58N-521	104.2	36.9	-27.0	-210.6	5.3
58N-523	104.6	37.3	-27.1	-211.2	5.3
58N-525	105.0	37.7	-27.1	-210.8	5.7
58N-527	105.4	38.1	-27.1	-211.4	5.3
58N-529	105.8	38.5	-26.8	-209.8	4.8
58N-531	106.2	38.9	-27.0	-210.8	4.9
58N-533	106.6	39.3	-27.2	-212.1	5.4
58N-535	107.0	39.7	-27.1	-211.4	5.7
58N-537	107.4	40.1	-27.1	-211.6	5.1
58N-539	107.8	40.5	-27.1	-211.5	4.8
58N-541	108.2	40.9	-27.2	-212.9	4.9
58N-543	108.6	41.3	-27.1	-211.8	4.8
58N-545	109.0	41.7	-27.2	-212.1	5.7
58N-547	109.4	42.1	-27.5	-213.6	6.0
58N-549	109.8	42.5	-26.8	-209.7	4.3
58N-551	110.2	42.9	-27.1	-211.3	5.1

Sample ID	Distance from Left Edge (cm)	Distance from Center (cm)	$\delta^{18}\text{O}$ (‰ VSMOW)	$\delta\text{D}$ (‰ VSMOW)	dx
58N-553	110.6	43.3	-27.2	-212.7	5.2
58N-555	111.0	43.7	-27.3	-212.6	5.3
58N-557	111.4	44.1	-27.2	-211.8	5.9
58N-559	111.8	44.5	-27.4	-213.2	5.9
58N-561	112.2	44.9	-27.2	-212.9	5.1
58N-563	112.6	45.3	-27.3	-212.4	5.6
58N-565	113.0	45.7	-27.2	-212.4	5.5
58N-567	113.4	46.1	-27.1	-210.9	5.9
58N-569	113.8	46.5	-27.4	-212.4	6.5
58N-571	114.2	46.9	-27.3	-212.8	5.9
58N-573	114.6	47.3	-27.3	-212.1	5.9
58N-575	115.0	47.7	-27.2	-212.0	5.9
58N-577	115.4	48.1	-27.1	-211.0	5.8
58N-579	115.8	48.5	-25.8	-207.4	-0.9
58N-581	116.2	48.9	-27.3	-213.7	4.9
58N-583	116.6	49.3	-27.1	-211.2	5.3
58N-585	117.0	49.7	-27.0	-210.8	5.3
58N-587	117.4	50.1	-27.0	-210.2	5.7
58N-589	117.8	50.5	-27.1	-210.6	6.1
58N-591	118.2	50.9	-27.3	-211.6	6.8
58N-593	118.6	51.3	-27.3	-210.6	7.7
58N-595	119.0	51.7	-27.0	-211.2	4.7
58N-597	119.4	52.1	-27.1	-210.9	6.0
58N-599	119.8	52.5	-27.0	-210.7	5.4
58N-601	120.2	52.9	-27.1	-210.9	5.7
58N-603	120.6	53.3	-27.0	-210.4	5.2
58N-605	121.0	53.7	-26.8	-209.6	4.9
58N-607	121.4	54.1	-26.9	-209.8	5.4
58N-609	121.8	54.5	-26.7	-208.8	4.9
58N-611	122.2	54.9	-26.7	-208.9	5.0
58N-613	122.6	55.3	-27.1	-210.7	6.4
58N-615	123.0	55.7	-27.3	-210.5	7.6
58N-617	123.4	56.1	-27.1	-210.4	6.7
58N-619	123.8	56.5	-26.9	-207.9	7.0
58N-621	124.2	56.9	-27.2	-210.4	6.9
58N-623	124.6	57.3	-26.8	-208.8	5.8
58N-625	125.0	57.7	-26.8	-208.7	5.5
58N-627	125.4	58.1	-27.0	-207.8	8.2
58N-629	125.8	58.5	-26.8	-208.1	6.3
58N-631	126.2	58.9	-27.1	-208.1	8.4
58N-633	126.6	59.3	-26.9	-207.9	7.6
58N-635	127.0	59.7	-26.9	-207.3	8.0
58N-637	127.4	60.1	-26.6	-206.9	6.2

Sample ID	Distance from Left Edge (cm)	Distance from Center (cm)	$\delta^{18}\text{O}$ (‰ VSMOW)	$\delta\text{D}$ (‰ VSMOW)	dx
58N-639	127.8	60.5	-26.5	-206.6	5.0
58N-641	128.2	60.9	-26.3	-203.8	6.3
58N-643	128.6	61.3	-26.5	-206.2	6.0
58N-645	129.0	61.7	-26.5	-205.8	5.9
58N-647	129.4	62.1	-26.5	-206.2	5.5
58N-649	129.8	62.5	-26.6	-205.5	7.2
58N-651	130.2	62.9	-26.6	-206.0	6.4
58N-655	131.0	63.7	-26.3	-203.5	7.0
58N-659	131.8	64.5	-26.4	-205.1	5.9
58N-661	132.2	64.9	-25.8	-201.7	4.8
58N-663	132.6	65.3	-25.7	-199.7	6.1
58N-665	133.0	65.7	-24.8	-197.5	0.7
58N-667	133.4	66.1	-25.7	-201.7	4.0
58N-669	133.8	66.5	-25.4	-199.4	3.8
58N-671	134.2	66.9	-24.8	-193.9	4.5
58N-673	134.6	67.3	-25.6	-200.5	4.2

## References

- Ager, T. A., and Brubaker, L., 1985, Quaternary palynology and vegetational history of Alaska, *in* Bryant, V. M., and Holloway, R. G., eds., *Pollen Records of Late-Quaternary North American Sediments*: Dallas, Texas, American Association of Stratigraphic Palynologists Foundation, p. 353-383.
- Ahmed, M., Anchukaitis, K. J., Asrat, A., Borgaonkar, H. P., Braida, M., Buckley, B. M., Buntgen, U., Chase, B. M., Christie, D. A., Cook, E. R., Curran, M. A. J., Diaz, H. F., Esper, J., Fan, Z.-X., Gaire, N. P., Ge, Q., Gergis, J., Gonzalez-Rouco, J. F., Goosse, H., Grab, S. W., Graham, N., Graham, R., Grosjean, M., Hanhijarvi, S. T., Kaufman, D. S., Kiefer, T., Kimura, K., Korhola, A. A., Krusic, P. J., Lara, A., Lezine, A.-M., Ljungqvist, F. C., Lorrey, A. M., Luterbacher, J., Masson-Delmotte, V., McCarroll, D., McConnell, J. R., McKay, N. P., Morales, M. S., Moy, A. D., Mulvaney, R., Mundo, I. A., Nakatsuka, T., Nash, D. J., Neukom, R., Nicholson, S. E., Oerter, H., Palmer, J. G., Phipps, S. J., Prieto, M. R., Rivera, A., Sano, M., Severi, M., Shanahan, T. M., Shao, X., Shi, F., Sigl, M., Smerdon, J. E., Solomina, O. N., Steig, E. J., Stenni, B., Thamban, M., Trouet, V., Turney, C. S. M., Umer, M., van Ommen, T., Verschuren, D., Viau, A. E., Villalba, R., Vinther, B. M., von Gunten, L., Wagner, S., Wahl, E. R., Wanner, H., Werner, J. P., White, J. W. C., Yasue, K., Zorita, E., and Consortium, P. k., 2013, Continental-scale temperature variability during the past two millennia: *Nature Geoscience*, v. 6, no. 5, p. 339-346.
- Alley, R. B., and Clark, P. U., 1999, The deglaciation of the northern hemisphere: A global perspective: *Annual Review of Earth and Planetary Sciences*, v. 27, p. 149-182.
- Andersen, K. K., Azuma, N., Barnola, J. M., Bigler, M., Biscaye, P., Caillon, N., Chappellaz, J., Clausen, H. B., DahlJensen, D., Fischer, H., Fluckiger, J., Fritzsche, D., Fujii, Y., Goto-Azuma, K., Gronvold, K., Gundestrup, N. S., Hansson, M., Huber, C., Hvidberg, C. S., Johnsen, S. J., Jonsell, U., Jouzel, J., Kipfstuhl, S., Landais, A., Leuenberger, M., Lorrain, R., Masson-Delmotte, V., Miller, H., Motoyama, H., Narita, H., Popp, T., Rasmussen, S. O., Raynaud, D., Rothlisberger, R., Ruth, U., Samyn, D., Schwander, J., Shoji, H., Siggard-Andersen, M. L., Steffensen, J. P., Stocker, T., Sveinbjornsdottir, A. E., Svensson, A., Takata, M., Tison, J. L., Thorsteinsson, T., Watanabe, O., Wilhelms, F., White, J. W. C., and Project, N. G. I. C., 2004, High-resolution record of Northern Hemisphere climate extending into the last interglacial period: *Nature*, v. 431, no. 7005, p. 147-151.
- Balascio, N. L., Kaufman, D. S., and Manley, W. F., 2005, Equilibrium-line altitudes during the Last Glacial Maximum across the Brooks Range, Alaska: *Journal of Quaternary Science*, v. 20, no. 7-8, p. 821-838.
- Bartlein, P. J., Anderson, K. H., Anderson, P. M., Edwards, M. E., Mock, C. J., Thompson, R. S., Webb, R. S., and Whitlock, C., 1998, Paleoclimate simulations for North America over the past 21,000 years: Features of the simulated climate and comparisons with paleoenvironmental data: *Quaternary Science Reviews*, v. 17, no. 6-7, p. 549-585.

- Beget, J., 1990, Middle Wisconsinan climate fluctuations recorded in Central Alaskan loess: *Geographie Physique Et Quaternaire*, v. 44, no. 1, p. 3-13.
- Berger, A., and Loutre, M. F., 1991, Insolation values for the climate of the last 10 million years: *Quaternary Science Reviews*, v. 10, no. 4, p. 297-317.
- Bond, G. C., and Lotti, R., 1995, Iceberg discharges into the North-Atlantic on millennial time scales during the last glaciations: *Science*, v. 267, no. 5200, p. 1005-1010.
- Bowen, G. J., and Wilkinson, B., 2002, Spatial distribution of delta O-18 in meteoric precipitation: *Geology*, v. 30, no. 4, p. 315-318.
- Bray, M. T., French, H. M., and Shur, Y., 2006, Further cryostratigraphic observations in the CRREL permafrost tunnel, Fox, Alaska: *Permafrost and Periglacial Processes*, v. 17, no. 3, p. 233-243.
- Briner, J. P., and Kaufman, D. S., 2008, Late Pleistocene mountain glaciation in Alaska: key chronologies: *Journal of Quaternary Science*, v. 23, no. 6-7, p. 659-670.
- Briner, J. P., Kaufman, D. S., Manley, W. E., Finkel, R. C., and Caffee, M. W., 2005, Cosmogenic exposure dating of late Pleistocene moraine stabilization in Alaska: *Geological Society of America Bulletin*, v. 117, no. 7-8, p. 1108-1120.
- Bronk Ramsey, C., 2009, Bayesian analysis of radiocarbon dates: *Radiocarbon*, v. 51, p. 337-360.
- Brown, C. E., 1998, *Applied Multivariate Statistics in Geohydrology and Related Sciences*, Berlin, Springer-Verlag.
- Clark, I., and Fritz, P., 1997, *Environmental Isotopes in Hydrogeology*, New York, Lewis Publishers, 328 p.:
- Clark, P. U., Dyke, A. S., Shakun, J. D., Carlson, A. E., Clark, J., Wohlfarth, B., Mitrovica, J. X., Hostetler, S. W., and McCabe, A. M., 2009, The Last Glacial Maximum: *Science*, v. 325, no. 5941, p. 710-714.
- Clegg, B. F., and Hu, F. S., 2010, An oxygen-isotope record of Holocene climate change in the south-central Brooks Range, Alaska: *Quaternary Science Reviews*, v. 29, no. 7-8, p. 928-939.
- Craig, H., 1961, Isotopic variations in meteoric waters: *Science*, v. 133, no. 346, p. 1702-&.
- Dansgaard, W., 1964, Stable isotopes in precipitation: *Tellus*, v. 16, no. 4, p. 436-468.
- Darby, D. A., Bischof, J. F., Spielhagen, R. F., Marshall, S. A., and Herman, S. W., 2002, Arctic ice export events and their potential impact on global climate during the late Pleistocene: *Paleoceanography*, v. 17, no. 2, p. 17.
- Derksen, C., and Brown, R., 2012, Spring snow cover extent reductions in the 2008-2012 period exceeding climate model projections: *Geophysical Research Letters*, v. 39.
- Dortch, J. M., Owen, L. A., Caffee, M. W., and Brease, P., 2010, Late Quaternary glaciation and equilibrium line altitude variations of the McKinley River region, central Alaska Range: *Boreas*, v. 39, no. 2, p. 233-246.
- Douglas, T. A., Fortier, D., Shur, Y. L., Kanevskiy, M. Z., Guo, L. D., Cai, Y. H., and Bray, M. T., 2011, Biogeochemical and Geocryological Characteristics of Wedge and Thermokarst-Cave Ice in the CRREL Permafrost Tunnel, Alaska: *Permafrost and Periglacial Processes*, v. 22, no. 2, p. 120-128.
- Elias, S. A., and Crocker, B., 2008, The Bering Land Bridge: a moisture barrier to the dispersal of steppe-tundra biota?: *Quaternary Science Reviews*, v. 27, no. 27-28, p. 2473-2483.



- England, J. H., and Furze, M. F. A., 2008, New evidence from the western Canadian Arctic Archipelago for the resubmergence of Bering Strait: *Quaternary Research*, v. 70, no. 1, p. 60-67.
- Epstein, S., and Mayeda, T., 1953, Variation of O-18 content of waters from natural sources: *Geochimica Et Cosmochimica Acta*, v. 4, no. 5, p. 213-224.
- Fox-Dobbs, K., Leonard, J. A., and Koch, P. L., 2008, Pleistocene megafauna from eastern Beringia: Paleoecological and paleoenvironmental interpretations of stable carbon and nitrogen isotope and radiocarbon records: *Palaeogeography Palaeoclimatology Palaeoecology*, v. 261, no. 1-2, p. 30-46.
- French, H., 2007, *The Periglacial Environment*, Chichester, Wiley, 458 p.:
- French, H., and Shur, Y., 2010, The principles of cryostratigraphy: *Earth-Science Reviews*, v. 101, no. 3-4, p. 190-206.
- Fritz, P., Suzuki, O., Silva, C., and Salati, E., 1981, Isotope hydrology of groundwaters in the Pampa del Tamarugal, Chile: *Journal of Hydrology*, v. 53, no. 1-2, p. 161-184.
- Gaglioti, B. V., Barnes, B. M., Zazula, G. D., Beaudoin, A. B., and Wooller, M. J., 2011, Late Pleistocene paleoecology of arctic ground squirrel (*Uroditellus parryi*) caches and nests from Interior Alaska's mammoth steppe ecosystem, USA: *Quaternary Research*, v. 76, no. 3, p. 373-382.
- Gat, J. R., 1996, Oxygen and hydrogen isotopes in the hydrologic cycle: *Annual Review of Earth and Planetary Sciences*, v. 24, p. 225-262.
- Griffing, C., 2011, *Pleistocene climate in Alaska from stable isotopes in an ice wedge*: University of Nevada, Las Vegas, 65 p.
- Hamilton, T. D., Craig, J. L., and Sellmann, P. V., 1988, The Fox Permafrost Tunnel - A Late Quaternary geologic record in Central Alaska: *Geological Society of America Bulletin*, v. 100, no. 6, p. 948-969.
- Harry, D. G., and Gozdzik, J. S., 1988, Ice wedges: growth, thaw transformation, and palaeoenvironmental significance: *Journal of Quaternary Science*, v. 3, p. 39-55.
- Hemming, S. R., 2004, Heinrich events: Massive late pleistocene detritus layers of the North Atlantic and their global climate imprint: *Reviews of Geophysics*, v. 42, no. 1.
- Hijmans, R. J., Cameron, S. E., Parra, J. L., Jones, P. G., and Jarvis, A., 2005, Very high resolution interpolated climate surfaces for global land areas: *International Journal of Climatology*, v. 25, p. 1965-1978.
- Hinzman, L. D., Bettez, N. D., Bolton, W. R., Chapin, F. S., Dyurgerov, M. B., Fastie, C. L., Griffith, B., Hollister, R. D., Hope, A., Huntington, H. P., Jensen, A. M., Jia, G. J., Jorgenson, T., Kane, D. L., Klein, D. R., Kofinas, G., Lynch, A. H., Lloyd, A. H., McGuire, A. D., Nelson, F. E., Oechel, W. C., Osterkamp, T. E., Racine, C. H., Romanovsky, V. E., Stone, R. S., Stow, D. A., Sturm, M., Tweedie, C. E., Vourlitis, G. L., Walker, M. D., Walker, D. A., Webber, P. J., Welker, J. M., Winker, K., and Yoshikawa, K., 2005, Evidence and implications of recent climate change in northern Alaska and other arctic regions: *Climatic Change*, v. 72, no. 3, p. 251-298.
- Johnsen, S. J., Dahl-Jensen, D., Gundestrup, N., Steffensen, J. P., Clausen, H. B., Miller, H., Masson-Delmotte, V., Sveinbjornsdottir, A. E., and White, J., 2001, Oxygen isotope and palaeotemperature records from six Greenland ice-core stations:



- Camp Century, Dye-3, GRIP, GISP2, Renland and NorthGRIP: *Journal of Quaternary Science*, v. 16, no. 4, p. 299-307.
- Jouzel, J., Masson-Delmotte, V., Cattani, O., Dreyfus, G., Falourd, S., Hoffmann, G., Minster, B., Nouet, J., Barnola, J. M., Chappellaz, J., Fischer, H., Gallet, J. C., Johnsen, S., Leuenberger, M., Loulergue, L., Luethi, D., Oerter, H., Parrenin, F., Raisbeck, G., Raynaud, D., Schilt, A., Schwander, J., Selmo, E., Souchez, R., Spahni, R., Stauffer, B., Steffensen, J. P., Stenni, B., Stocker, T. F., Tison, J. L., Werner, M., and Wolff, E. W., 2007a, Orbital and millennial Antarctic climate variability over the past 800,000 years: *Science*, v. 317, no. 5839, p. 793-796.
- Jouzel, J., Stievenard, M., Johnsen, S. J., Landais, A., Masson-Delmotte, V., Sveinbjornsdottir, A., Vimeux, F., von Grafenstein, U., and White, J. W. C., 2007b, The GRIP deuterium-excess record: *Quaternary Science Reviews*, v. 26, no. 1-2, p. 1-17.
- Kanevskiy, M., Fortier, D., Shur, Y., Bray, M., and Jorgenson, T., 2008, Detailed cryostratigraphic studies of syngenetic permafrost in the winze of the CRREL Permafrost Tunnel, Fox, Alaska: Fairbanks, AK, Institute of Northern Engineering.
- Katayama, T., Tanaka, M., Moriizumi, J., Nakamura, T., Brouckov, A., Douglas, T. A., Fukuda, M., Tomita, F., and Asano, K., 2007, Phylogenetic analysis of bacteria preserved in a permafrost ice wedge for 25,000 years: *Applied and Environmental Microbiology*, v. 73, no. 7, p. 2360-2363.
- Kendall, C., and Coplen, T. B., 2001, Distribution of oxygen-18 and deuterium in river waters across the United States: *Hydrological Processes*, v. 15, no. 7, p. 1363-1393.
- Kokorowski, H. D., Anderson, P. M., Mock, C. J., and Lozhkin, A. V., 2008, A re-evaluation and spatial analysis of evidence for a Younger Dryas climatic reversal in Beringia: *Quaternary Science Reviews*, v. 27, no. 17-18, p. 1710-1722.
- Lacelle, D., Lauriol, B., Zazula, G., Ghaleb, B., Utting, N., and Clark, I. D., 2013, Timing of advance and basal condition of the Laurentide Ice Sheet during the last glacial maximum in the Richardson Mountains, NWT: *Quaternary Research*, v. 80, no. 2, p. 274-283.
- Lacelle, D., St-Jean, M., Lauriol, B., Clark, I. D., Lewkowicz, A., Froese, D. G., Kuehn, S. C., and Zazula, G., 2009, Burial and preservation of a 30,000 year old perennial snowbank in Red Creek valley, Ogilvie Mountains, central Yukon, Canada: *Quaternary Science Reviews*, v. 28, no. 27-28, p. 3401-3413.
- Lachenbruch, A. H., 1962, Mechanics of thermal contraction cracks and ice-wedge polygons in permafrost, *Geological Society of America Special Papers*, p. 69.
- Lachniet, M. S., Lawson, D. E., and Sloat, A. R., 2012, Revised C-14 dating of ice wedge growth in interior Alaska (USA) to MIS 2 reveals cold paleoclimate and carbon recycling in ancient permafrost terrain: *Quaternary Research*, v. 78, no. 2, p. 217-225.
- Lachniet, M. S., and Patterson, W. P., 2009, Oxygen isotope values of precipitation and surface waters in northern Central America (Belize and Guatemala) are dominated by temperature and amount effects: *Earth and Planetary Science Letters*, v. 284, no. 3-4, p. 435-446.

- Lisiecki, L. E., and Raymo, M. E., 2005, A Pliocene-Pleistocene stack of 57 globally distributed benthic delta O-18 records: *Paleoceanography*, v. 20, no. 1, p. 17.
- Long, A., and Pewe, T. L., 1996, Radiocarbon dating by high-sensitivity liquid scintillation counting of wood from the Fox Permafrost Tunnel near Fairbanks, Alaska: *Permafrost and Periglacial Processes*, v. 7, no. 3, p. 281-285.
- Lynch, A. H., Chapman, W. L., Walsh, J. E., and Weller, G., 1995, DEVELOPMENT OF A REGIONAL CLIMATE MODEL OF THE WESTERN ARCTIC: *Journal of Climate*, v. 8, no. 6, p. 1555-1570.
- Mackay, J. R., 1975, Closing of ice-wedge cracks in permafrost, Garry Island, Northwest Territories: *Canadian Journal of Earth Sciences*, v. 12, no. 9, p. 1668-1674.
- , 1990, Some observations on the growth and deformation of epigenetic, syngenetic and anti-syngenetic ice wedges: *Permafrost and Periglacial Processes*, v. 1, p. 15-29.
- Mann, D. H., Groves, P., Kunz, M. L., Reanier, R. E., and Gaglioti, B. V., 2013, Ice-age megafauna in Arctic Alaska: extinction, invasion, survival: *Quaternary Science Reviews*, v. 70, p. 91-108.
- MathWorks, 2005, MatLab: Natick, MA, MathWorks.
- Matmon, A., Briner, J. P., Carver, G., Bierman, P., and Finkel, R. C., 2010, Moraine chronosequence of the Donnelly Dome region, Alaska: *Quaternary Research*, v. 74, no. 1, p. 63-72.
- Meyer, H., Dereviagin, A., Siegert, C., Schirrmeister, L., and Hubberten, H. W., 2002, Palaeoclimate reconstruction on Big Lyakhovsky Island, North Siberia - Hydrogen and oxygen isotopes in ice wedges: *Permafrost and Periglacial Processes*, v. 13, no. 2, p. 91-105.
- Meyer, H., Schirrmeister, L., Andreev, A., Wagner, D., Hubberten, H.-W., Yoshikawa, K., Bobrov, A., Wetterich, S., Opel, T., Kandiano, E., and Brown, J., 2010a, Lateglacial and Holocene isotopic and environmental history of northern coastal Alaska - Results from a buried ice-wedge system at Barrow: *Quaternary Science Reviews*, v. 29, no. 27-28, p. 3720-3735.
- Meyer, H., Schirrmeister, L., Yoshikawa, K., Opel, T., Wetterich, S., Hubberten, H. W., and Brown, J., 2010b, Permafrost evidence for severe winter cooling during the Younger Dryas in northern Alaska: *Geophysical Research Letters*, v. 37.
- Meyer, H., Yoshikawa, K., Schirrmeister, L., and Andreev, A., The Vault Creek Tunnel (Fairbanks Region, Alaska): A Late Quaternary palaeoenvironmental permafrost record, *in Proceedings Ninth International Conference on Permafrost (NICOP)*, Fairbanks, Alaska, 2008, p. 1191-1196.
- Miller, G. H., Brigham-Grette, J., Alley, R. B., Anderson, L., Bauch, H. A., Douglas, M. S. V., Edwards, M. E., Elias, S. A., Finney, B. P., Fitzpatrick, J. J., Funder, S. V., Herbert, T. D., Hinzman, L. D., Kaufman, D. S., MacDonald, G. M., Polyak, L., Robock, A., Serreze, M. C., Smol, J. P., Spielhagen, R., White, J. W. C., Wolfe, A. P., and Wolff, E. W., 2010, Temperature and precipitation history of the Arctic: *Quaternary Science Reviews*, v. 29, no. 15-16, p. 1679-1715.
- Mock, C. J., Bartlein, P. J., and Anderson, P. M., 1998, Atmospheric circulation patterns and spatial climatic variations in Beringia: *International Journal of Climatology*, v. 18, no. 10, p. 1085-1104.

- Muhs, D. R., Ager, T. A., and Beget, J. E., 2001, Vegetation and paleoclimate of the last interglacial period, central Alaska: *Quaternary Science Reviews*, v. 20, no. 1-3, p. 41-61.
- Muhs, D. R., Ager, T. A., Bettis, E. A., McGeehin, J., Been, J. M., Beget, J. E., Pavich, M. J., Stafford, T. W., and Stevens, D. S. P., 2003, Stratigraphy and palaeoclimatic significance of Late Quaternary loess-palaeosol sequences of the Last Interglacial-Glacial cycle in central Alaska: *Quaternary Science Reviews*, v. 22, no. 18-19, p. 1947-1986.
- Muhs, D. R., and Budahn, J. R., 2006, Geochemical evidence for the origin of late Quaternary loess in central Alaska: *Canadian Journal of Earth Sciences*, v. 43, no. 3, p. 323-337.
- Opel, T., Dereviagin, A. Y., Meyer, H., Schirrmeister, L., and Wetterich, S., 2011, Palaeoclimatic Information from Stable Water Isotopes of Holocene Ice Wedges on the Dmitrii Laptev Strait, Northeast Siberia, Russia: *Permafrost and Periglacial Processes*, v. 22, no. 1, p. 84-100.
- Osterkamp, T. E., Jorgenson, M. T., Schuur, E. A. G., Shur, Y. L., Kanevskiy, M. Z., Vogel, J. G., and Tumskey, V. E., 2009, Physical and Ecological Changes Associated with Warming Permafrost and Thermokarst in Interior Alaska: *Permafrost and Periglacial Processes*, v. 20, no. 3, p. 235-256.
- Overland, J. E., Adams, J. M., and Bond, N. A., 1999, Decadal variability of the Aleutian low and its relation to high-latitude circulation: *Journal of Climate*, v. 12, no. 5, p. 1542-1548.
- Popp, S., Diekmann, B., Meyer, H., Siegert, C., Syromyatnikov, I., and Hubberten, H. W., 2006, Palaeoclimate signals as inferred from stable-isotope composition of ground ice in the Verkhoyansk foreland, Central Yakutia: *Permafrost and Periglacial Processes*, v. 17, no. 2, p. 119-132.
- Raffi, R., and Stenni, B., 2011, Isotopic Composition and Thermal Regime of Ice wedges in Northern Victoria Land, East Antarctica: *Permafrost and Periglacial Processes*, v. 22, no. 1, p. 65-83.
- Reimer, P. J., Baillie, M. G. L., Bard, E., Bayliss, A., Beck, J. W., Blackwell, P. G., Ramsey, C. B., Buck, C. E., Burr, G. S., Edwards, R. L., Friedrich, M., Grootes, P. M., Guilderson, T. P., Hajdas, I., Heaton, T. J., Hogg, A. G., Hughen, K. A., Kaiser, K. F., Kromer, B., McCormac, F. G., Manning, S. W., Reimer, R. W., Richards, D. A., Southon, J. R., Talamo, S., Turney, C. S. M., van der Plicht, J., and Weyhenmeyer, C. E., 2009, INTCAL09 and MARINE09 radiocarbon age calibration curves, 0-50,000 years cal BP: *Radiocarbon*, v. 51, no. 4, p. 1111-1150.
- Rodionov, S. N., Overland, J. E., and Bond, N. A., 2005, Spatial and temporal variability of the Aleutian climate: *Fisheries Oceanography*, v. 14, p. 3-21.
- Rozanski, K., Araguasaraguas, L., and Gonfiantini, R., 1992, Relation between long-term trends of O-18 isotope composition of precipitation and climate: *Science*, v. 258, no. 5084, p. 981-985.
- Rozanski, K., Johnsen, S. J., Schotterer, U., and Thompson, L. G., 1997, Reconstruction of past climates from stable isotope records of palaeo-precipitation preserved in continental archives: *Hydrological Sciences Journal-Journal Des Sciences Hydrologiques*, v. 42, no. 5, p. 725-745.

- Schlung, S. A., Ravelo, A. C., Aiello, I. W., Andreasen, D. H., Cook, M. S., Drake, M., Dyez, K. A., Guilderson, T. P., LaRiviere, J. P., Stroynowski, Z., and Takahashi, K., 2013, Millennial-scale climate change and intermediate water circulation in the Bering Sea from 90 ka: A high-resolution record from IODP Site U1340: *Paleoceanography*, v. 28, no. 1.
- Schuur, E. A. G., Bockheim, J., Canadell, J. G., Euskirchen, E., Field, C. B., Goryachkin, S. V., Hagemann, S., Kuhry, P., Lafleur, P. M., Lee, H., Mazhitova, G., Nelson, F. E., Rinke, A., Romanovsky, V. E., Shiklomanov, N., Tarnocai, C., Venevsky, S., Vogel, J. G., and Zimov, S. A., 2008, Vulnerability of permafrost carbon to climate change: Implications for the global carbon cycle: *Bioscience*, v. 58, no. 8, p. 701-714.
- Sellmann, P. V., 1967, Geology of the USA CRREL Fox permafrost tunnel, Fairbanks, Alaska, Volume Technical Report 199: Hanover, New Hampshire, US Army CRREL, p. 22.
- Serreze, M. C., Walsh, J. E., Chapin, F. S., Osterkamp, T., Dyurgerov, M., Romanovsky, V., Oechel, W. C., Morison, J., Zhang, T., and Barry, R. G., 2000, Observational evidence of recent change in the northern high-latitude environment: *Climatic Change*, v. 46, no. 1-2, p. 159-207.
- Shur, Y., French, H. M., Bray, M. T., and Anderson, D. A., 2004, Syngenetic permafrost growth: Cryostratigraphic observations from the CRREL tunnel near Fairbanks, Alaska: *Permafrost and Periglacial Processes*, v. 15, no. 4, p. 339-347.
- Souchez, R., Jouzel, J., Lorrain, R., Sleewaegen, S., Stievenard, M., and Verbeke, V., 2000, A kinetic isotope effect during ice formation by water freezing: *Geophysical Research Letters*, v. 27, no. 13, p. 1923-1926.
- Stokes, C. R., Clark, C. D., Darby, D. A., and Hodgson, D. A., 2005, Late pleistocene ice export events into the Arctic Ocean from the McClure Strait Ice Stream, Canadian Arctic Archipelago: *Global and Planetary Change*, v. 49, no. 3-4, p. 139-162.
- Streten, N. A., 1974, Some features of summer climate of Interior Alaska: *Arctic*, v. 27, no. 4, p. 273-286.
- Svensson, A., Andersen, K. K., Bigler, M., Clausen, H. B., Dahl-Jensen, D., Davies, S. M., Johnsen, S. J., Muscheler, R., Parrenin, F., Rasmussen, S. O., Roethlisberger, R., Seierstad, I., Steffensen, J. P., and Vinther, B. M., 2008, A 60 000 year Greenland stratigraphic ice core chronology: *Climate of the Past*, v. 4, no. 1, p. 47-57.
- USGS, 1997, Alaska 300m digital elevation model: EROS Alaska Field Office.
- USNIP, 2011, Isotopes in precipitation at Denali National Park AK03.
- Vasil'chuk, Y. K., 2013, Syngenetic Ice Wedges: Cyclical Formation, Radiocarbon Age and Stable Isotope Records by Yuriy K. Vasil'chuk, Moscow University Press, Moscow, 2006. 404pp. ISBN 5-211-05212-9: *Permafrost and Periglacial Processes*, v. 24, no. 1, p. 82-93.
- Vasil'chuk, Y. K., and Vasil'chuk, A. C., 1998, Oxygen-isotope and C-14 data associated with late Pleistocene syngenetic ice-wedges in mountains of Magadan region, Siberia: *Permafrost and Periglacial Processes*, v. 9, no. 2, p. 177-183.
- Wetterich, S., Rudaya, N., Tumskey, V., Andreev, A. A., Opel, T., Schirrmeister, L., and Meyer, H., 2011, Last Glacial Maximum records in permafrost of the East Siberian Arctic: *Quaternary Science Reviews*, v. 30, no. 21-22, p. 3139-3151.

- Wiles, G. C., D'Arrigo, R. D., Villalba, R., Calkin, P. E., and Barclay, D. J., 2004, Century-scale solar variability and Alaskan temperature change over the past millennium: *Geophysical Research Letters*, v. 31, no. 15.
- Wilson, A. T., 1998, C-14 studies of natural ice: *Radiocarbon*, v. 40, no. 2, p. 953-962.

## VITA

Alison Renee Sloat

### Education

---

**Ph.D. in Geoscience** Expected May 2014  
University of Nevada Las Vegas GPA: 3.9  
**Dissertation:** *Modern to late Pleistocene stable isotope climatology of Alaska*  
Advisor: Dr. Matthew Lachniet

**M.S. in Environmental Sciences** June 2008  
California State University San Bernardino GPA: 3.9  
**Thesis:** *Characterization of natural spring waters of the San Bernardino mountains using stable isotopes of oxygen and hydrogen*  
Advisor: Dr. Erik Melchiorre

**B.S. in Geological Sciences with Honors** June 2005  
California State University San Bernardino GPA: 3.8  
**Emphasis:** Environmental Geology

Summer Geology Field Camp  
July 2004  
Southern Utah University, Cedar City, UT

### Related Experience - Teaching

---

**First Year Seminar Coordinator and Lecturer** 7/2013 - Present  
College of Sciences, UNLV

**First Year Seminar Coordinator and Instructor** 8/2012 - 7/2013  
College of Sciences, UNLV

**First Year Seminar Instructor** 8/2011 - 5/2012  
College of Sciences, UNLV

**Head Physical Geography Laboratory Teaching Assistant** 1/2012 - 5/2012  
Department of Geoscience, UNLV

**Physical Geography Lecturer** 8/2011 - 12/2011  
Department of Geoscience, UNLV

**Part-time Physical Geography Lecturer and Laboratory Instructor** 1/2011 - 5/2011  
College of Southern Nevada, Cheyenne Campus, North Las Vegas, NV

### Related Experience - Industry

---

**Geology Intern** 5/2012 - 8/2012

Aera Energy, Bakersfield, CA

**Senior Staff Geologist**

10/2007 - 6/2009

Leighton Group, Rancho Cucamonga, CA

**Senior Staff Geologist**

3/2007 - 10/2007

Geosyntec Consultants, Riverside, CA

**Staff Geologist**

8/2004 - 3/2007

GeoPentech Consultants, Santa Ana, CA

**Presentations and Publications**

---

Lachniet, M.S., Lawson, D.E., Sloat, A.R., 2012. Revised  $^{14}\text{C}$  dating of ice wedge growth in interior Alaska (USA) to MIS 2 reveals cold paleoclimate and carbon recycling in ancient permafrost terrain. *Quaternary Research* 78, 217-225.

Sloat, A.R., Lachniet, M.S., 2012. Latitude and moisture source control precipitation  $\delta^{18}\text{O}$  and  $\delta\text{D}$  values in Alaska. UNLV GeoSymposium, Las Vegas, NV.

Sloat, A.R., Lachniet, M.S., Lawson, D.E., 2011.  $\delta^{18}\text{O}$  and  $\delta\text{D}$  suggest episodic Late Pleistocene ice wedge growth in Central Alaska. American Geophysical Union annual meeting, San Francisco, CA.

Sloat, A.R., Lachniet, M.S., Lawson, D.E., 2010. A surface water isoscape of Alaska reveals the climate, moisture source, and physiographic controls on  $\delta^{18}\text{O}$  and  $\delta\text{D}$ . American Geophysical Union annual meeting, San Francisco, CA.

**Awards Received**

---

2nd Place, 2012 UNLV GeoSymposium Graduate Poster

2011 Geological Society of America Research Grant, Outstanding Mention Award

UNLV Fay and Jack Ross Scholar Fellowship for one Ph.D. Student, 2009 - 2011

International Arctic Research Center Permafrost Field Course Awardee, Summer 2010

CSUSB Outstanding Undergraduate Geology Student, 2005

**Dissertation Examination Committee**

---

Dr. Matthew Lachniet, Chairperson

Dr. Daniel Lawson, Committee Member

Dr. Ganqing Jiang, Committee Member

Dr. Steve Rowland, Committee Member

Dr. Liam Frink, Graduate College Representative